Structural Behavior of Steel-Concrete-Steel Immersed Tunnels with Imperfections and Varying Interface Conditions

Vasileia Matoula Michou

Delft University of Technology

TU Delft

DELFT UNIVERSITY OF TECHNOLOGY, FACULTY OF CIVIL ENGINEERING AND GEOSCIENCES

Master Thesis

Structural Behavior of Steel-Concrete-Steel Immersed Tunnels with Imperfections and Varying Interface Conditions

Vasileia Matoula Michou (5603749)

Thesis committee:
Prof. Dr. ir. J.G. (Jan) Rots
Dr. ir. C.B.M. Blom
Ir. C.M.P 't Hart

November 17, 2024

Acknowledgments

First and foremost, I would like to express my sincere gratitude to my committee members, Prof. Dr. ir. J.G. (Jan) Rots, Dr. ir. C.B.M. Blom, and Ir. C.M.P 't Hart, for their support throughout my master's thesis journey. Your encouragement and guidance have been invaluable in helping me navigate the challenges of this research. I am especially grateful to my mentor, Dr. ir. C.B.M. Blom, whose wisdom and insights guided me during the most trying times. Your inspiration has not only shaped me as an engineer but also enriched my personal growth.

I also want to express my heartfelt appreciation to my family for their endless support and encouragement. Their belief in me has been a constant source of strength, and without their love and guidance, I would not be standing here today, poised to graduate from the Faculty of Civil Engineering at TU Delft. A special mention goes to my greatest blessing, my twin sister Vanda, whose remarkable patience and unwavering support have meant everything to me, demonstrating that love truly knows no bounds.

Additionally, I am deeply thankful for my small family in the Netherlands, my friends, who have been there for me every step of the way. Their encouragement and warmth have made this journey an exciting and memorable adventure. I would like to give special thanks to Abi and Blas, who stepped into the roles of personal mentors and presentation trainers. Their willingness to help me at every turn has made a significant difference in my experience.

As this journey draws to a close, I reflect on the immense growth and learning I have experienced. This chapter of my life has been filled with valuable lessons and unforgettable moments that I will cherish forever. I am proud of what I have accomplished, and I look forward to the future with hope and excitement.

Abstract

This master's thesis investigates the design and structural behavior of Steel-Concrete-Steel (SCS) composite immersed tunnels, addressing challenges posed by traditional reinforced concrete designs. These challenges - limitations in weight, constructability, and long-term durability, particularly in deep-water environments - are exacerbated by the increasing demand for larger capacity tunnels and the need for efficient, sustainable construction methods. This research explores the impact of construction-induced irregularities, such as interface gaps and shear connector deformation, on the load-carrying capacity and overall performance of SCS tunnels. The study focuses on how irregularities produced during different construction phases affect both the local and global structural behavior of the composite cross-section.

The research approach involves four distinct stages. First, a thorough examination of existing literature provides a foundation of knowledge regarding immersed composite tunnels, encompassing material properties, construction stages, and manufacturing processes. Second, a detailed SCS composite immersed tunnel design is developed, incorporating findings from a reinforced concrete tunnel case study to inform geometry and material selection. Third, numerical analysis using DIANA software is conducted. This includes 2D finite element modeling (FEM) of an SCS composite beam and a 2D FEM of the complete SCS cross-section to investigate the interaction between steel plates and concrete core under various interface conditions (strong bond versus slip) and imperfections (gaps, reduced shear connector effectiveness). Both linear elastic and nonlinear material behavior are considered.

The findings highlight the critical role of horizontal interface connections and the nonlinear behavior of concrete in determining the overall load-carrying capacity and stability of SCS tunnels. The primary load-bearing mechanism identified is the compressive strut within the concrete core; however, the study reveals that the structure's failure is consistently initiated by the failure of this compressive strut, due to crushing under load. This failure mode underscores the limitations of traditional composite theory design methods and highlights the importance of the strut - and - tie model for more accurate design approaches. Construction imperfections significantly impact structural performance: strong interface connections are crucial for effective load transfer, while webs (vertical steel plates) enhance stability. The research concludes with recommendations to improve design practices, emphasizing the importance of strong horizontal connections and careful construction to maintain compressive strut integrity and avoid premature failure.

Contents

Chapter 1

Introduction

1.1 Context

For more than a century immersed tunnels have established an important role in the construction environment. In the recent years, the increasing traffic rate gave rise to the need of widening the cross section and making use of its spaces efficiently. Thus, longer and deeper immersed tunnels have become a real challenge that applies on the existing needs of construction and the emerging technology. These changes lead to new adjustments of the design codes and different designing and construction methods. For example, larger length adds to the requirements of ventilation systems and traffic lanes while the large depth challenges the structural design, depending on the soil conditions. Nevertheless, the new concepts are deviating a lot in terms of constructability and feasibility from the original idea of immersed tunnel that was firstly ever studied.

The idea of this type of structure was firstly developed in United States and Canada due to the need of the construction of a railroad tunnel. The next thirty years, the concept was further evolved and established in the United States, following the emerging technology of steel shell structures. Later on, the first constructed tunnel in Rotterdam introduced this kind of structure in Europe. Shallow river crossings with multiple-lane requirements led to the concrete box design which differed a lot from the initial steel shell design scheme. This new idea was expanded to Europe, marking the difference in the construction type of immersed tunnels between continents. As the need of crossing waterways and creating a better transportation system keeps increasing, a composite cross section design has been brought on and it is under research due to its multiple advantages. The initiative for the development of such a composite structure was first introduced by Japan while many tests and a lot of experimentation have been carried out in the United Kingdom. Nowadays, there are various steel-concrete-steel (SCS) immersed tunnels (sandwich) constructed in the world aiming to familiarise with the new construction idea and address the shortfall of the composite controversial design. Some of them are Osaka Port Sakishima, which connects the Osaka City and Sakishima, a man-made island in Japan, the Kobe Port Minatojima Tunnel, the Okinawa Naha Port Submerged Tunnel and the Shenzheng-Zhongshan Mega Sea Link which also connects the east and west man-made islands in China. However, still many details are to be discovered on account of being a recent development and Europe has yet to include and implement it in its underground projects.

The SCS composite construction is characterised as a very elegant solution among the other types of immersed tunnels and it is described by its high strength, high stiffness, good ductility and good construction efficiency. The detailed cross section consists of outer and inner panels with transverse and longitudinal

plates which form three-layer boxes (chambers of steel plates) for concrete pouring. This design results in an ideal configuration as the concrete core accounts for the compressive loadings and the steel plates for the tensile ones. The concrete layer is required to be composed of a very fluid self - compacting mix in order to reach an adequate quality of its filling performance. This type of concrete, which belongs to the category of engineered cementious composite mixtures, attributes to a high strength and high ductility structure. The connection between and steel plates and the concrete core is accomplished by stiffeners and shear studs placed on the inner face of both steel plates (top and bottom steel layer) aiming to achieve the composite action. In addition to these, L-shaped welding ribs are also applied on the inner face of the plates which contribute to the stiffness and create a strong bond between the three layers.

Through out the years, many challenges emerged and were investigated in order to make the construction of such composite structure possible. Structurally, many of them mostly appear due to the complexity of the composite section. Since the number of composite immersed tunnels built is relatively small, and their structural systems are not as clear and explicit as reinforced concrete or steel structures, some technical performance indicators still need to be investigated. In the loading phase, the three-layer boxes tend to deform due to bending causing imperfections and failure of the composite connection. Thus, the shear studs can no longer resist the shear loading in the compression zone, leading to large deformation and interface gaps between the steel plates and the poured concrete. Furthermore, the slenderness of the structure, apart from benefiting the structure in terms of cost-effectiveness and reduced material usage, it is also a drawback. Specifically, high loads in the slender structure can lead to local high strain/stress concentration points which might exceed the design's limitations. In terms of construction, difficulties arise at the initial stages due to the fluid mixture of concrete core. Many placing techniques are implemented in order to achieve the fluidity of concrete through and around the whole section and avoid voids in the bonds of the core between steel plates and studs. However, the lack of voids cannot be guaranteed and measurements should be taken into account in order to deal with the irregularities of the structure.

With an optimal design to be used, an understanding of the failure mechanisms and the bonding relationships between the different materials could be used to devise the most effective designing process. While 2D models and analytical solutions have been already developed, there is still a need for investigating further the composite performance of the cross section and clarifying whether the role of the shear components is contributing sufficiently to the design. A focused analysis of a small beam segment can provide highly accurate insights into the behavior of the cross-section, offering a detailed view of the interaction between layers. This localized approach, combined with a magnified analysis (2D model cross-section) of the three-layer boxes, can effectively reveal the influence of voids on the overall cross-sectional behavior.

1.2 Problem Statement

Although in the last few decades the sandwich tunnel connection has been investigated and implemented more and more on underground projects, there are still some difficulties left to cope with in regard to its constructability. In order to achieve an effective design, with high strength, good ductility and durability level the critical components which lead to different failure mechanisms in the different construction phases should be studied. The source of irregularities and imperfections of the design should be investigated as well as the local and global behavior of the structure. The strain/stress concentration points, the interface gaps between the steel plates and the concrete core, the possible welding points imperfections, the deformations of the shear studs as well as the extent of influence of the confined concrete's inner voids need to be analysed.

1.3 Research Objective

The objective of this research is analysing how and if the irregularities and imperfections produced during the construction phases of the structure can affect the local and global behavior of the composite cross section. Irregularities are described by gaps in the interface of the steel plate and the shear connectors, deformation of the shear studs during pouring of concrete, inner voids inside the steel chambers, welding imperfection in the interface connection of the steel plates and/or welding imperfection in the connection of the steel plate with the shear connectors.

1.4 Research Questions

The main research question for the study is formulated as,

"How do the irregularities produced during the different construction phases affect the local and global behavior of the composite cross section?"

Based on the main research question, the sub-questions are:

1. What are the most critical components in SCS tunnel design that contribute significantly to the overall strength, stiffness, and stability of the structure?

2. How are the stresses distributed in the roof element of the composite cross-section?

3. What are the governing bearing mechanisms and global failure mechanisms of the structure?

4. How does the presence of shear connectors influence the structure in case of disconnections (gaps)?

5. To what extent the interface gap between the steel plates and the concrete core influence the strength level of the structure? Is it insignificant?

Chapter 2

Approach

The research approach involves four distinct stages: a thorough examination of existing literature, the study area of the designing process, the application of software-based simulations encompassing both systematic and case-specific investigations, and a reflective analysis of the results. These stages, when combined, offer a comprehensive idea of the behavior of a composite tunnel and its utility based on the different variations.

The first phase involves an extensive literature study, which forms the foundation of this research. A systematic review of papers, academic journals and technical reports is conducted to gather relevant information on various aspects related to immersed composite tunnels. This includes understanding the properties of the materials used, the applications and the different stages of the construction, as well as the manufacturing processes.

The second phase of the research is dedicated to the theory and design of composite structures based on the two different materials, steel and concrete, by exploring the mathematical equations and governing principles that need to be followed in the designing phase. Therefore, to effectively carry out this study, a deep understanding of the adequate designing process should be investigated based on the knowledge of hydro- and geo- dynamics, as well as the utilization and impact of various materials, along with their collective interactions.

The third stage of the research is focused on running computer simulations using DIANA software. This phase includes both a systematic investigation and a practical case study based on the design. The systematic study is the most important part of this phase, carefully examining and improving the research approach. It explores factors such as boundary conditions, modeling techniques, output parameters, and software functionality. This in-depth examination establishes a framework for understanding how different variables affect the performance of the immersed composite structure. Specifically, the tunnel cross section under research will be modelled firstly in SCIA based on a static preliminary design of a frame. Later on, with the use of DIANA software, a 2D small beam model will be generated and analysed. A detailed 2D finite element analysis of the entire cross section will be completed after the evaluation of the first 2D model. Changing parameters and dimensions will lead to a better insight of the different components and materials used. The bond between steel and concrete will be analysed based on the stress strain relationship, and validation of the computational results will be checked to ensure the model's accuracy, as well as the internal and the global stability of the structure.

In the research's concluding phase, a reflective analysis is undertaken, aiming to place the research findings

in context while recognizing its limitations, challenges, and unresolved inquiries. This phase highlights the significance of the 2D simulations of the immersed composite structure under different loading conditions while it also serves as a foundational element for drawing conclusions, emphasizing the role of composite connections in the new and emerging designs of immersed tunnels.

Chapter 3

Literature Study

The literature review carried out in this research project forms an important foundation, offering crucial insights and knowledge before the application of advanced software to build models and perform finite element analysis. It delves into various critical aspects, facilitating a detailed understanding of the complex domain of immersed composite tunnels.

The literature study begins by briefly examining immersed tunnels and the path that has lead to the composite design, exploring its distinctive attributes and diverse applications. This initial part provides the necessary background for comprehending the unique challenges associated with this type of construction.

Following that, the literature review explores in detail the domain of steel-concrete-steel immersed tunnels. This section aims to refresh the foundational principles and the principal challenges of the behaviour of this complicated cross-section within the constructed environment.

Finally, the literature review also involves an investigation of comparable studies and research initiatives. The inclusion of these external viewpoints aims to place the current research within the broader context of composite immersed construction, allowing for a contextualized assessment of its importance.

3.1 History of immersed tunnels

An immersed tunnel is a type of underwater passage constructed by assembling prefabricated tunnel sections or segments on land, which are then floated into position and submerged into a trench prepared on the seabed. This construction method contrasts with traditional boring techniques used in regular tunnels, where excavation occurs directly underground without the need for floating and submerging sections. Immersed tunnels minimize environmental disruption during construction and can provide expedited transportation solutions in aquatic environments. Over the years, they have become essential components of modern infrastructure, facilitating the efficient movement of people and goods across waterways while maintaining navigational access. [1]

The development of immersed tunnels began to take shape in the early 20th century as engineering techniques advanced and the growing demand for efficient underwater transportation systems emerged. The Holland Tunnel, opened in 1927, is considered the first modern immersed tunnel. Connecting New York City with Jersey City, this tunnel is particularly notable for its innovative ventilation systems and structural designs that served to deal with heavy traffic. The construction process involved precasting large

segments of the tunnel on land, floating them to the construction site, and submerging them into a trench. This method not only reduced construction time but also minimized the environmental impact associated with underwater projects, thus setting a precedent for future immersed tunnel designs and construction techniques. [2]

In the following years, the success of the Holland Tunnel inspired further advancements in this type of construction. The Detroit-Windsor Tunnel, completed in 1930, was built to facilitate traffic between the United States and Canada. Employing similar immersed construction techniques, this tunnel emphasizes the feasibility and efficiency of immersed tunnels for international transportation. This essential route has fostered economic and social connectivity between the two nations and contributed to the growth of regional commerce [3].

As urbanization and infrastructure demands increased globally, the mid-20th century witnessed a rise in immersed tunnel construction, especially in regions with significant maritime traffic. Throughout the 1970s and 1980s, various immersed tunnels were developed across Europe, taking advantage of improved construction techniques and innovations. One notable example is the Køge Bay Tunnel in Denmark, opened in 1996, which showcased the ongoing evolution of construction methods and materials used in immersed tunnels.[4]

The completion of the Seikan Tunnel in Japan in 1988 marked another significant milestone in the field of tunnel engineering. While not exclusively an immersed tunnel—featuring both immersed and bored sections - the Seikan Tunnel runs beneath the Tsugaru Strait and exemplifies significant advancements in underwater construction methods. Spanning 53,85 km (33,5 miles), it is one of the longest underwater tunnels globally and was specifically designed to withstand severe weather conditions, including typhoons and seismic activity, underscoring the need for resilience in modern engineering. [5]

In recent years, technological advancements have driven further innovations in immersed tunnel design and construction. For instance, the Zhangzhou Bay Tunnel, completed in 2016 in China, employed advanced construction methods that blended traditional immersed tunneling techniques with modern technology, resulting in enhanced strength and reduced project duration. [6]

The Øresund Link, completed in 2000, serves as a prominent example of the versatility and potential of immersed tunnels. Connecting Denmark and Sweden, this project features an immersed tunnel section integrated with a bridge, highlighting the importance of this technology in large-scale infrastructure projects.[7]

3.2 Rise of composite immersed tunnels

While regular immersed tunnels, constructed primarily from reinforced concrete, provide effective solutions for underwater transportation, they are not without their limitations. For instance, the inherent weight of concrete sections can lead to challenges in both construction logistics and structural performance, particularly in deeper waters where buoyancy and structural integrity become critical considerations. Additionally, conventional designs can be more susceptible to issues such as corrosion and maintenance difficulties over time, especially when exposed to harsh marine environments.

As infrastructure demands continue to grow, there is an increasing need for designs that not only address the limitations of traditional immersed tunnels but also offer enhanced performance, durability, and cost-effectiveness. This has prompted engineers and researchers to explore innovative tunnel designs that integrate new materials and construction techniques.

In response to these challenges, the Steel-Concrete-Steel (SCS) composite immersed tunnel design has emerged as a promising alternative. This innovative design serves to capitalize on the strengths of both steel and concrete, resulting in a tunnel structure that is not only lighter but also possesses superior load-bearing capacity and enhanced durability under extreme conditions. The SCS design presents a 'sandwich' structure that integrates outer and inner steel plates with a concrete core, offering a combination of tensile and compressive strength that significantly improves performance over traditional designs. [8]

3.2.1 Examples of composite immersed tunnels

Over the years, numerous efforts have been undertaken to construct this type of composite infrastructure, with a multitude of distinct examples found across various continents worldwide. Listed below are some of the examples, each accompanied by crucial details regarding the structure's significant attributes.

Kobe Part Minatajima lhnnel: Thejima immersed tunnel is an important engineering project located in Japan, aimed at improving transportation connectivity in the Kobe area. It features a sandwich composite design, consisting of outer steel layers encasing an inner concrete core, which effectively balances strength and lightweight properties. This innovative structure enhances resistance to water pressure and seismic forces, making it particularly suitable for regions vulnerable to earthquakes. The construction involved precast segments that were floated to the site and submerged, highlighting modern advancements in tunnel engineering. Overall, the project exemplifies the advantages of composite materials in achieving durability and safety in infrastructure. [9]

Channel Tunnel (Eurotunnel): The Channel Tunnel, linking the United Kingdom and France, stands as an iconic illustration of sandwich immersed tunnels. This remarkable structure comprises two parallel railway tunnels, featuring an outer steel shell for protection, an inner concrete layer providing buoyancy, and an additional inner concrete layer ensuring structural integrity. [10]

Okinawa Naha Port Submerged Tunnel: Theaha Port submerged tunnel is an important infrastructure project aimed at improving transportation networks in Okinawa, Japan. Utilizing a sandwich composite design, the tunnel consists of outer steel layers surrounding a reinforced concrete core, resulting in a lightweight yet durable structure. This submerged configuration helps minimize disruption to surface activities, ensuring that maritime operations remain unaffected while decreasing land traffic. Designed to withstand environmental factors such as wave impacts and seismic events, the tunnel showcases modern engineering techniques that prioritize functionality, safety, and environmental sustainability.[9]

Guldborgsund Tunnel: Linking the Danish islands of Falster and Lolland, the Guldborgsund Tunnel is a highway tunnel engineered with a sandwich structure to endure the challenges of its underwater environment. [11]

Osaka Yumeshima Tunnel: The Osaka Yumeshima Tunnel is a rail-road tunnel located in Japan, finished in 2009. It is notable for its hybrid structure, featuring both full sandwich and open sandwich design elements. The roof and walls of the tunnel are constructed as full sandwich structures, while the floor slab follows an open sandwich design. This tunnel serves as a crucial transportation link, facilitating rail and road connections in the region. [9]

Shen-Zhong Tunnel: The most recent application of the sandwich design is also applied for the Shenzheng-Zhongshan mega sea link in China, which actually is a tunnel and bridge combination. The highway link features multiple lanes in each direction, designed for a high-speed limit and a long design life. Construction has been ongoing for several years, and the project's completion is now at the midway point. This project is comparable in scale to the recent Hong Kong-Zhuhai-Macao immersed tube and bridge highway

link project.[12]

Figure 3.1: Cross-section of Shen-Zhong Tunnel [13]

Figure 3.2: Steel element of Shen-Zhong Tunnel completed in a shipyard [13]

3.3 SCS composite immersed tunnel

A detailed overview of the SCS composite tunnel design is presented in this section. The key components of the design are illustrated in the figure below.

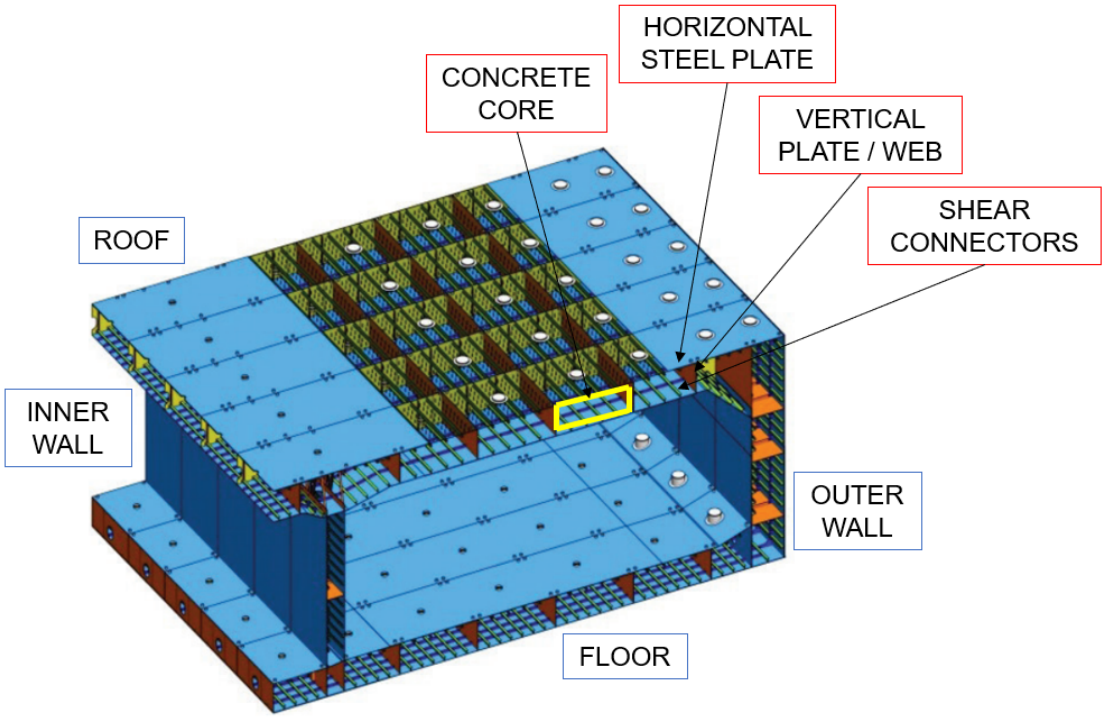

Figure 3.3: Concept of a SCS cross-section [13]

This type of composite construction stands out as an elegant and highly effective solution among the various types of immersed tunnels. It is characterized by its strength, high stiffness, good ductility, and construction efficiency. The intricate cross-sectional design comprises both outer and inner panels, incorporating transverse and longitudinal plates that form three-layered boxes, akin to chambers (boxes) composed of steel plates, for the subsequent pouring of concrete. This innovative design yields an optimal configuration, where the concrete core bears the compressive loadings, while the steel plates resist the tensile forces.

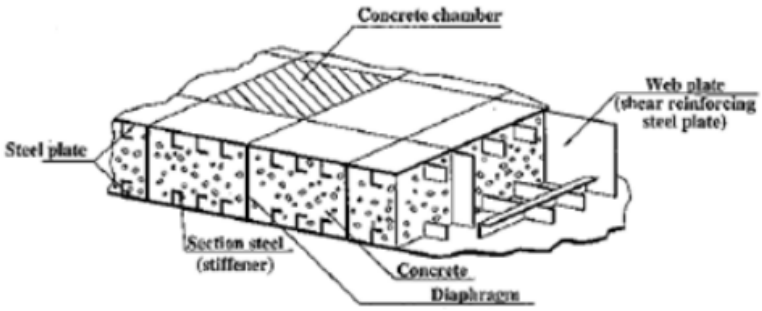

Figure 3.4: Detail of SCS element

Achieving this structural balance requires the use of a highly fluid and self-compacting concrete mixture to ensure a high-quality filling performance. This particular concrete mixture falls under the category of engineered cementitious composites, known for imparting both strength and ductility to the resulting structure. Typically, the distance between the vertical steel plates (webs) is maintained at approximately 3 meters, with these plates intricately linked to the unreinforced concrete. This connection is achieved through the strategic placement of stiffeners and shear studs on the inner surface of both steel plates, consisting of the top and bottom steel layers. These elements are essential for achieving the composite action, optimizing the tunnel's structural performance.[13]

Furthermore, L-shaped welding ribs are thoughtfully applied to the inner face of the plates, serving to enhance stiffness and establish a strong bond across all three layers. This meticulous attention to detail in the design and construction of composite immersed tunnels ensures their resilience and longevity, making them an ideal choice for underwater tunnel projects where strength, durability, and efficiency are essential.[13]

3.4 Benefits and objectives of SCS immersed tunnels

Steel-concrete-steel (SCS) immersed tunnels have become a practical solution that combines the benefits of steel and concrete to address the needs of growing urban areas. By using modern engineering techniques, SCS tunnels provide various features that enhance their functionality and applicability, making them a good choice for underwater construction projects.

3.4.1 Functional benefits

Composite immersed tunnels find diverse and crucial applications across various domains, contributing to the improvement of infrastructure and sustainable development.

- **Longer spans**: The SCS design enables longer spans between supports, which reduces the number of required foundations. This capability not only minimizes construction time but also lessens the environmental impact by reducing disruption to underwater habitats and sediment during the construction phase. The reduction in the number of support structures can lead to a more streamlined and aesthetically pleasing design, allowing for broader navigation channels beneath bridges and tunnels. [9]

- **Deeper Submergence**: Enhanced strength and stiffness are fundamental characteristics of the SCS design, allowing it to accommodate deeper submergence levels without compromising safety or structural integrity. This quality enables engineers to build tunnels in locations where traditional designs might be insufficient, thus expanding the potential for underwater infrastructure and connectivity. [9]

- **Greater Load-Carrying Capacity**: By combining the tensile strength of steel with the compressive strength of concrete, SCS tunnels have an increased capacity to handle heavy traffic loads. This design also allows the structure to effectively manage challenging soil conditions and external forces, making them suitable for high-traffic environments such as urban centers. [14]

In summary, the steel-concrete-steel design offers several notable benefits, particularly in scenarios which demand innovative engineering solutions.

3.4.2 Objectives for using SCS immersed tunnels

As civil engineering focuses more on sustainability and strong structures, there is a greater need to examine design options for immersed tunnels. Understanding the specific objectives of steel-concrete-steel (SCS)

tunnels is important for knowing why they are also chosen. [15]

- **Enhanced structural performance** : The composite nature of SCS tunnels results in improved overall performance compared to traditional designs. This includes higher strength, stiffness, and load-carrying abilities, which are essential for ensuring the safety and longevity of the tunnel in the face of adverse conditions such as seismic activity or extreme weather.

- **Optimized construction**: SCS tunnels can significantly simplify construction processes by reducing the need for numerous foundations. This not only makes the construction logistics less complex but also accelerates project timelines. Fewer foundations lead to less excavation and disturbance, reducing costs and expediting the project's overall completion.

- **Increased durability**: One of the most significant advantages of SCS immersed tunnels is their enhanced resistance to corrosion and deterioration over time. By utilizing steel, which is inherently resistant to tensile forces, and concrete, which can provide a robust barrier to environmental factors, the sandwich structure better withstands the harsh conditions associated with underwater environments. This durability ensures that SCS tunnels remain reliable even under prolonged exposure to seawater, sediments, and fluctuating pressures.

Steel-concrete-steel (SCS) immersed tunnels are increasingly important in modern civil engineering due to their ability to achieve longer spans, accommodate deeper submersion, and handle heavy loads, all while reducing construction time and enhancing durability. These features make SCS tunnel designs a significant improvement over traditional tunnel designs. As infrastructure demands continue to rise globally, SCS designs are expected to play a crucial role in future underwater construction. This importance is further supported by various research and experiments conducted on SCS immersed tunnels. The following studies offer valuable insights into their structural performance and material properties, helping to improve design practices for effective use in different engineering applications.

3.5 Disadvantages of SCS immersed tunnel

After discussing the advantages of sandwich (steel-concrete-steel) composite immersed tunnels, such as their durability, high load-bearing capacity, and enhanced structural performance, it is essential to consider the associated disadvantages. While this structure present a robust solution for underwater tunneling, they also come with certain drawbacks that must be addressed during the planning and construction phases. The following points outline the key disadvantages to bear in mind:

- Complex construction process: The intricate construction demands precise engineering and advanced techniques, which can complicate the overall execution of the project. [12]

- High cost: Utilizing premium materials and specialized construction methods often results in increased project costs compared to alternative tunneling approaches.[12]

- Corrosion risks: Steel components face the risk of corrosion without adequate protection, potentially impacting the structure's long-term integrity.[2]

- Limited repair options: Addressing damage or leaks can be challenging and may involve disruptive and complex solutions to restore full functionality without compromising the tunnel. [12]

In summary, while sandwich composite immersed tunnels offer substantial benefits, an understanding of these disadvantages is crucial to ensure their successful implementation and sustainable operation.

3.6 Research initiatives and experiments

3.6.1 Research on SCS immersed tunnels

Research related to steel-concrete-steel (SCS) immersed tunnels has been increasingly focused on understanding their structural performance, material properties, construction techniques, and durability under challenging conditions. One primary area of investigation is the structural performance of SCS immersed tunnels, which examines their behavior under various loading conditions, including static and dynamic loads. Understanding how the composite action of steel and concrete contributes to increased strength and stability is fundamental, particularly in seismic conditions. Notably, Chen (2018) highlighted the seismic performance of composite immersed tunnels in their study published in the Journal of Engineering Geology. [14]

Another significant focus has been on the material properties and behavior of the components used in SCS tunnels. Research has underlined the strengths and durability of steel and concrete in these composite structures, emphasizing their robustness and watertight performance over the long term in marine environments. For example, a study by Luttikholt, Doorduyn, De Wit and Li (2022) assessed the analysis and performance of steel–concrete composite immersed tunnels, adding to the understanding of material efficiency and resilience. [12]

The application of finite element modeling has also gained importance in recent research aimed at optimizing SCS tunnel design. Investigations utilizing finite element analysis (FEA) have shown how simulation can predict structural responses to various loading scenarios, enhancing safety and performance considerations for tunnel construction. Researchers from Tongji University in Shanghai conducted an important investigation into the advanced finite element modeling of SCS immersed tunnels, providing significant insights into their structural mechanical behavior. Their findings were presented at the International Conference on Advances in Steel Structures. [14]

Construction techniques and challenges associated with SCS tunnels are another key research area. Studies focusing on construction methodologies highlight the logistical considerations related to the assembly and underwater placement of sandwich components, thus improving execution efficiency. [16] Researchers from Rizvi College of Engineering in Mumbai explored the construction and design challenges associated with composite immersed tunnels, emphasizing various underground methods to tackle urban congestion issues. Their study evaluates how different tunneling techniques influence induced ground surface settlements and identifies key factors such as geological conditions and tunnel geometry that significantly impact these settlements. This research offers important insights to guide future tunnel construction projects, serving as a valuable resource for contractors, engineers, and designers. [17]

Finally, there is ongoing exploration of innovative design approaches for SCS tunnels, with a focus on methodologies that enhance functionality and structural performance. Yan, Liew, Zhang and Sohel (2015) investigated innovative design concepts for SCS composite immersed tunnels in their publication in "Material and Structures", contributing to the growing body of knowledge in this area.[18]

Overall, the growing area of research surrounding SCS immersed tunnels highlights significant advancements in the understanding of their performance under various conditions, material efficiency, and innovative construction techniques, furthering the application of this modern engineering solution in infrastructure development.

3.6.2 SCS tunnel element experiments

Research on steel-concrete-steel (SCS) immersed tunnels has included several key experiments focusing on their structural performance, material behavior, and optimization techniques. One significant study

conducted at the University of Wales in Cardiff involved ultimate load testing of SCS sandwich elements, including beams, columns, and joints. This experiment specifically aimed to evaluate the structural performance of SCS tunnel elements under maximum load conditions and validate previous findings regarding their behavior. The results demonstrated that most components exhibited ductile behavior, with only one beam experiencing sudden failure due to issues with the tension plate connector. These findings underscore the critical importance of ensuring secure connections between the steel and concrete components in SCS tunnel designs. This initial phase of testing laid the groundwork for further studies aimed at creating a comprehensive design guide for SCS construction. [15]

Other studies, particularly fatigue tests, were performed to assess the durability of SCS connections under repeated loading conditions. These tests evaluated various factors, such as plate thickness, stud length, and concrete strength within the context of SCS connections rather than the tunnel elements themselves. The results indicated that failures primarily arose from cracking of the tension plate connectors at the weld-affected zones, highlighting the necessity for meticulous consideration of connection areas in future designs.[19]

Additionally, advanced finite element modeling has been utilized to simulate the behavior of SCS immersed tunnels under various loading scenarios. While these models provide valuable insights into the connections and composite action, they often do not focus specifically on the SCS tunnel elements. This gap highlights the need for more targeted research on the structural integrity and performance of the elements themselves. Liew, Yan and Huang (2017) note that further investigations into the distinct behaviors of the SCS structures can significantly enhance design methodologies. [20]

In summary, it can be observed that the existing experiments predominantly either focus on SCS connections or assess various aspects of the SCS system without specifically analyzing SCS tunnel elements. This distinction sets the stage for my thesis, which will concentrate on conducting a finite element analysis of the SCS tunnel element itself. By addressing this specific focus, my research aims to fill the existing gaps in understanding the behavior of SCS tunnel elements, ultimately contributing to the advancement of design methodologies for these innovative structures.

3.7 Challenges of SCS tunnels

Over the passage of time, the construction of composite immersed tunnel has encountered a numerous of challenges, primarily resulting from the complex nature of its composite cross-section. These challenges have arisen in part due to the relatively limited number of composite immersed tunnels constructed, resulting in a less well-defined and explicit understanding of their structural systems compared to conventional reinforced concrete or steel structures. Consequently, there remains a need for ongoing investigation into a variety of technical performance indicators.

One notable challenge materializes during the loading phase when the three-layer boxes are subject to bending forces, causing deformation. This deformation can lead to imperfections within the structure and, in more severe instances, even result in the failure of the composite connections. As a consequence, the shear studs, which play a critical role in resisting shear loading within the compression zone, may prove inadequate, leading to significant deformation and the formation of interface gaps between the steel plates and the poured concrete.

Moreover, the slenderness of this structure, while advantageous in terms of cost-efficiency and reduced material usage, introduces its own set of complications. High loads applied to the slender structure can lead to localized strain and stress concentrations, potentially surpassing the design's stipulated limits.

In the area of construction, challenges emerge during the initial phases, primarily due to the requirement

for a fluid concrete core mixture. Various placement techniques have been employed to ensure the uniform flow of concrete throughout the entire section, thus preventing the formation of voids in the bonds between the core, steel plates, and studs. Nevertheless, the complete elimination of voids proves to be a challenging task, necessitating measurements and strategies to address the inherent irregularities within the structure. [21]

In the context of SCS sandwich tunnels, fire safety is a more significant concern compared to other tunnel types. [22] This heightened concern arises from the steel's excellent heat absorption properties. Given that the steel is exposed on the outer side of the structure, it becomes more susceptible to heat generation within the tunnel. In contrast, reinforced concrete tunnels have steel bars encased in concrete, mitigating this issue. To address the fire safety challenge of SCS sandwich tunnels, a fire-resistant layer is applied to the outer steel shell.

These challenges highlight the complicated and unique nature of composite immersed tunnels, emphasizing the imperative need for continual research, innovation, and precise engineering to overcome structural and construction obstacles and guarantee the successful realization of this composite structure. To address these challenges effectively and to gain a deeper understanding of the behavior of SCS, finite element analysis (FEM) has become a crucial tool for simulating and analyzing the complex interactions within these structures. The next chapter will dig into the application of FEM to SCS tunnels, examining the fundamental principles of FEM, its advantages in modeling these complex structures, and the specific applications of FEM in addressing the challenges discussed above. By examining previous research that has successfully utilized FEM for similar applications, it can be achieved a deeper understanding of the potential of FEM for optimizing the design and construction of SCS tunnels.

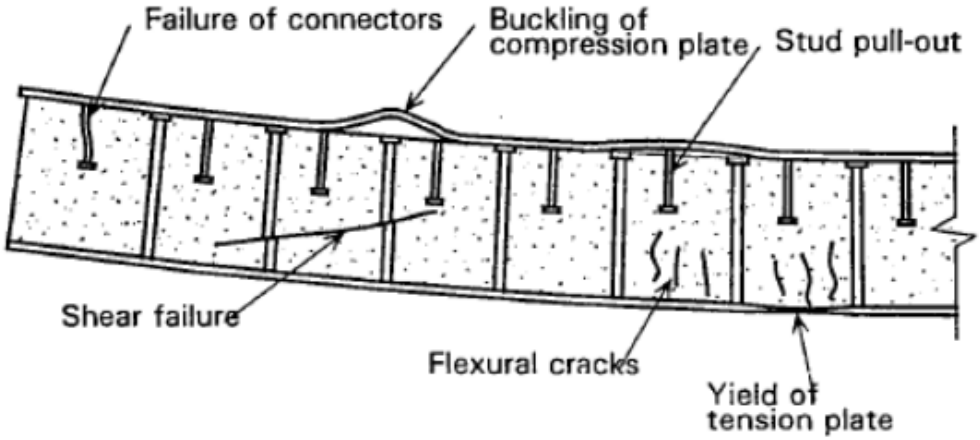

Figure 3.5: Failure modes of SCS tunnel element

3.7.1 Modeling and analysis of sandwich immersed tunnels using FEM

While the composite structure represents a promising design for immersed tunnels, its relatively recent introduction means that significant research, including extensive finite element analysis (FEM), is still needed to fully understand its complex behavior and optimize its performance. This is especially true given the limited number of existing tunnels of this type, necessitating ongoing investigation to explore the complex interactions between its components.

Over the years, several research efforts have focused on the numerical simulation of SCS sandwich tunnels,

exploring the behavior of these structures.

A 2018 study titled "Lateral Static Analysis on Steel-Concrete-Steel Composite Structure in Immersed Tunnel of Shenzhen-Zhongshan Link" investigated the **lateral static behavior** of an SCS composite structure using a 3D solid nonlinear finite element model. [14] This research revealed that both the horizontal top and bottom steel plates, along with the concrete core, contribute significantly to the **lateral bending resistance** of the tunnel element. The transverse plates (webs) and the concrete play a more critical role in providing shear resistance. The FEM analysis also illustrated the distribution of shear force between the steel and concrete through the shear connectors, highlighting the significance of the shear connectors (stiffeners and studs) for a stable and well-connected design. The study concluded that the shear regions experience higher shear forces, while the bending-moment regions experience larger pull-out forces.

Another study released in 2019 focused on the **shear resistance** of steel-concrete-steel composite structures with bidirectional webs, commonly used in large-scale immersed tunnels. [22] The research utilized a 3D nonlinear finite element model to analyze the shear behavior of this design under various loading conditions. After validating the accuracy and efficiency of a simplified model design, a parametric analysis was conducted to determine the influence of various factors, such as concrete properties, axial web dimensions, and shear-span ratio, on shear resistance. The study proposed a theoretical method for predicting shear resistance, incorporating dowel action and small shear-span ratios, to improve accuracy.

A 2022 research titled "Experimental and numerical investigation of the cross-sectional mechanical behaviour of steel-concrete-steel immersed tube tunnel" investigated the **mechanical behavior** of SCS immersed tunnel nodes. [8] The study performed experimental tests on T and L-shaped nodes subjected to vertical axial compression and lateral displacement loads. To validate the experimental findings, a numerical simulation was created, demonstrating good agreement between the model and experimental results. The research focused on the **damage mechanisms** of the tunnel nodes under seismic loading, pointing out the importance of local reinforcement in the outermost vertical walls to ensure sufficient ductility. The study concluded that the modeling method effectively simulated the mechanical properties of the structure, providing valuable guidance for the design of SCS immersed tunnels.

Future Research Directions

While significant progress has been made in understanding the behavior of SCS immersed tunnels using FEM, several areas for future research remain. It is understandable that further development in FEM models is needed in order to explore in depth the complex phenomena such as cracking propagation, the interaction between concrete and steel under various type of loading and the impact of localized stress concentrations.

Existing research has primarily focused on the base behavior and stability of SCS tunnels, seeking to understand the overall performance of the structure and its components. However, a broader perspective is needed to examine the design in a more realistic, real-world context, particularly considering the imperfections that inevitably arise during construction.

This thesis will focus on the interface connection between concrete and steel plates, an area that has not been extensively investigated for the sandwich design immersed tunnel. Specifically, the research aims to understand how imperfections such as voids in the concrete core, deformations of the connectors, and gaps in the interface between the horizontal plates and concrete affect the overall stability and performance of the structure. This deeper understanding will be crucial for developing solid and reliable design strategies for this innovative structure.

Chapter 4

Reinforced concrete tunnel

4.1 Purpose of the case study

This case study aims to understand the key uncertainties related to the behavior of SCS composite immersed tunnels. The goal is to gain a deeper understanding of how these tunnels respond to loads and deform, especially considering the challenges posed by various failure modes and construction imperfections. It is needed to investigate how different construction phases can lead to various types of failure, and how imperfections like voids and shear stud deformation impact the overall performance of the tunnel. To achieve this, it will be developed a sophisticated 2D model that can accurately simulate the behavior of the composite tunnel. This model will help identify the critical parameters and factors that influence the stability and reliability of these tunnels.

4.2 Reinforced concrete tunnel

4.2.1 Dimensions

The initial step in the tunnel element design process involves establishing the tunnel's dimensions. This can be accomplished through the application of empirical rules or by drawing upon past experiences. Subsequently, an assessment is carried out to verify the tunnel's ability to withstand bending moment, shear, and normal forces. If necessary, the dimensions will be adjusted to meet the structural requirements. A detailed summary of these dimensions can be found in Table 1, and a visual representation is provided in the figure below.

Dimensions	Value	Unit
Total width of tube	15000	mm
Width of gallery	1200	mm
Floor thickness	1300	mm
Roof thickness	1100	mm
Outer wall thickness	1200	mm
Inner wall thickness	800	mm
Inner height tunnel	7200	mm
Total height tunnel	9600	mm
Total width tunnel	36800	mm

Table 4.1: Dimensions of reinforced concrete tunnel

4.2.2 Loadings

In order to determine the loading conditions imposed on the tunnel, a comprehensive understanding of various factors is essential. These include the material properties, dimensions of the structural elements, material thicknesses, and the depth beneath the water surface. A detailed summary of these crucial parameters can be found in Table 4.2 below. The first column of Table 4.2 provides information on the specific weight of the materials used in the tunnel's construction. In the second column, the precise dimensions of the tunnel are outlined, encompassing its width, height, and other relevant structural aspects. The third column offers insights into the water and ground levels, providing context for the tunnel's placement and the external forces it encounters. This data serves as the foundation for assessing and understanding the tunnel's loading conditions.

Material properties		Dimensions	[m]	Reference levels	[m]
$\rho_{sediment}[kN/m^3]$	17,5	Protection layer	1,0	Design HWL	1,68
$\rho_{backfill}[kN/m^3]$	20	Roof thickness	1,1	Ground level	-3,45
$\rho_{rock}[kN/m^3]$	22	Asphalt thickness	0,12	Road level	-11,53
$\rho_{water}[kN/m^3]$	10,35	Ballast concrete	1,1	Bottom level	-14,05
$\phi_{soil}[deg]$	30	Floor thickness	1,3		
K_0	0,5	Inner height	7,2		

Table 4.2: Material properties, dimensions, and levels

The process begins with the assessment of hydraulic loading on the tunnel element. To achieve this, hydraulic stresses are evaluated across the height of the tunnel's cross-section. Subsequently, the total vertical stress is determined. By subtracting the hydraulic stress from this total vertical stress, we obtain the effective vertical stress. With an internal friction angle of 30°, the coefficient of lateral earth pressure at rest remains a key factor to be defined based on the formula $K_0 = 1 - sin(\varphi) = 1 - 0,5$. This information allows for the calculation of the effective horizontal stress, achieved by multiplying the effective vertical stress by the coefficient of lateral earth pressure. Consequently, the total horizontal stress on the tunnel can be derived by summing the hydraulic stress with the effective horizontal stress. These computations are detailed in table 4.3 below.

Levels	[m]	$\sigma_{hydraulic}[kN/m^3]$	$\sigma_{soil}[kN/m^3]$	$\sigma_{eff}[kN/m^3]$	$\sigma_{kh}[kN/m^3]$	$\sigma_{h}[kN/m^3]$
Water level	2	0	0	0	0	0
Ground level	-3,45	56,41	56,41	0	0	56,4075
Top side roof	- 4,45	66,76	78,41	11,65	5,83	72,5825
Bottom side roof	-5,55	78,15	100,41	22,27	11,14	89,275
Top side floor	-12,75	152,67	244,41	91,75	45,88	198,54
Bottom side floor	- 14,05	166,12	270,41	104,29	52,15	218,27

Table 4.3: Hydraulic stress distribution

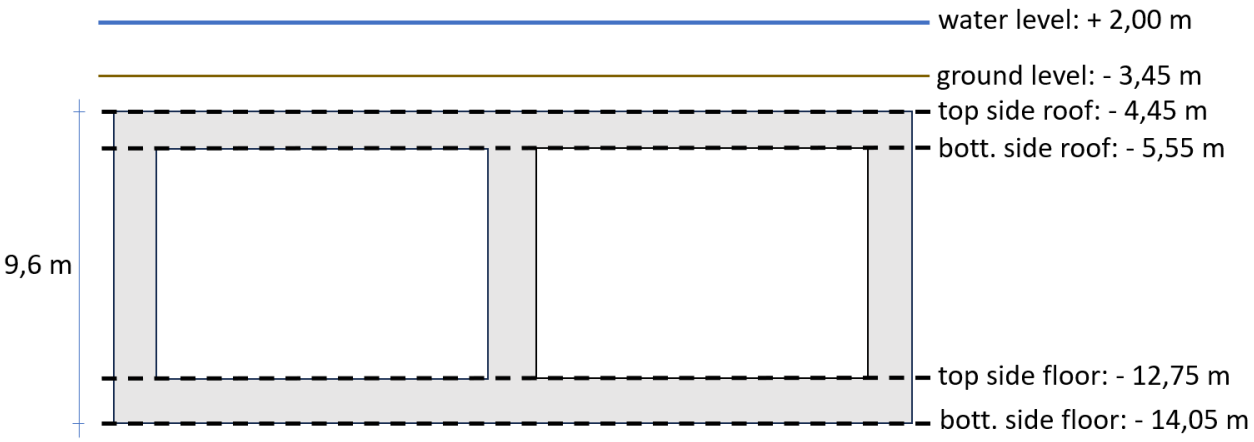

Figure 4.1: Drawing of cross-section's load levels

The subsequent phase involves the assessment of additional loads acting on the structure. These encompass a spectrum of forces, such as compacting weight, earth load (backfill), rock protection, ballast concrete, and traffic load. To account for the varying influences of these load categories, specific load factors are employed, as outlined in Table 4.4. These factors play a crucial role in ensuring the structural integrity and safety of the system, as they enable engineers to appropriately assess and address the diverse stresses and pressures imposed upon it. By considering these load factors, the design and construction processes are optimized to meet the required safety and performance standards, thereby enhancing the reliability and durability of the structure.

Loads	Load types	SLS	ULS	ULS - favorable
Self - weight	Permanent	1,0	1,25	0,95
Hydrostatic load MWL	Permanent	1,0	1,15	0,95
Earth load	Permanent	1,0	1,15	0,95
Rock protection	Permanent	1,0	2,0	0,95
Ballast concrete	Permanent	1,0	1,25	0,95
Traffic load	Variable	1,0	1,50	0,00

Table 4.4: Loads, load types and load factors

The next phase involves the determination of additional structural loads. These encompass compacting weight, earth fill pressure, protective measures against rock, the influence of ballast concrete, and the load imposed by traffic. Each of these load categories is subject to specific load factors, as delineated in Table 4.4.

Following this, the cumulative loading on the tunnel, considering both Serviceability and Ultimate Limit States (SLS and ULS), will be determined. However, it is imperative to account for the intrinsic weight of the structural elements themselves. To compute this, the product of concrete and steel cross-sectional areas is multiplied by their respective material densities. Notably, the estimation of steel area involves the application of a maximum reinforcement ratio of approximately 2%. As a result, the total self-weight of the roof and floor slabs is quantified, in accordance with the procedures detailed in Table 4.5 and Table 4.6. This meticulous process is vital for comprehensively evaluating the structural capacities of the tunnel under diverse conditions.

Material densities	kN/m^3
Water	10,35
Concrete	23,2
Steel	77
Ballast concrete	23,2

Table 4.5: Material properties

Self - weight roof							**q** [kN/m]
$A_{c,roof}$	38960000	mm^2		38,96	m^2		27,94
$A_{s,roof}$	809600	mm^2		0,81	m^2		1,69
						Total	27,63
Self - weight floor							**q** [kN/m]
$A_{c,floor}$	45760000	mm^2		45,76	m^2		30,47
$A_{s,floor}$	956800	mm^2		0,96	m^2		2,00
						Total	32,47

Table 4.6: Surface area of steel/concrete & self-weight of roof/floor

In the final stage, the comprehensive load analysis for the tunnel comes together. This involves combining the self-weight of each structural component, considering the hydrostatic pressure, and including the loads from ballast concrete, rock, and soil. The result is the total load imposed on the tunnel's roof, floor, and outer wall, as detailed in Table 4.7. This table provides a thorough overview of the load conditions, addressing both the Serviceability Limit State (SLS) and the Ultimate Limit State (ULS).

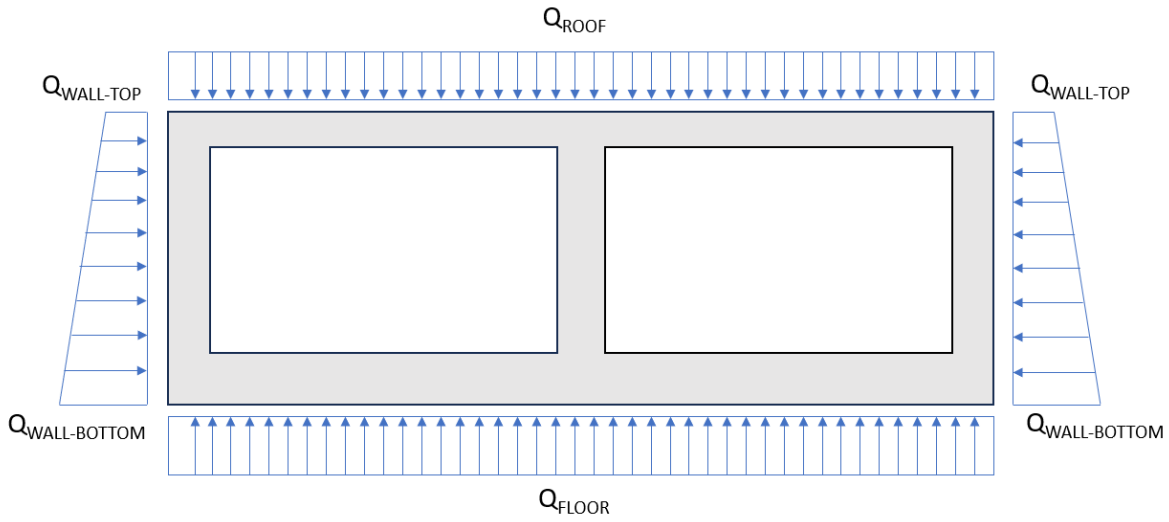

Figure 4.2: Drawing of cross-section's loading

Roof			**Floor**		
Load types	**SLS**	**ULS**	**Load types**	**SLS**	**ULS**
Self - weight	27,63	34,54	Self - weight	32,47	40,59
Hydrostatic load MWL	66,76	76,77	Hydrostatic load MWL	-166,12	-191,04
Rock protection	11,65	23,30	Ballast concrete	10,92	13,64
			Traffic load UDL	10,00	0,00
Total [kN/m]	106,04	134,61 *downwards*	**Total [kN/m]**	-112,74	-136,80
Walls - Top			**Walls - Bottom**		
Load types	**SLS**	**ULS**	**Load types**	**SLS**	**ULS**
Hydrostatic load MWL	72,58	83,47	Hydrostatic load MWL	218,27	251,01
Backfill	5,83	6,67	Backfill	52,15	59,98
Total [kN/m]	78,41	90,17	**Total [kN/m]**	270,41	310,97

Table 4.7: The load q for each element in SLS & ULS

4.2.3 Design moment calculation

The design moment, denoted as M_{ed}, is calculated for the purpose of subsequent comparison with the moment resistance of the cross-sectional elements. The moment M_{ed} exhibits variation along the different sections of the tunnel span. In its initial assessment, M_{ed} is approximated through the conventional rule of thumb based on the formula $M_{ed} = \frac{1}{10} \times q \times l^2$. At the chosen span of 15m, it is anticipated that the design moment or crack width may surpass the moment resistance or maximum allowable crack width of an element, even when the maximum reinforcement ratio is applied. In such instances, it can be inferred that the reinforced concrete tunnel has reached its limit. In addition to the moment capacity assessment and crack width control, the same procedure will be reiterated for the normal stress check and shear capacity assessment. The manual calculation of the design forces has been executed, and the outcomes are presented in Table 4.8.

Internal forces approximation - ULS			**Internal forces approximation - SLS**		
$M_{ed,roof}$	3028,70	kNm	$M_{ed,roof}$	2385,85	kNm
$M_{ed,floor}$	3113,12	kNm	$M_{ed,floor}$	2564,51	kNm
V_{roof}	1009,57	kN	V_{roof}	795,29	kN
V_{floor}	1026,05	kN	V_{floor}	845,50	kN
N_{roof}	697,77	kN	N_{roof}	606,76	kN
N_{floor}	1227,69	kN	N_{floor}	1067,56	kN

Table 4.8: Hand calculation of the design forces

SCIA software is employed to verify the manual calculations for the Ultimate Limit State (ULS). Figure 4.1 illustrates the total loading, based on Table 4.7, applied in the cross - section while figures 4.2 and 4.3 illustrate the moment and shear distribution respectively.

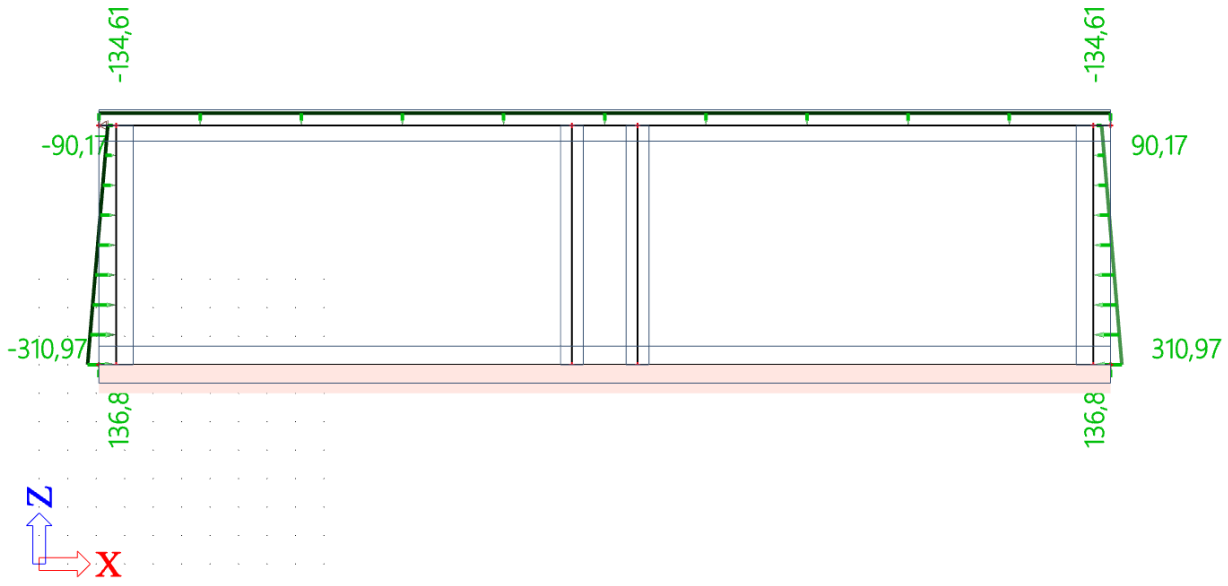

Figure 4.3: Total loading

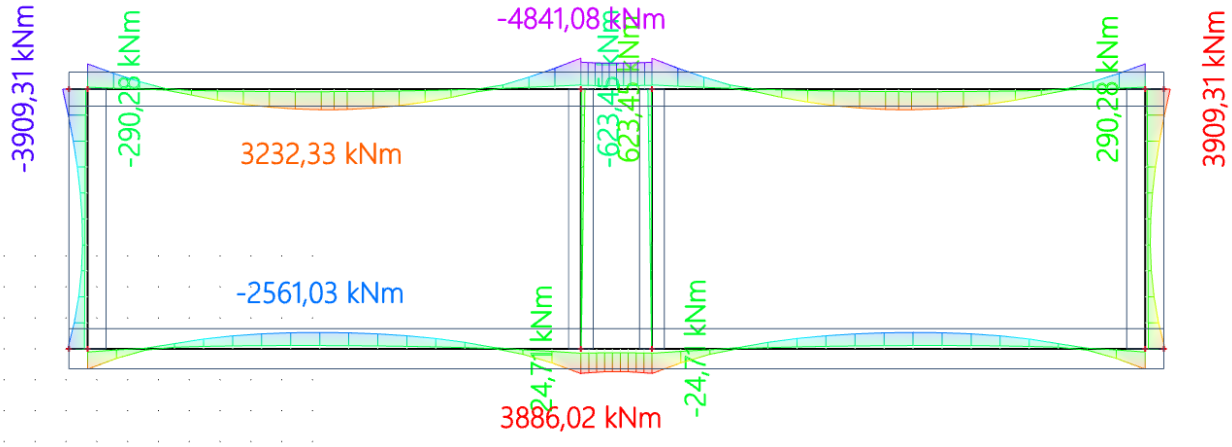

Figure 4.4: Bending moments diagram

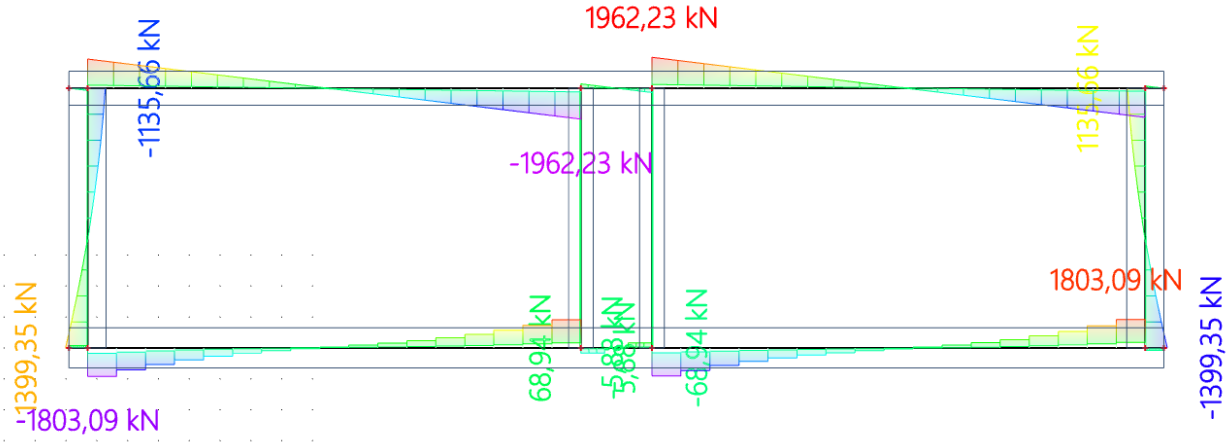

Figure 4.5: Shear forces diagram

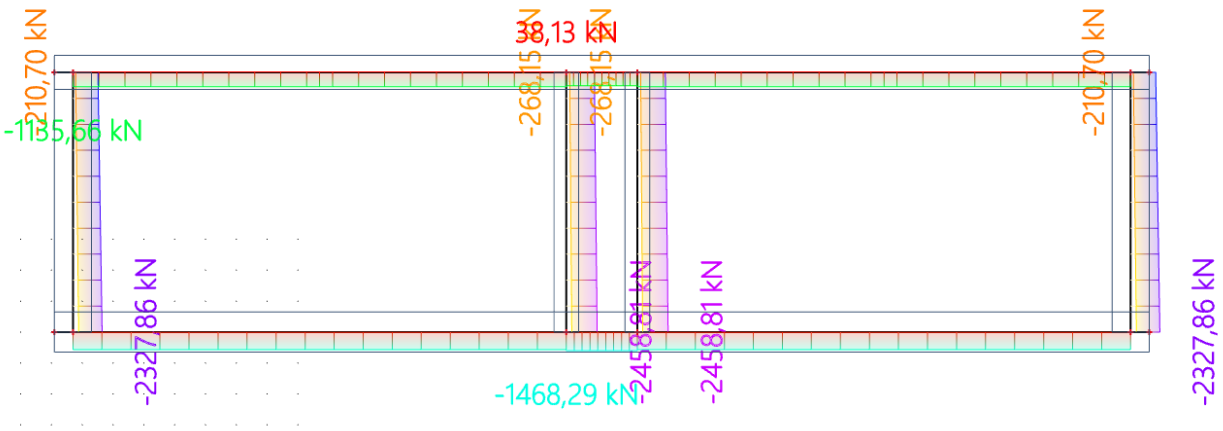

Figure 4.6: Axial forces diagram

The results indicate that the manual calculations align with the outcomes from the SCIA software. Variations between the manual calculations and the model can be attributed to assumptions regarding the uniform bedding. However, both methods yield consistent results for typical distributions of normal, moment, and shear forces.

4.3 Capacity of the reinforced concrete tunnel

Having established the dimensions of the structural elements and quantified the applied loads on the reinforced concrete tunnel, the next step involves determining the tunnel's structural capacity. To achieve this, first it must be defined the material properties that govern its behavior. In this analysis, we employ reinforcing steel of B500 grade and concrete of class C35.

The material's yielding stresses will be divided by appropriate material factors to generate the design yield stresses. This process applies to both compressive and tensile stresses within the concrete. As a frame of context, the Table 4.9 below provides values for Young's modulus corresponding to steel and concrete materials.

Material properties			
Steel	kN/mm^2	**Concrete**	kN/mm^2
E_s	210000	E_c	35000
f_y	500	f_{ck}	35
γ_s	1,15	γ_c	1,5
f_{yd}	434,8	f_{cd}	23,33
		$f_{ctk,0,05}$	2,0
		f_{ctd}	1,33

Table 4.9: Material characteristics for steel & concrete

The dimensions of the elements and the calculated loads, as previously established, are consolidated in the

table 4.10 below.

Dimensions		
Total width of the tube	15	m
Width of gallery	1,2	m
Roof thickness	1,1	m
Floor thickness	1,3	m
Outer wall thickness	1,2	m
Inner wall thickness	0,8	m
Inner height tunnel	7,2	m
Total height tunnel	9,6	m
Tunnel length	35,2	m
Total loading [kN/m]	**SLS**	**ULS**
q_{roof}	106,04	134,61
q_{floor}	-112,74	-136,80
$q_{sidewall-top}$	78,41	90,17
$q_{sidewall-bottom}$	270,41	310,97

Table 4.10: Hand calculation of the design forces

4.3.1 Roof element

Following the determination of cross-sectional dimensions, loadings, material properties, and safety factors, the calculation of the concrete tunnel element's structural capacity can be initiated. The initial step involves evaluating the moment resistance capacity of the roof. To accomplish this, it is imperative to establish the precise location and area of reinforcement.

Table 4.11 has been assembled to provide a comprehensive reference for the essential cross-sectional parameters, while Figure 4.4 visually illustrates the layout of the reinforcement, enhancing the understanding of this crucial component.

Cross - sectional parameters			**Reinforcement data**		
I_c	0,111	m^4	Cover distance	60	mm
$W_{c,top}$	0,202	m^3	$\phi_{stirrup}$	20	mm
$W_{c,bottom}$	0,202	m^3	$\phi_{tensile}$	40	mm
$Width_{roof}/m$	1	m	$\phi_{compression}$	25	mm
$Height_{roof}/m$	1,1	m	Reinforcement spacing - 1	100	mm
$A_{c,eff}/m$	1,1	m^2	Reinforcement spacing - 2	120	mm

Table 4.11: Roof's cross - sectional properties & reinforcement data

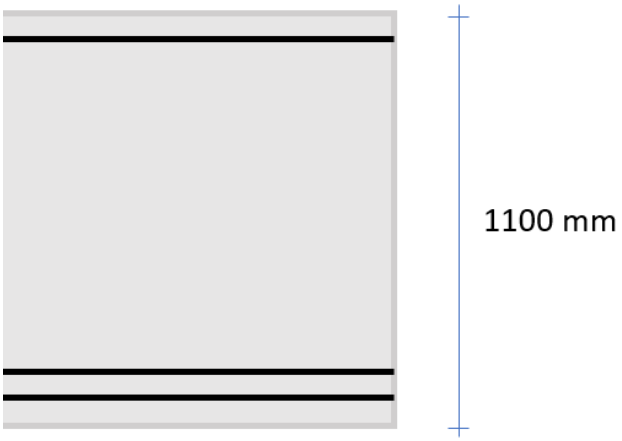

Figure 4.7: Reinforcement layout (tensile zone: 8 ϕ40 and 8 ϕ40, compression zone: 10 ϕ25)

Moment capacity calculation (ULS)

The primary objective is to conduct unity checks to ensure the structural capacity of the tunnel. Once the parameters for the roof's cross-section are selected, the quantities of tensile and compressive reinforcement, as well as the arrangement of stirrups, can be established. The precise placement of these elements is crucial, as it determines the internal lever arm, a critical factor contributing to the design moment resistance of the cross - section.

The first stage involves calculating the strains within the roof element. To achieve this, we need to consider the cross - sectional area and the ULS (Ultimate Limit State) strain in the concrete. The only missing parameter required to calculate the strain in each element of the cross - section is the height of the compression zone (Xu). An iterative calculation method is employed to determine the compression zone height, facilitated by a spreadsheet program (excel). Based on these calculations, it is determined that the compression zone height is **438,3** mm. With this crucial parameter known, we can proceed to calculate the strains, as detailed in Table 4.12 and 4.13 below.

Distances $d_s[mm]$		**Tensile reinforcement**			**Compressive reinforcement**		
1st layer	1020	1st layer	10472	mm^2	1st layer	4909	mm^2
2nd layer	960	2nd layer	10472	mm^2			
d_{eff}	990	Total	20944	mm^2			
Stirrups							
1st layer	942,5	mm^2			A_{sw}	2827	mm^2/m

Table 4.12: Reinforcement area

Effective depths			**Strains**	
			ϵ_{cu}	-3,50‰
d_{c1}	72,5	mm	ϵ_{c1}	-2,92‰
d_0	0	mm	ϵ_0	0‰
d_{s2}	960	mm	ϵ_{s2}	4,17‰
d_{s1}	1020	mm	ϵ_{s1}	4,65‰
d_{s0}	1100	mm	ϵ_{s0}	5,28‰

Table 4.13: Reinforcement layout & strains

After establishing the strains, the next step involves calculating the forces within the reinforcement and the concrete compression zone. Maintaining horizontal force equilibrium is crucial, ensuring that the sum of forces aligns with the axial load on the element. With this balance in place, it becomes possible to calculate the design moment resistance, $M_{Rd}{}^{\mathrm{d}}$ of the roof element by multiplying these forces by their respective eccentricities.

The calculated moment of resistance is then compared to the moment generated by the applied loading, M_{Ed}. If the moment resistance of the cross - section exceeds the moment resulting from the loading, the cross - section successfully passes the moment capacity check. These vital steps are concisely presented in Table 4.14 for a roof element.

Steel & Concrete Forces			Moment Resistance		
$N_{cd,2}$	-5113	kN	$M_{cd,2}$	-5064	kNm
$N_{cd,1}$	-2557	kN	$M_{cd,2}$	-2065	kNm
$N_{s,druk}$	-2134	kN	$M_{s,druk}$	-2193	kNm
N_{s2}	4553	kN	M_{s2}	637	kNm
N_{s1}	4553	kN	M_{s1}	364	kNm
N_d	698	kN	$M_{N_{Ed}}$	384	kNm
$\sum_F$	0	kN	M_{Rd}	7937	kNm
			M_{Ed}	3028	kNm
			U_{check}	***0,38***	

Table 4.14: Roof's cross - sectional properties & reinforcement data

Normal stress capacity calculation (ULS)

The second check to be conducted pertains to the compressive stress assessment within the roof element, arising from the combination of normal force and moment. The calculation for this assessment proceeds as follows:

$$\sigma_{(c)} = -\frac{N}{A_{c,eff}} - \frac{M}{W_{top}} \tag{4.1}$$

where:

N is the normal force in the roof element

$A_{c,eff}$ is the effective cross - sectional area of the roof

M is the design moment

W is the sectional modulus

Utilizing the formula provided above, the outcome of the unity check for normal stresses is presented in Table 4.15 below.

Normal stresses		
f_{cd}	-23,3	N/mm^2
$\sigma_{c,top}$	-14,4	N/mm^2
U_{check}		***0,62***

Table 4.15: Normal stresses

Shear force capacity calculation (ULS)

The structural integrity is further evaluated by analyzing its shear capacity. Initially, this evaluation is performed without the presence of shear reinforcement (stirrups). To determine the shear resistance for concrete, the following formula is employed:

$$V_{rd,c} = \left[C_{rd,c} \times k \times (100 \times \rho x f_{ck})^{\frac{1}{3}} + k_1 \times \sigma_{cp}\right] \times b_w \times d \tag{4.2}$$

In which:

$$k = 1 + \sqrt{\frac{200}{d}} \leq 2,0$$
$$d = \text{effective depth in mm}$$
$$\rho = \frac{A_s}{b \times d} \leq 0,02$$
$$\sigma_{cp} = \frac{N_{ed}}{A_c} < 0,2 f_{cd}$$
$$\text{Unity Check} = \frac{V_{ed}}{V_{rd,c}} < 1,0$$

where:
ρ = reinforcement ratio
A_s = reinforcement area
b = width of the cross - section in tensile zone
σ_{cp} = stress due to axial loading
N_{ed} = axial force in the cross - section due to compression
f_{cd} = design concrete compressive stress

It is essential to highlight that the cross - sectional design lacks the intrinsic ability to resist shear forces independently, necessitating the introduction of shear reinforcement. This imperative step prompts a subsequent assessment of the shear capacity for the reinforced cross - section. The formula employed to determine the necessary shear reinforcement is as follows:

$$V_{rd,s} = \frac{A_{sw}}{S} \times z \times f_{yd} \times cot\theta \tag{4.3}$$

$$V_{rd,max} = \alpha \times b \times z \times v_1 \times f_{cd} \times (cot\theta + tan\theta) \tag{4.4}$$

where:
A_{sw} = cross - sectional area of shear reinforcement
s = spacing of stirrups
$z = 0,9d$ = effective depth of the cross - section
θ = angle of inclined strut
α = coefficient for the compression chord
b = width of the cross - section
v_1 = strength reduction factor for concrete in shear

The unity check will be based on the lower value obtained from the calculation of shear force resistance (above formula 4.3 and 4.4). The results for the shear capacity of the cross - section are illustrated in the Table 4.16 below. The unity check formula utilized is as follows:

$$\text{Unity Check} = \frac{V_{ed}}{min(V_{rd,s}; V_{rd,max})} < 1,0$$

Shear resistance					
V_{ed}	1009,7	kN			
N_{ed}	- 697,8	kN			
Bearing capacity with stirrups					
$C_{rd,c}$	0,12	[-]	θ	21,8°	
k	1,45	[-]	α	90°	
α_{cw}	1,02	[-]	v_1	0,52	[-]
d_{eff}	990	mm	z	835	mm
ρ_1	0,198	[-]	A_{sw}	942	mm^2
σ_{cp}	0,6	N/mm^2	$V_{rd,s}$	2567	kN
$V_{rd,c}$	802	kN	$V_{rd,max}$	3552	kN
s	333,3	mm	a_l	418	mm
V_{rd}	***2567***	kN	U_{check}	***0,40***	

Table 4.16: Shear force resistance

The results show that the shear force capacity is met. Nevertheless, the compression angle θ can range from 21,8° to 45°, leading to variations in $V_{rs,d}$ and $V_{rd,max}$. Varying the parameter θ reveals that the most effective and optimized number of stirrups is achieved when the angle is set at 21,8°. Consequently, this unity check represents the optimal configuration for the applied stirrups.

Crack width control reinforced concrete tunnel (SLS)

The subsequent analysis focuses on the crack width control, which is a crucial aspect of serviceability limit state (SLS) verification. This involves considering moments and normal forces in the SLS context. To calculate crack width, the initial step is to determine the concrete compression zone, which necessitates an iterative process addressed using a spreadsheet model (excel). By maintaining a moment and force balance, expressed as $\Sigma_M = 0$ and $\Sigma_N = 0$, it is possible to derive the unknown concrete strain ϵ_c and the compression zone x in the serviceability limit context. Subsequently, the stress distribution across the height of the element is determined, enabling the calculation of force distribution throughout the cross - section. Complying with the force equilibrium principle, the net sum of forces is required to be zero. This approach allows for the computation of stress in the reinforcing steel. The results of these calculations are presented in Table 4.17 and 4.18 below.

Serviceability Limit State				
N_{rep}	607	kN	$M_{rep,sls}$	-2386
x_u	524,7	mm	$\epsilon_{c3'}$	-2,45‰
Eccentricities			**Strains**	
e_{c1}	925	mm	ϵ_{c1}	-0,69‰
$e_{s,druk}$	1028	mm	$\epsilon_{s,druk}$	-0,60‰
e_{s2}	140	mm	ϵ_{s2}	0,57‰
e_{s1}	80	mm	ϵ_{s1}	0,65‰

Table 4.17: Strains

Forces			**Moments**		
N_{c1}	-2590	kN	M_{c1}	-2396	kNm
$N_{s,druk}$	-585	kN	$M_{s,druk}$	-601	kNm
N_{s2}	1201	kN	M_{s2}	168	kNm
N_{s1}	1367	kN	M_{s1}	109	kNm
N_{rep}	607	kN	$M_{N_{rep}}$	334	kNm
			$M_{rep,sls}$	2386	kNm
Σ_F	0	kN	Σ_M	0	kNm
σ_s			121		kN/m^2

Table 4.18: Forces, moments and steel stress

With the determination of the stress in the reinforcing steel, it becomes possible to calculate the expected crack width using the following formula:

$$w_k = S_{r,max} \times [\epsilon_{sm} - \epsilon_{cm}] \tag{4.5}$$

In which:

$$
\begin{aligned}
S_{r,\max} &= \text{maximum crack spacing} \\
\epsilon_{sm} &= \text{mean strain in the reinforcement} \\
\epsilon_{cm} &= \text{mean strain in concrete between cracks} \\
\epsilon_{sm} - \epsilon_{cm} &= \frac{\sigma_s - k_t \frac{f_{ct,\text{eff}}}{\rho_{\text{eff}}} [1 + \rho_{\text{eff}}]}{E_s} \geq 0.6 \frac{\sigma_s}{E_s} \\
\rho_{\text{eff}} &= \frac{A_s + \xi A_p}{A_{c,\text{eff}}}
\end{aligned}
$$

where:
σ_s = stress in the reinforcement
$f_{ct,eff}$ = concrete tensile stress
α = ratio $\frac{E_s}{E_{cm}}$
ρ = effective reinforcement ratio
E_s = Elasticity modulus of steel
k_t = factor dependant on the duration of the load
A_s = area of steel reinforcement
$A_{c,eff}$ = effective area of concrete

The calculations were performed using Microsoft Excel, and the results are presented in Table 4.19, as shown below:

Crack width								
$\epsilon_{sm} - \epsilon_{cm}$	0,55	‰	c	60	mm	k_t	0,4	[-]
α_e	5,87	[-]	$s_{1,max}$	731	mm	ϕ_{eq}	40	mm
$\rho_{p,eff}$	0,122	[-]	$s_{r,max}$	260	mm	k_x	0,8	[-]
h_{eff}	187	mm	k_1	0,8	[-]	w_k	0,14	mm
$A_{c,eff}$	187426	mm^2	k_2	0,5	[-]	w_{max}	0,20	mm
$f_{ct,eff}$	3,21	N/mm^2	k_3	3,4	[-]			
ξ_1	1	[-]	k_4	0,425	[-]	U_{check}	***0,90***	

Table 4.19: Crack width check

The results of the unity check presented in Table 4.19 confirm that the observed crack width remains within the permissible maximum limit. As a result, no additional measures are required, and the quantity of reinforcement is deemed sufficient for the tunnel element.

4.3.2 Floor element

With the cross-sectional dimensions, applied loads, material properties, and safety factors established, the structural capacity of the concrete tunnel element can now be determined. The main objective at this juncture is to assess the moment resistance capacity of the floor. To accomplish this, precise details regarding the positioning of the reinforcement and the associated area must be outlined. This meticulous planning is pivotal in ensuring the structural integrity and safety of the tunnel element. To gain a thorough grasp of these crucial parameters, attention is directed to Table 4.20, providing a concise summary of the intricate cross-sectional properties essential for this calculation.

Cross - sectional parameters			**Reinforcement data**		
I_c	0,183	m^4	Cover distance	60	mm
$W_{c,top}$	0,282	m^3	$\phi_{stirrup}$	20	mm
$W_{c,bottom}$	0,282	m^3	$\phi_{tensile}$	40	mm
$Width_{floor}/m$	1	m	$\phi_{compression}$	25	mm
$Height_{floor}/m$	1,3	m	Reinforcement spacing - 1	100	mm
$A_{c,eff}/m$	1,3	m^2	Reinforcement spacing - 2	140	mm

Table 4.20: Floor's cross - sectional properties & reinforcement data

Moment capacity calculation (ULS)

Continuing the process applied to the roof, the strains are computed, and the reinforcement details are examined based on the cross-sectional characteristics of the floor. The height of the compressive zone for the ultimate limit state of the design was calculated to be equal to 394,2 mm. Tables 4.21 and 4.22 present the corresponding outcomes. Table 4.23 illustrates the results of the floor's moment resistance and the unity check.

Distances $d_s[mm]$		**Tensile reinforcement**			**Compressive reinforcement**		
1st layer	1220	1st layer	8976	mm^2	1st layer	4909	mm^2
2nd layer	1140	2nd layer	8976	mm^2			
d_{eff}	1180	Total	17952	mm^2			
Stirrups							
1st layer	942,5	mm^2			A_{sw}	2827	mm^2/m

Table 4.21: Reinforcement area

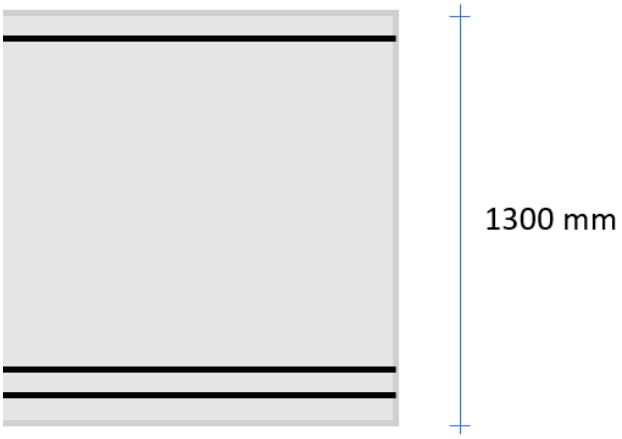

Figure 4.8: Reinforcement layout (tensile zone: 7 ϕ40 and 7 ϕ40, compression zone: 10 ϕ25)

Effective depths			**Strains**	
			ϵ_{cu}	-3,50‰
d_{c1}	72,5	mm	ϵ_{c1}	-2,86‰
d_0	0	mm	ϵ_0	0‰
d_{s2}	1140	mm	ϵ_{s2}	6,62‰
d_{s1}	1220	mm	ϵ_{s1}	7,33‰

Table 4.22: Reinforcement layout & strains

Steel & Concrete Forces			**Moment Resistance**		
$N_{cd,2}$	-4599	kN	$M_{cd,2}$	-5526	kNm
$N_{cd,1}$	-2300	kN	$M_{cd,2}$	-2385	kNm
$N_{s,druk}$	-2134	kN	$M_{s,druk}$	-2620	kNm
N_{s2}	3903	kN	M_{s2}	624	kNm
N_{s1}	3903	kN	M_{s1}	312	kNm
N_d	1227,7	kN	$M_{N_{Ed}}$	798	kNm
$\sum_F$	0,00	kN	M_{Rd}	8796	kNm
			M_{Ed}	3078	kNm
			U_{check}	***0,35***	

Table 4.23: Floor's cross - sectional properties & reinforcement data

Normal stress capacity calculation (ULS)

The next check to be performed concerns the evaluation of compressive stress within the floor element, resulting from the interaction of normal force and moment. The calculation for this assessment unfolds based in the procedure described for the roof and the results are presented on Table 4.24 below.

Normal stresses		
f_{cd}	-23,33	N/mm^2
$\sigma_{c,top}$	-9,97	N/mm^2
U_{check}	***0,43***	

Table 4.24: Normal stresses

Shear force capacity calculation (ULS)

The shear capacity calculations are examined based on the same procedure explained for the roof element in section 4.3.1. The results for the shear resistance are presented in the following table.

Shear resistance					
V_{ed}	1026		kN		
N_{ed}	- 1227,7		kN		
Bearing capacity with stirrups					
$C_{rd,c}$	0,12	[-]	θ	21,8°	
k	1,45	[-]	α	90°	
α_{cw}	1,04	[-]	v_1	0,52	[-]
d_{eff}	1180	mm	z	1002	mm
ρ_1	0,0142	[-]	A_{sw}	942	mm^2
σ_{cp}	0,9	N/mm^2	$V_{rd,s}$	3078	kN
$V_{rd,c}$	902	kN	$V_{rd,max}$	4313	kN
s	333,3	mm	a_l	501	mm
V_{rd}	***3078***	kN	U_{check}	***0,33***	

Table 4.25: Shear force resistance

The results show that the shear force capacity is met. Nevertheless, the compression angle θ can range from 21,8° to 45°, leading to variations in $V_{rs,d}$ and $V_{rd,max}$. Varying the parameter θ reveals that the most effective and optimized number of stirrups is achieved when the angle is set at 21,8°. Consequently, this unity check represents the optimal configuration for the applied stirrups.

Crack width control reinforced concrete tunnel (SLS)

As mentioned above, in chapter 4.2.4.1.4, this analysis focuses on controlling crack width, a key aspect of serviceability limit state (SLS) verification. It involves considering moments and normal forces in the SLS context. To calculate crack width, the process starts by iteratively determining the concrete compression zone using a spreadsheet model. This ensures compliance with moment and force balance principles, where $\Sigma_M = 0$ and $\Sigma_N = 0$. This approach enables the calculation of stress in the reinforcing steel. The results of these calculations are available in Tables 4.26 and 4.27 for further evaluation.

Serviceability Limit State					
N_{rep}	- 1068	kN	M_{rep}	2537	kNm
x_u	605,2	mm	$\epsilon_{c3'}$	-2,44‰	
Eccentricities			**Strains**		
e_{c1}	1098	mm	ϵ_{c1}	-0,60‰	
$e_{s,druk}$	1228	mm	$\epsilon_{s,druk}$	-0,52‰	
e_{s2}	160	mm	ϵ_{s2}	0,53‰	
e_{s1}	80	mm	ϵ_{s1}	0,60‰	

Table 4.26: Strains

Forces			**Moments**		
N_{c1}	-2583	kN	M_{c1}	-2837	kNm
$N_{s,druk}$	-514	kN	$M_{s,druk}$	-631	kNm
N_{s2}	944	kN	M_{s2}	151	kNm
N_{s1}	1086	kN	M_{s1}	87	kNm
N_{rep}	1086	kN	$M_{N_{rep}}$	694	kNm
			$M_{rep,sls}$	2537	kNm
Σ_F	0	kN	Σ_M	0	kNm
σ_s			121	kN/m^2	

Table 4.27: Forces, moments and steel stress

With the determination of the stress in the reinforcing steel, it becomes possible to calculate the expected crack width using the following formula (4.5) mentioned previously and described procedure. The results are presented in Table 4.26, as shown below:

Crack width								
$\epsilon_{sm} - \epsilon_{cm}$	0,48	‰	c	60	mm	k_t	0,4	[-]
α_e	5,87	[-]	$s_{1,max}$	903	mm	ϕ_{eq}	40	mm
$\rho_{p,eff}$	0,078	[-]	$s_{r,max}$	292	mm	k_x	0,80	[-]
h_{eff}	232	mm	k_1	0,80	[-]	w_k	0,14	mm
$A_{c,eff}$	231602	mm^2	k_2	0,50	[-]	w_{max}	0,20	mm
$f_{ct,eff}$	3,21	N/mm^2	k_3	3,40	[-]			
ξ_1	1	[-]	k_4	0,425	[-]	U_{check}	***0,88***	

Table 4.28: Crack width check

The outcomes of the unity check in Table 4.26 affirm that the observed crack width stays within acceptable limits. Hence, there is no need for further actions, and the reinforcement quantity is considered adequate for the tunnel element.

4.3.3 Outer wall elements

The same procedures, as described earlier for the roof and floor, are replicated for the outer wall. The results are presented below. Initially, the moment resistance capacity of the floor must be determined, necessitating the specification of reinforcement placement and its corresponding area. Refer to table 4.29 for a summary of the cross-sectional parameters.

Cross - sectional parameters			Reinforcement data		
I_c	0,144	m^4	Cover distance	60	mm
$W_{c,top}$	0,240	m^3	$\phi_{stirrup}$	20	mm
$W_{c,bottom}$	0,240	m^3	$\phi_{tensile}$	40	mm
$Width_{outer-wall}/m$	1	m	$\phi_{compression}$	25	mm
$Height_{outer-wall}/m$	1,2	m	Reinforcement spacing - 1	100	mm
$A_{c,eff}/m$	1,2	m^2	Reinforcement spacing - 2	120	mm

Table 4.29: Outer wall's cross - sectional properties & reinforcement data

Moment capacity calculation (ULS)

Based on the same procedure followed previously for the roof and the floor, the moment capacity is calculated and illustrated in Table 4.32 below. All the essential data required to derive the presented results are included in Table 4.30 and 4.31.

Distances $d_s[mm]$		**Tensile reinforcement**			**Compressive reinforcement**		
1st layer	1120	1st layer	12566	mm^2	1st layer	4909	mm^2
2nd layer	1040	2nd layer	12566	mm^2			
d_{eff}	1080	Total	25133	mm^2			
Stirrups							
1st layer	942,5	mm^2			A_{sw}	2827	mm^2/m

Table 4.30: Reinforcement area

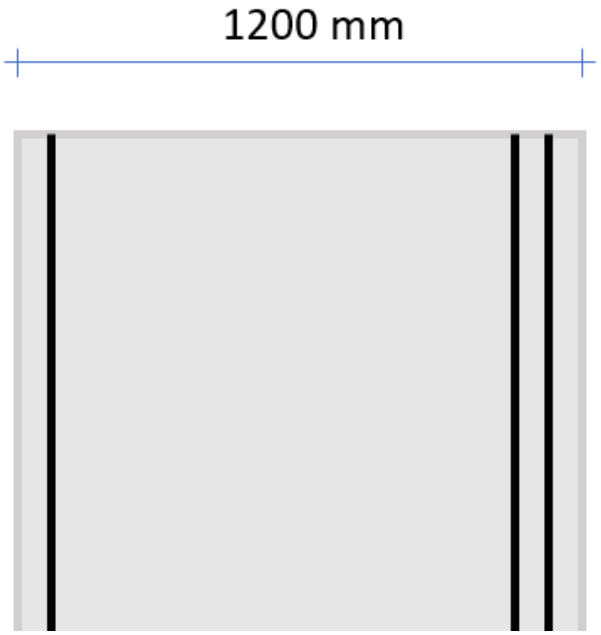

Figure 4.9: Reinforcement layout (tensile zone: 10 ϕ40 and 10 ϕ40, compression zone: 10 ϕ25)

Effective depths			**Strains**	
			ϵ_{cu}	-3,50‰
d_{c1}	72,5	mm	ϵ_{c1}	-3,04‰
d_0	0	mm	ϵ_0	0‰
d_{s2}	1040	mm	ϵ_{s2}	3,11‰
d_{s1}	1120	mm	ϵ_{s1}	3,62‰

Table 4.31: Reinforcement layout & strains

Steel & Concrete Forces			Moment Resistance		
$N_{cd,2}$	-6426	kN	$M_{cd,2}$	-6826	kNm
$N_{cd,1}$	-3213	kN	$M_{cd,1}$	-2676	kNm
$N_{s,druk}$	-2134	kN	$M_{s,druk}$	-2406	kNm
N_{s2}	5464	kN	M_{s2}	874	kNm
N_{s1}	5464	kN	M_{s1}	437	kNm
N_d	846	kN	$M_{N_{Ed}}$	507	kNm
$\sum_F$	0,00	kN	M_{Rd}	10090	kNm
			M_{Ed}	2029	kNm
			U_{check}	***0,20***	

Table 4.32: Outer wall's cross - sectional properties & reinforcement data

Normal stress capacity calculation (ULS)

In Table 4.33 is presented the unity check for the normal force of the outer wall elements.

Normal stresses		
f_{cd}	-23,33	N/mm^2
$\sigma_{c,top}$	-7,75	N/mm^2
U_{check}	***0,34***	

Table 4.33: Normal stresses

Shear force capacity calculation (ULS)

The intermediate steps for the shear force capacity of the element will not be detailed here as they were mentioned in 4.2.4.1. The final results of the calculations are presented in Table 4.34.

Shear resistance					
V_{ed}	1780,3	kN			
N_{ed}	- 846	kN			
Bearing capacity with stirrups					
$C_{rd,c}$	0,12	[-]	θ	21,8°	
k	1,45	[-]	α	90°	
α_{cw}	1,03	[-]	v_1	0,52	[-]
d_{eff}	1080	mm	z	896	mm
ρ_1	0,02	[-]	A_{sl}	23167	mm^2/mm
σ_{cp}	0,6	N/mm^2	$V_{rd,s}$	2752	kN
$V_{rd,c}$	878	kN	$V_{rd,max}$	3818	kN
s	333,3	mm	a_l	724	mm
V_{rd}	***2752***	kN	U_{check}	***0,65***	

Table 4.34: Shear force resistance

Crack width control reinforced concrete tunnel (SLS)

The results for the crack width examination are also presented below in Table 4.46. The procedure's results, before the final step (unity check), are also presented in Tables 4.44 and 4.45.

Serviceability Limit State				
N_{rep}	-1010	kN	$M_{rep,sls}$	1764
x_u	650,3	mm	$\epsilon_{c3'}$	0,00245
Eccentricities			**Strains**	
e_{c1}	983	mm	ϵ_{c1}	-0,46‰
$e_{s,druk}$	1128	mm	$\epsilon_{s,druk}$	-0,41‰
e_{s2}	160	mm	ϵ_{s2}	0,27‰
e_{s1}	80	mm	ϵ_{s1}	0,33‰

Table 4.35: Strains

Forces			Moments		
N_{c1}	-2132	kN	M_{c1}	-2096	kNm
$N_{s,druk}$	-400	kN	$M_{s,druk}$	-451	kNm
N_{s2}	690	kN	M_{s2}	110	kNm
N_{s1}	832	kN	M_{s1}	67	kNm
N_{rep}	1010	kN	$M_{N_{rep}}$	606	kNm
			$M_{rep,sls}$	1764	kNm
Σ_F	0	kN	Σ_M	0	kNm
σ_s		66		kN/m^2	

Table 4.36: Forces, moments and steel stress

With the determination of the stress in the reinforcing steel, it becomes possible to calculate the expected crack width using the following formula (4.5) mentioned previously and described procedure. The results are presented in Table 4.26, as shown below:

Crack width								
$\epsilon_{sm} - \epsilon_{cm}$	0,25	‰	s_1	125	mm	k_t	0,4	[-]
α_e	5,87	[-]	$s_{1,max}$	530	mm	ϕ_{eq}	40	mm
$\rho_{p,eff}$	0,137	[-]	$s_{r,max}$	254	mm	k_x	0,80	[-]
h_{eff}	183	mm	k_1	0,80	[-]	w_k	0,06	mm
$A_{c,eff}$	183242	mm^2	k_2	0,50	[-]	w_{max}	0,20	mm
$f_{ct,eff}$	3,21	N/mm^2	k_3	3,40	[-]			
ξ_1	1	[-]	k_4	0,425	[-]	U_{check}	***0,39***	

Table 4.37: Crack width check

Based on the results of Table 4.46, there is no need for further actions, and the reinforcement quantity is considered adequate for the tunnel element.

4.4 Uplift and immersion calculations

Upon the completion of a tunnel element's construction, both ends of the element are meticulously sealed with bulkheads. This marks a significant milestone in the overall construction process, ensuring the structural integrity of the element. However, this is just one phase of a multifaceted project, and several subsequent phases must be carefully orchestrated to bring the project to fruition.

As the construction process advances, the focus shifts toward the buoyancy aspect of the tunnel elements. The objective is to enable these massive structures to float up to their intended positions and, conversely, be immersed as needed. This critical phase of the project hinges on the meticulous application of buoyancy balance equations. These equations serve as the guiding principles, checking whether the tunnel elements are well-equipped for the challenges of floating and immersion.

It is important to highlight that these equations are invaluable tools for ensuring the successful deployment of the tunnel elements. In case the existing cross - sectional design fails to meet the stringent balance conditions required for buoyancy, it necessitates diligent and expert-driven adjustments and modifications to the design. These adaptations may involve re - configuring the dimensions, materials, or structural properties of the tunnel elements, all in the pursuit of buoyancy perfection.

With the dimensions of the tunnel elements, as well as their buoyancy considerations, thoroughly addressed, the project advances to the uplift and immersion phases. These critical stages demand a comprehensive understanding of the weight distribution within the tunnel element. To determine the exact weight, precise calculations of the concrete and steel areas used in the construction process are indispensable. These weight calculations serve as a cornerstone for project success, allowing for a clear and accurate assessment of the tunnel elements' behavior during the buoyancy operations. In the detailed tables provided (Tables 4.38 and 4.39), a substantial amount of data is presented, offering deep insights into the structural integrity and buoyancy characteristics of the tunnel elements.

Roof	b $[mm]$	h $[mm]$	A $[mm^2]$	**Floor**	b $[mm]$	h $[mm]$	A $[mm^2]$
Outer wall 1	1200	1100	1320000	Outer wall 1	1200	1300	1560000
Roof 2	15000	1100	16500000	Floor 2	15000	1300	19500000
Inner wall 2	800	1100	880000	Inner wall 2	800	1300	1040000
Gallery roof 4	1200	1100	1320000	Gallery floor 4	1200	1300	1560000
Inner wall 3	800	1100	880000	Inner wall 3	800	1300	1040000
Roof 6	15000	1100	16500000	Floor 6	15000	1300	19500000
Outer wall 4	1200	1100	1320000	Outer wall 4	1200	1300	1560000
Gallery floor 1	1200	200	240000	Toe ($\times 2$)	1600	1300	2080000

Walls	b $[mm]$	h $[mm]$	A $[mm^2]$
Outer wall 1	1200	7200	8460000
Inner wall 2	800	7200	57600000
Inner wall 3	800	7200	57600000
Outer wall 4	1200	7200	8640000
Total concrete area		115600000 mm^2	115,6 m^2

Table 4.38: Determination of concrete area

Mass reinforcing steel	ρ	$I \quad [mm]$	$A_c \quad [mm^2]$	$A_s \quad [m^2]$
Floor reinforcement	2 %	36800	47840000	956800
Roof reinforcement	2 %	36800	40480000	809600
Outer wall reinforcement	2 %	19200	23040000	460800
Inner wall reinforcement	2 %	19200	15360000	307200
Total steel area	2534400 mm^2		2,534 m^2	

Table 4.39: Determination of steel area

By utilizing the calculated surface areas, it becomes feasible to ascertain the weight of the element by multiplying these areas with the specific weight. As a result, the total weight of the structure can be precisely determined. Subsequently, the focus shifts to calculating the necessary volume of ballast concrete to be applied after the immersion process. This calculation is streamlined by taking into account the previously determined total height of the structure, allowing for a meticulous evaluation of the required space for the ballast concrete.

$$h_{ballast} = h_{total} - h_{free-traffic} - h_{equipment} - h_{asphalt} \tag{4.6}$$

$$h_{ballast,max} = 7,2 - 5,0 - 1,1 - 0,12 = 0,98$$

$$h_{ballast,average} = 0,98 - 2\% \times \frac{15}{2} = 0,83 \tag{4.7}$$

where:

$h_{ballast}$: the height of the ballast concrete

h_{total}: the total inner height of the structure

$h_{free-traffic}$: the free height height that is required for the traffic

$h_{equipment}$: the height that is needed for the installations

$h_{asphalt}$: the height of the asphalt which will be designed with a 2% slope

The procedure for buoyancy balance calculation can be extended by applying the formulas 4.6 and 4.7. This process entails two critical checks, one relating to the conditions for floating up and the other to the conditions for immersion. The first check stipulates that the hydrostatic load should exceed the weight of the tunnel element by approximately 1%.

$$Weight_{floating-up} = 0,99 \times buoyancyforce$$

The second check requires an additional increase in the element's weight, to allow for a safety margin of 7,5% against floating up. This weight increase is achieved by introducing water, which will subsequently be replaced with an appropriate amount of ballast concrete.

$$Weight_{immersion} = 1,075 \times buoyancyforce$$

The detailed results can be found in Tables 4.40 and 4.41 below.

Floating - up calculation				
Total areas	m^3	kN/m^3	kN	$factor$
Concrete	115,60	24,50	2832,20	1,0
Steel	2,53	53,50	135,59	1,00
Ballast	0,00	23,50	0,00	1,0
Hydrostatic load	353,28	10,35	3656,45	1,0
Check	0,81		< 1,00	

Table 4.40: Floating-up check

Immersion calculation				
Total areas	m^3	kN/m^3	kN	$factor$
Concrete	115,60	24,50	2832,20	1,0
Steel	2,53	77,00	195,15	1,00
Ballast	27,90	23,50	655,65	1,0
Earth	0,00	9,00	0,00	1,0
Hydrostatic load	353,28	10,35	3656,45	1,0
Check	1,01		> 1,00	

Table 4.41: Immersion check

Based on the preceding calculations, it can be concluded that the designed reinforced concrete tunnel element meets the criteria for both buoyancy and immersion. To address potential uncertainties related to concrete density and casting accuracy, a slightly reduced concrete specific weight is considered when assessing the immersion conditions.

Chapter 5

Steel-Concrete-Steel tunnel

5.1 Dimensions

The initial phase involves dimensioning the tunnel element, a process that will be subsequently validated for moment and shear resistance. If necessary, adjustments to the dimensions can be made. Refer to Table 5.1 for a detailed breakdown of these dimensions.

Dimensions	$Roof_{outside}$	$Roof_{inside}$	$Floor_{outside}$	$Floor_{inside}$	$Walls_{outside}$	$Walls_{inside}$
$h \quad [mm]$	1100	1100	1300	1300	1200	1200
$b \quad [mm]$	1000	1000	1000	1000	1000	1000
$t_{sc} \quad [mm]$	25	35	25	35	25	25
$t_{st} \quad [mm]$	35	25	35	25	25	25
$h_c \quad [mm]$	1040	1040	1240	1240	1150	1150
$t_{web} \quad [mm]$	15	15	15	15	15	15
$c.t.c._{web} \quad [mm]$	3000	3000	3000	3000	2500	2500
$A_c \quad [mm^2]$	1040000	1040000	1240000	1240000	1150000	1150000

Table 5.1: SCS dimentions

5.2 Loadings

To assess the load acting on the tunnel, it is essential to establish specific material properties, element dimensions, material thickness, and the depth relative to the water surface. These crucial parameters can be found in Table 5.2, which provides material-specific weights in the first column, tunnel dimensions in the second column, and water and ground levels in the last column.

Material properties		Dimensions	[m]	Reference levels	[m]
$\gamma_{sediment}[kN/m^3]$	17,5	Protection layer	1,0	Design HWL	2,68
$\gamma_{backfill}[kN/m^3]$	20	Roof thickness	1,1	Ground level	-8,45
$\gamma_{rock}[kN/m^3]$	22	Asphalt thickness	0,12	Road level	-16,43
$\gamma_{water}[kN/m^3]$	10,35	Ballast concrete	1,1	Bottom level	-19,05
$\phi_{soil}[deg]$	30	Floor thickness	1,3		
K_0	0,5	Inner height	7,2		

Table 5.2: Material properties, dimensions, and levels

The process commences with a thorough evaluation of the hydraulic loads acting upon the tunnel element. This evaluation involves a comprehensive assessment of hydraulic stresses distributed along the tunnel's cross-section. Subsequent to this assessment, the total vertical stress is accurately determined. By deducting the hydraulic stress from this overall vertical stress, the resulting value is recognized as the effective vertical stress. Taking into consideration an internal friction angle of 30°, the coefficient of lateral earth pressure at rest, denoted as K_0 and calculated through the formula $K_0 = 1 - sin(\varphi) = 1 - 0,5$, becomes a pivotal parameter. This value is essential for the computation of the effective horizontal stress, obtained by multiplying the effective vertical stress by the coefficient of lateral earth pressure. As a result, the total horizontal stress acting on the tunnel can be derived by combining the hydraulic stress and the effective horizontal stress. These detailed calculations are provided in Table 5.3 for a better understanding.

Levels	[m]	$\sigma_{hydraulic}[kN/m^3]$	$\sigma_{soil}[kN/m^3]$	$\sigma_{eff}[kN/m^3]$	$\sigma_{kh}[kN/m^3]$	$\sigma_h[kN/m^3]$
Water level	2	0	0	0	0	0
Ground level	-3,45	56,4075	56,4075	0	0	56,4075
Top side roof	-4,45	66,7575	78,4075	11,65	5,8250	72,5825
Bottom side roof	-5,55	78,1425	100,4075	22,265	11,1325	89,275
Top side floor	-12,75	152,6625	244,4075	91,745	45,8725	198,535
Bottom side floor	14,05	166,1175	270,4075	104,290	52,1450	218,2625

Table 5.3: Hydraulic stress distribution

The applied loads on the structure can be categorized into self-weight, earth load (associated with backfill), rock protection, ballast concrete, and traffic load. Table 5.4 below provides a detailed numerical classification of these loads.

Loads	Load types	SLS	ULS	ULS - favorable
Self - weight	Permanent	1,0	1,25	0,95
Hydrostatic load MWL	Permanent	1,0	1,15	0,95
Earth load	Permanent	1,0	1,15	0,95
Rock protection	Permanent	1,0	2,0	0,95
Ballast concrete	Permanent	1,0	1.25	0,95
Traffic load	Variable	1,0	1,50	0,00

Table 5.4: Loads, load types and load factors

To calculate the total load of the structure, the initial step involves determining the self-weight of the element, considering the distinct materials employed. This necessitates the multiplication of the steel and concrete areas by their respective specific masses. Material properties are detailed in Table 5.5, and the resulting self-weight of these two materials is summarized in Table 5.6.

Material densities	kN/m^3
Water	10,35
Concrete	23,2
Steel	77
Ballast concrete	23,2

Table 5.5: Material properties

Self - weight roof							**q** [kN/m]
$A_{c,roof}$	37.478.000	mm^2		37,478	m^2		24,95
$A_{s,roof}$	3.096.800	mm^2		3,097	m^2		6,48
						Total	31,43
Self - weight floor							**q** [kN/m]
$A_{c,floor}$	45.760.000	mm^2		45,760	m^2		30,47
$A_{s,floor}$	3.393.800	mm^2		3,394	m^2		7,10
						Total	37,57

Table 5.6: Surface area of steel/concrete & self-weight of roof/floor

The next phase involves determining the overall load on the tunnel roof/floor. This encompasses the summation of the self-weight of the structure, ballast concrete, hydraulic pressure, rock protection, and backfill. The consolidated values are presented in Table 5.7 below.

Roof			Floor		
Load types	**SLS**	**ULS**	**Load types**	**SLS**	**ULS**
Self - weight	31,43	39,29	Self - weight	37,57	46,96
Hydrostatic load MWL	66,76	76,77	Hydrostatic load MWL	-166,1175	-191,040
Rock protection	11,65	23,30	Ballast concrete	10,9145	13,64
			Traffic load UDL	10,00	0,00
Total [kN/m]	109,84	139,36 *downwards*	**Total [kN/m]**	-107,6367	-130,43
Walls - Top			**Walls - Bottom**		
Load types	**SLS**	**ULS**	**Load types**	**SLS**	**ULS**
Hydrostatic load MWL	72,580	83,470	Hydrostatic load MWL	218,2625	251,0019
Backfill	5,825	6,670	Backfill	52,145	59,977
Total [kN/m]	78,410	90,167 *upwards*	**Total [kN/m]**	270,4075	310,969

Table 5.7: The load q for each element in SLS & ULS

5.3 Design moment calculation

The design moment, represented by M_{ed}, undergoes calculation to facilitate subsequent comparison with the moment resistance of the cross-sectional elements. M_{ed} varies across different sections of the tunnel span. In its initial evaluation, M_{ed} is approximated using the conventional rule of thumb, expressed as $M_{ed} = \frac{1}{10} \times q \times l^2$. At the chosen span of 15m, there is an anticipation that the design moment or crack width might exceed the moment resistance or the maximum allowable crack width of an element, even with the application of the maximum reinforcement ratio. In such cases, it can be inferred that the reinforced concrete tunnel has reached its limit. Alongside the moment capacity assessment and crack width control, a similar procedure will be iterated for the normal stress check and shear capacity assessment. The manual computation of the design forces has been executed, and the results are detailed in Table 5.8.

Internal forces approximation - ULS			Internal forces approximation - SLS		
$M_{ed,roof}$	3105,4	kNm	$M_{ed,roof}$	2447,2	kNm
$M_{ed,floor}$	2970,6	kNm	$M_{ed,floor}$	2450,5	kNm
V_{roof}	1025,1	kN	V_{roof}	815,7	kN
V_{floor}	990,2	kN	V_{floor}	816,8	kN
N_{roof}	697,8	kN	N_{roof}	606,8	kN
N_{floor}	1227,7	kN	N_{floor}	1067,6	kN

Table 5.8: Hand calculation of the design forces

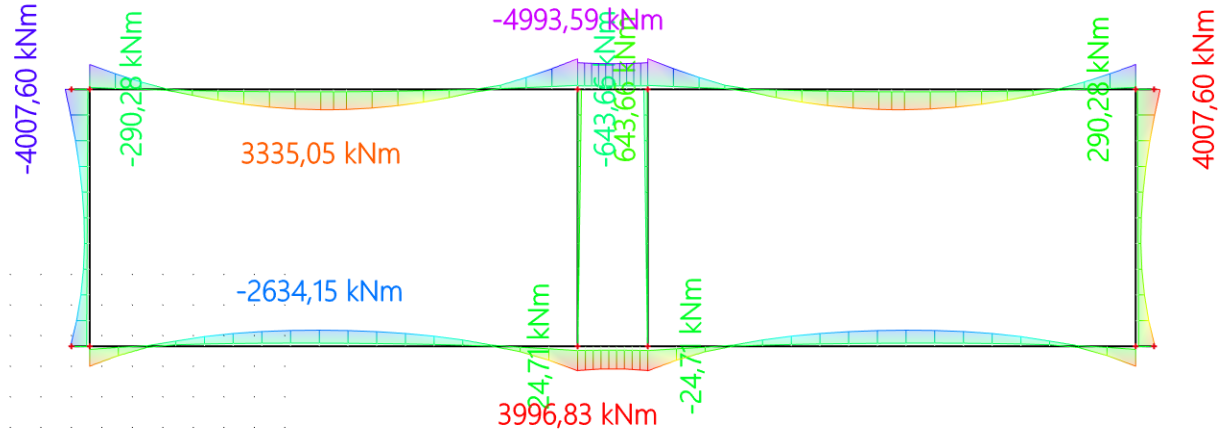

Figure 5.1: Bending moments diagram

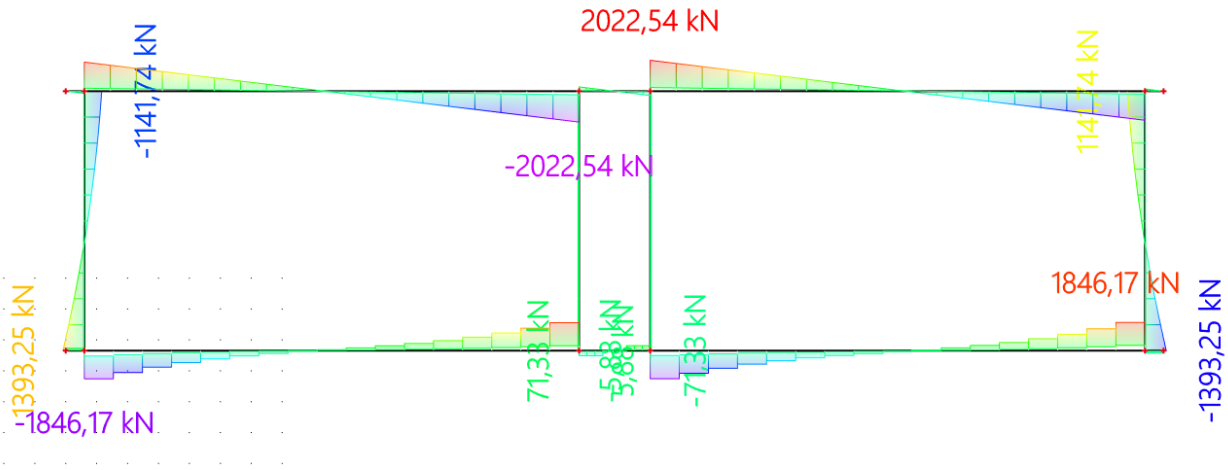

Figure 5.2: Shear forces diagram

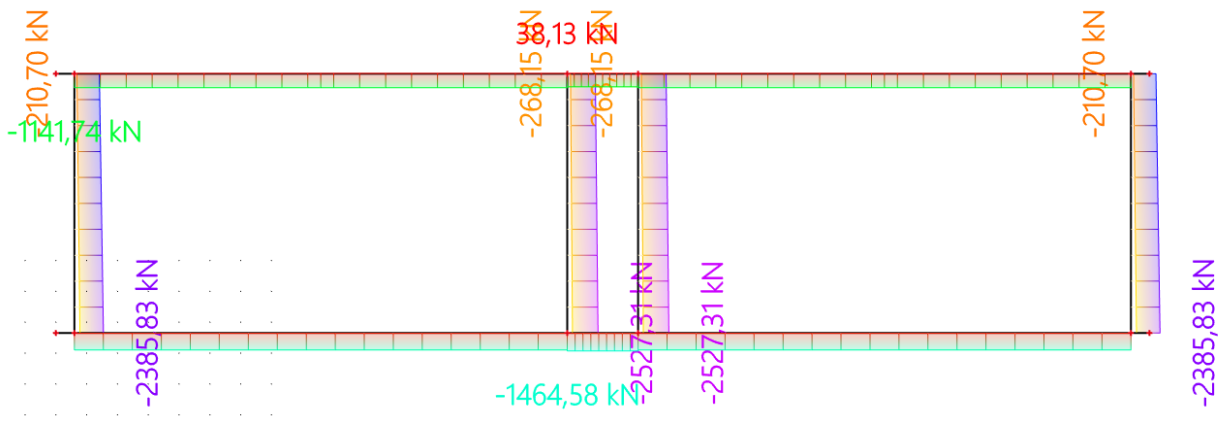

Figure 5.3: Axial forces diagram

5.4 Capacity of SCS tunnel

Now that the dimensions and loading details for the SCS tunnel elements are determined, follows the calculation of their capacity. The first step is to specify the materials used, which include concrete class C35 and steel class S355. The properties of these materials can be found in Table 5.9.

Material properties			
Steel S500 $[N/mm^2]$		**Concrete C35** $[N/mm^2]$	
f_y	500	f_{ck}	35
γ_s	1,15	γ_c	1,5
f_{yd}	434,78	f_{cd}	23,33
		$f_{ctk,0,05}$	2,25
		f_{ctd}	1,50
Elasticity modulus			
E_s $[N/mm^2]$		210000	
E_c $[N/mm^2]$		35000	

Table 5.9: Material properties of steel & concrete

The next step involves determining the dimensions for each tunnel element, distinguishing between the outer and inner parts. This distinction is crucial due to the varying flexural moment, resulting in different tensile and compressive stresses on each side. The flexural moment's impact generates diverse internal forces, prompting separate calculations and checks for the inner and outer sides of each element. Figure 5.1 visually illustrates the differentiation between the outer and inner parts, while Table 5.10 offers a concise summary of the initially chosen dimensions for the tunnel elements. This includes total height (h), chosen width unit (b), thickness of the steel plate in the compression zone (t_{sc}), thickness of the steel plate in the tensile zone (t_{st}), height of the concrete core (h_c), thickness of the diaphragm plates (t_{web}), and the center-

to-center distance of the diaphragm.

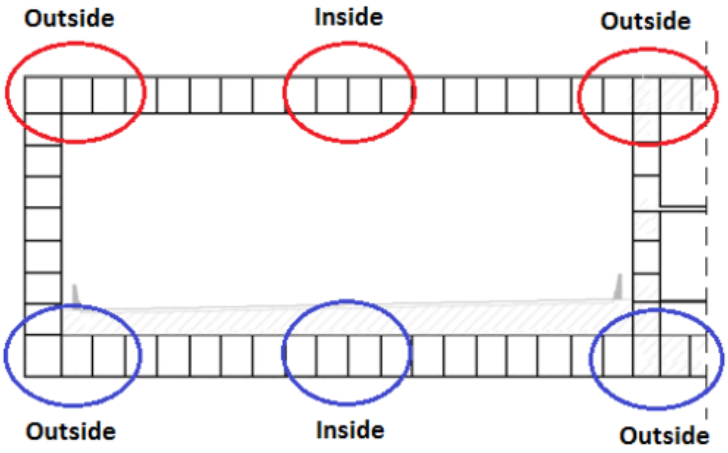

Figure 5.4: Outside and inside sections (roof: red, floor:blue)

Dimensions	$Roof_{outside}$	$Roof_{inside}$	$Floor_{outside}$	$Floor_{inside}$	$Walls_{outside}$	$Walls_{inside}$
h $[mm]$	1100	1100	1300	1300	1200	1200
b $[mm]$	1000	1000	1000	1000	1000	1000
t_{sc} $[mm]$	25	35	25	35	25	25
t_{st} $[mm]$	35	25	35	25	25	25
h_c $[mm]$	1040	1040	1240	1240	1150	1150
t_{web} $[mm]$	15	15	15	15	15	15
$c.t.c._{web}$ $[mm]$	3000	3000	3000	3000	2500	2500
A_c $[mm^2]$	1040000	1040000	1240000	1240000	1150000	1150000

Table 5.10: Elements outside's and inside's dimensions

5.4.1 Shear capacity of SCS tunnel (ULS)

The initial step involves determining the dimensions of the cross - section, paving the way for subsequent capacity checks. The first check pertains to the shear force capacity, which consists of two components: the concrete shear force capacity and the steel shear force capacity. Beginning with the determination of the concrete shear force capacity, the process unfolds with consecutive steps. First, the height of the concrete zone is established, followed by the calculation of the total concrete area. With the ultimate allowable shear stress in concrete defined, the shear force resistance of the concrete component is then calculated. The entire process is captured in the formulas below.

$$h_c = h - t_{sc} - t_{st}$$

$$A_c = h_c \times b$$

$$f_{ctk} = 0,7 \times 0,3 \times f_{cd}^{\frac{2}{3}}$$

$$f_{ctd} = \frac{f_{ctk}}{\gamma}$$

$$\tau_{rd,c,min} = 0,4 \times f_{ctd}$$

$$Vrd,c = \tau_{rd,c,min} \times A_c$$

where:
h = total height of the cross - section
t_{sc} = thickness of steel plate in compression zone
t_{st} = thickness of steel plate in tensile zone
h_c = height of the concrete core
b = chosen width unit
A_c = concrete area
f_{cd} = compressive design stress of concrete
f_{ctk} = tensile characteristic stress of concrete
f_{ctd} = tensile design stress of concrete
$\tau_{rd,c,min}$ = allowable shear stress in concrete
$V_{rd,c}$ = shear resistance of concrete core

Now, next step involves the calculation of the second component, which is the shear resistance of the steel. Firstly, it needs to be determined the height of the diaphragm (web) to calculate the total steel area contributing to the shear force resistance of the cross - section. With this area and the known design yield stress of the steel, the steel shear force resistance can be calculated using the summarized procedure below.

$$h_{s,web} = h - t_{sc} - t_{st}$$

$$A_{v,s} = h_{s,web} \times t_{web}$$

$$V_{rd,s} = A_{v,s} \times f_{yd}$$

$$Vrd,c+s = V_{rd,c} \times V_{rd,s}$$

where:
$h_{s,web}$ = height of the web
$A_{v,s}$ = steel area that contributes to shear resistance
$V_{rd,s}$ = shear resistance of steel
$V_{rd,c+s}$ = total shear resistance of steel and concrete

The outcomes of the described procedures above are displayed in Table 5.11.

Shear capacity	$Roof_{outside}$	$Roof_{inside}$	$Floor_{outside}$	$Floor_{inside}$	$Walls_{outside}$	$Walls_{inside}$
$\tau_{rd,c,min}$ $[N/mm^2]$	0,6	0,6	0,6	0,6	0,6	0,6
$V_{rs,c}$ $[kN]$	623,2	623,2	743,0	743,0	689,1	689,1
$h_{s,web}$ $[mm]$	1040	1040	1240	1240	1150	1150
$A_{v,s}$ $[mm^2]$	15600	15600	18600	18600	17250	17250
$V_{rd,s}$ $[kN]$	6782,6	6782,6	8087,0	8087,0	7500,0	7500,0
$V_{rd,c+s}$ $[kN]$	7405,8	7405,8	8830,0	8830,0	8189,1	8189,1
V_{rd} $[kN/m]$	2468,6	2468,6	2943,3	2943,3	3275,6	3275,6

Table 5.11: Shear force capacity

The determined shear force resistance of the cross section will be compared with the design shear force V_{ed} resulting from external loading and self - weight based on the numerical results of SCIA (not based on the analytical - by hand calculation as it is less accurate). Table 5.12 provides the design shear forces checks for all the elements of the tunnel cross - section.

Roof					
$V_{ed,roof}$ $[kN]$	2022,5	$V_{rd,roof}$ $[kN]$	2468,6	U_{check}	0,82
Floor					
$V_{ed,floor}$ $[kN]$	1846,2	$V_{rd,floor}$ $[kN]$	2943,3	U_{check}	0,63
Wall$_{top}$					
$V_{ed,wall_{top}}$ $[kN]$	1141,7	$V_{rd,wall_{top}}$ $[kN]$	3275,6	U_{check}	0,35
Wall$_{bottom}$					
$V_{ed,wall_{bottom}}$ $[kN]$	1393,3	$V_{rd,wall_{bottom}}$ $[kN]$	3275,6	U_{check}	0,43

Table 5.12: Shear force capacity checks

5.4.2 Moment capacity of SCS tunnel (ULS)

Following the shear force resistance calculations, the moment capacity of the composite tunnel element will be examined. This assessment includes the roof, floor, and wall elements of the tunnel, considering the varying tensile and compression zones. For each element, two moment resistance calculations will be conducted, accounting for two different steel plate configurations. The dimensions of the steel plates and concrete layer are optimized to ensure that the moment resistance M_{rd} of the cross - section surpasses the design moment M_{ed}. The determination of the moment resistance involves the procedure described below with the use of the following formulas.

$$N_{sc} = b \times t_{sc} \times f_{yd}$$

$$N_{st} = b \times t_{st} \times f_{yd}$$

$$N_{cu} = N_{st} - N_{sc} + N_{axial}$$

$$x_u = \frac{N_{cu}}{0,85 \times b \times f_{cd}} \geq 0,2 \times h_c$$

where:
b = width
t_{sc} = thickness of the steel plate in compression zone
t_{st} = thickness of the steel plate in tensile zone
f_{yd} = design yield strength of steel
N_{sc} = normal force of steel plate in compression zone
N_{st} = normal force of steel plate in tensile zone
N_{su} = normal force of of concrete in compression
f_{cd} = design compressive strength of concrete
h_c = height of concrete
x_u = height of the compression zone in Ultimate Limit State (ULS)

The initial stage involves computing the compressive and tensile forces within the steel plates. This is achieved by multiplying the steel area by the design yield strength of steel. Consequently, the concrete compressive force N_{cu} in the ultimate limit state can be determined. The distribution of forces and the respective lever arms across the cross section are visually depicted in Figure 5.2(a). These forces, along with their internal lever arms, collectively generate a moment known as the moment resistance. The determination of moment resistance involves a two-step process. Initially, the moment arising from compressive forces, denoted as $M_{rd,c}$, is calculated. This comprises two components: the normal force in the steel element and the concrete compressive force. To establish equilibrium, the normal force in the bottom steel plate is omitted from the moment calculation by considering the center of this plate as the reference line. This approach allows for the determination of moment resistance attributed to compressive forces, as illustrated in Figure 5.2(b). Similar steps are taken for the moment due to the tensile force in the bottom steel plate, referred to as $M_{rd,t}$. The internal level arm is selected to exclude the force in the steel plate from the moment equilibrium calculation, as depicted in Figure 5.2(c) below.

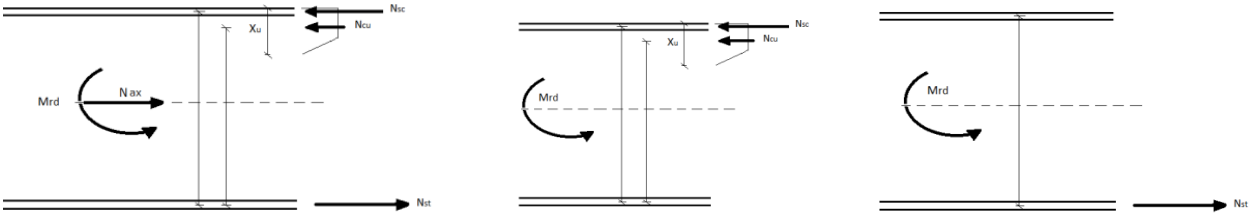

(a) Cross - sectional forces (b) Compressive forces and $M_{rd,c}$ (c) Tensile force and $M_{rd,t}$

Figure 5.5: Different stages for the calculation of M_{rd}

The governing moment for design is determined by selecting the smallest value between the moments calculated from the compressive and tensile forces based on the procedure described above. The moment per meter is obtained by dividing this selected moment by the width. Table 5.13 below presents the results after the calculations.

Bending capacity	$Roof_{outside}$	$Roof_{inside}$	$Floor_{outside}$	$Floor_{inside}$	$Walls_{outside}$	$Walls_{inside}$
$N_{sc,rd}$ $[kN]$	10869,6	15217,4	10869,6	15217,4	10869,6	10869,6
$N_{st,rd}$ $[kN]$	15217,4	10869,6	15217,4	10869,6	10869,6	10869,6
$N_{cu,rd}$ $[kN]$	5045,6	-5045,6	5575,5	-5575,5	1492,6	-1492,6
N_{axial} $[kN]$	-697,8	697,8	-1227,7	1227,7	-1492,6	1492,6
x_u $[mm]$	254,4	254,4	281,1	281,1	75,3	75,3
$M_{pl,rd,c}$ $[kNm]$	16591,7	10839,6	20017,6	16514,3	14228,7	10771,3
$M_{pl,rd,t}$ $[kNm]$	16720,1	10892,0	19411,2	13294,0	12525,2	12474,8
$M_{pl,rd}$ $[kNm]$	16591,7	10839,6	19411,2	13294,0	12525,2	10771,3
$M_{pl,rd/m}$ $[kNm/m]$	16591,7	10839,6	19411,2	13294,0	12525,2	10771,3
M_{ed} $[kNm]$	4993,6	3335,1	3996,8	2634,2	4007,1	2005,9
$\boldsymbol{U}_{check}$	0,30	0,31	0,21	0,20	0,32	0,19

Table 5.13: Moment capacity unity checks

5.5 Design of studs and stiffeners

To ensure a strong connection between the steel plate and concrete, stiffeners and/or studs are utilized. As their name suggests, these stiffeners not only add rigidity to the steel plate but also prevent deformation during the concrete pouring phase. Welded on both sides of the steel plates, these components efficiently transfer forces from the steel to the concrete. Figure 5.3 illustrates the arrangement of studs and stiffeners on the upper steel plate of a sandwich element.

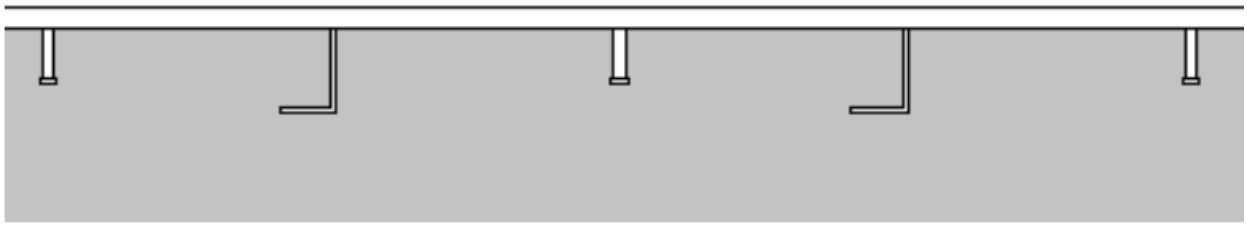

Figure 5.6: Arrangement of shear studs and stiffeners

To comprehend the appropriate procedure, it is crucial to highlight the behavior of the elements. The shearing aspect to be analyzed in the cross - section occurs between the plates and the concrete core. Therefore, the initial step involves determining the longitudinal force (figure 5.7), starting with the calculation of the neutral axis for each element, based on figure 5.8.

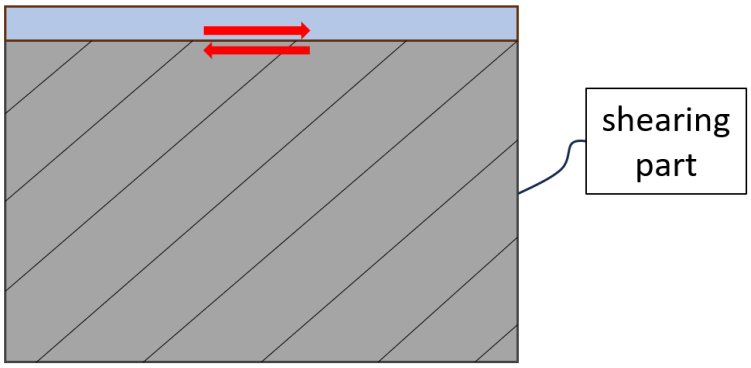

Figure 5.7: Longitudinal shear of the connection between concrete core and steel plate

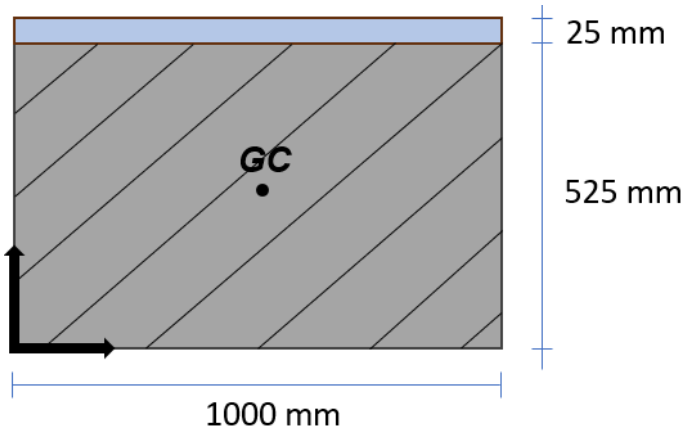

Figure 5.8: Dimensions used for calculation of roof's neutral axis

	Roof	*Floor*	*Walls*
$A_{s,top}$ $[mm^2]$	25000	25000	25000
A_c $[mm^2]$	1040000	1240000	1150000
$z_{s,top}$ $[mm]$	537,5	637,5	587,5
z_c $[mm]$	262,5	312,5	287,5
e_{GC} $[mm]$	282,8	332,9	307,7

Table 5.14: Centre of gravity results

Table 5.14 summarizes the centre of gravity results for each element of the cross-section based on the following formula:

$$e_{GC} = \frac{w_c \times z_c + w_{s,top} \times z_{s,top}}{w_c + w_{s,top}} = \frac{(25000 \times 77 \times 537,5) + (1040000 \times 23,2 \times 262,5)}{(25000 \times 77) + (1040000 \times 23,2)} = 282,8 \quad mm$$

where:

w_c = weight of concrete area based on the following formula: $w_c = A_c \times \rho_c$ where ρ_c: density of concrete

$w_{s,top}$ = weight of top steel plate area based on the following formula: $w_{s,top} = A_{s,top} \times \rho_s$ where ρ_s: density of steel

z_c = distance of the centre point of the concrete block to the reference axis

$z_{s,top}$ = distance of the centre point of the top steel plate to the reference axis

Subsequent calculations include the moment of inertia F_{izz}, the first moment of area S_z^a, and finally, the shear force per unit length S_x^a. Below it is shown the procedure for the roof (the same procedure follows for all the elements).

$$I_{zz} = \frac{1}{12} \times 1000 \times (550^3) = 1,4E+10 \quad mm^4$$

$$S_z^a = 525 \times 1000 \times (282,8 - \frac{525}{2}) = 1,4E+10 \quad mm^3$$

$$S_x^a = -\frac{V_z \times S_z^a}{I_{zz}} = -\frac{2022,5}{1272,7} = -1556,1 \quad N/mm$$

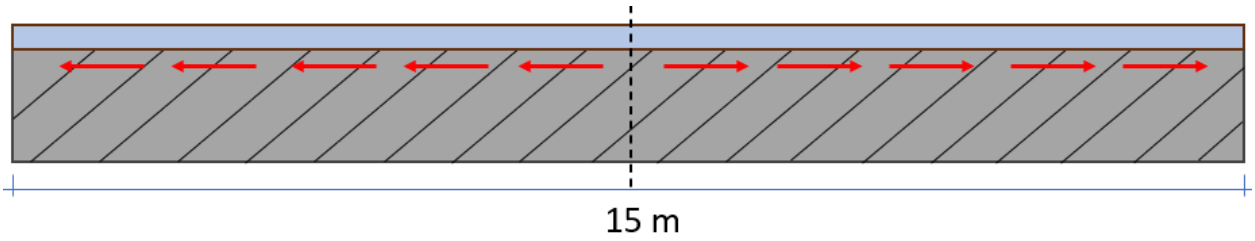

Figure 5.9: Development of the longitudinal shear force in the roof element

The longitudinal shear force of the roof element has been determined, allowing for the calculation of the total shear force as well.

$$R_s = \frac{1}{2} \times 1556,1 \times 7500 = 5835,5 \quad kN$$

The capacity of the stiffener is currently being evaluated. This element is expected to yield if the maximum stress at the interface between the stiffener and the steel plate is exceeded. As a result, the maximum moment that the stiffener can sustain can be calculated as follows:

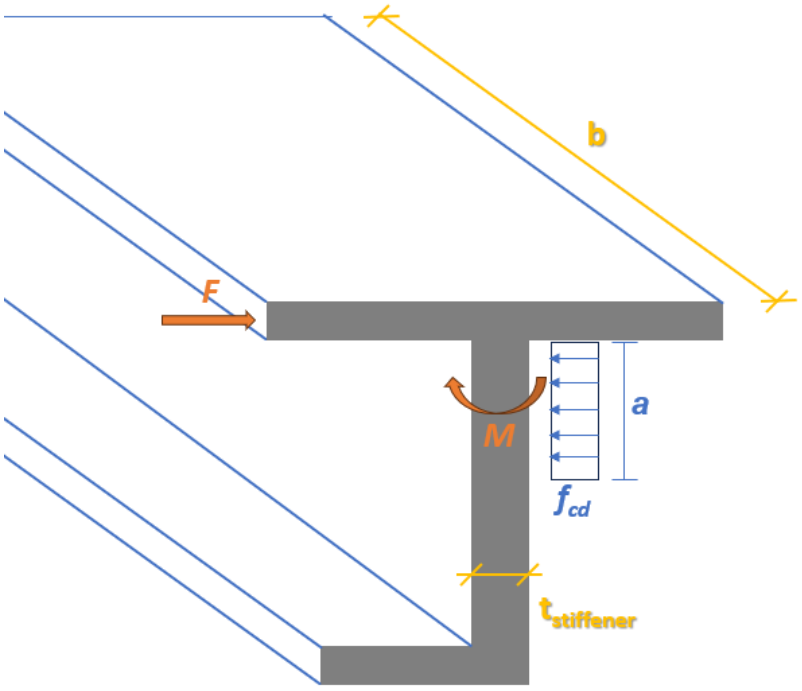

Figure 5.10: Forces acting on the stiffener

$$M = \sigma \times W \quad with \quad W = \frac{1}{4} \times b \times t_{stiffener}^2$$

where:
$M =$ bending moment
$\sigma =$ yielding stress f_{yd}
$W =$ cross section modulus
$t_{stiffener} =$ thickness of stiffener

The resisting bending moment of the stiffener must counterbalance the bending moment generated by its interaction with the concrete, as shown in Figure 5.10. From equilibrium of forces and bending moment it is concluded the following:

$$F = F_{stiffener} = a \times b \times f_{cd} \quad and \quad M = \frac{1}{2} \times a \times a \times b \times f_{cd}$$

where:
$b =$ width of the stiffener
$f_{cd} =$ design compressive stress of concrete

The only unknown in these equations is the "a" which can be found by solving for "a" the equilibrium equation of bending moments. Thus, it is:

$$a = \sqrt{\frac{2 \times f_{yd} \times W}{f_{cd} \times b}}$$

The next step involves calculating the capacity of the shear stud. The minimum length of a stud should be four times its diameter, which must fall within a range of 16 mm to 25 mm ($16mm \geq d_{stud} \geq 25mm$). There are two potential failure mechanisms for steel studs: one involves shear failure of the steel stud, while the other relates to the crushing of concrete (see figure 5.11 for reference). The capacity of the shear stud will be evaluated for both failure mechanisms. To determine the required number of studs, the lower of the two capacities will be used, as this is considered the governing one.

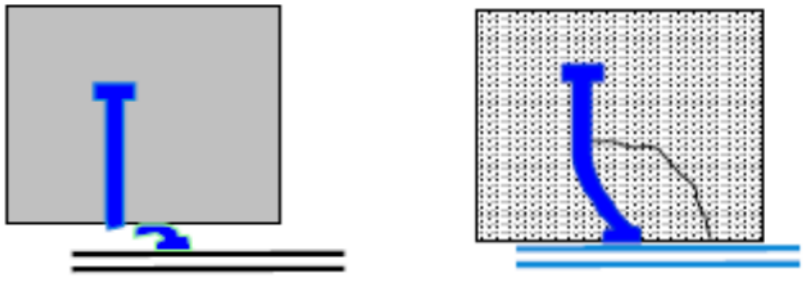

Figure 5.11: Failure mechanisms of shear stud (left: shearing, right: crushing of concrete)

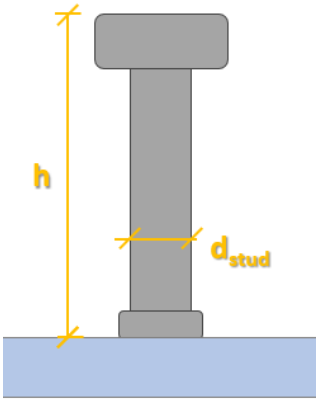

Figure 5.12: Dimensions of steel stud

The shear force capacity of the steel stud can be calculated based on the following formula:

$$F_{stud}^{shearing} = 0,8 \times f_{yd} \times \frac{1}{4} \times \pi \times d_{stud}^2$$

where:
f_{yd} = design yield stress of steel
d_{stud} = diameter of steel stud

The shear force capacity of the steel stud due to crushing of concrete can be calculated based on the following formula:

$$F_{stud}^{crushing} = 0,29 \times \alpha \times d_{stud}^2 \times \frac{\sqrt{f_{ck} \times E_{cm}}}{\gamma_v}$$

where:
f_{ck} = characteristic compressive strength of concrete
E_{cm} = modulus of elasticity of concrete
$\alpha = 1,0$
$\gamma_v = 1,25$

The contributions of both the stiffener and the stud are summed and the total capacity force of the shear connectors is:

$$F_{total} = F_{stud}^{shearing} + F_{stud}^{crushing}$$

The results of the procedures explained above are summarized in the following tables for all the elements of the SCS tunnel's cross-section.

	$Roof$	$Floor$	$Walls$
e_{GC} $[mm]$	282,8	332,9	307,7
I_{zz} $[mm^4]$	1,4E+10	2,3E+10	1,8E+10
S_z^a $[mm^3]$	1,1E+7	1,3E+7	1,2E+7
S_x^a $[N/mm]$	1556,1	1027,7	838,4
R_s $[kN]$	5835,5	3853,9	3144

Table 5.15: Total shear force of stiffener

	$Roof$	$Floor$	$Walls$
f_{yd} $[N/mm^2]$	322,7	322,7	322,7
f_{cd} $[N/mm^2]$	23,3	23,3	23,3
f_{ck} $[N/mm^2]$	35	35	35
E_{cm} $[N/mm^2]$	34077	34077	34077
d_{stiff} $[mm]$	15	15	15
W $[mm^3]$	56250	56250	56250
a $[mm]$	39,5	39,5	39,5
$F_{stiffener}$ $[kN]$	**920,5**	**920,5**	**920,5**
d_{stud} $[mm]$	20	20	20
$F_{stud}^{shearing}$ $[kN]$	**81,1**	**81,1**	**81,1**
$F_{stud}^{crushing}$ $[kN]$	101,3	101,3	101,3

Table 5.16: Shear force capacity of stiffener and stud

The next step consists of determining the layout for the stiffeners (150x150x15 mm³) and the studs (20 mm diameter, 80 mm height).

As noted earlier, it is essential for the studs and stiffeners to effectively transfer forces from the steel plates to the concrete. Although the forces in the steel plates vary along the length of the element (roof, floor, and wall), a uniform layout will be used across the entire element, as implementing multiple layouts in practice is not practical. Consequently, the calculation will utilize the maximum governing steel force, highlighted in bold in Table 5.16. The layout for the studs and stiffeners will be determined based on the following formula:

$$F_{stiffener} \times + F_{stud} \times n \geq N_{s,max}$$

where:

$L =$ stiffener's unit length

$n =$ number of studs welded to the plate

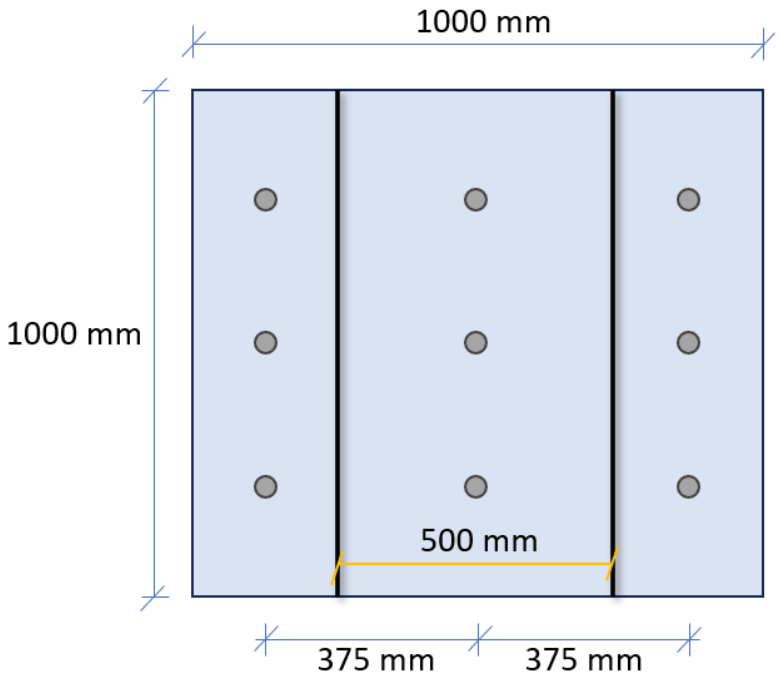

Figure 5.13: Top view layout of the shear connectors

5.6 Uplift and immersion calculations

As already mentioned in the previous chapter for the reinforced concrete tunnel design, the concepts of buoyancy and immersion play a vital role in the design and construction of immersed tunnels. It is important for the tunnel segments to be engineered to both float and facilitate their immersion into the water. To ensure these conditions are met, balance equations are utilized. If the cross-sectional design fails to satisfy these balance equations, adjustments to the cross-section will need to be made.

The design specifies a maximum element span of 15 meters, which is essential for the reference project. In the prior section, the dimensions of the elements in a sandwich tunnel configuration were established, providing the base for the subsequent uplift and immersion calculations. Before performing these calculations, it is necessary to assess the weight of the tunnel element, which relies on determining the areas occupied by the concrete and steel materials. These calculations are documented in tables 5.17 and 5.18 below.

Roof	b $[mm]$	h $[mm]$	A $[mm^2]$	**Floor**	b $[mm]$	h $[mm]$	A $[mm^2]$
Outer wall 1	1200	1100	1320000	Outer wall 1	1200	1300	1560000
Roof 2	15000	1100	16500000	Floor 2	15000	1300	19500000
Inner wall 2	800	1100	832000	Inner wall 2	800	1300	1040000
Gallery roof 4	1200	1100	1248000	Gallery floor 4	1200	1300	1560000
Inner wall 3	800	1100	832000	Inner wall 3	800	1300	1040000
Roof 6	15000	1100	15600000	Floor 6	15000	1300	19500000
Outer wall 4	1200	1100	1248000	Outer wall 4	1200	1300	1560000
Gallery floor 1	1200	200	240000	Toe ($\times 2$)	1600	1300	2080000

Walls	b $[mm]$	h $[mm]$	A $[mm^2]$
Outer wall 1	1200	7200	8460000
Inner wall 2	800	7200	57600000
Inner wall 3	800	7200	57600000
Outer wall 4	1200	7200	8640000
Total concrete area		115600000 mm^2	113,6 m^2

Table 5.17: Determination of concrete area

Roof	t $[mm]$	l $[mm]$	A $[mm^2]$	**Floor**	t $[mm]$	l $[mm]$	A $[mm^2]$
Outer side roof	35	35200	1232000	Outer side floor	35	36800	1288000
Inner side roof	25	31200	780000	Inner side floor	25	32800	820000
Web plate roof	15	11,8	191360	Web plate floor	15	12,3	228160

Walls	t $[mm]$	l $[mm]$	A $[mm^2]$
Outer side wall outside	25	9600	480000
Inner side wall inside	25	7200	1080000
Web plate walls	15	3	168480
Total steel area		6268000 mm^2	6,3 m^2

Table 5.18: Determination of steel area

After calculating the surfaces, the weight of the structure can be obtained by multiplying the area by its specific weight. This enables the determination of the total weight of the structure. The next step is to find out how much ballast concrete will be necessary after the immersion process. Since the overall height of the structure has already been established, the volume needed for the ballast concrete can be calculated as follows:

$$h_{ballast} = h_{total} - h_{free-traffic} - h_{equipment} - h_{asphalt} \tag{5.1}$$

$$h_{ballast,max} = 7,2 - 5,0 - 1,1 - 0,12 = 0,98$$

$$h_{ballast,average} = 0,98 - 2\% \times \frac{15}{2} = 0,83 \tag{5.2}$$

where:

$h_{ballast}$: the height of the ballast concrete

h_{total}: the total inner height of the structure

$h_{free-traffic}$: the free height height that is required for the traffic

$h_{equipment}$: the height that is needed for the installations

$h_{asphalt}$: the height of the asphalt which will be designed with a 2% slope

The buoyancy balance calculation can be refined using formulas 5.1 and 5.2, which involve two key checks: one for floating conditions and another for immersion. The floating condition requires the hydrostatic force to exceed the tunnel element's weight by approximately 1%.

$$Weight_{floating-up} = 0,99 \times buoyancyforce$$

The second check requires increasing the element's weight by 7,5% for safety against buoyancy. This is done by adding water, which will later be replaced with ballast concrete.

$$Weight_{immersion} = 1,075 \times buoyancyforce$$

The detailed results can be found in Tables 5.19 and 5.20 below.

Floating - up calculation				
Total areas	m^3	kN/m^3	kN	$factor$
Concrete	113,56	23,50	2668,66	1,0
Steel	6,27	53,50	335,34	1,00
Ballast	0,00	23,50	0,00	1,0
Hydrostatic load	340,00	10,00	3400,00	1,0
Check	0,88		< 1,00	

Table 5.19: Floating-up check

Immersion calculation				
Total areas	m^3	kN/m^3	kN	$factor$
Concrete	113,56	24,50	2782,22	1,0
Steel	6,27	77,00	482,64	1,00
Ballast	24,90	23,50	585,15	1,0
Earth	0,00	9,00	0,00	1,0
Hydrostatic load	340,00	10,35	3519,00	1,0
Check	1,09		> 1,00	

Table 5.20: Immersion check

The previous calculations indicate that the designed SCS composite tunnel element satisfies the requirements for both buoyancy and immersion. To account for possible variations in concrete density and casting precision, a conservative estimate of the concrete's specific weight is used in the assessment of immersion conditions.

Chapter 6

Simplified SCS composite beam finite element model

The chapter begins with a small-scale composite beam model as a first step in understanding the behavior of the roof element of the SCS immersed tunnel. This simplified model is chosen as it is aimed to simulate and implement a representative portion of the roof, providing knowledge into the interaction between the different components of the design (concrete, steel, and interface steel material) before proceeding with the complexity of a full 2D cross-section finite element model. Specifically, it allows for a focused analysis on a smaller and more manageable portion of the structure, allowing for an understanding of the behaviors and interactions within the design. Furthermore, it enables the efficient study of the linear and nonlinear characteristics of the different materials used, using DIANA FE software. This analysis is actually helping to determine the most critical material properties and how they influence the overall structural response. Finally, less computational time and effort is required compared to a full 2D cross-section model.

6.1 Beam composition and interaction

The beam consists of flange steel plates, steel webs, and concrete. Interaction occurs between the concrete and steel components. This interaction depends on the quality of the connection between the two materials. The connection can vary from strong (bond) to weak (slip). The figure below represents the concept of the design with a non-composite beam on the left and a composite beam on the right. In the first figure, the slip between the concrete slab and steel beam is evident due to the lack of interaction between these two distinct materials. However, on the right side of the figure, we observe composite action resulting from the bond created by shear connectors. These connectors reduce deflection and strain between the sections. While shear connectors cannot achieve a perfectly rigid connection between materials, they significantly minimize interface slip. By simulating adequately the connection it can be investigated how the quality of the connection and the interaction of the different materials influence the structural response of the design. Note that the example below does not match with the design in question.

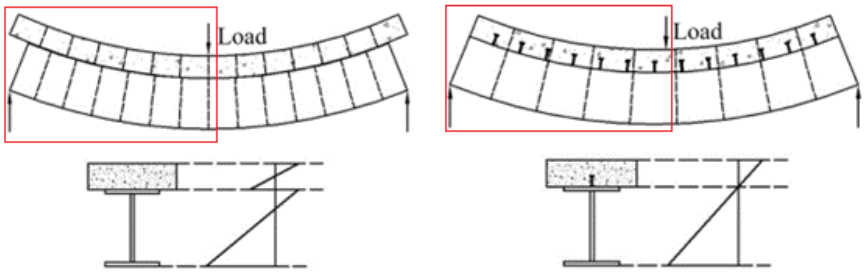

Figure 6.1: Non-composite and composite beam - ADD REFERENCE OF IMAGE

6.2 Model principles and material properties

The design principle for the finite element model utilizes the axis of symmetry and the foundational concept of a simply supported beam subjected to a point load at its right end. The boundary conditions will be established based on this concept.

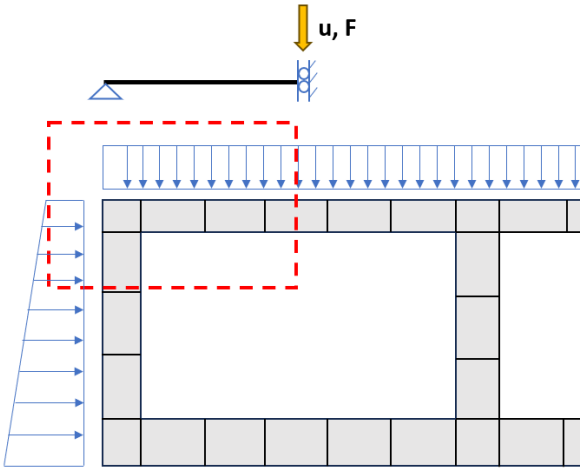

Figure 6.2: Boundary conditions based on the section of interest

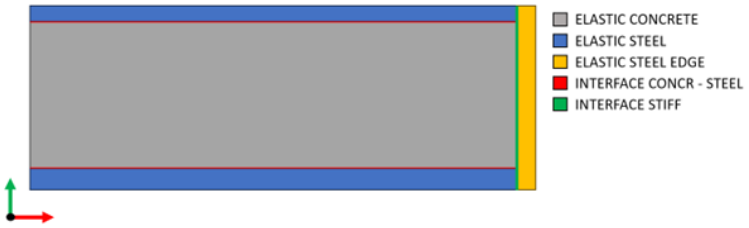

Figure 6.3: Design model of the beam

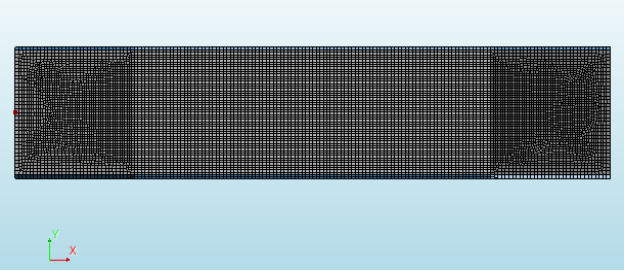

Figure 6.4: Mesh

Figure 6.5: Boundary conditions of the SCS composite beam

- **Boundary conditions for the model**

When choosing boundary conditions, certain decisions need to be made. For a half-model approach, as shown in figure 6.5, the symmetry axis along the vertical line of the loading position is selected. The boundary is fixed in the horizontal direction but can displace vertically. On the left side of the model, determining the location of vertical restraints is complex. However, it is decided to constrain all points along the left line vertically while allowing free horizontal movement.

If the vertical webs are included, the model shows as follows.

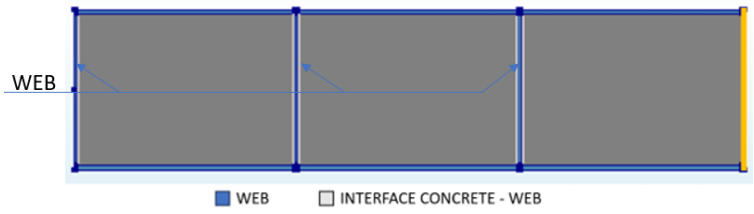

Figure 6.6: Webs

The tables below provide the details of the material properties for concrete, steel, and the interface. This master's thesis will investigate the structural behavior under various imperfections that can arise in the design, such as voids in the concrete and deformations of shear connectors, as discussed in the problem statement and literature review. These imperfections are critical to the connections between concrete and steel and can significantly impact the stability of the structure.

To simulate these conditions, variations in the values for the interface connections in the composite design will be applied. The notation and naming of these variations are briefly outlined in table 6.2. The potential imperfections include strong, weak, and no connection. In the cases of strong and weak connections, the tangential stiffness k_t will be modified from the standard value to a much lower numerical value (figure 6.7 and 6.8 respectively). In the case of no connection, the interface will be removed entirely, rendering the stiffness values irrelevant for the connection. Additional details regarding the specific values for each of these imperfection scenarios will be provided in the relevant sections of the model.

Material	Interface	
Linear Material Properties		
	Value	Units
Type	2D line interface	
Normal stiffness modulus - y	2E+08	N/mm^3
Shear stiffness modulus - x	2E+08	N/mm^3

Table 6.1: Interface material properties for a strong connection interface

Strong connection	Bond	$k_n = k_t = 2E + 08$	N/mm^3
Weak connection	Slip	$k_n = 2E + 08$ and $k_t = 2E - 08$	N/mm^3
Disconnection	Gap	k_n, k_t do not apply	-

Table 6.2: Variations of connection design imperfections

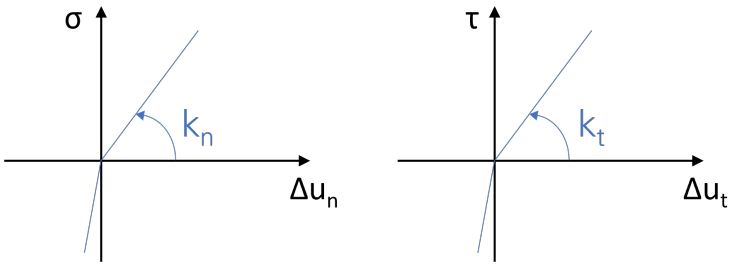

Figure 6.7: Strong connection interface element

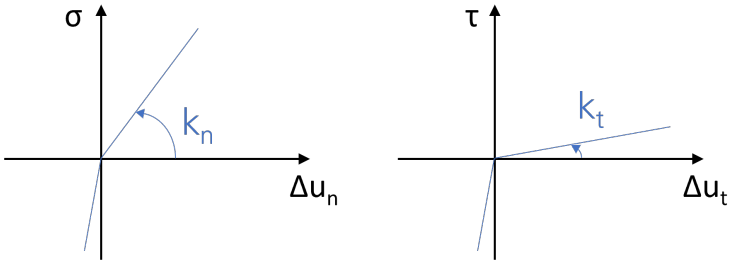

Figure 6.8: Weak connection interface element (no-tension)

Material	Concrete	
Linear Material Properties		
	Value	Units
Young's Modulus, E	3.5E+10	N/m^2
Poisson's ratio, v	0.15	-
Mass density, ρ	2400	kg/m^3
Nonlinear Material Properties		
Tensile Behavior		
Tensile curve	Hordijk	
Tensile strength	3.21E+06	N/m^2
Tensile Fracture Energy, G_{Fk}	18324.5	N/m
Crack bandwidth specification - Rots		
No residual tensile strength after cracking		
Confinement model - Damaged based		
Compressive Behavior		
Compressive curve	Parabolic	
Compressive strength	2.33E+07	N/m^2
Compressive Fracture Energy, G_{Fk}	29233.9	N/m
No residual compressive strength		
Reduction model - Vecchio and Collins 1993		
Confinement model - Selby and Vecchio		

Table 6.3: Concrete material properties

Material	Steel	
Linear Material Properties		
	Value	Units
Young's Modulus, E	2.1E+11	N/m^2
Poisson's ratio, v	0.15	-
Mass density, ρ	7850	kg/m^3
Nonlinear Material Properties		
Von Mises and Tresca plasticity		
Plasticity model - Von Mises plasticity		
Hardening function - No hardening		
Yield stress	4.35E+08	N/m^2

Table 6.4: Steel material properties

6.3 Analytical problem solution of the composite beam

The dimensions and the analytical solution of the SCS composite beam model are presented in tables 6.6 and 6.7 respectively. In this model, a vertical displacement of 25 mm is applied, allowing the force to be

approximated using the deflection formula for a simply supported beam, as illustrated in Figure 6.9. Displacement controlled analysis was chosen to achieve a smooth load path behavior and to address significant nonlinearity. Since the structure will be investigated under material nonlinearity conditions, the displacement control method ensures smooth solution progression by focusing on specific deformation levels. This approach enhances numerical stability and ensures effective convergence.

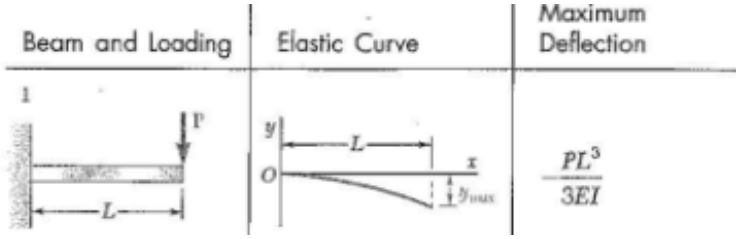

Figure 6.9: Beam deflection formula

To calculate the force, it is necessary to first determine the moment of inertia of the composite beam. This involves finding the neutral axis of the composite cross-section. The procedure for calculating the neutral axis, along with the necessary steps, is explained in the following lines.

$$e_{NC} = \frac{A_{c,tr} \times z_c + A_{s,top} \times z_{s,top} + A_{s,bottom} \times z_{s,bottom}}{A_{c,tr} + A_{s,top} + A_{s,bottom}} \tag{6.1}$$

In which:

$A_{c,tr}$ = transformed area of concrete based on the formula $A_{c,tr} = \frac{A_c}{n}$ where $n = \frac{E_s}{E_c}$

$A_{s,top}$ = area of the top steel plate

$A_{s,bottom}$ = area of the bottom steel plate

z_c = distance from the centre point of the concrete box to the reference axis

$z_{s,top}$ = distance from the centre point of the top steel plate to the reference axis

$z_{s,bottom}$ = distance from the centre point of the bottom steel plate to the reference axis

A_c $[mm^2]$	1040000	n	5,9
$A_{c,tr}$ $[mm^2]$	176810,6	$z_{c,tr}$ $[mm]$	262,5
$A_{s,top}$ $[mm^2]$	25000	$z_{s,top}$ $[mm]$	537,5
$A_{s,bottom}$ $[mm^2]$	35000	$z_{s,bottom}$ $[mm]$	17,5
e_{NC} $[mm]$	531,8		

Table 6.5: Neutral axis of the roof's composite cross-section

b = t	1000	mm		u	25	mm
h_1 (top plate)	25	mm		l	5000	mm
h_2 (concrete core)	1040	mm		E_s	210000	N/mm^2
h_3 (bottom plate)	35	mm		E_c	35000	N/mm^2
$y_{top(NC)}$	568,2	mm		$y_{bot(NC)}$	531,8	mm

Table 6.6: Geometry & material characteristics

	$A\ [mm^2]$	$I_y\ [mm^4]$	$d\ [mm]$	Ad^2	$I_{yy} = I_y + Ad^2$
1	25000	1,3E+06	555,7	7,7E+09	7,7E+09
2	1040000	9,4E+10	23,2	5,6E+08	9,4E+10
3	35000	3,6E+06	514,3	9,3E+09	9,3E+09
$I_{yy,steel,total}$	1,7E+10	mm^4	$E_s I_{yy,steel,total}$	3,6E+15	Nmm^2
$I_{yy,concrete,total}$	9,4E+10	mm^4	$E_c I_{yy,concrete,total}$	3,3E+15	Nmm^2
$EI_{yy,composite}$	6,9E+15	Nmm^2	F_{total}	4120073,5	N

Table 6.7: Analytical solution

For the strong connection (bond) of the composite beam, the deflection formula presented in table 6.7 is used: $w = \frac{Fl^3}{3EI_{yy,composite}}$. Solving for the displacement (u) gives a total force of 4120,1 kN. In the case where only concrete is activated, the same formula applies, but with $E_c I_{yy,concrete,total}$ taken into account, resulting in a force of 1980,3 kN.

6.4 Linear elastic analysis of the SCS composite beam

The finite element model research begins with the simplified composite beam illustrated in Figure 6.3. This beam consists solely of horizontal steel plates, where a horizontal interface connection is established between the steel plates and the concrete core. The subsequent analysis will explore the same beam with a restrained left end, represented by a vertical steel plate at the composite beam's left edge. After examining the behavior in both scenarios, the study will introduce the most accurate simulated model, reflecting the realistic design of the roof element of the SCS tunnel. In this more realistic model, vertical steel plates, known as webs, will be introduced to form composite boxes, or chambers, as described in the literature chapter. The accompanying figures (figure 6.10, 6.11 and 6.12) provide an overview of the beam for the different scenarios, detailing horizontal and vertical interfaces to clearly explain the nomenclature of different model analyses. Table 6.8 outlines the various analyses conducted for the scenarios described above.

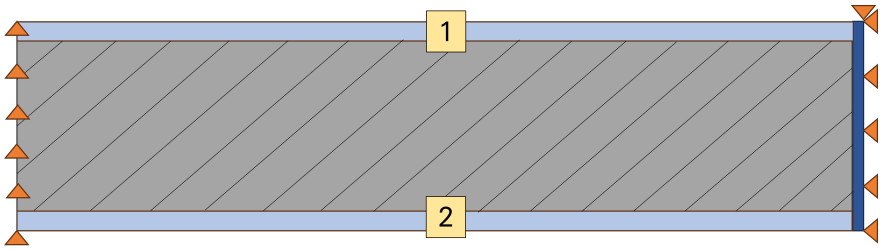

Figure 6.10: Beam with horizontal interfaces, without webs

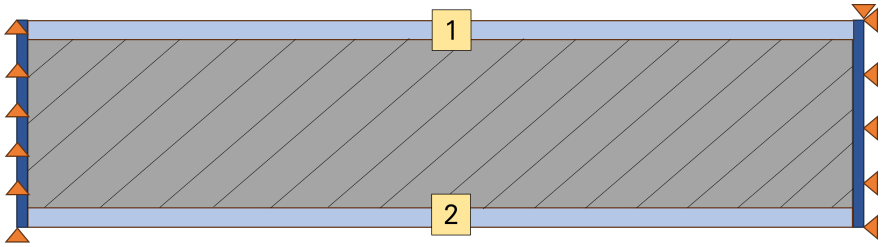

Figure 6.11: Beam with horizontal interfaces and restrained end, without webs

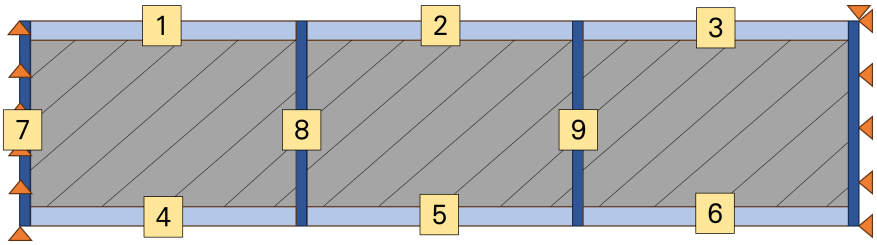

Figure 6.12: Beam with webs

Beam with horizontal interfaces, without webs (figure 6.8)		
	Strong connection	Weak connection
L-01	1-2	-
L-02	-	1-2
Beam with horizontal interfaces and restrained end, without webs (figure 6.9)		
	Strong connection	Weak connection
L-03	-	1-2
Beam with webs (figure 6.10)		
	Strong connection	Weak connection
L-04	1-9	-
L-05	-	1-9

Table 6.8: Overview of nonlinear material analyses models

* *L-01: Linear elastic analysis - case model 01*

6.4.1 Beam with horizontal interfaces, without webs

The initial step of the investigation is focused on a simplified design, including solely horizontal steel plates. The simplification will provide a preliminary understanding of the composite's beam structural behavior. Subsequently, the vertical plates will be added to create a detailed model that more accurately reflects the design of the SCS tunnel element.

Strong connection

The investigation begins with a linear static analysis of a strong (bond) connection for the interface elements. In the context of the designed finite element model, the full bond connection is established by applying high normal stiffness k_n and shear stiffness k_t to the interface elements between the steel plates and the concrete core. According to finite element theory, the initial stiffness must be significantly higher than that of a typical adjacent element, ensuring that the initial deformation remains negligible in comparison. To achieve this, the stiffness is typically set to, for example, 1000 times that of an adjacent element. For the normal stiffness, k_n is defined as $1000\frac{E}{t}$, while the shear stiffness, k_t, is defined as $1000\frac{G}{t}$. In this analysis, a normal stiffness of 2×10^8 N/mm^3 was applied, which is approximately 47 times greater than what is calculated using the formula $1000 \times \frac{E}{t}$, which results in a typical value of approximately 4200000 N/mm^3. This same value was also applied to the shear stiffness, thereby ensuring that the connections between the steel plates and the concrete core are considered rigid.

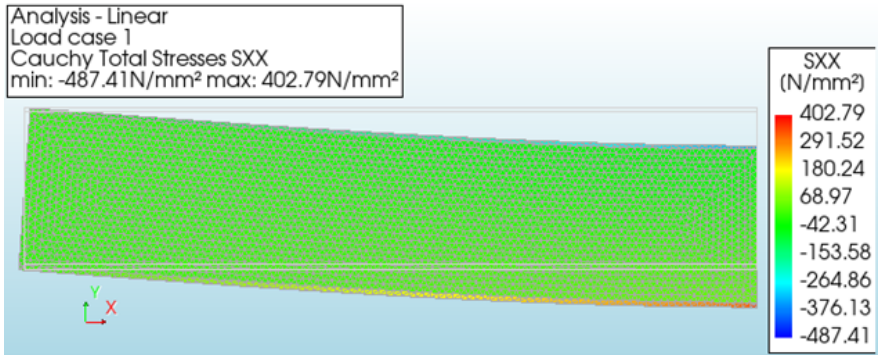

Figure 6.13: Strong connection (bond) deformation - stresses Sxx (model L-01)

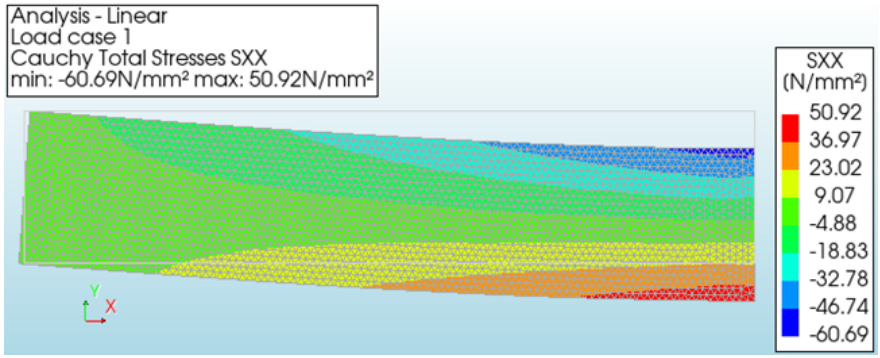

Figure 6.14: Strong connection (bond) - concrete slab (model L-01)

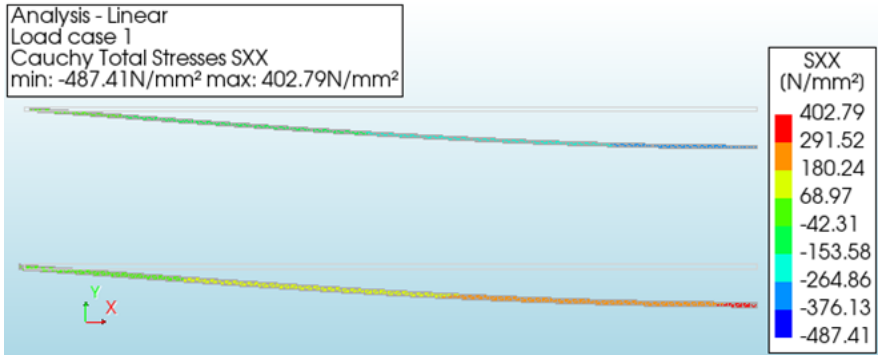

Figure 6.15: Strong connection (bond) - steel plates (model L-01)

- Bernoulli strains, according stresses: Bernoulli's theory states that in bending beams, plane sections remain plane and perpendicular to the neutral axis, leading to a linear strain distribution across the beam's depth. According to Hooke's Law ($\sigma = E \cdot \epsilon$), stress ($\sigma$) also follows a linear pattern, with maximum stress occurring at the extreme fibers - compressive at the top and tensile at the bottom. This fundamental understanding allows for a clear observation of the behavior of the modeled beam, which exhibits similar characteristics. Specifically, compression is observed in the top part of the beam, while tension is present in the bottom part.

- Steel stress in plates gradually increases: The contour plots of stress in steel plates reveal that stress gradually increases with the applied load. This gradual increase is primarily influenced by the material properties of steel and the distribution of forces resulting from bending moments and shear forces. As the load intensifies, the stress concentration in the plates becomes more pronounced, highlighting the structural behavior under the applied deformation.

Weak connection

The following figures represent the linear static analysis of a weak (slip) connection for the interface elements. The slip, in terms of the designed finite element model, is defined by low shear stiffness of the interface elements between the steel plates and the concrete core while the normal stiffness is kept high as applied for the full bond connection. The shear stiffness in this analysis is low (numerically 0 value) and equal to $2 \times 10^{-}8$ N/mm^3 compared to the stiffness of a typical finite element for the steel material equal to 1620000 N/mm^3 (with $G = 81000\ N/mm^2$).

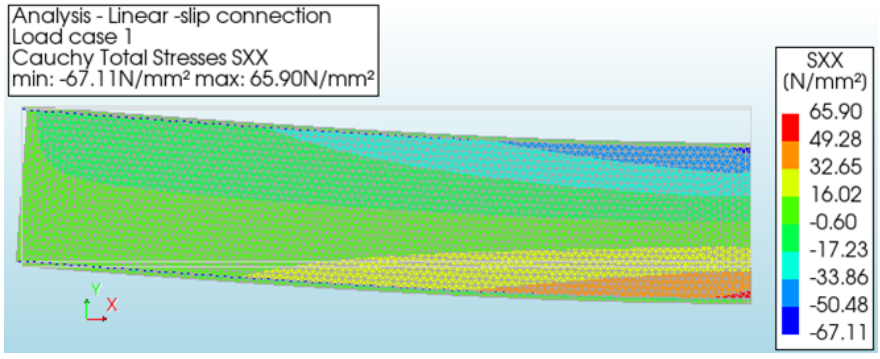

Figure 6.16: Weak connection (slip) deformation - stresses Sxx (model L-02)

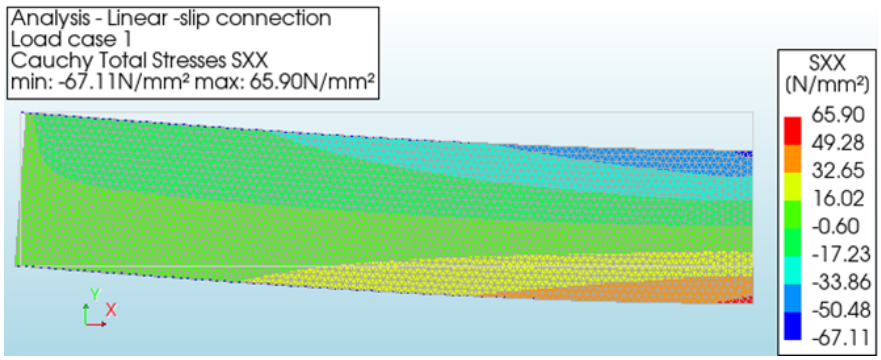

Figure 6.17: Weak connection (slip) - concrete slab (model L-02)

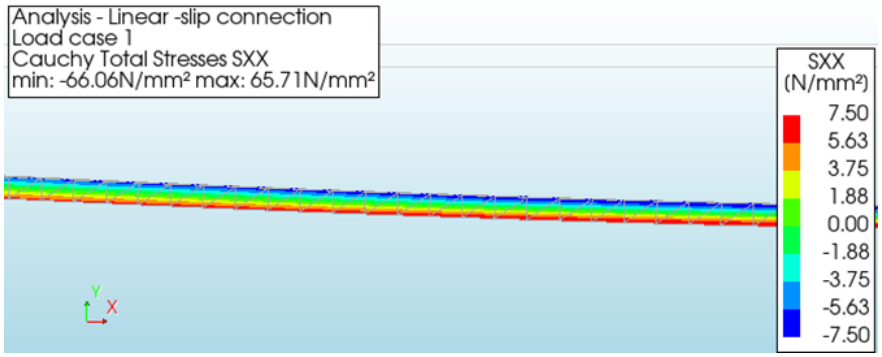

Figure 6.18: Close up of bottom plate: visible bending behavior (model L-02)

The contour plot in figure 6.18 reveals a clear pattern: compression at the top of the plate and tension lines at the bottom.

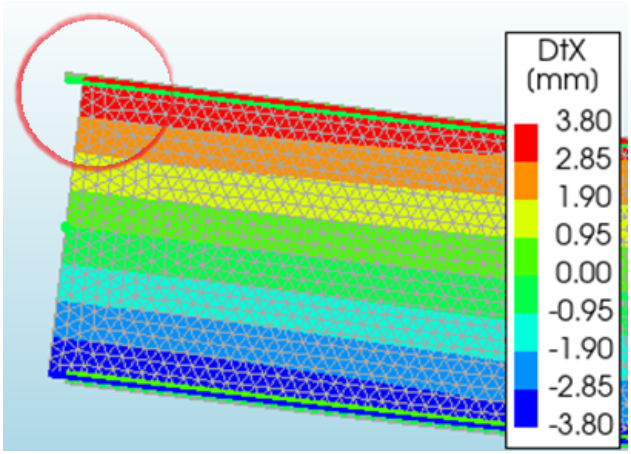

Figure 6.19: Visible slip at the boundary of the beam (model L-02)

Due to slip, there is a clear deformation difference at the boundary.

In case of the tunnel, the end of the plate is not able to freely deform. There is a restrain. In the following paragraph the behaviour of a restrained end beam is investigated.

6.4.2 Weak connection with restrained end

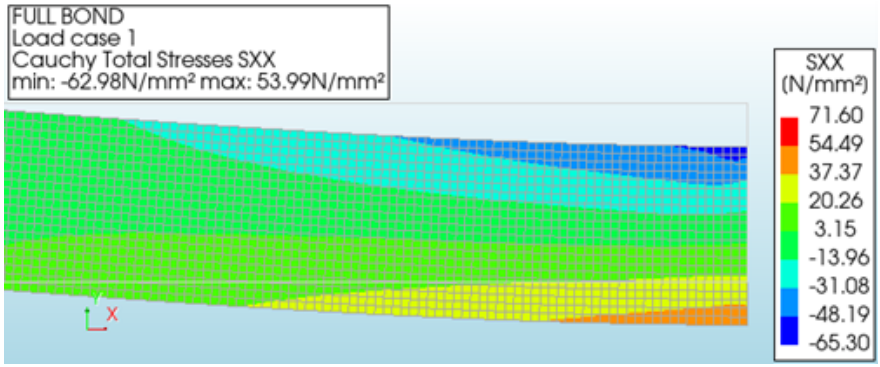

Figure 6.20: Weak connection (slip) with restrained end - concrete slab (model L-03)

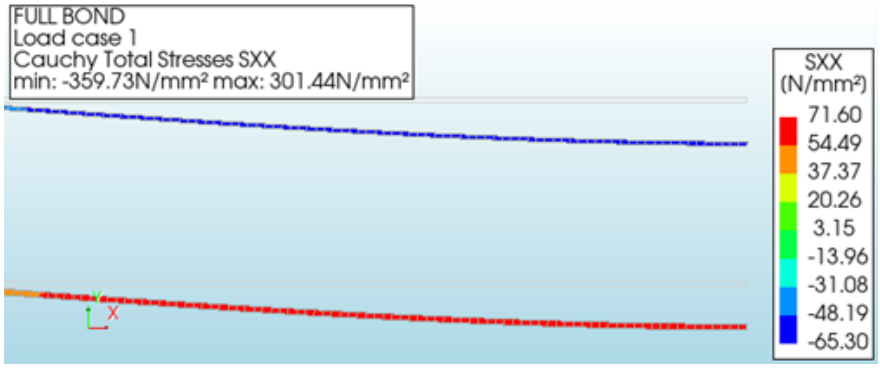

Figure 6.21: Weak connection (slip) with restrained end - steel plates (model L-03)

In figure 6.21 it can be observed that there is a uniform stress distribution along the steel plates of the beam. The plates serve as external pre-stressing elements, and their stresses remain uniform along the lengths.

Conclusions

Based on the above investigation the model's behavior for the different scenarios can be concluded in the following graph. The blue line corresponds to the linear static analysis of the strong connection (model L-01), the orange one represents a weak connection (model L-02) and the yellow one represents a weak connection when the model has a restrained end (model L-03).

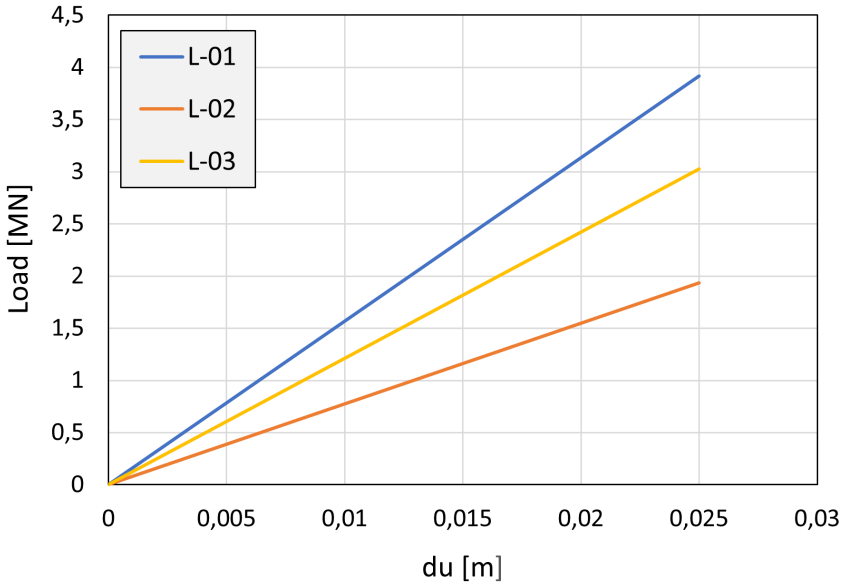

Figure 6.22: Force - displacement graph

- Using the strong connection linear model results in a load of 3915,86 kN, close to the expected analytical value of 4120,08 kN (with an error of about 5%).
- Weak connection linear model yields a load of 1932,43 kN, closely matching the expected value for the case accounting only on the concrete beam (1980,30 kN, with an error of about 2,5%).
- Weak connection linear model with restrained end shows an intermediate load of 3026,50 kN. This behaviour resembles externally pre-stressed concrete structures, where steel plate stresses remain constant along the beam length.

The third bullet point is particularly interesting because boxed tunnels have vertical webs in addition to top and bottom steel plates. These vertical webs may act as fixed points, while the plates function as external pre-stressed systems. Further analysis will focus on these vertical webs.

6.4.3 Model with webs

The SCS tunnel design is composed by horizontal and vertical steel plates. The vertical plates enhance the structure's stability and, as mentioned in the literature study, are responsible for sustaining and transferring the shear loading. Up to this point, the research has considered a model with horizontal steel plates, however it is crucial to incorporate the vertical plates (webs) to fully capture the composite design of the tunnel element. Thus, the same analysis will be applied for a the composite beam model including vertical plates.

Figures 6.23 and 6.24 visually illustrate the stress distribution for the strong and weak connection models, as determined by the linear static analysis.

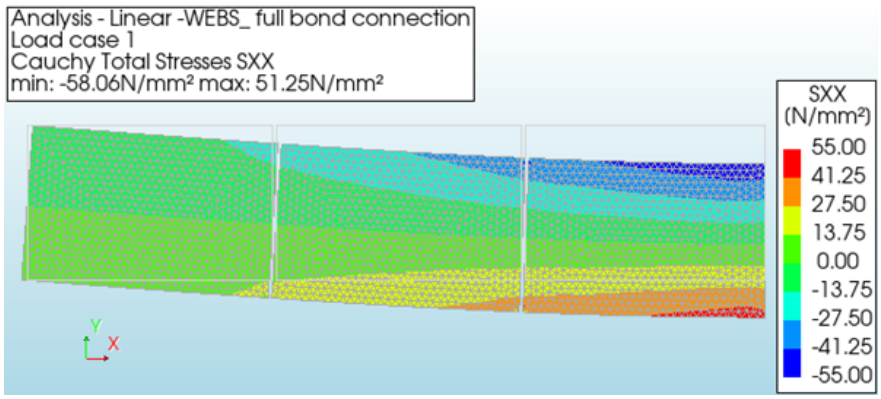

Figure 6.23: Strong connection with webs - Stress Sxx (model L-04)

In a perfect bonded situation, the webs have no influence on the force - displacement curve.

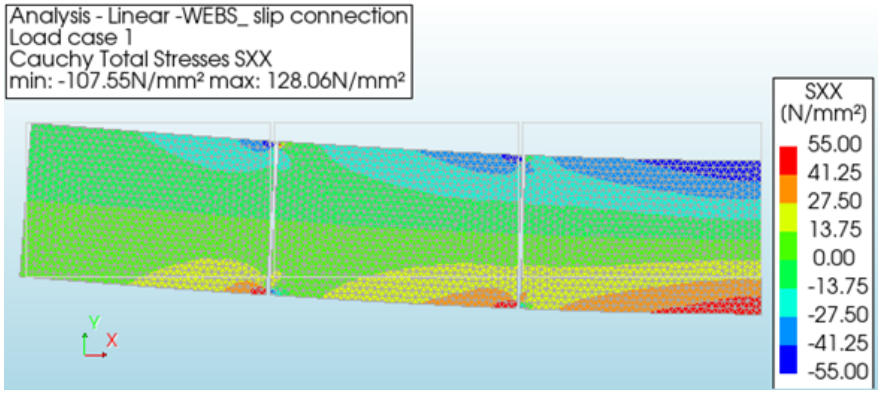

Figure 6.24: Weak connection with webs - Stress Sxx (model L-05)

It can be observed that slip affects all interfaces, clearly influencing the stress distribution. Based on these, the conclusion is presented in the following graph.

Conclusions

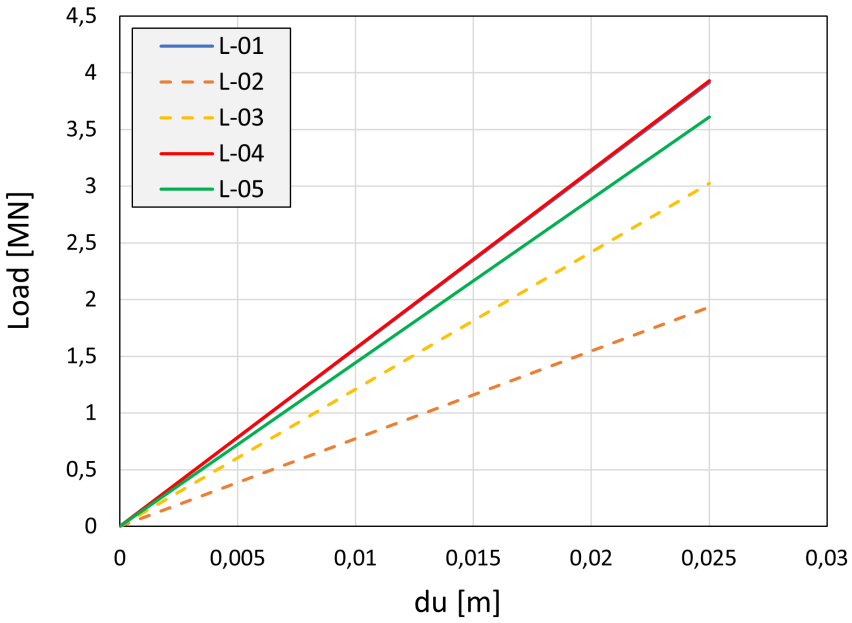

Figure 6.25: Force - displacement graph

- The webs do not significantly influence load capacity in the case of a perfect bonded condition.
- In the case of weak connection at the interface, the webs act as anchorage, similar to fixed ends with external pre-stressed concrete, providing additional support.

In the next section, there will be considered nonlinear material behaviour.

6.5 Nonlinear analysis of the SCS composite beam

Having completed the linear elastic analysis using ideal material responses for concrete and steel, it is crucial to consider the nonlinear characteristics. The initial analysis focuses on introducing nonlinearity in the concrete material, after which nonlinearity in the steel material will be examined separately as well. Following these analyses, nonlinearity will be applied to both concrete and steel. The table below outlines the sequence of various nonlinear analyses conducted, highlighting the variations applied for both strong and weak connection at the interfaces. The numbered interfaces in the table correspond to the enumerated interfaces shown in Figure 6.12 (paragraph 6.4).

Nonlinear concrete models		
	Strong connection	Weak connection
A-01	1-9	-
A-02	-	1-9
A-03	1-6	7-9
A-04	7-9	1-6
Nonlinear steel models		
	Strong connection	Weak connection
B-01	1-9	-
B-02	-	1-9
B-03	7-9	1-6
Nonlinear concrete and steel models		
	Strong connection	Weak connection
C-01	1-9	-
C-02	-	1-9

Table 6.9: Overview of nonlinear material analyses models

* *A-01: Nonlinear concrete analysis - case model 01*
* *B-01: Nonlinear steel analysis - case model 01*
* *C-01: Nonlinear concrete and steel analysis - case model 01*

6.5.1 Nonlinear concrete behavior

As previously stated, this section will examine the SCS composite beam under conditions of nonlinear concrete material. Both strong and weak connections will be applied at the horizontal and vertical interfaces to analyze the structural behavior.

Strong connection

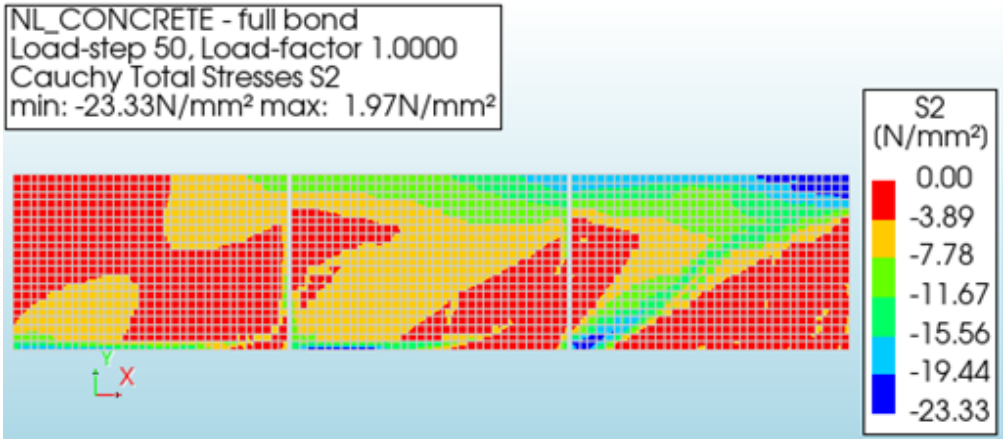

Figure 6.26: Strong connection: crushing of concrete - Principal stresses S2 (model A-01)

In the model, compressive struts form, and cracks develop along these struts.

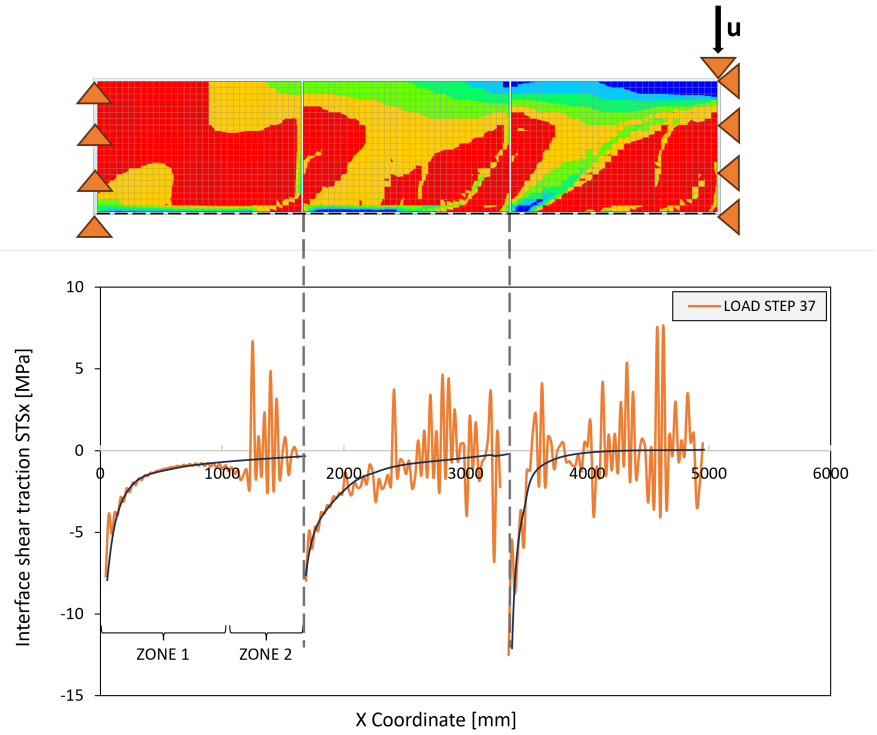

Figure 6.27: Shear interface tractions along the bottom interface connection (model A-01)

Graph 6.27 illustrates the shear interface traction between the bottom steel plate and the concrete core along the beam's length in the x-direction. The shear traction values are observed to fall within the expected range, specifically between 3,21 MPa, which represents the maximum tensile strength of concrete, and 23,3 MPa, the maximum compressive strength, as concrete is the dominant component of the composite structure. This behavior aligns with the principles outlined in Mohr's circle for concrete finite elements, where the shear behavior is anticipated to fluctuate between these maximum compressive and tensile strengths. The graph demonstrates that the selected shear conditions yield values that accurately reflect the various loading scenarios of compression and tension.

The interface is divided into two distinct zones. Zone 1 exhibits a smooth curve, consistent with the averaged drawn curve, indicating a coherent load transfer process. This stability can be attributed to the influence of the compressive strut formation and the boundary conditions on the left, which restrict vertical translation. Consequently, high compressive stresses reach the starting node of the interface, affecting the element values in Zone 1 as it seeks equilibrium. In contrast, as one moves away from the compressive strut region towards Zone 2, the nodes at the end of the interface experience diminished influence from the high compressive stresses present in Zone 1. The behavior in Zone 2 becomes more disturbed, resulting from a combination of low stress values at the end of Zone 1, tension loads transferred from the web, and compressive loads from the subsequent interface's strut. The wobbling effect observed in the graph can be attributed to the challenges faced by the nodes in reaching equilibrium among the varying stress sources.

Overall, a similar behavioral pattern is observed across all interfaces, reinforcing the conclusion that the interface functions as a fully bonded connection between the steel plates and the concrete core, with no slip effects impacting the structure. Higher shear traction values are consistently noted in all interfaces at the starting area (Zone 1), where the influence of high compressive stresses significantly affects the structural

behavior of the composite beam.

Weak connection

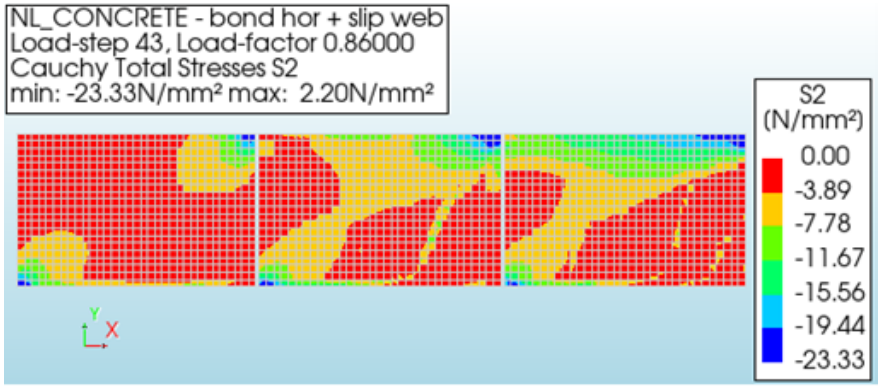

Figure 6.28: Weak connection: crushing of concrete - Principal stresses S2 (model A-02)

The compressive strut is clearly visible in Figure 6.28, and the bearing mechanism resembles the strut-and-tie model. This observation is crucial because it highlights the limitations of bending theory in fully capturing the complex behavior of the SCS beam.

Bending theory assumes a continuous stress distribution across the section, but the strut-and-tie model offers a more accurate representation of the load path in scenarios where localized stress concentrations are likely to occur, such as in composite structures with steel plates, webs, and non-linear concrete. The strut-and-tie model simplifies the analysis by recognizing that load is transferred through discrete compressive struts (acting like "ties" between concentrated forces) and tensile ties (reinforcing bars) working together to resist the applied load. This is illustrated in Figure 6.29, where the idealized strut-and-tie model closely resembles the behavior observed in the composite beam model under non-linearity material conditions.

This resemblance is particularly important because the SCS beam design faces similar challenges due to the presence of vertical webs and the non-linearity of the concrete core, which create complex load paths that are not effectively captured by bending theory alone.

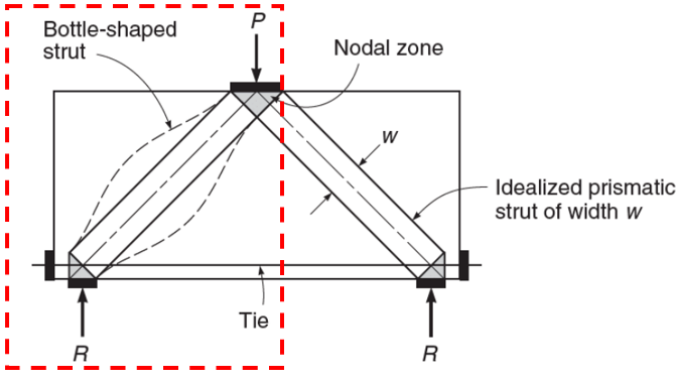

Figure 6.29: Strut and tie model formation on a beam with a middle point load [23]

In examining the interface connection between the bottom steel plate and the concrete core, the "zip effect" is noticeable, which illustrates the propagation of slip from right to left along the line. The accompanying graph depicts the path line of slip along the bottom interface for model analysis A-02, where a weak connection is applied to the horizontal interfaces of the composite beam.

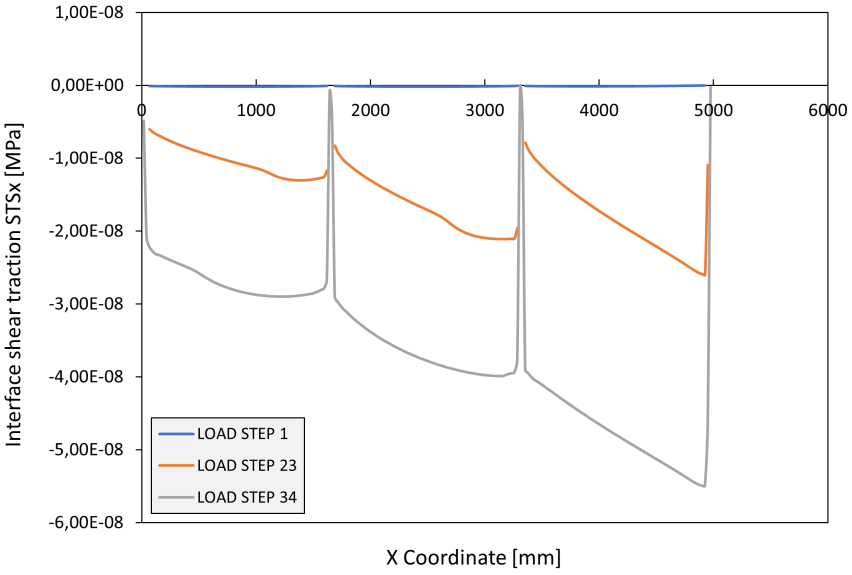

Figure 6.30: Shear tractions along the bottom line interface connection

The graph illustrates three distinct lines: the blue line represents the initial load step in the analysis, the orange line indicates an intermediate load step, and the grey line marks the final converged step. Notably, slip is most pronounced at the bottom interface of the third box, specifically at the edge where the displacement load is applied. As anticipated, sliding between the bottom steel plate and the concrete initiates from the right end, where the displacement load is introduced. Furthermore, it is important to note that the values on the order of E-08, regarded as numerically negligible, indicate a weak connection between the steel plates and the concrete core. This observation is consistent with the input parameters of the linear interface element.

Conclusions

The results are concluded in figure 6.31 below.

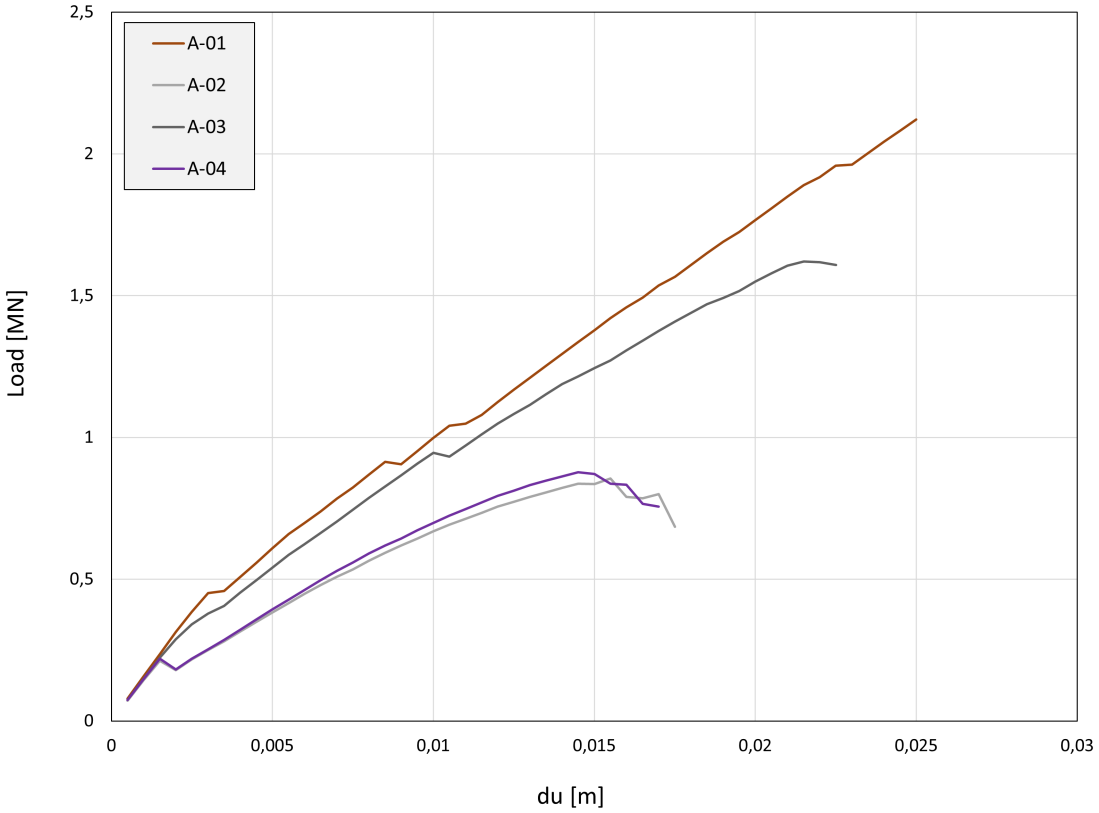

Figure 6.31: Force - displacement graph for the different combinations of strong and weak horizontal and vertical interface connections for the nonlinear concrete model

- The extreme cases are the strong and weak connection models (model A-01 and A-02 respectively), presenting the highest and lowest capacities, respectively. The worst - case scenario involves slip at the horizontal interface, regardless of whether the web interface is bonded or slipping. Thus the critical component is the horizontal interface.

- Nonlinear material behaviour of concrete significantly influences the structural capacity of the design. The governing bearing mechanism relies on compressive struts, following the strut-and-tie model, rather than Bernoulli bending.

The graph shows that the strong connection (model A-01) model achieves the highest load capacity, while the weak connection (model A-02) model results in the lowest capacity. Intermediate cases, such as weak connections at the horizontal interface with strong connected webs (model A-03), show moderate load capacities. It has also been investigated whether solely nonlinear steel behaviour (with linear concrete) has major implications. It turns out that the steel behaves linearly, and the structure is not influenced. The following graph provides as overview of the global behaviour of the models with nonlinear steel.

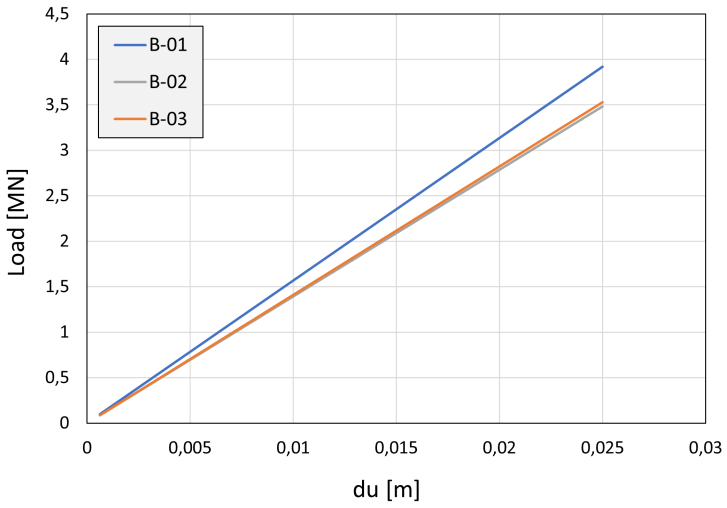

Figure 6.32: Force - displacement graph for nonlinear steel

The nonlinear steel - bond model results in a load equal to 3918,95 kN. By comparing this value to the value of the linear webs bond model, which is equal to 3929,05 kN, it can be concluded that the activation of the non-linearity of steel does not have influence on the capacity of the structure and that indeed the steel behaves linearly.

6.5.2 Nonlinear concrete and steel behaviour

This paragraph investigates the worst-case scenario for the structure, incorporating nonlinear behavior for both steel and concrete. Specifically, it examines the behavior of the beam when weak connection (slip) is introduced at both the horizontal and vertical (webs) interfaces between the steel plates and the concrete core.

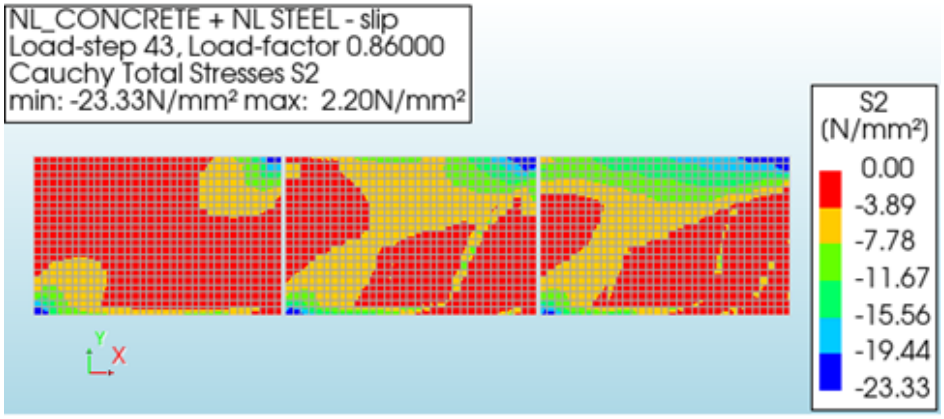

Figure 6.33: Nonlinear concrete and nonlinear steel model - weak connection (model C-02)

The results of this model align with those from the previous paragraph. The nonlinear behavior of steel has a limited effect on the overall capacity of the structure when considering the already nonlinear behavior of

concrete. While the graph demonstrates a similar global behavior across various scenarios, this suggests that steel's non-linearity is not the primary driver of failure when the concrete is already behaving non -linearly.

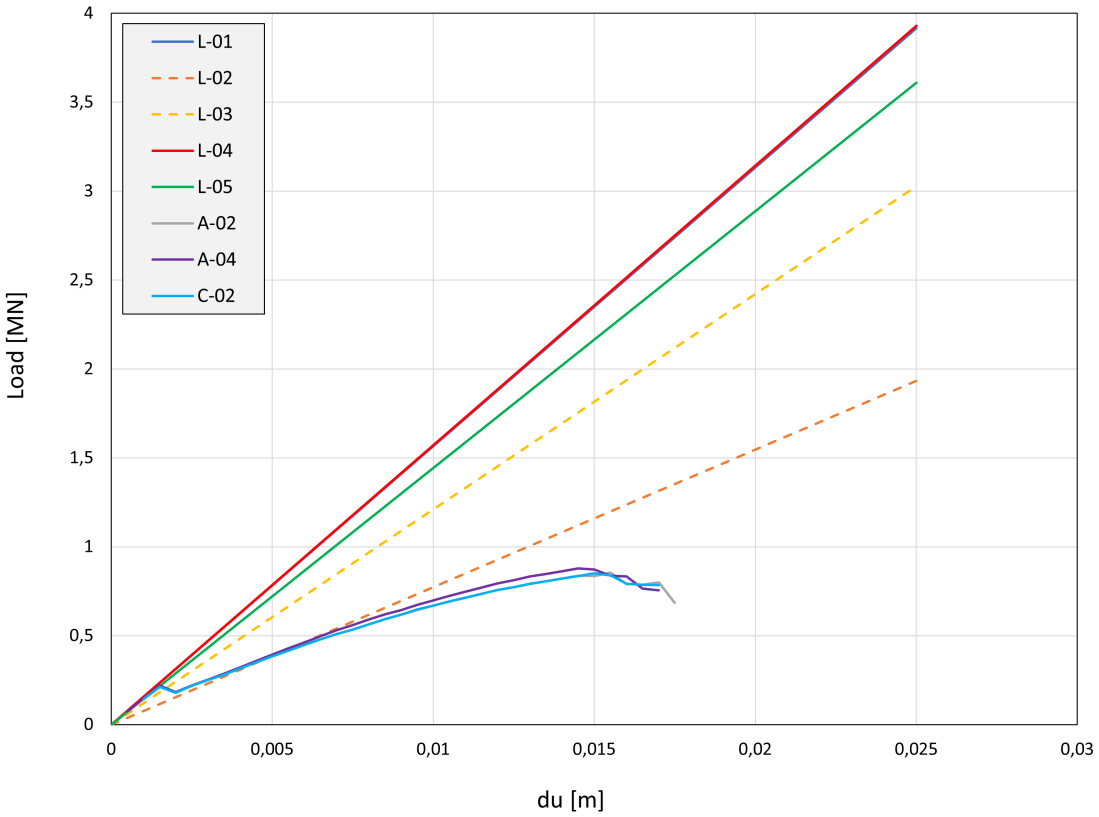

Figure 6.34: Force - displacement graph for nonlinear concrete and steel

Overall, it is concluded that:

- The bearing principle relies on compressive struts.
- The selection of these two nonlinear graphs is based on the worst-case scenario. Regardless of whether the web has a strong or weak connection, the horizontal interface is critical when subjected to low stiffness (slip).

The investigation aims to determine if the absence of interfaces, meaning no connection between concrete and steel (gap) or imperfections (e.g. incomplete concrete filling on the steel boxes) influence the structural behaviour of the element. It is expected that if such gaps intersect the assumed compressive struts, the bearing capacity will be affected.

6.6 Influence of disconnection between concrete and steel plates

The interface between the concrete slab and the steel plates is crucial for load transfer and connection within the SCS beam design. The finite element analysis has demonstrated that the horizontal interface plays a significant role in determining the structural capacity of the composite structure. If this connection is removed, load transfer between the different materials will cease, leading to failure.

Based on these findings, the most critical components influencing the structural capacity of the SCS beam design are the horizontal interfaces between the steel plates and the concrete core, along with the nonlinear behavior of the concrete. While the nonlinear behavior of steel also contributes, its impact on the overall capacity is less significant when compared to the nonlinear concrete.

Nevertheless, the analysis will focus on a model that incorporates nonlinear behavior for both steel and concrete, as this represents the most challenging scenario. The stiffness of the horizontal and vertical interfaces will be systematically varied (by applying either strong or weak connection on the interface) to examine its impact on the structure's capacity.

Based on the enumerated interfaces in Figure 6.12, the table below details the various case scenarios for the nonlinear model, including applied disconnections at specific interface locations of the composite beam.

Nonlinear concrete and steel models with disconnection at the top left interface connection			
	Strong connection	Weak connection	Disconnection
D-01	2-9	-	1
D-02	7-9	2-6	1
D-03	-	2-9	1
Nonlinear concrete and steel models with disconnection at the top line interface connection			
	Strong connection	Weak connection	Disconnection
D-04	4-9	-	1-3
D-05	7-9	4-6	1-3
D-06	-	4-9	1-3
Nonlinear concrete and steel models with disconnection at the bottom line interface connection			
	Strong connection	Weak connection	Disconnection
D-07	1-3, 7-9	-	4-6
D-08	7-9	1-3	4-6
D-09	-	1-3, 7-9	4-6
Nonlinear concrete and steel models with disconnection at the bottom right interface connection			
	Strong connection	Weak connection	Disconnection
D-10	1-5, 7-9	-	6
D-11	7-9	1-5	6
D-12	-	1-5, 7-9	6

Table 6.10: Overview of nonlinear material analyses models

** D-01: Nonlinear concrete and steel analysis with disconnection - case model 01*

6.6.1 Disconnection top left

The initial investigation into the impact of disconnections will focus on a gap located at the top left of the composite beam. Figures 6.35 and 6.36 illustrate the deformed shape of the stresses SXX, clearly revealing the presence of the disconnection.

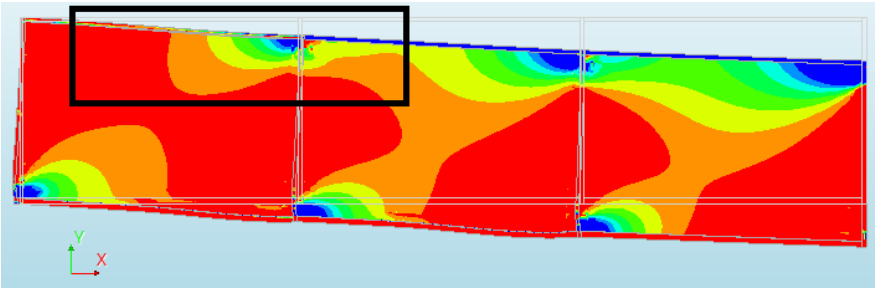

Figure 6.35: Disconnection on the top left - stresses SXX - visible gap

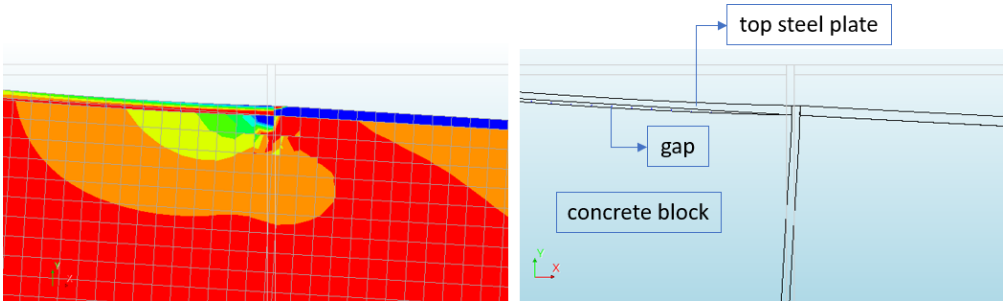

Figure 6.36: Gap on the top left - stresses SXX - zoom - in

Figure 6.37 illustrates the principal stresses (S2) of the composite beam at the last converged step before failure of the compressive strut. The figure reveals that the disconnection interrupts the continuous path of the compressive strut. This interruption weakens the ability of the compressive strut to transfer loads effectively. It can be observed that the gap causes a significant change in the stress distribution, resulting in a reduction of the compressive stresses in the area near the gap. This disruption is visible as a less concentrated stress pattern, indicating a breakdown in the load transfer mechanism. This disruption of the compressive strut leads to a decrease in the overall load-carrying capacity of the composite beam, as the primary load transfer mechanism is compromised. This ultimately contributes to the failure of the structure, making it more vulnerable to instability under additional loading.

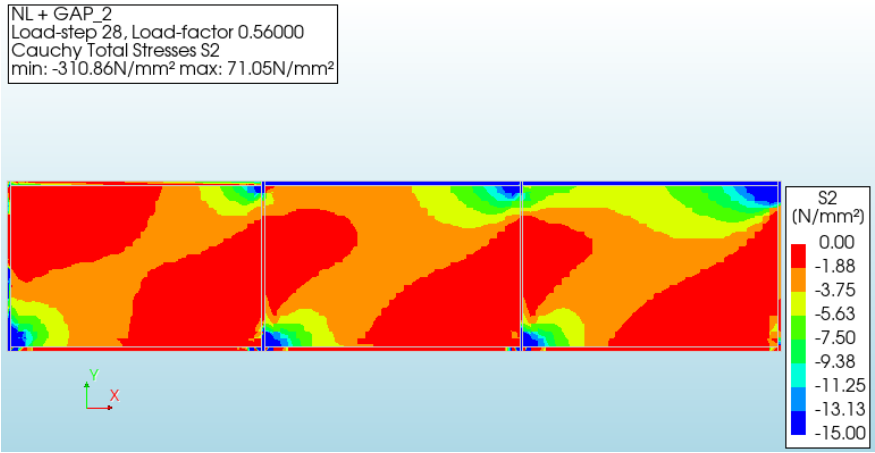

Figure 6.37: Gap on the top left (model D-02) - principal stresses S2

6.6.2 Disconnection top left and weak connection at interfaces

This analysis focuses on examining the behavior of the composite beam under conditions of non-linear concrete and steel materials, the disconnection at the top left between the top steel plate and the concrete core, and low tangential stiffness (slip) at both the horizontal and vertical steel plates. This scenario is regarded as the worst-case, as it involves the simultaneous occurrence of two types of imperfections: missing shear connectors (disconnection) and poorly placed shear connectors (weak connection).

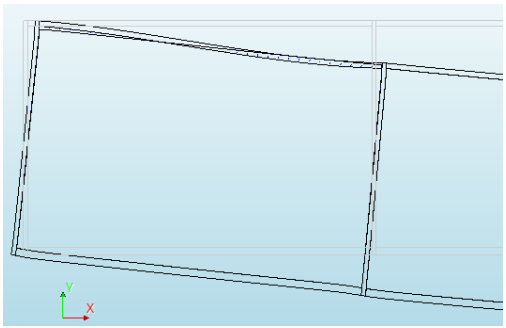

Figure 6.38: Disconnection on the top left - gap detail

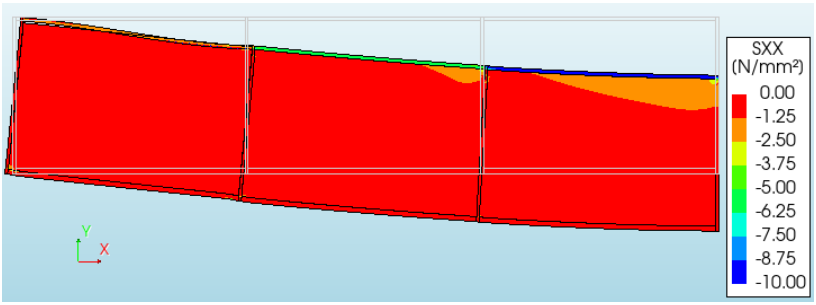

Figure 6.39: Disconnection on the top left (model D-03) - stresses SXX

The following figures (figures 6.40 and 6.41) illustrate that the compressive strut did not develop, indicating a failure in load transfer. In step 2 of the analysis, the contour plot of the compressive stresses (S2) indicates that the compressive strut was nearly formed at the right edge of the beam, where the displacement load was applied. However, this formation did not occur, as the compressive stress remained undeveloped until the final converged step of the analysis, just prior to the failure of the SCS composite beam.

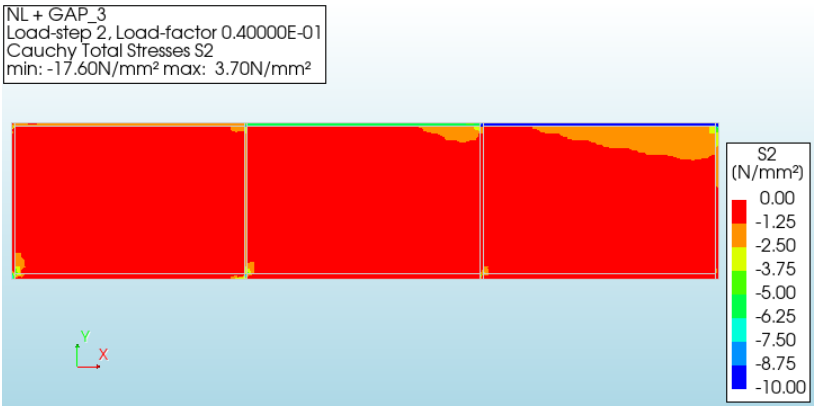

Figure 6.40: Disconnection on the top left (model D-03) - stresses S2 (step 2)

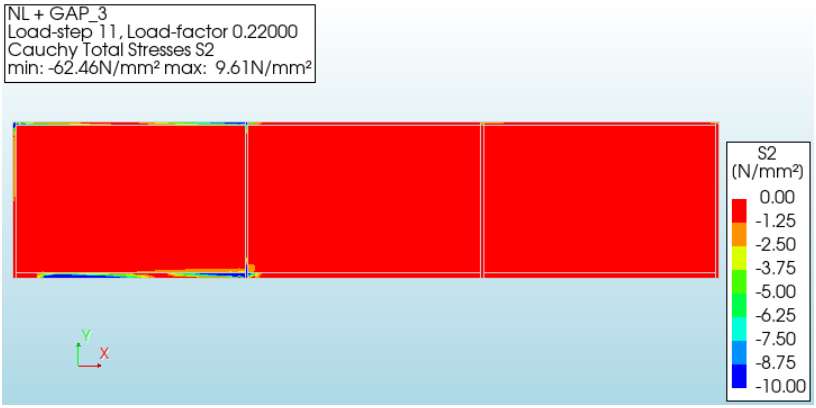

Figure 6.41: Disconnection on the top left (model D-03) - stresses S2 (last converged step)

As illustrated earlier, the zip effect is similarly depicted in the case of disconnection at the top left of the composite beam. The graph below presents the shear tractions along the bottom interface line of the model. Once more, the propagation of sliding behavior is observed, resulting from the weak connection applied at the horizontal interfaces of the beam.

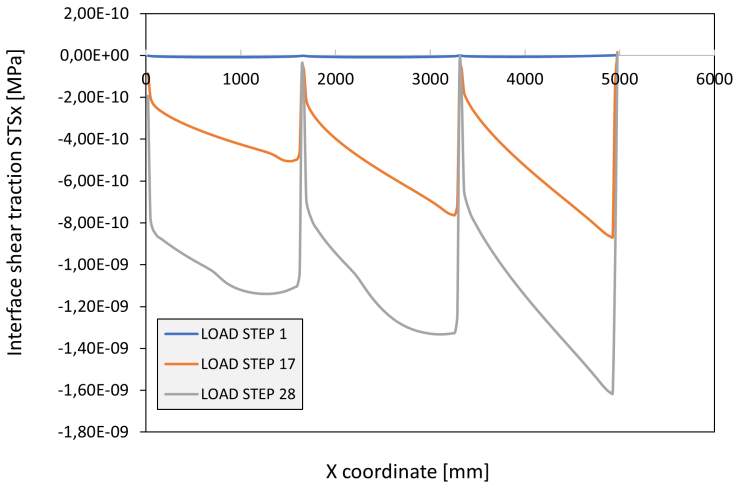

Figure 6.42: Shear traction along the bottom interface (model D-02)

6.6.3 Disconnection top line

The next step in the analysis involves disconnection (gap) along the entire top line interface between the concrete boxes and the steel plates. Figures 6.43 and 6.44 illustrate the stresses SXX in the deformed shape, providing a clearer visual representation of the gap extending along the top line of the model.

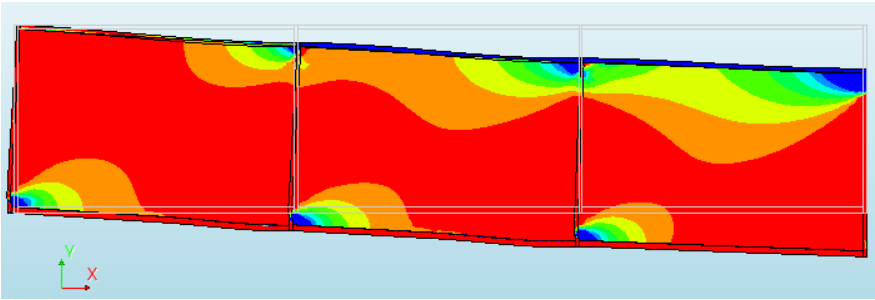

Figure 6.43: Disconnection on the top line - stresses SXX - visible gap along the top line

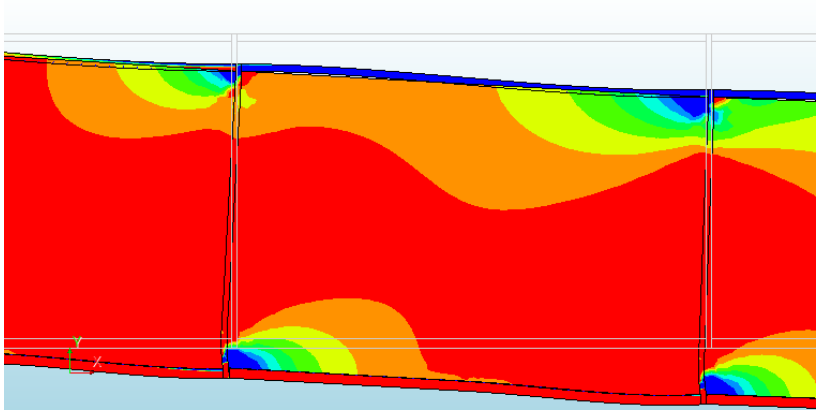

Figure 6.44: Disconnection on the top line - stresses SXX - zoom - in

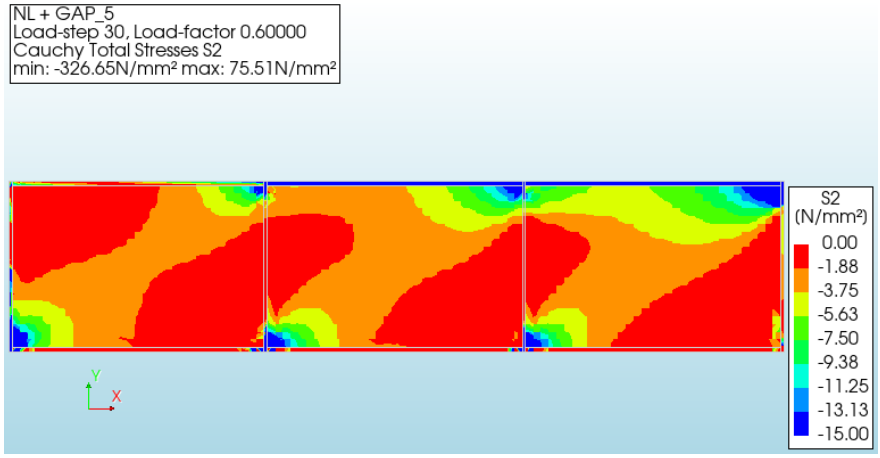

Figure 6.45: Disconnection on the top line (model D-05) - principal stresses S2

Figure 6.45 shows the last converged step of the analysis, revealing the failure of the compressive strut located at the right side of the beam. There is a visible increase in stress concentration, indicating that the load is being redirected to other areas of the composite beam, potentially leading to further cracking and failure. This shift in stress flow supports the conclusion that the compressive strut is failing.

6.6.4 Disconnection bottom line

Figure 6.46 illustrates the stresses SXX for a disconnection applied at the entire bottom line of the connection interface between the concrete boxes and the bottom steel plates. Furthermore, it can be clearly observed the gap schematized at the bottom line of the concrete boxes. The steel plates do not present the same deformation at the concrete boxes. Figure 6.47 illustrates the same stress pattern observed in other models with disconnection locations, highlighting the subsequent failure of the compressive strut.

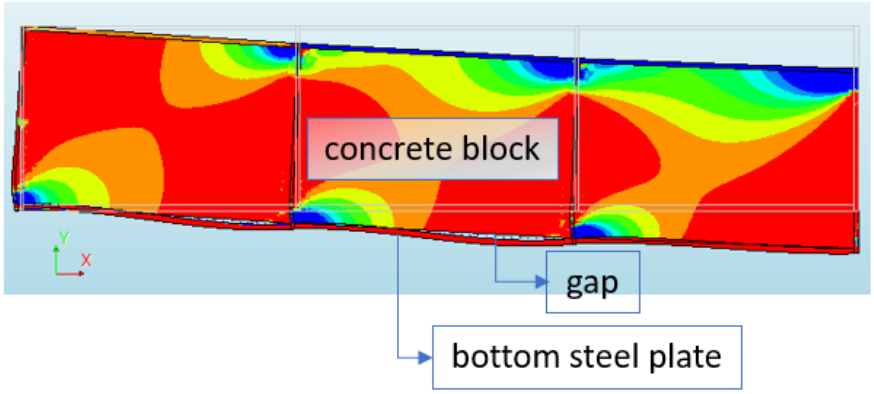

Figure 6.46: Disconnection on the bottom line - stresses SXX - visible gap

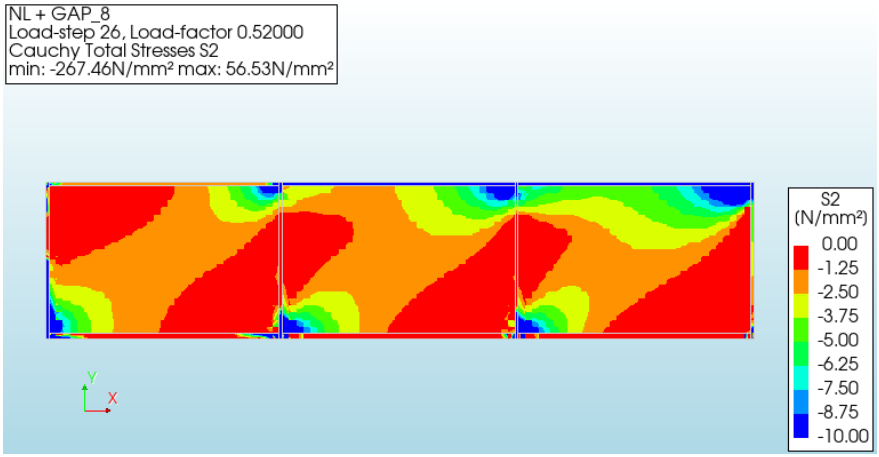

Figure 6.47: Disconnection on the bottom line (model D-08) - principal stresses S2

6.6.5 Disconnection bottom right

The final step in the investigation of the disconnection's impact on the composite design focuses on a gap located at the bottom right interface connection. Figure 6.48 displays the stresses SXX and the deformed shape of the design featuring the gap, while figure 6.49 depicts the formation of the compressive strut at the last converged step of the analysis before total failure. This figure provides a clear visual representation of the compressive strut's failure.

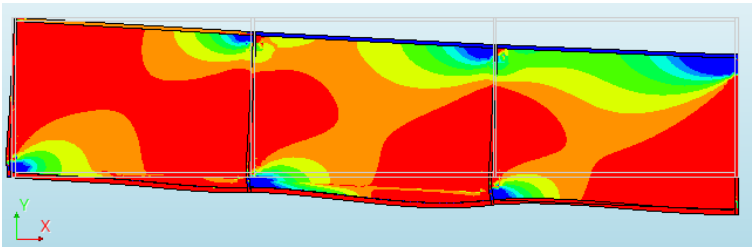

Figure 6.48: Disconnection on the bottom right - stresses SXX - visible gap

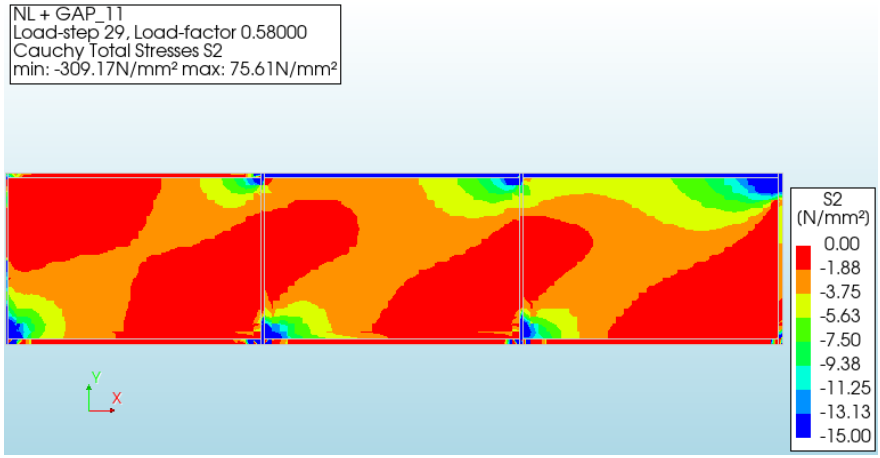

Figure 6.49: Disconnection on the bottom right (model D-11) - principal stresses S2

Overall, a distinct separation in the stress pattern can be observed, indicating that the compressive strut is no longer functioning as a continuous load path, and the load is not being effectively transferred through the concrete core.

In this model analysis, with the bottom right interface disconnected, the zip effect initiates at the adjacent interface. The propagation of the sliding effect mirrors the previously mentioned cases.

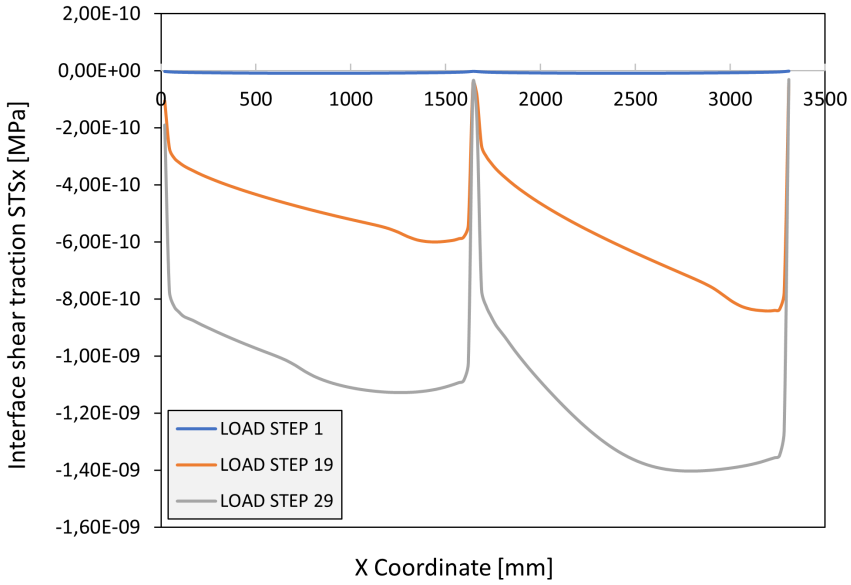

Figure 6.50: Shear traction along the bottom interface (model D-11)

Conclusions

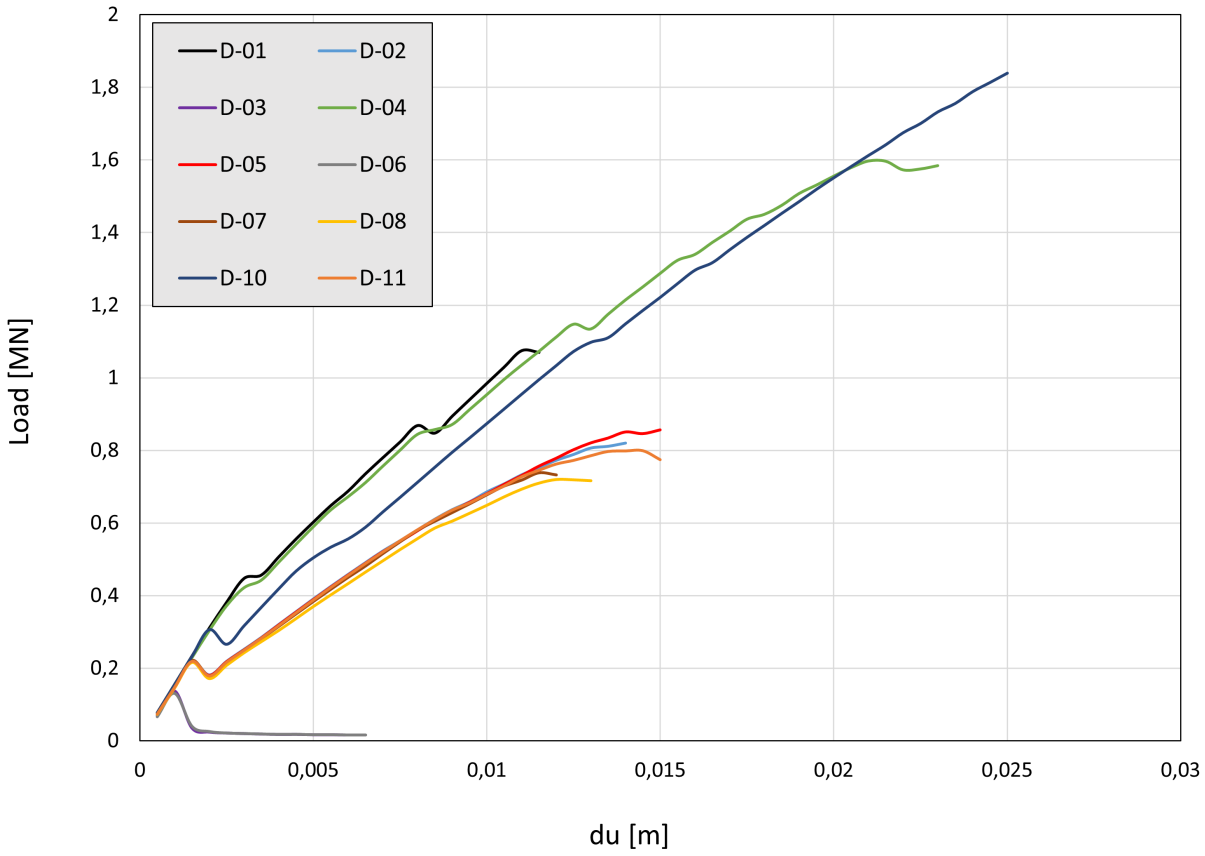

Figure 6.51: Global behaviour graph for nonlinear analysis of concrete and steel with different disconnection locations

Figure 6.51 presents the global behavior of the worst-case scenario model analysis, which incorporates both concrete and steel non-linearities. The model is evaluated under various combinations of imperfections, such as disconnections and varying differing qualities of connections at the horizontal and vertical interfaces of the composite design. The figure highlights three specific scenarios (three distinct behaviours):

1. The first scenario features a non-linear material model with a disconnection and fully bonded connections at both the horizontal and vertical interfaces (models D-01, D-04, D-10).

2. The second scenario depicts a non-linear material model with a disconnection and weak connections applied only at the horizontal interface (models D-02, D-05, D-08, D-11).

3. The third scenario presents a non-linear material model with a disconnection and weak connections at both the horizontal and vertical interfaces (models D-03, D-06).

The conclusions drawn from this analysis are outlined below:

- The analysis reveals that the connection between the concrete and the vertical steel plates (webs) is the most critical component of the designed model. Figure 6.51 shows that when a weak connection is applied at the vertical interfaces (along with non-linearity of concrete and weak connection at the horizontal interfaces) the structure fails to transfer the load. As a result, the compressive strut does not form, as illustrated in contour plots 6.40 and 6.41, leading to an immediate structural failure.

- It can be observed that the location of a disconnection is significant only when strong connections are applied at both interfaces. Thus, in cases where the different material components are strongly bonded, the most detrimental location for a disconnection appears to be along the entire bottom line of the beam. However, it is important to highlight that, given the filling process for the constructed boxes of the tunnel element, the occurrence of an imperfection such as a gap (disconnection) is unlikely. Concrete is poured from the bottom up, with pipelines extending along the height of the tunnel element through the steel plate boxes. As a result, the presence of gaps at the bottom of the boxes is not viewed as a realistic scenario for the structure.

- It is evident that, regardless of the gap size, all models with weak connection applied at the horizontal interface demonstrate low capacity, and the differences in their capacities are minimal. Consequently, it can be concluded that the gap size does not significantly impact the structure's capacity when the non-linearity of the concrete and slip at the interfaces are present.

Given that it has been concluded that models with varying gap sizes primarily fail due to the failure of the compressive strut, it is essential to validate this conclusion through an analysis of the stress-strain relationship of concrete. The figure below demonstrates that maximum compressive strength has been achieved across all variations of the gap between the horizontal steel plates and the concrete boxes. The data presented in this graph was derived from models that incorporated non-linear material behavior, included a gap, and accounted for slip due to the low stiffness of the horizontal interface. It is important to note that in these models, the webs were fully bonded. Without this full bonding, the formation of a compressive strut would not occur, as established in section 6.6.2.

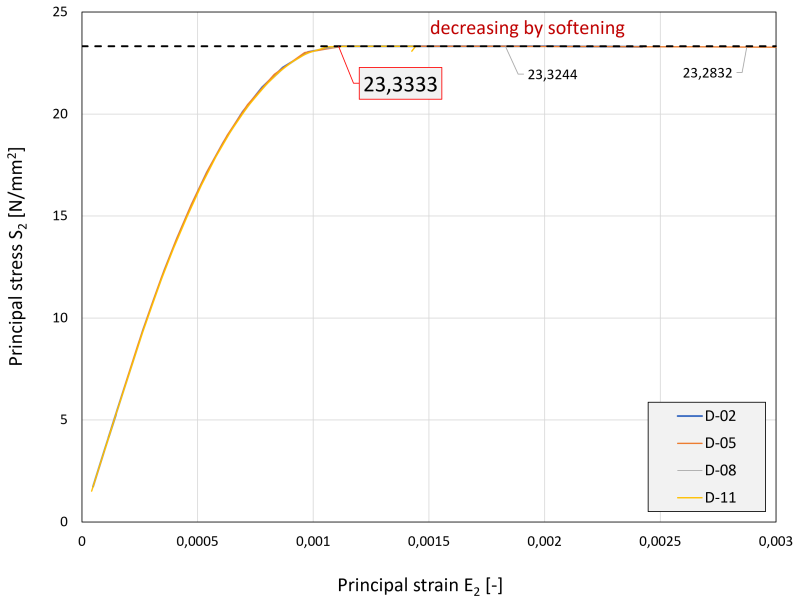

Figure 6.52: Stress - strain relationship of concrete when different disconnections are applied (with weak connection at horizontal interfaces)

Figure 6.52 illustrates the failure of concrete due to crushing. Although the graph shows a linear trend after reaching the maximum compressive stress of 23,33 N/mm^2, it is important to note that this perception is misleading; the stress is actually decreasing as a result of softening. The decline in values is subtle, making the difference from the maximum value difficult to discern. Therefore, it is crucial to emphasize that the presence of a gap disrupts the formation of the compressive strut, ultimately leading to failure.

6.7 Conclusion

The figure below summarizes the most critical scenarios identified in the investigation up to this point. The non-linearity of concrete and the slip at the horizontal connection interfaces are the primary factors to consider; therefore, the global behaviors of the analyses that incorporate both elements should be presented for a comprehensive overview of the conclusions.

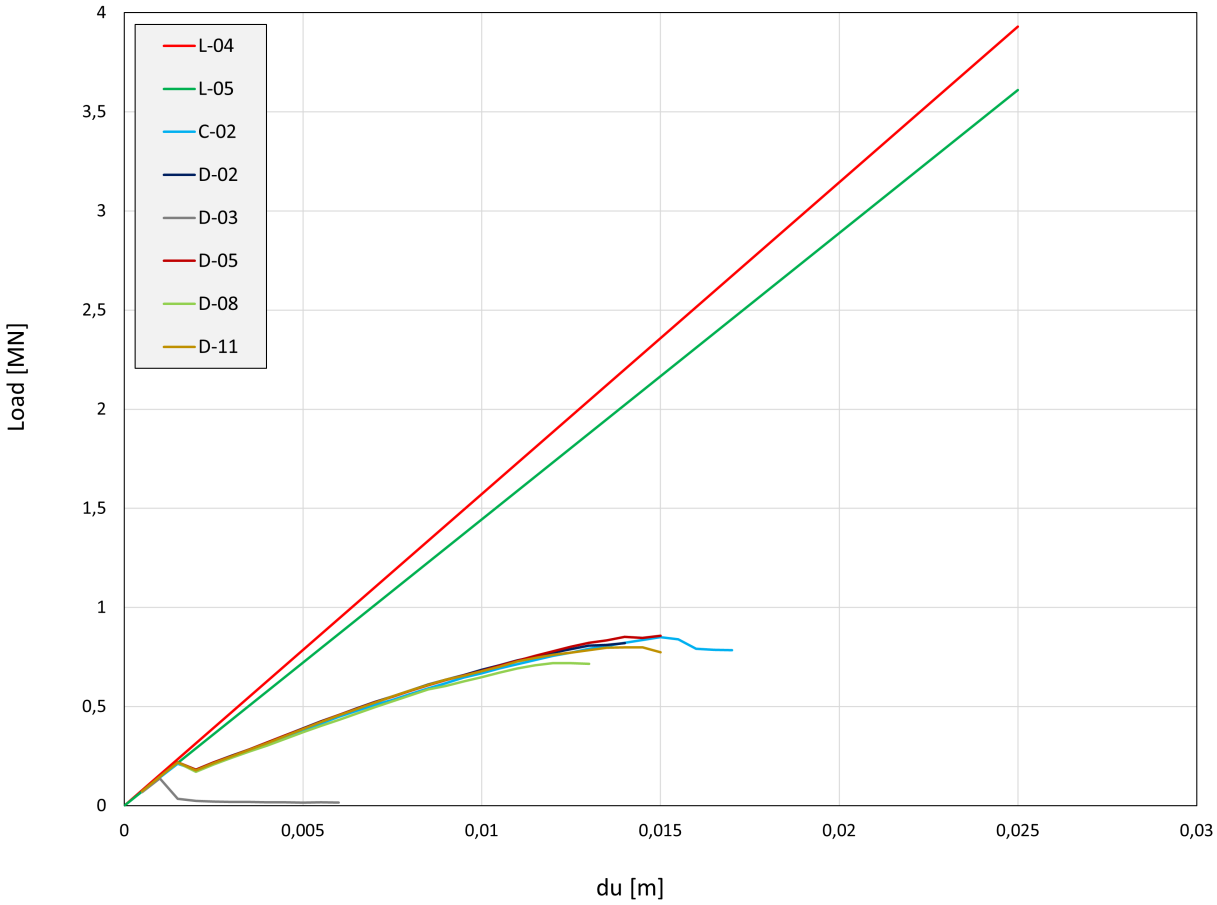

Figure 6.53: Force - displacement graph

- Non-linearity of concrete and disconnection influence: From the graph provided, it is evident that the non-linearity of concrete has significant impact on the structure's capacity. It is observed that the bearing capacity behaviour of the models with disconnection (lack of interface) and weak connection at the horizontal interfaces is similar once the non-linearity of concrete is activated.

- Disconnection size and location, and compressive strut disruption: The size or location of the disconnection does not play a significant role, as the compressive strut is disrupted regardless (due to crushing of concrete).

- Weak connection at vertical interface: Based on the graph, when weak connections are present at both the horizontal and vertical interfaces (model D-03), the structure fails almost immediately. The webs (vertical steel plates), while helpful when strongly connected, do not fully compensate for the capacity loss resulting from nonlinear concrete, weak horizontal connections, and disconnections. Therefore, strong connections at the vertical interfaces are critical for overall structural stability.

The overall major conclusion of the SCS composite beam apart from the specific case scenarios that have been investigated is summarised below:

- Analysis of the various model simulations reveals that the primary failure mechanism of the structure is governed by the strut and tie model. This observation indicates that relying solely on composite bending theory to determine the ultimate limit state capacity of the structure may not be appropriate. Given the significant influence of factors such as the non-linearity of concrete and slip at the horizontal interfaces, it becomes essential to explore alternative analytical approaches that better account for these complexities. A strut and tie model provides a more accurate representation of load transfer mechanisms, particularly in scenarios where traditional bending theory falls short. Consequently, investigating a more suitable analytical solution specifically designed for this type of design could enhance the reliability of capacity predictions and improve overall structural performance. By doing so, the design process can be better aligned with the actual behavior of the structure under loading conditions, leading to safer and more efficient engineering outcomes.

In the former paragraphs the quality of the connection in the composite beam is investigated based on the assumption of a clamped or free rotated end as the boundary condition. However, the main source of this investigation is the connection of the composite SCS tunnel cross-section. Therefore, in order to achieve a more realistic approach and conclude on the boundary conditions and the critical components that influence the structure's connection, a 2D model of the entire cross-section should be simulated and studied.

Chapter 7

Full SCS tunnel cross-section finite element model

This chapter will be dedicated to explaining the modeling of the entire cross-section and conducting an in-depth investigation of the behavior of the SCS composite structure, including results and final conclusions intended to enhance the understanding of the immersed tunnel element.

7.1 Schematization of SCS cross-section

In this section, it will be explained how the detailed model is schematized. For the simple model, the composite beam was represented using beam elements and plane-stressed elements with a representative modulus of elasticity and a specified element height. In the detailed model, the SCS (Steel-Concrete-Steel) sandwich tunnel element is modeled to reflect its real-world design. This means that the steel parts for the inner and outer sides of the roof, floor, and wall elements have specific thicknesses. The same applies to the diaphragms connecting the inner and outer steel plates.

Next, the elements used in the finite element analysis with DIANA software and their configuration will be discussed in detail. The concrete core boxes will be modeled by using quadratic plain stress elements CQ16M and CT12M. These plane stress elements (also known as membrane elements) operate within a single flat plane—the xy plane neglecting the thickness direction. They are thin and require a small thickness, denoted as 't,' in relation to the other dimension 'b' of the element's plane. For the specific cross-section tunnel element in this case, the applied thickness is minimal—just 1 meter—compared to the larger dimensions 'x' (52 meters) and 'y' (9,6 meters) of the element's plane, as calculated for the composite structure. This simplification helps reduce the problem from 3D to 2D, making computations more efficient. Furthermore, plane stress elements are well-suited for accurately capturing results near stress concentration regions. They also facilitate visualizing stress distribution within the plane, making it easier to analyze local stresses more efficiently.

The horizontal and vertical plates (webs) will be modeled using Class-III beam element CL9BE. Beam elements of this class are fully numerically integrated Mindlin beam elements commonly employed in finite element models to represent structural members such as beams, trusses, and frames. Class III beam elements are one-dimensional and can deform under axial loads, shear forces, and bending moments. They are characterized by their ability to transfer loads along their length and can experience flexural, axial, and

shear deformations. In three-dimensional space, these elements have six degrees of freedom at each node, corresponding to three translational movements (x, y, z) and three rotational movements (about the x, y, and z axes). However, for a two-dimensional model analysis like this one, the degrees of freedom are typically simplified. In this case, each end node usually has three degrees of freedom: two translational movements (u_x and u_y), and a rotational movement around the vertical axis (ϕ_z).

CQ16M is an 8-node quadrilateral isoparametric plane stress element while CT12M is a six-node triangular isoparametric plane stress element, as shown in figure 7.1. These elements come in square and triangular shapes respectively and can be used for various types of analyses, including linear, nonlinear, and cracking.

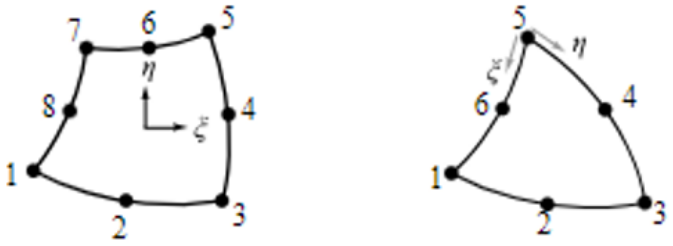

Figure 7.1: Structural plane-stress element - CQ16M and CT12M

The connectors used in the design, stiffeners and shear studs, will not be physically simulated in the software. Thus, to accurately represent the connection between the concrete core and the steel plates, we introduce interface elements into the model. These elements are assigned a stiffness value that reflects the connection strength between the steel and concrete. Specifically, a high stiffness (denoted as 'k') is entered for the steel-concrete connection, assuming full initial connection. Refer to figure 7.2 for the schematic representation of the applied interface element CL12I which will be used in the finite element model.

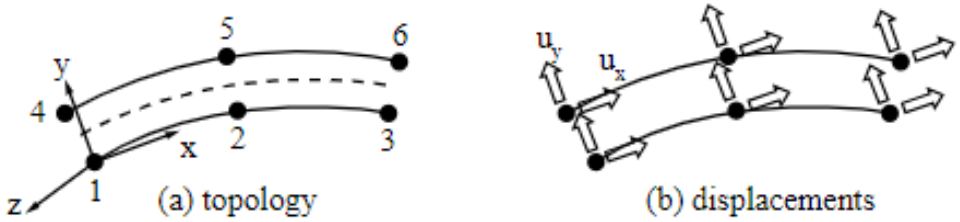

Figure 7.2: Structural interface element CL12I

Since the steel and concrete elements cannot be connected directly, four interface elements are applied on each side of the concrete square. This is the layout as it will be modelled in Diana. The dots in figure 7.3 are not modelled points but the nodes of each element. These interface elements are repeated with different dimensions for the roof, floor and wall elements.

FE Type	CQ16M	CT12M	CL12I	CL9BE
DOFs	16 (2/node) - 2 translations	12 (2/node) - 2 translations	12 (2/node) - 2 translations	9 (3/node) 2 translations & 1 rotation
Interpolation Scheme	quadratic	quadratic	quadratic	quadratic
Integration Scheme	3 x 3	3	3	2
Shape Dimension	2D	2D	2D	2D
Topological Dimension	2D	2D	2D	1D
Stress Components	Sxx, Syy, Sxy	Sxx, Syy, Sxy	Sxx, Syy, Sxy	Nx, Qy, Mz
Shear Deformations	no	yes	yes	yes

Table 7.1: Type of finite element used and their properties

In the figure below is presented a layout of the elements used in the model for each one of the different parts of the cross section, steel plates, concrete core and interface connections.

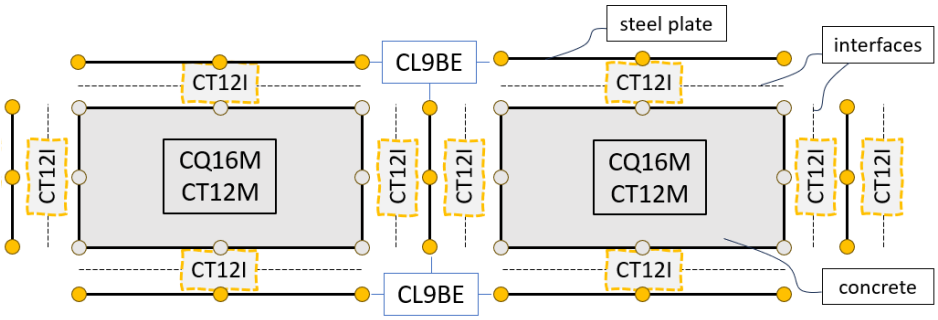

Figure 7.3: Layout of SCS cross-section's finite elements

In addition to the material geometry elements in the cross-section, another element is used to determine forces and moments across the entire structure. Diana Software provides an element called the composed element CL3CM depicted in the figure 7.4. By integrating stresses from individual elements (such as floor, roof, and walls), the cross-sectional results are calculated. Geometry adjustments are necessary: a central line for the roof, floor, and wall components is created, CL3CM properties are assigned to this line, and a thickness is set to encompass all three layers (steel-concrete-steel).

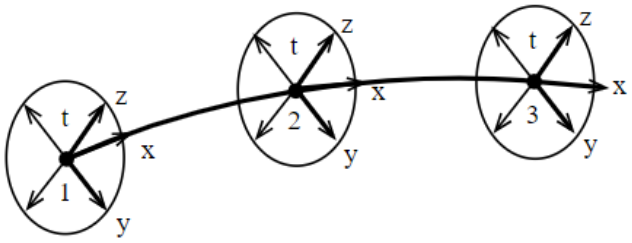

Figure 7.4: Composed element CL3CM

The figure 7.5 below illustrates the composed element within the tunnel cross-section (perimetrical composed line with red color, inside walls composed line in blue and pink color).

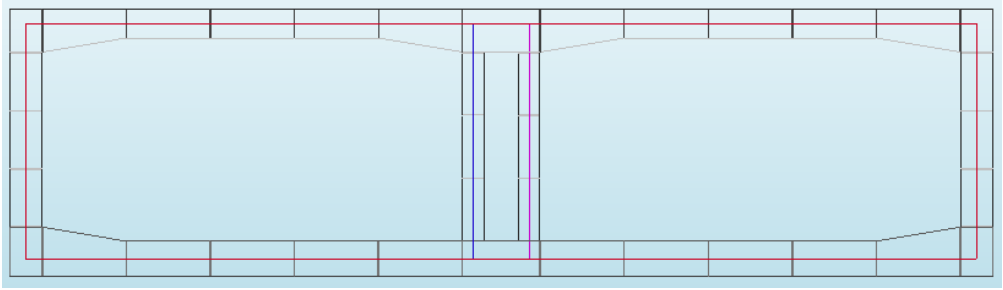

Figure 7.5: Position of the composed element lines

7.1.1 Geometry

In this section, the construction of the detailed model in DIANA will be explained. The table 7.2 below presents the cross-sectional geometry used as the initial input for the design. In addition, table 7.3 provided the applied dimensions of the steel plates in the composite structure.

Dimensions			
Width of one tunnel tube [mm]	15000		
Total width of the tunnel's cross-section [mm]	52000		
Total height of the tunnel's cross-section [mm]	9600		
Inner height of the tunnel's cross-section [mm]	7600		
	Roof	**Floor**	**Wall**
Total height of the element - h [mm]	1100	1300	2075
Unit width of the element - b [mm]	1000	1000	1000
Center to center distance of diaphragm (web) - ctc [mm]	3000	3000	1185

Table 7.2: Cross-section's dimensions

Dimensions - Steel plates	**Roof**	**Floor**	**Wall**
Thickness steel plate outside - $t_{outside}$ [mm]	35	35	15
Thickness steel plate inside - t_{inside} [mm]	25	25	15
Clear height of concrete core [mm]	1040	1240	1170
Thickness of the diaphragm (web) [mm]	15	15	15

Table 7.3: Steel plates dimensions

The cross-section's geometry is shown in the figure 7.6 below. While all connections are physically represented, the stiffeners and studs are modeled as interface connections, as previously mentioned.

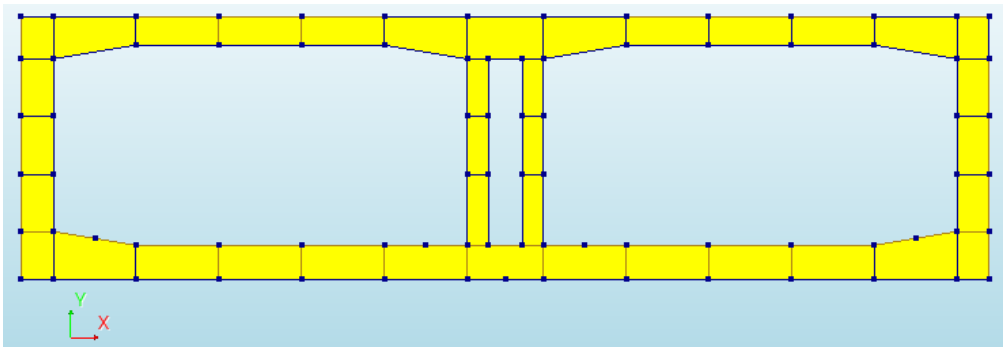

Figure 7.6: Cross-section of the SCS tunnel elements with distinct thicknesses

7.1.2 Boundary conditions

For the tunnel cross-section are provided two sets of supports. First one is about a point support in the axes of symmetry below the floor element. The point support is restraining the x translation. The second support set is places along the floor element restraining the y translation in order to simulate the bedding. The applied bedding support condition is actually defined by springs where the interface connection that will be applied later on. The figure below provides a zoomed-in view of the supported portion of the cross-section.

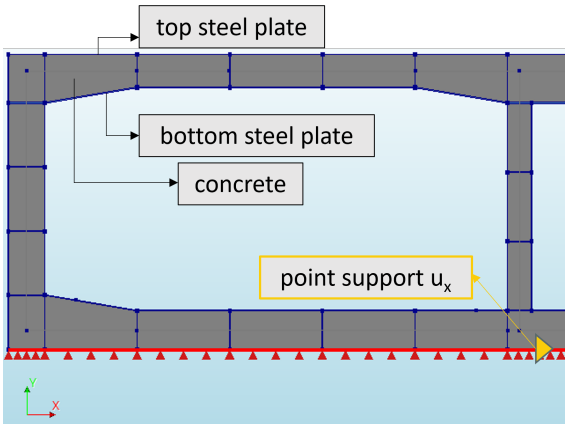

Figure 7.7: Constraints

7.1.3 Meshing

Selecting an appropriate mesh is crucial for accurate modeling. The mesh division should strike a balance: it must be fine enough to yield accurate results, yet not overly dense to avoid excessive computation time. In this case, the element size for steel plates, interfaces and concrete core was chosen to be 0.2 m. Figure 7.8 below illustrates the divisions within the SCS sandwich element cross-section.

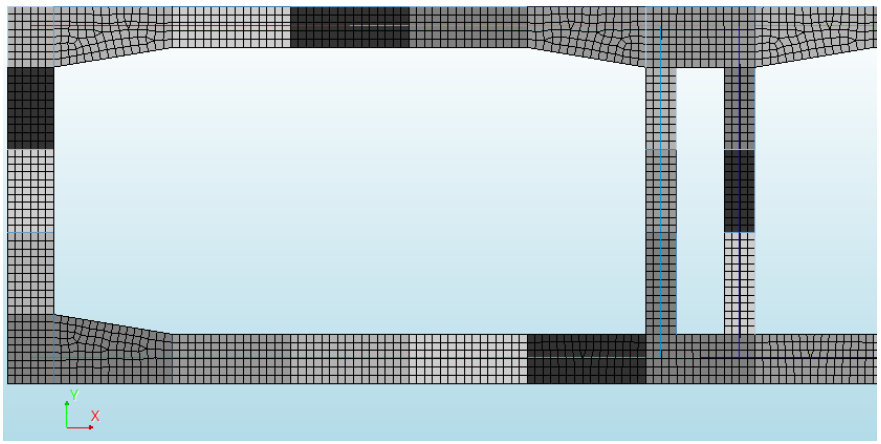

Figure 7.8: Element size in composite cross-section

7.1.4 Loads

The loads acting on the tunnel element are categorized into permanent and variable loads. Permanent loading comprises self-weight, soil pressure, and hydraulic forces, while variable loads pertain to traffic loading. Figure 7.9 illustrates the permanent loading distribution across the cross-section, while Figure 7.10 depicts the applied traffic load, positioned approximately 1 meter from the inner and outer walls of the element.

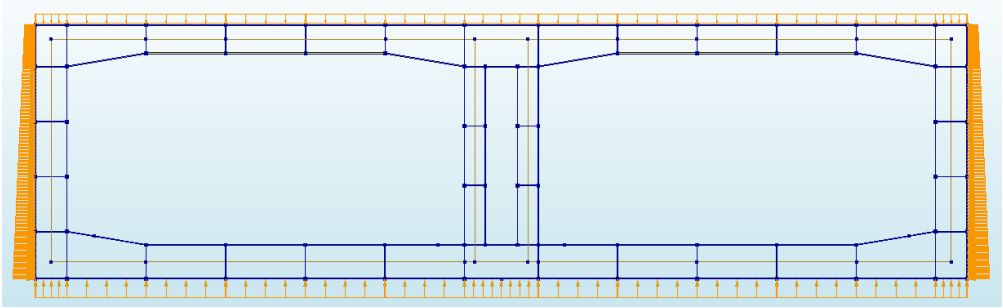

Figure 7.9: Permanent load

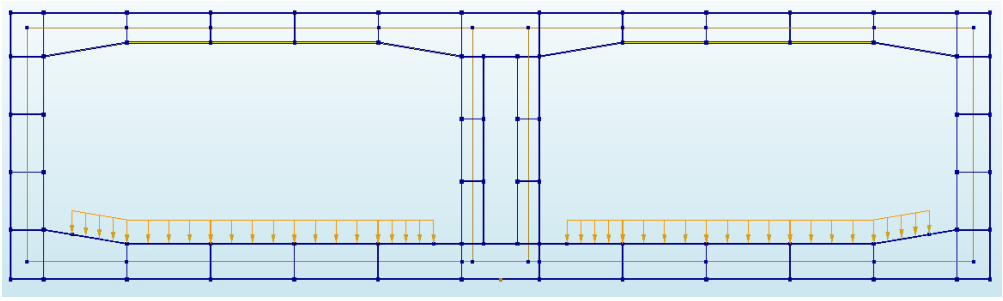

Figure 7.10: Variable load

7.1.5 Material and physical properties

In the context of the finite element model of the complete composite cross-section, the connection between steel and concrete relies on interface elements. The extent of this connection is determined by the stiffness constants specified in the Diana software. Initially, it is assumed that the steel and concrete elements are fully connected. Having a strong connection between the two materials requires a high stiffness value input in Diana. Specifically, the value of 1E+09 N/m^3 is assigned to the linear and tangential stiffness of the interfaces.

Material	Interface	
Linear Material Properties		
	Value	Units
Type	2D line interface	
Normal stiffness modulus - y	1E+09	N/m^3
Shear stiffness modulus - x	1E+09	N/m^3

Table 7.4: Interface material properties

The following tables provide a detailed overview of the characteristics used for both the linear and nonlinear behavior of concrete and steel materials in the finite element analyses.

Material	Concrete	
Linear Material Properties		
	Value	Units
Young's Modulus, E	3.5E+10	N/m^2
Poisson's ratio, v	0.15	-
Mass density, ρ	2400	kg/m^3
Nonlinear Material Properties		
Tensile Behavior		
Tensile curve	Hordijk	
Tensile strength	3.21E+06	N/m^2
Tensile Fracture Energy, G_{Fk}	18324.5	N/m
Crack bandwidth specification - Rots		
No residual tensile strength after cracking		
Confinement model - Damaged based		
Compressive Behavior		
Compressive curve	Parabolic	
Compressive strength	2.33E+07	N/m^2
Compressive Fracture Energy, G_{Fk}	29233.9	N/m
No residual compressive strength		
Reduction model - Vecchio and Collins 1993		
Confinement model - Selby and Vecchio		

Table 7.5: Concrete material properties

Material	Steel	
Linear Material Properties		
	Value	Units
Young's Modulus, E	2.1E+11	N/m^2
Poisson's ratio, v	0.15	-
Mass density, ρ	7850	kg/m^3
Nonlinear Material Properties		
Von Mises and Tresca plasticity		
Plasticity model - Von Mises plasticity		
Hardening function - No hardening		
Yield stress	4.35E+08	N/m^2

Table 7.6: Steel material properties

7.2 Load check

In this section, the main focus is on comparing the results obtained from the detailed Diana model with those from hand calculations. The primary objective of this comparison is to verify the accuracy of the model. If any discrepancies arise, the reasons behind them should be explained. Notably, the detailed SCS sandwich model represents fully connected elements. To achieve this, there should be an increase in the linear and tangential stiffness of the connection between the steel and concrete. By doing so, a more meaningful comparison can be obtained between the simplified and detailed models, as both are based on the assumption of fully connected elements.

The load cases applied on the cross-section of the tunnel are presented on the table below.

Load case	Loading type
1	Self-weight of the cross-section
2	Vertical loading on the roof
3	Vertical loading on the floor
4	Loading on the left side of the cross-section
5	Loading on the right side of the cross-section
6	Total loading

Table 7.7: Load cases of the structure

7.2.1 Load case 1 - Self-weight of the structure

The moment distribution graph in Figure 7.11 illustrates the results from structural analysis using Diana for the cross-section under self-weight. Notably, the center of the structure exhibits maximum positive moments, highlighted in red, attributed to vertical loads and support reactions. Additionally, negative moments (shown in blue) occur at both ends, attributed to the continuous support condition, corresponding to the bedding spring boundary.

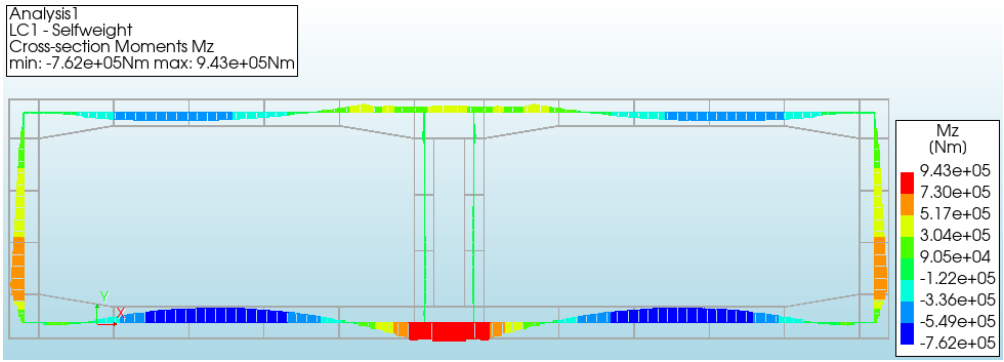

Figure 7.11: Moment distribution of load case 1 - Self-weight

7.2.2 Load case 2 - Vertical loading on the roof

Figure 7.12 below presents the results obtained from Diana for the moment distribution of the cross-section under load case 2 which corresponds to the vertical loading on the roof element of the structure.

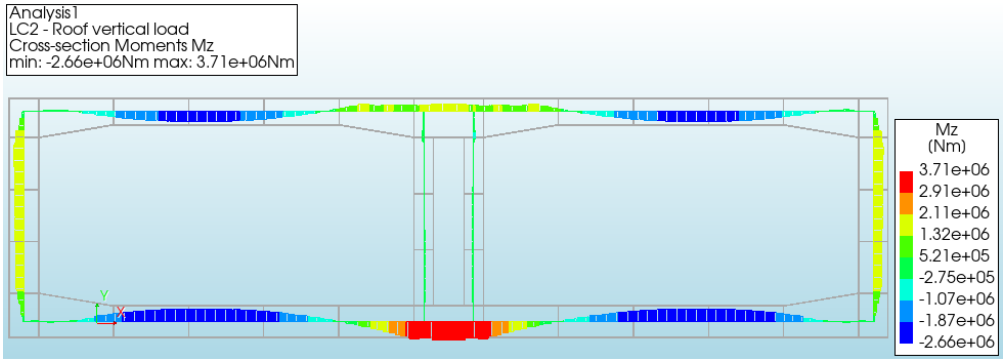

Figure 7.12: Moment distribution of load case 2 - Vertical loading on the roof

Taking into account the depicted values, a check can be made with the hand calculations resulting moments. The model which will be taken into account for the hand calculation will be based on the rule of thumb from mechanics as presented in the figure 7.13 below. The roof element can be schematized by a beam element which is fully inclined on both sides. The load on the top it is a uniform distributed load as mentioned above in paragraph 7.1.4 in figure 7.9.

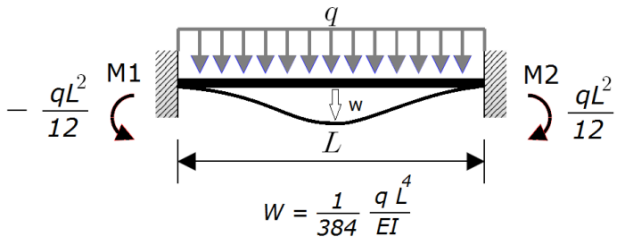

Figure 7.13: Rule of thumb

To determine the moments at the supported ends and mid-span of the roof element, the following formulas from the rules of thumb can be applied.

$$M_1 = M_2 = \frac{Q \times L^2}{12} \tag{7.1}$$

$$M_{tot} = \frac{1}{8} \times Q \times L^2 \tag{7.2}$$

$$w = \frac{1}{384} \frac{Q \times L^4}{EI} \tag{7.3}$$

The results for the roof element (load case 2) are given in the table below. A comparison it has been made with the Diana results in order to confirm the accuracy of the model.

Load case 2 - Roof					
Q_{roof}	171490	N/m	L	9.04	m
Moment hand calculation and Diana model					
Hand calculation			Diana model		
M_1	1167869.77	Nm	M_1	-1049430	Nm
M_2	1167869.77	Nm	M_2	581225	Nm
M_{Middle}	-583934.88	Nm	M_{Middle}	-1987630	Nm
M_{Total}	1751804.65	Nm	M_{Total}	1753528	Nm
$\approx 0.01\%$					

Table 7.8: Check roof element - load case 2

7.2.3 Load case 3 - Vertical loading on the floor

The procedure described above is applied to the floor element of the cross-section. The results of the moment distribution from the Diana model are presented in the figure below, while table 7.9 provides the verification based on hand calculation.

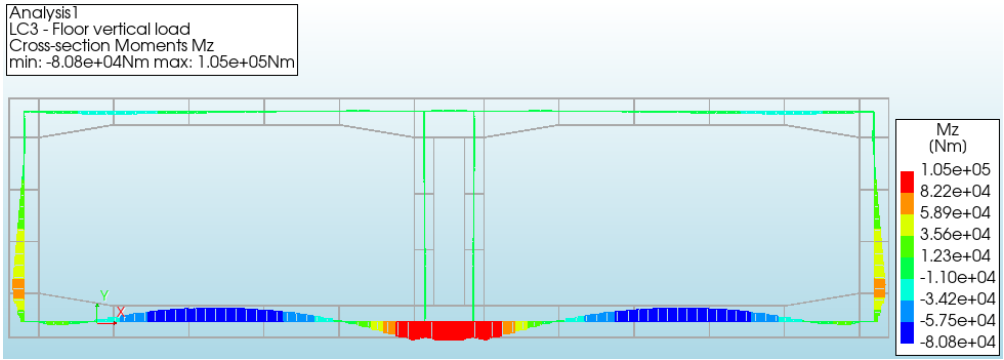

Figure 7.14: Moment distribution of load case 2 - Vertical loading on the floor

Load case 3 - Floor					
Q_{floor}	238810	N/m	L	10.03	m
Moment hand calculation and Diana model					
Hand calculation			Diana model		
M_1	2001722	Nm	M_1	-25217.10	Nm
M_2	2001722	Nm	M_2	26899.30	Nm
M_{Middle}	-1000861	Nm	M_{Middle}	-78588.30	Nm
M_{Total}	3002584	Nm	M_{Total}	79429.30	Nm
$\approx 97.35\%$					

Table 7.9: Check floor element - load case 3

The significant discrepancy between hand-calculated moments and those obtained from the DIANA model arises from the continuous spring boundary applied along the floor element. The rule of thumb, which assumes fixed supported ends for the beam, leads to different moment distributions. Specifically, there are expected smaller results when a continuous support system is applied along the beam. This aligns with the situation depicted in table 7.9.

7.2.4 Load case 4 - Loading on the left side of the cross-section

In Figure 7.15, the moment distribution of the wall element within the cross-section is presented. Based on the figure, it is evident that the displacement of the wall element is extremely small, almost negligible. The structure behaves like a rigid body in response to the forces acting on the outer wall.

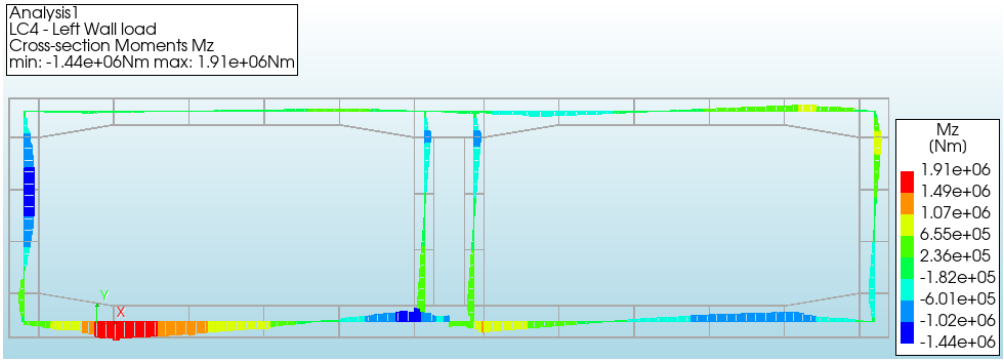

Figure 7.15: Moment distribution of load case 4 - Loading on the left side wall of the cross-section

This distribution arises from external loading caused by hydraulic stresses and soil conditions. Unlike the roof and floor elements, the distributed load is not uniform; it follows a trapezoidal pattern over the height of the wall. To calculate the moments accurately, it is needed to break down the problem into two steps. First, the load is divided into rectangular and triangular distributions. The relevant formulas for manual calculations can be found in the following figure.

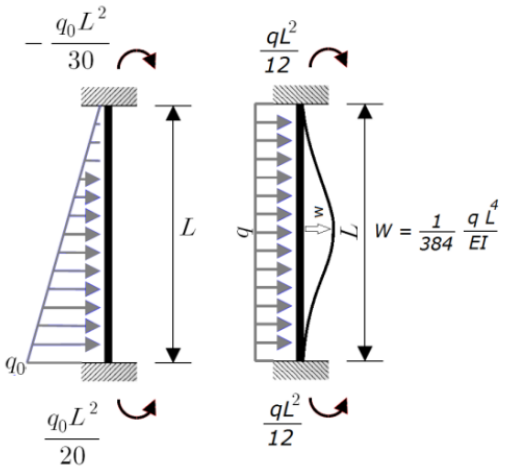

Figure 7.16: Rule of thumb for the non-uniform load over the height

The table below compares the results obtained from hand calculations with those from Diana's analysis. The percentage difference is provided at the end of the table.

Load case 4 - Left side wall					
$Q_{LeftWall,1}$	161583.75	N/m	L	8.4	m
$Q_{LeftWall,2}$	200483.12	N/m			
Moment hand calculation and Diana model for $Q_{rectangular}$					
Hand calculation			Diana model		
M_1	950112.45	Nm	M_1	250976	Nm
M_2	950112.45	Nm	M_2	-115762	Nm
M_{Middle}	-471536.23	Nm	M_{Middle}	-999268	Nm
$M_{Total,1}$	1425168.68	Nm	M_{Total}	1066875	Nm
Moment hand calculation and Diana model for $Q_{triangular}$					
Hand calculation			Diana model		
M_1	-471536.30	Nm	M_1	250976	Nm
M_2	707304.45	Nm	M_2	-115762	Nm
M_{Middle}	-294710.19	Nm	M_{Middle}	-999268	Nm
$M_{Total,2}$	-176826.11	Nm	M_{Total}	1066875	Nm
M_{Total}	1248342.56	Nm	M_{Total}	1066875	Nm
$\approx 14.54\%$					

Table 7.10: Check left side wall element - load case 4

7.2.5 Load case 5 - Loading on the right side of the cross-section

Figure 7.17 illustrates the moment distribution of the right-side wall within the cross-section, resulting from external loading due to hydraulic and soil stresses. The observations closely resemble those of the left-side

wall, with moment values so small that they can be considered negligible. To validate the results, the same procedure used for the left outside wall of the cross-section is followed, and once again, the error falls within acceptable limits of accuracy (table 7.11).

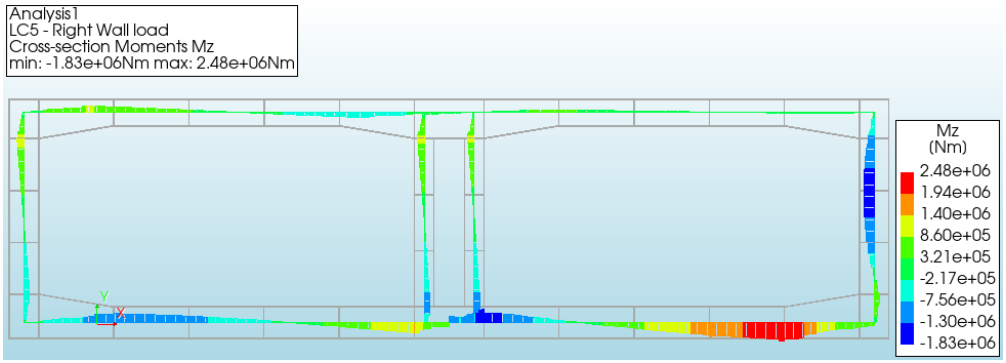

Figure 7.17: Moment distribution of load case 5 - Loading on the right side wall of the cross-section

Load case 4 - Left side wall					
$Q_{LeftWall,1}$	161583.75	N/m	L	8.4	m
$Q_{LeftWall,2}$	200483.12	N/m			
Moment hand calculation and Diana model for $Q_{rectangular}$					
Hand calculation			Diana model		
M_1	950112.45	Nm	M_1	-136539	Nm
M_2	950112.45	Nm	M_2	223949	Nm
M_{Middle}	-471536.23	Nm	M_{Middle}	-1313780	Nm
$M_{Total,1}$	1425168.68	Nm	M_{Total}	1357485	Nm
Moment hand calculation and Diana model for $Q_{triangular}$					
Hand calculation			Diana model		
M_1	-471536.30	Nm	M_1	-136539	Nm
M_2	707304.45	Nm	M_2	223949	Nm
M_{Middle}	-294710.19	Nm	M_{Middle}	-1313780	Nm
$M_{Total,2}$	-176826.11	Nm	M_{Total}	1357485	Nm
M_{Total}	1248342.56	Nm	M_{Total}	1357485	Nm
$\approx 8.05\%$					

Table 7.11: Check right side wall element - load case 5

7.2.6 Load case 6 - Total loading

The combination of load cases 1 to 5 results in the total loading on the cross-section. Figure 7.18 illustrates the total moment distribution across the cross-section, which will serve as the primary load for both linear and nonlinear analyses of the composite structure in subsequent steps.

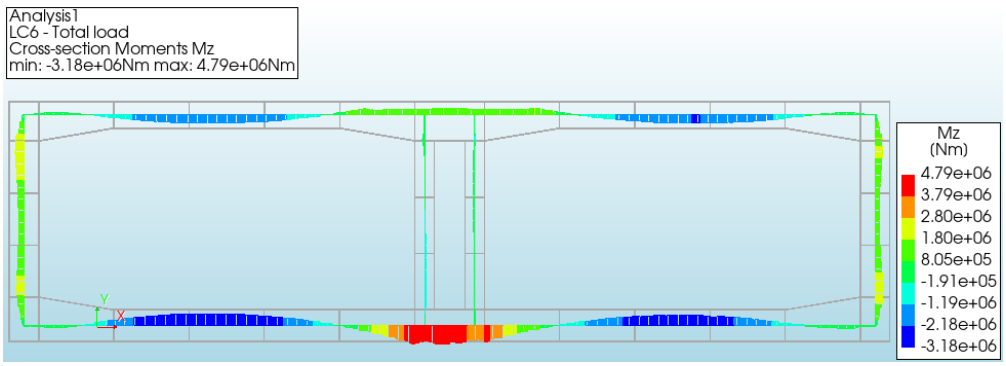

Figure 7.18: Moment distribution of load case 6 - Total loading

7.3 Linear elastic analysis of full SCS tunnel cross-section

Based on the previous discussion of the small beam, it can be concluded that the bonded interface of the webs is a key assumption. The webs significantly influence the structure's bearing capacity, making slip effects an unrealistic scenario for analysis, as they are integral to the design. Therefore, only a few analyses that incorporate slip at the webs will be included in the following sections to provide a brief understanding of this behavior and to validate the SCS composite beam. However, other critical components affecting bearing capacity, mainly considered, include the horizontal interfaces between the concrete core and the steel plates. To gain a deeper understanding of the structure, two extreme cases are analyzed: linear analyses with bond and slip at the horizontal interface. In this context, bond signifies a strong connection between the concrete core and steel plates, while slip indicates a weak connection. The load applied for the linear analysis was the total load plus three times the roof load.

7.3.1 Strong connection

This section presents the displacement of the strong connection in the Y direction, along with the stress distribution in the concrete slab and the steel plates.

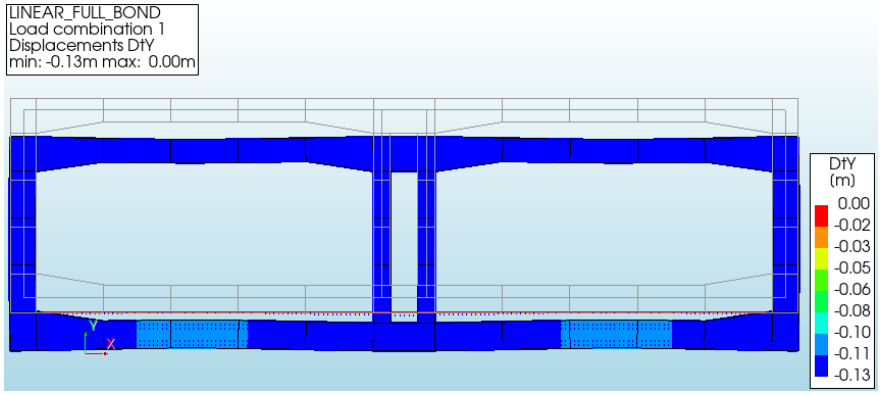

Figure 7.19: Displacements in Y direction

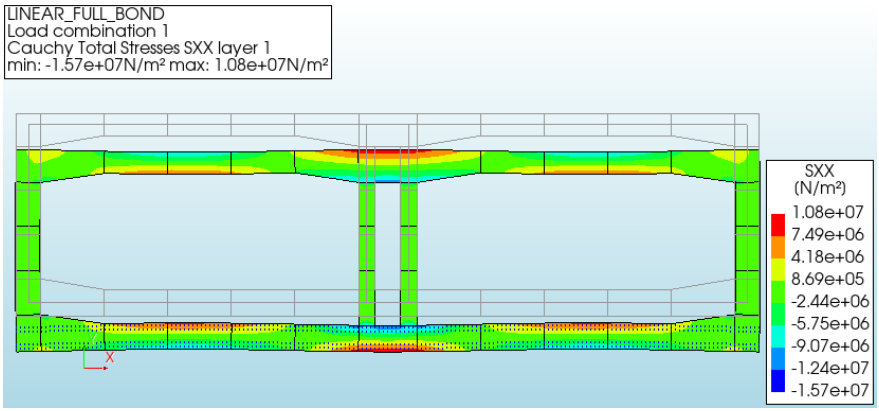

Figure 7.20: Concrete slab stresses

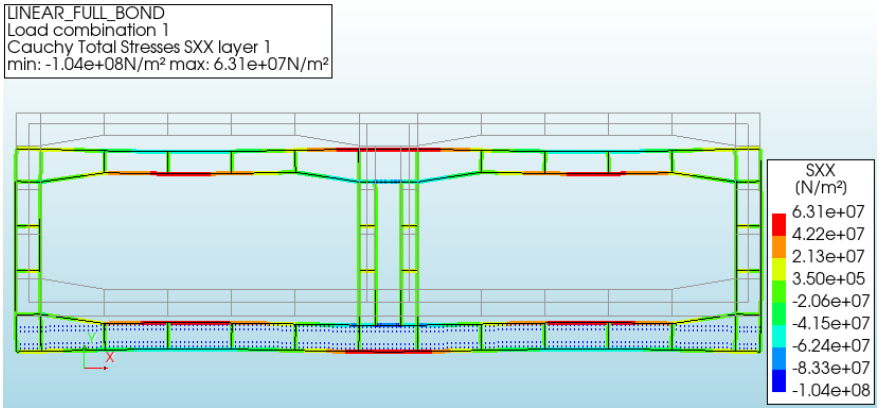

Figure 7.21: Steel plates stresses

7.3.2 Weak connection

As previously mentioned, the weak connection signifies a weak link between the steel plates and the concrete boxes. In this case, the normal stiffness of the interface elements is maintained at the same level as that used for the strong connection, while the shear stiffness is significantly lower, set to a numerical value of 1 N/m^3, just before instability issues arise in the software.

Weak connection only for the roof's horizontal interfaces

The displacement of the weak connection in the Y direction, along with the stress distribution in the concrete slab and steel plates, is presented here.

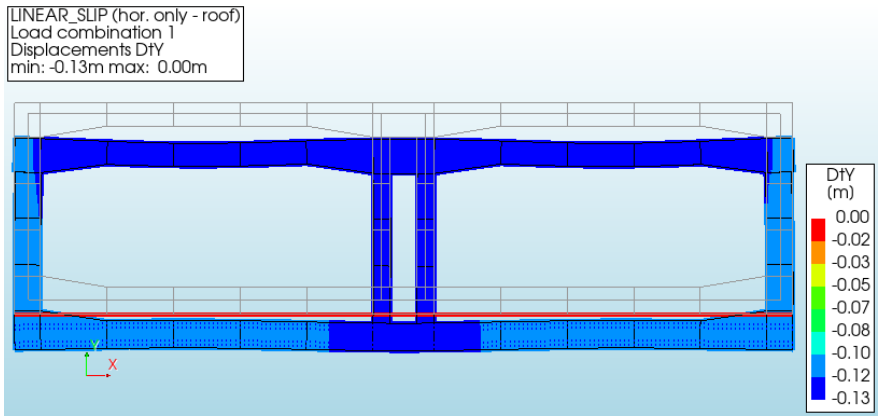

Figure 7.22: Displacements in Y direction

- A greater displacement value is noted for the roof element when a slip connection is applied at the horizontal interface between concrete and steel.

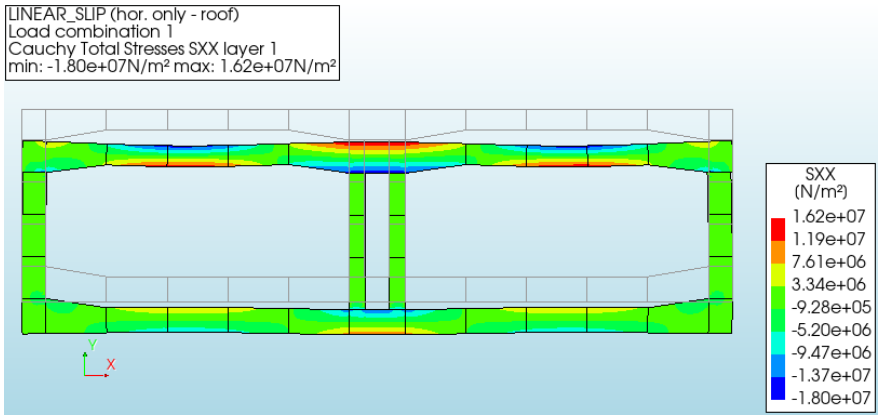

Figure 7.23: Concrete slab stresses

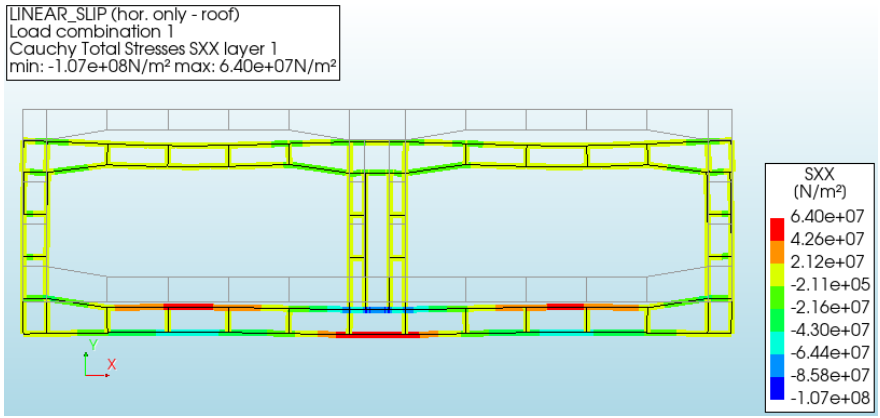

Figure 7.24: Steel plates stresses

- Higher stresses are observed on the roof element in comparison with the case of strong connection (bond) which is to be expected due to the lack of connection. The low stiffness value at the interfaces allows for relative movement between the concrete and the steel. Thus, the high stresses are reasonable as the concrete is less stiff and more prone to deformation under load compared to steel.

- In contrast, steel, being a more ductile and stiffer material, can better distribute the applied loads, resulting in lower stresses. Thus, the lower stresses observed in the steel as shown at the above contour plot (figure 7.24) can be explained by the weak connection, which restricts the transfer of load from the concrete to the steel plates.

Weak connection for both roof's horizontal and vertical interfaces (webs)

As stated earlier, this analysis will validate the critical role of the webs in the structure's design. A weak connection for both the horizontal and vertical plates (webs) is an improbable scenario and is not anticipated. This section presents the displacement of the weak connection in the Y direction, along with the stress distribution in the concrete slab and steel plates.

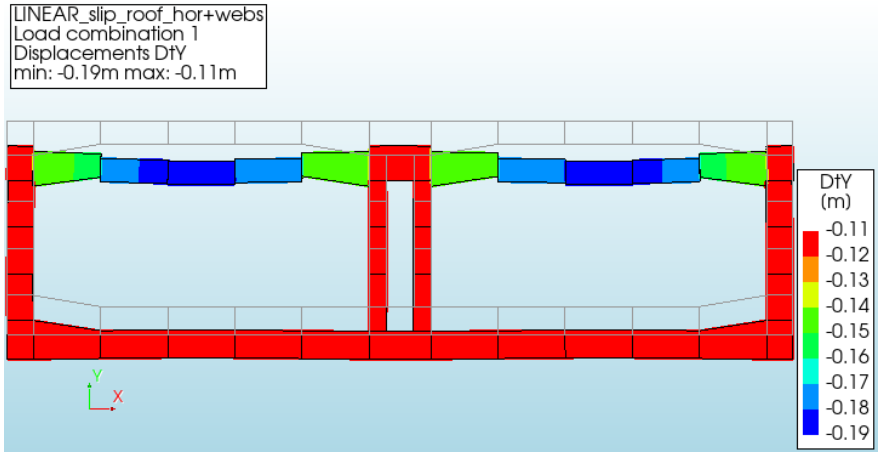

Figure 7.25: Displacements in Y direction

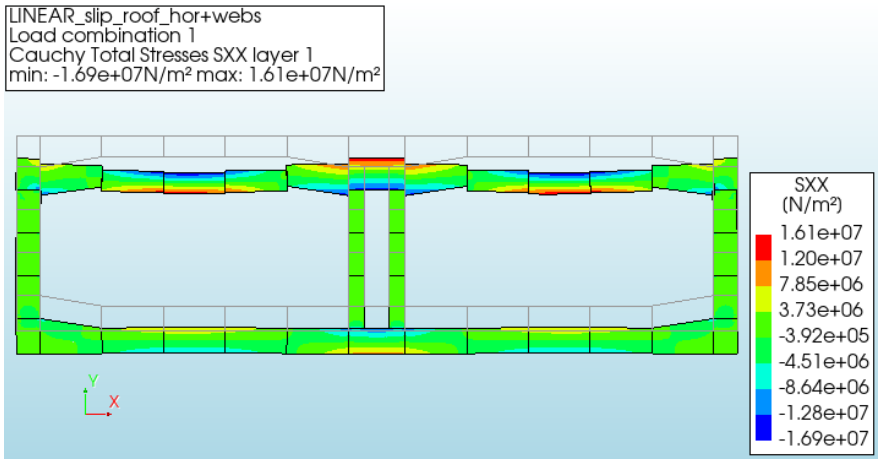

Figure 7.26: Concrete slab stresses

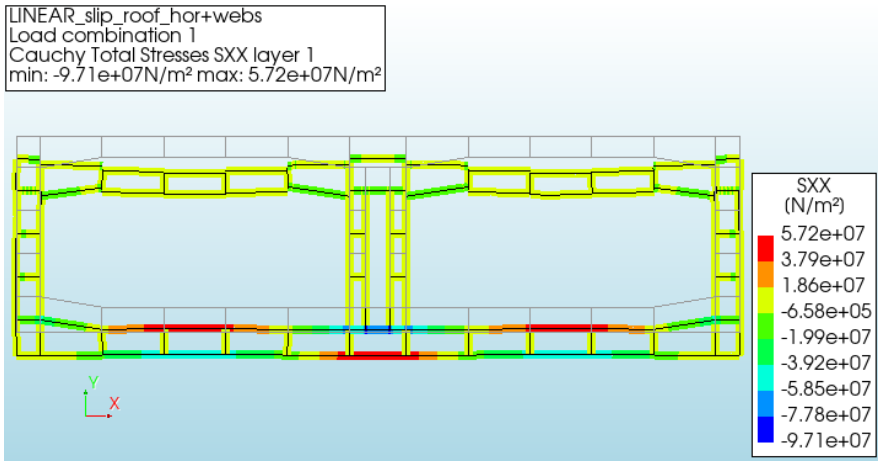

Figure 7.27: Steel plates stresses

- Higher concrete stresses and displacements are observed in the roof element when compared to cases with both strong and weak connections at the horizontal interfaces. This outcome is expected, as the webs have demonstrated their significance in the structural design, contributing to overall stability. On the other hand, steel stresses are lower than in the other cases due to the restricted and limited transfer of load.

7.3.3 Conclusions

From the linear analysis it is obtained the following graph for the global behaviour of the roof. The graphs present the global behaviour for the case of strong and weak connection of the roof element for the load combination of the total load plus three times the roof load.

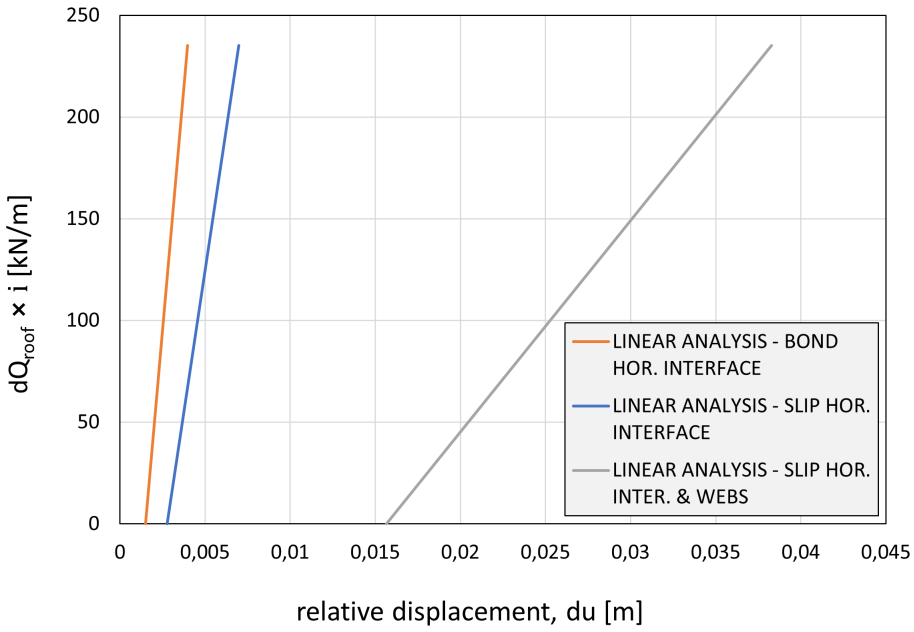

Figure 7.28: Distributed applied load - relative displacements graphs for the linear models

- In the linear analysis of the model, where strong connection is applied to the interface elements - denoted as bond connection - it is anticipated a higher capacity. This is because the structure exhibits greater rigidity and the materials are integrally connected, as evidenced by the steep slope of the orange line graph.

- A weak connection at both the horizontal and vertical interfaces has proven to be critical, as it results in a significant difference in slope on the global behavior graph. In contrast, while the weak connection at the horizontal interfaces shows some impact, the difference in capacity compared to the strong connection is not particularly significant.

7.4 Nonlinear analysis of full SCS tunnel cross-section

7.4.1 Nonlinear concrete behavior

In this section, the analysis will focus on the entire cross-section, incorporating nonlinear concrete and varying the connection between the steel plates and the concrete boxes. Initially, a finite element model of the SCS composite cross-section will be developed using nonlinear concrete and strong connection (bond) for the horizontal and vertical interfaces of the roof element. Following this, the same analysis will be conducted using weak connection (slip) for the horizontal and vertical interfaces.

Strong connection

The figure below presents a graph of the incremented distributed load on the roof compared to the relative vertical displacement, along with the analysis curve for nonlinear concrete behavior and fully bonded connection for both horizontal and vertical interfaces.

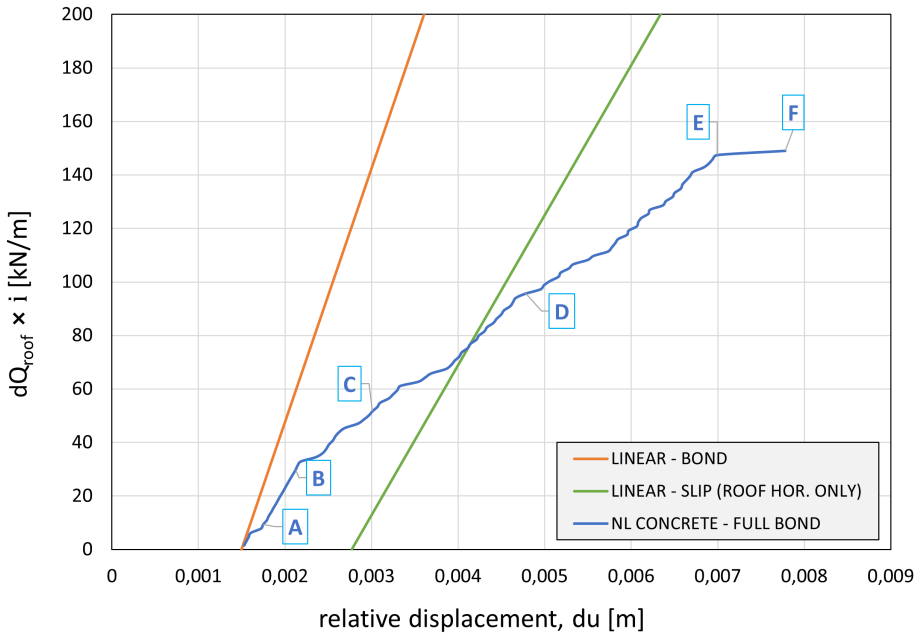

Figure 7.29: Distributed load Q - relative displacement du graph

To gain a clear understanding of the structure, the analysis will be divided into six steps (A, B, C, D, E, and

F). The objective is to capture the changes in the behavior of the roof element under the nonlinear properties of concrete.

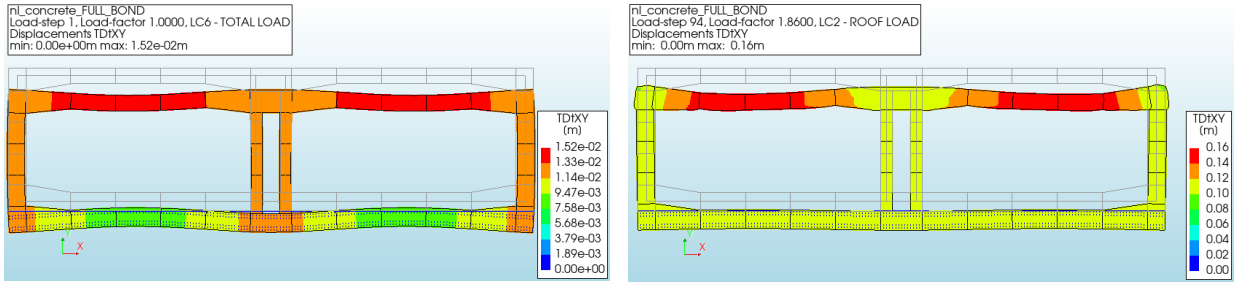

(a) First load step (b) Last load step

Figure 7.30: Displacements in Y direction for the first and last load step

- The first contour plot regarding the displacements of the first load step of the analysis shows relatively small displacements. This indicates that the structure is initially stable under the applied load with the strong connection.

- The second contour plot presents larger displacements, which indicates that as the load increases, the structure experiences larger deformation. This suggests that the strong connection effectively transfers the load between the concrete core and the steel plates. However, due to the non-linearity of concrete, instability is caused as the stress limit somewhere in the structure is reached.

Further investigation to discover the cause of instability of the structure is employed based on the different chosen steps on the global behaviour graph. Figure 7.31 illustrates the propagation of cracking in the roof elements corresponding to the marked steps A, B, C, D, E, and F on the global behavior graph (Figure 7.29).

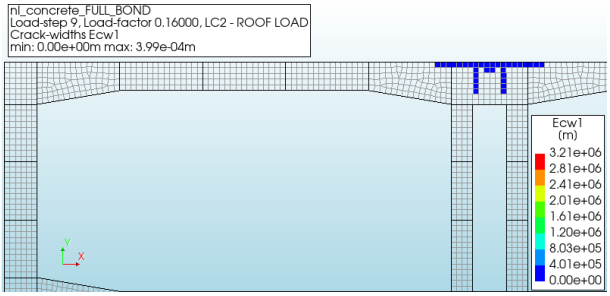

Step A: Cracking at the symmetry axis

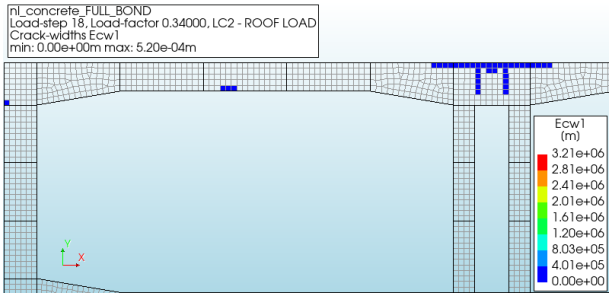

Step B: Initial cracking at span and joints

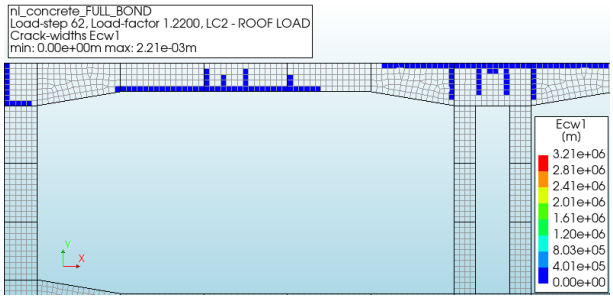

Step C: Cracking propagates along the height

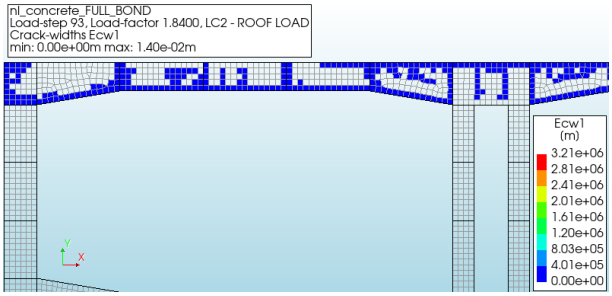

Step F: Severe crack damage (last converged step)

Figure 7.31: Cracking propagation in the roof element

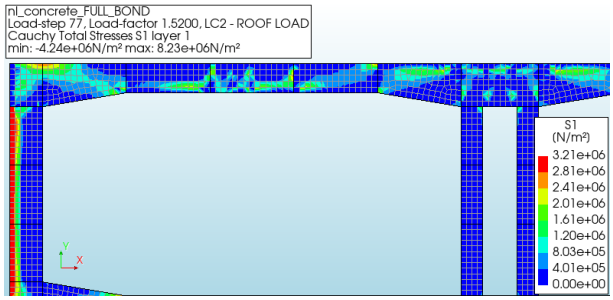

(a) Principal stress S1 (step 77)

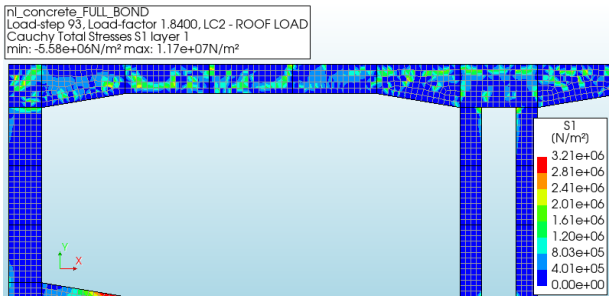

(b) Principal stress S1 at step F

Figure 7.32: Tensile principal stresses S1 at a random step and at the last converged step of the FE analysis

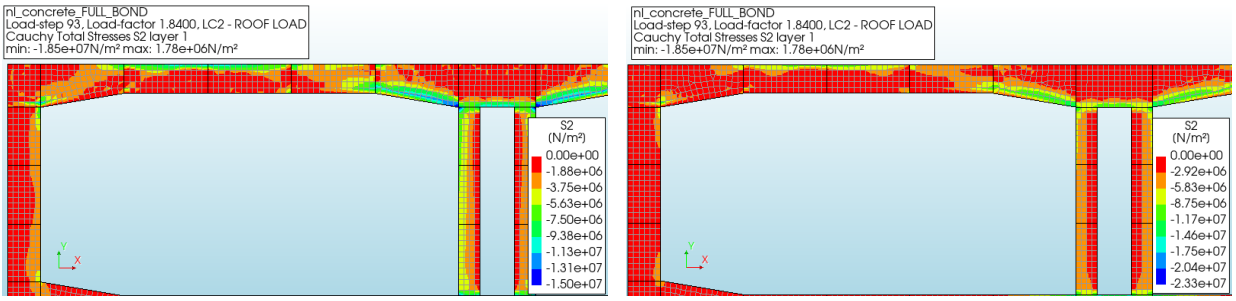

(a) Principal stress S2 at step F (fixed legend)

(b) Principal stress S2 at step F

Figure 7.33: Compressive principal stresses S2 at the last converged step of the FE analysis

- Cracking propagation: The first four contour plots show the development of cracks in the structure. Step A indicates the onset of initial cracking in the roof element at the symmetry axis of the cross-section, while step B marks the emergence of cracks at the opening and the left end joint of the roof element. Step C (similar D and E) illustrates the propagation of cracking toward the central portion of the roof, particularly around the opening. Finally, step F represents the point just before failure, highlighting the progression of cracking over a significant portion of the roof.

- Cracking and crushing: The last two images compare the tensile and compressive behaviour of concrete at the last load step before failure. The compressive strut on the right joint of the roof is created. This is clearly illustrated in figures 7.32(a) and 7.33(a), where the legend is adjusted to a smaller value of the maximum compressive strength of concrete to enhance visibility of the schematic representation of compressive struts in the boxes next to the roof element joints.

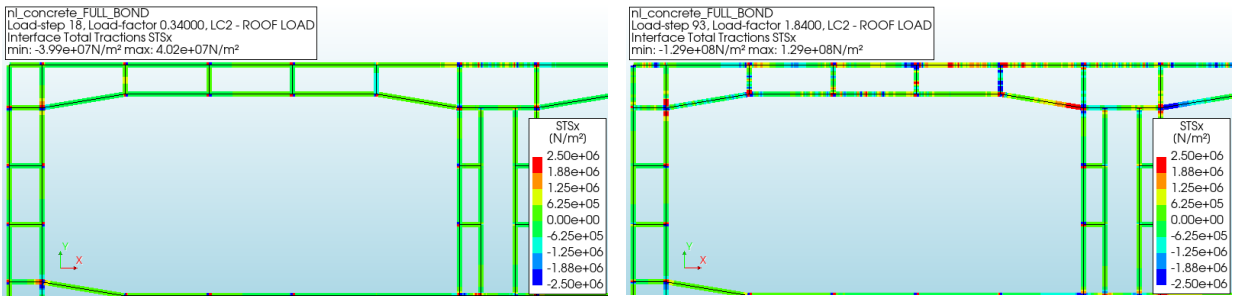

(a) Interface total traction STSx at step B

(b) Interface total traction STSx at step F

Figure 7.34: Interface total tractions STSx of the roof's interfaces (fixed legend)

- Figure 7.34 displays the interface tractions at both an early stage of the analysis (step B) and the final stage (step F). It is clear that as the load increases, slip becomes increasingly apparent, beginning at the joints between the horizontal and vertical plates (webs) of the composite boxes and propagating along their length.

Weak connection

An attempt was made to perform a nonlinear analysis with weak connections on both the horizontal and vertical interfaces. However, instability issues emerged during the initial step of the finite element analysis. Consequently, it became evident that conducting a nonlinear concrete analysis that incorporates weak connection at the webs is not feasible, given the complexities involved and the critical role that the webs play

in the structural design of the SCS tunnel cross-section.

Conclusions

So far, it can be concluded that the non-linearity of concrete plays a crucial role in the structural performance. The nonlinear concrete analysis with strong connections (bond) at the interfaces demonstrates a significant difference in the structure's capacity when compared to the linear analysis (figure 7.29). The linear analysis reveals behavior consistent with bending theory, as indicated by the compression and tension observed in the stress SXX contour plots. In contrast, when non-linearity is introduced, the formation of compressive struts becomes apparent, along with notable differences in stress concentrations in the principal stress contour plots.

However, the analysis involving nonlinear concrete with weak connections (slip) at both the horizontal and vertical interfaces of the roof element was not successfully completed due to instability issues. It was found that when slip is applied at the webs, the structure is unable to sustain any load. This observation suggests that slip at the webs should be avoided in future analyses, as the webs play a vital role in the structural integrity and overall performance.

7.4.2 Nonlinear concrete and steel behavior

Based on the results from the finite element analysis of the composite beam in Chapter 6, it was concluded that incorporating nonlinear steel behavior into the nonlinear concrete finite element model does not significantly affect the results. To verify this conclusion, an additional analysis was performed using nonlinear behavior for both concrete and steel in the roof element of the complete 2D cross-section model, assuming strong interface connections (bond). The figure below demonstrates the similarity in global behavior between the two analyses.

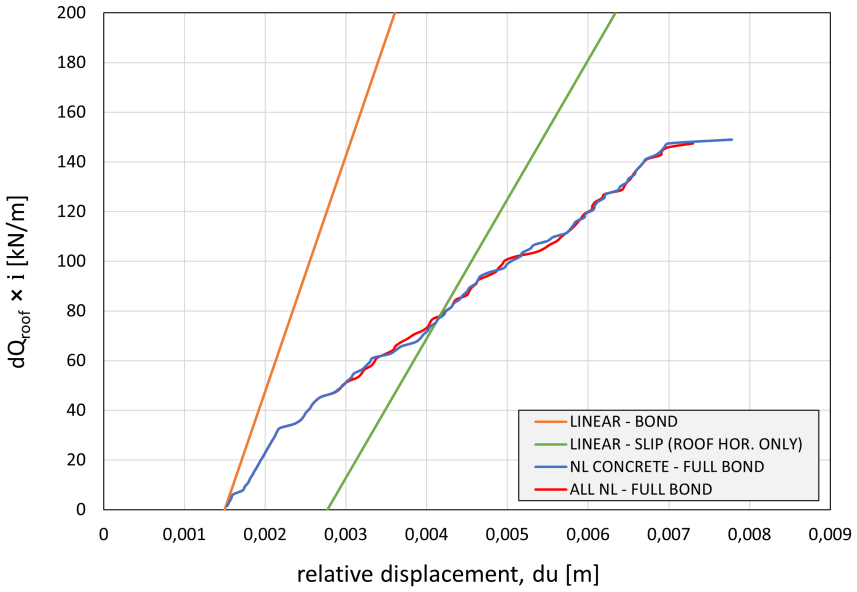

Figure 7.35: Global behavior behavior results in comparison

Figure 7.35 demonstrates the comparable global behavior observed in both analyses conducted. A closer examination of the stress-strain relationship in the top left section of the roof element, where higher stresses

are present, reveals that the steel exhibits linear behavior up to the final converged step of the analysis. The contour plot below (fig. 7.36) indicates stress levels lower than the yielding stress of 4,35E+08 N/m^2 for the nonlinear steel material. Additionally, the graph on the right (figure 7.37), corresponding to a node selected in the same top left section of the roof element (red rectangular box), provides further confirmation of the linearity of the steel throughout the analysis.

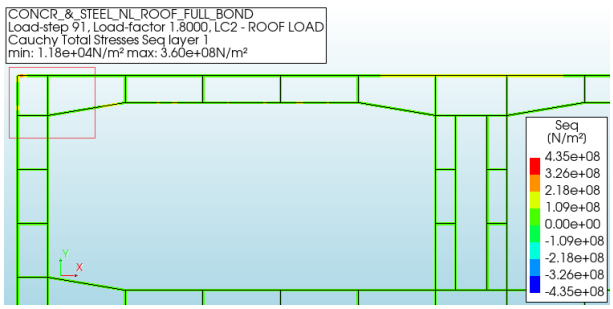

Figure 7.36: Stress Seq - roof's steel plates

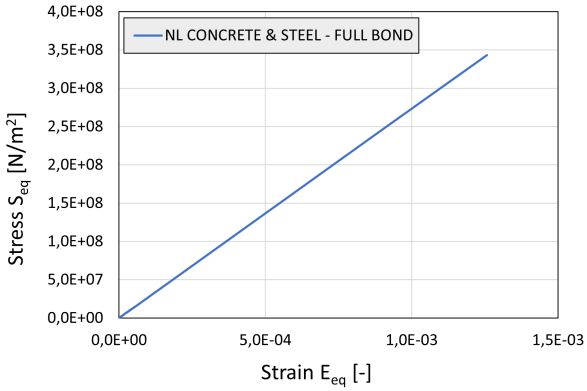

Figure 7.37: Steel's stress - strain relationship

Thus, based on the consistent results, the finite element study of the cross-section will be continued with nonlinear concrete analysis models to simplify the finite element model analysis and reduce computational times.

7.5 Influence of horizontal interface weak connection

In this section, the nonlinear concrete finite element model will be investigated by varying the locations of the weak connection on the horizontal interfaces. As previously mentioned, the application of weak connection at the vertical interfaces has resulted in instability issues during the analysis. Although weak connection was also applied to the webs in this section, similar difficulties arose. Therefore, the application of weak connections will be limited to the horizontal interfaces only.

7.5.1 Weak connection at bottom line interface of the roof element

The following figure presents the displacement in the Y direction from the finite element analysis using nonlinear concrete and weak connection (slip) at the horizontal interfaces of the roof element.

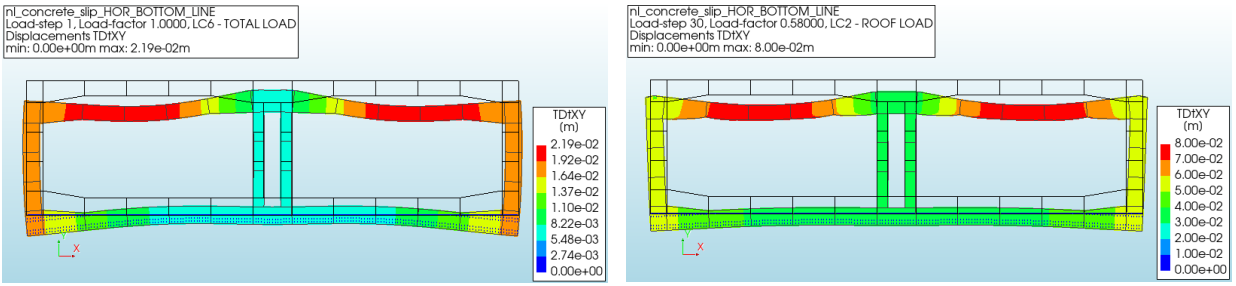

(a) First load step (b) Last load step

Figure 7.38: Displacements in Y direction for the first and last load step

- At the first load step, the structure shows small displacements, suggesting initial stability. At the last load step, it can be observed a significant increase of the displacement values, more specifically at the span and the corners, indicating more relative movement between the two materials due to slip.

To gain an understanding of the behavior, a detailed analysis will be conducted focusing on the global behavior graph below and the marked steps within it. These steps indicate changes in slope and phenomena related to the behavior of the roof element.

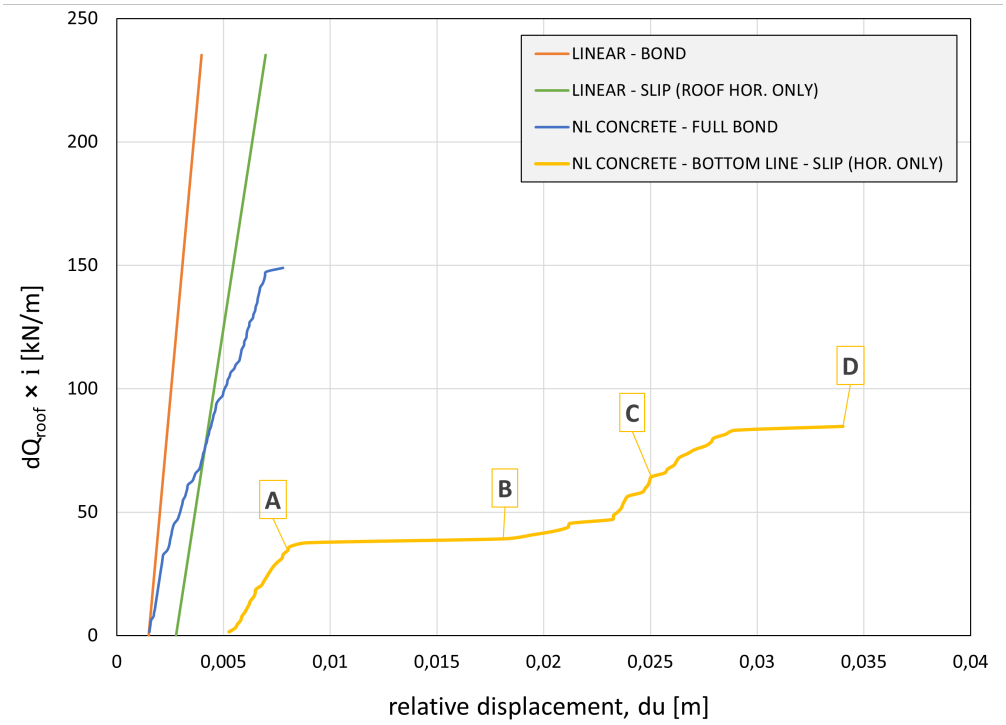

Figure 7.39: Distributed load Q - displacement du graph

- The nonlinear analysis with weak connection at the bottom line of the roof presents a step-like progression with distinct flat sections, indicating periodic slip. In contrast, the other curve which represents solely the non-linearity of concrete in the analysis shows more continuous and smooth increases in load with displacement. This indicates that the model with bottom line slip connection experiences

more pronounced slip at certain points, leading to less stiffness and more flexibility compared to the other conditions.

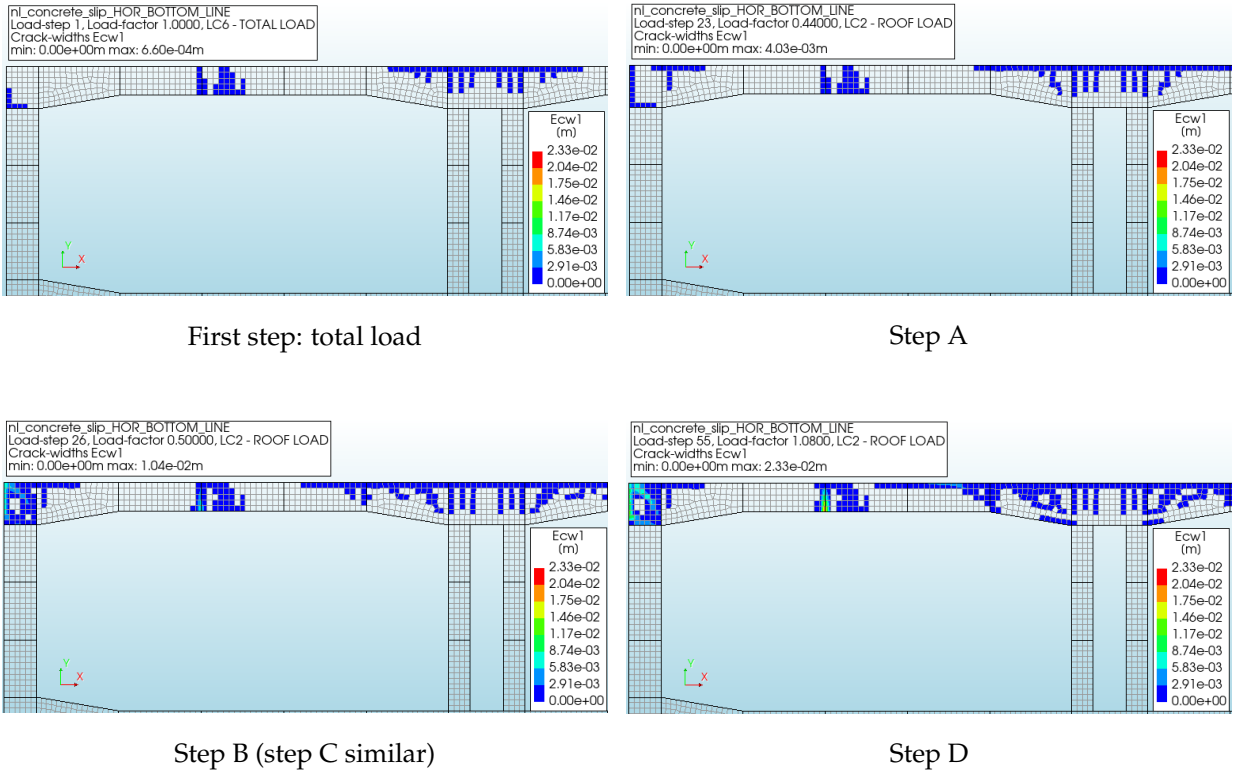

First step: total load

Step A

Step B (step C similar)

Step D

Figure 7.40: Cracking propagation in the roof element

- Based on the crack-width plots in figure 7.40 the cracking is already initiated due to the applied total load. In the first load step the cracks at the span and the extremes are already noticeable, indicating the structure's initial response to the load. This is consistent with the observation that the structure is initially stable under the applied load. Step A presents the propagation of cracking towards the middle span. This slip reaction shown in global behavior graph helps also explain the progression of cracking toward the opening. By step B, the cracking has not only extended but the values of the crack - width have also increased (maximum crack width value at step A is 4,03E-03 m, while at step B, it is 1,04E-02 m). In parallel, the cracking is propagating not only towards the middle span but also along the height of the roof element. This indicates that as the load progresses, the slip connections result in increased crack - widths, leading to reduced stiffness and higher flexibility in the structure. In the final step, significant crack - width values are observed, indicating that the slip connection permits greater movement, resulting in larger cracks that extend along the entire roof element section.

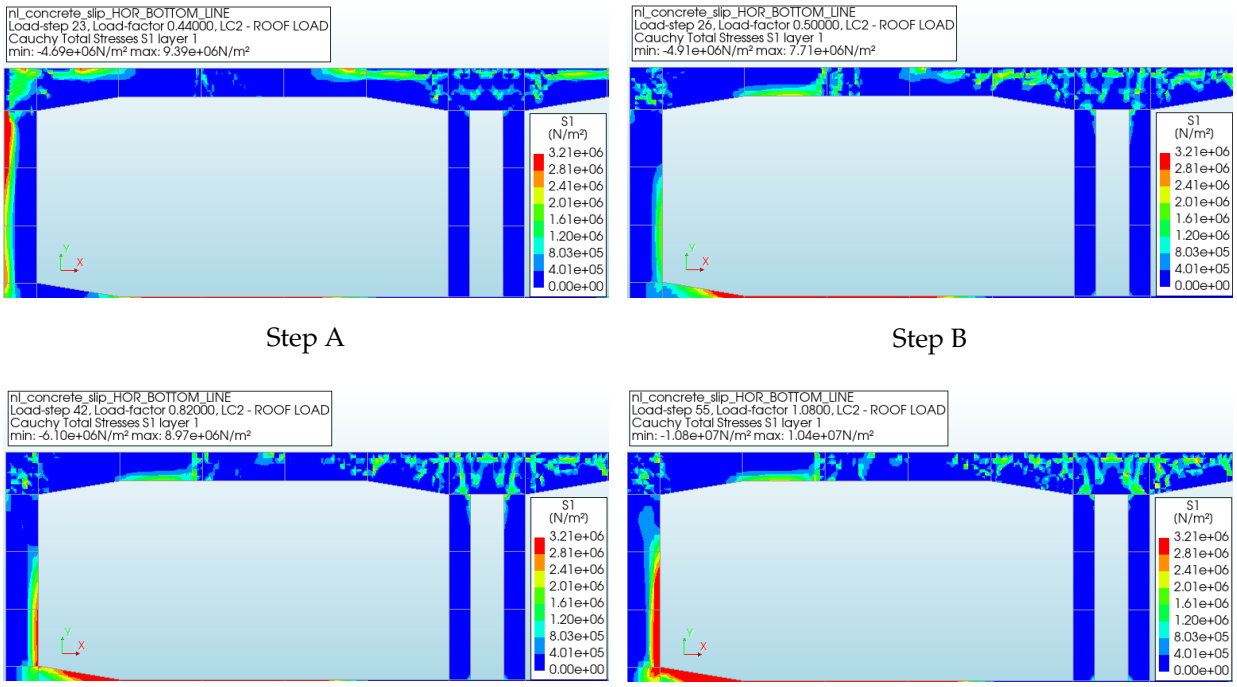

Figure 7.41: Principal stresses S1

- Step A and B mark the difference on the global behaviour of the structure. This can be observed at the graph as sudden of slope (flat section) occurs, where load steps 23 till 26 belong (from step A to step B). From Step B onward, including Step C and extending to the final step, the contour plot reveals significant cracking zones. The final contour plot presents maximum tensile stresses, highlighting the critical points where the structure is most vulnerable to tension (span and joints). It can be concluded that the quick propagation of cracking (due to slip) at the span and the joints, cause a significant decrease on the bearing capacity of the structure.

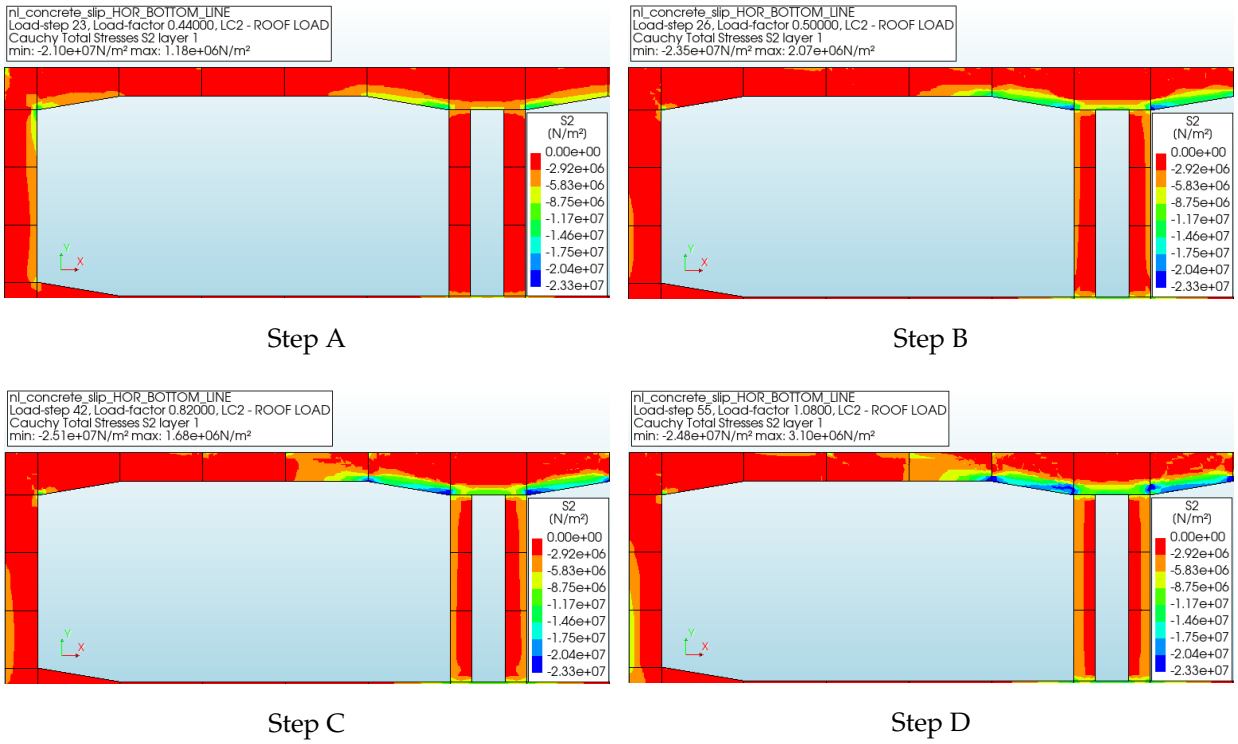

Figure 7.42: Principal stresses S2

- In the final steps, C and D, the schematization of the compressive strut at the junction of the roof element and the interior walls of the cross-section is evident. This representation of the compressive strut is critical, as structural failure follows from this point. This conclusion is further supported by the accompanying figure.

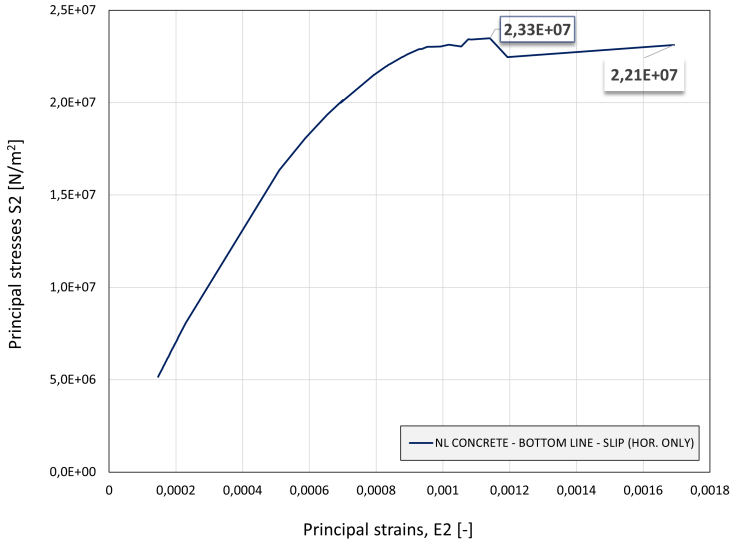

Figure 7.43: Stress - strain relationship of the compressive behavior of concrete of the analysis

Figure 7.43 confirms that the compressive strut is failing, as a point in the bottom right corner adjacent to the joint of the middle inner walls has reached the maximum compressive strength of the concrete. Specifically, this value of 23,33E+07 is attained between steps 50 and 51 of the analysis. The analysis stops at the last converged step, step 55, by which time the softening phase of the concrete has already begun.

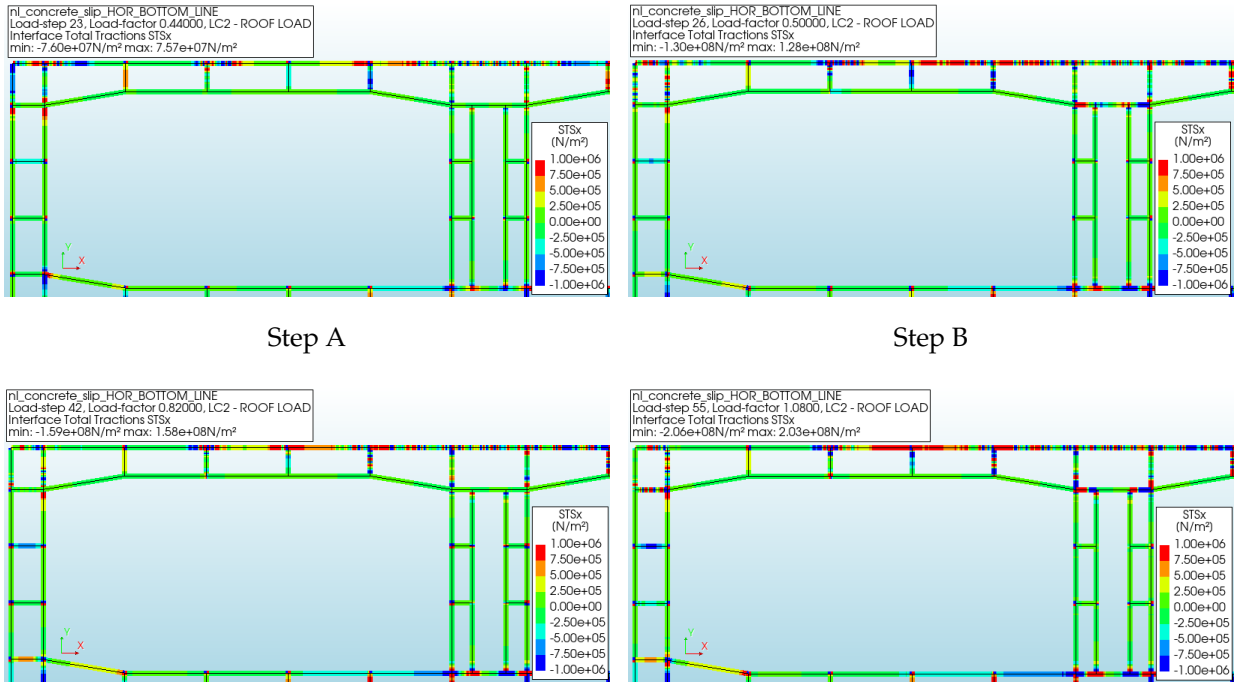

Figure 7.44: Interface tractions STSx of the interfaces

Figure 7.44 shows the interface tractions (STSx) at the interfaces. It can be observed that the bottom line of the roof element, where the weak connection is implemented, behaves as if there is no connection, resulting in zero load transfer and, consequently, zero tractions in the contour plot. In contrast, the sliding effect caused by slip at the bottom line is clearly evident at the top line of the roof element, where the connection is strong, making this portion of the roof element the only active area for load transfer. It is noted that starting from Step A, where the slip phenomenon initiates in the global behavior graph, tractions begin to appear, and by Step D, they have increased significantly, particularly in the zone where failure of the compressive strut is observed.

7.5.2 Weak connection at the top line interface of the roof element

The following figure presents the principal tensile and compressive stresses from the analysis, in which the non-linearity of concrete is considered with a weak connection at the top line interface of the roof element. The legends of the contour plots have been adjusted to visualize the compressive strut at the edges of the opening and the propagation of excessive cracking toward the middle span.

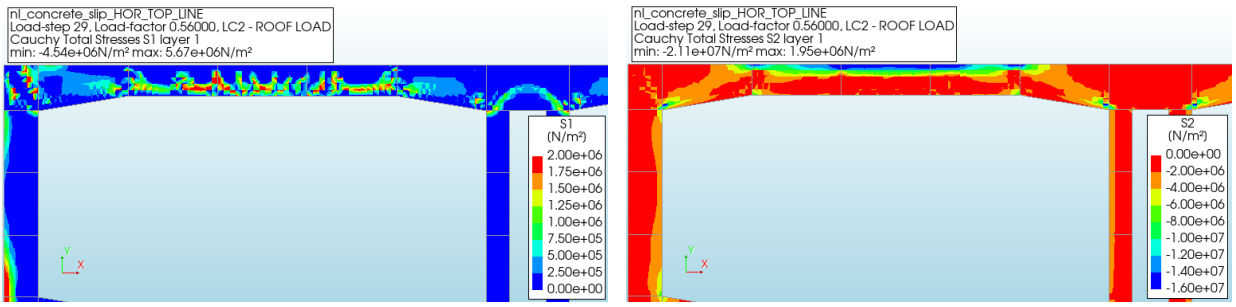

Principal stresses S1 (fixed legend) Principal stresses S2 (fixed legend)

Figure 7.45: Tensile and compressive principal stresses at the last converged step

7.5.3 Conclusions for entire line interface

Figure 7.46 also includes the global behavior graph, which demonstrates a similar pattern to the global behavior curve observed previously for the weak connection at the bottom line interface. This pattern begins with a pronounced flat section where the slip initiates, followed by a recovery in stiffness due to the mobilization of the compressive strut and redistribution of stresses, leading to the final stage of failure.

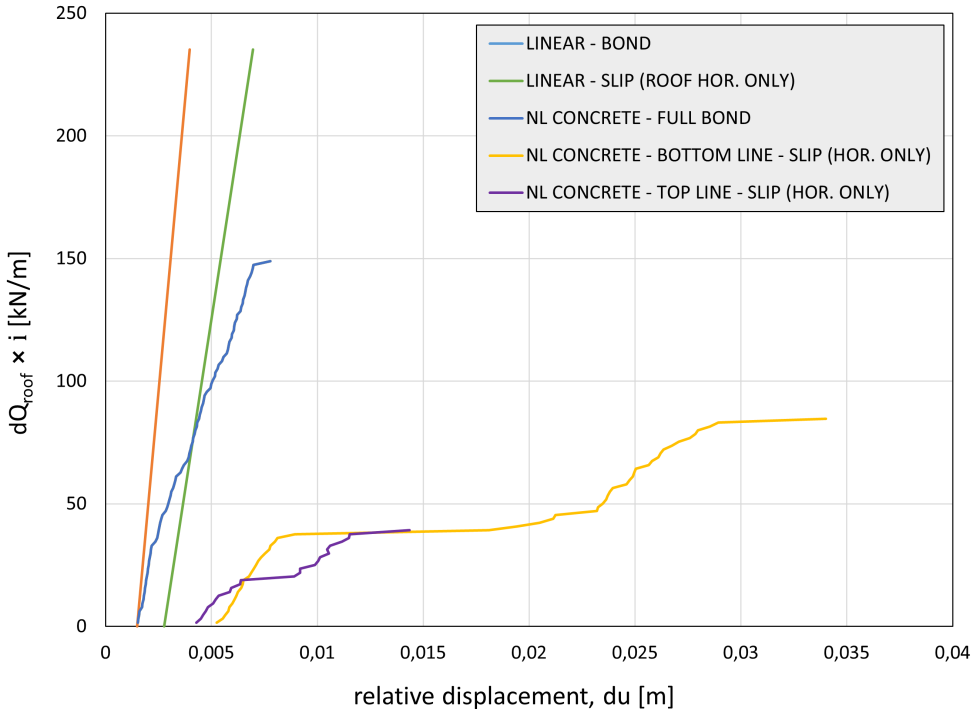

Figure 7.46: Distributed load - displacement graph

From this graph, it can be concluded that the location of the weak connection plays a significant role in affecting the structure's capacity. Specifically, the capacity of the analysis with a weak connection at the top line of the roof element is considerably lower compared to the capacity of the model with a weak connection

at the bottom line. This difference is closely related to the location where the load is applied. Since the roof load is applied at the top line, having a strong connection in this area is critical for effective load transfer.

7.5.4 Weak connection at 1 box of the roof element

The following figure illustrates the displacement in the Y direction at the first and last load step for the weak connection at a randomly selected box of the roof element, highlighted with a red rectangular line.

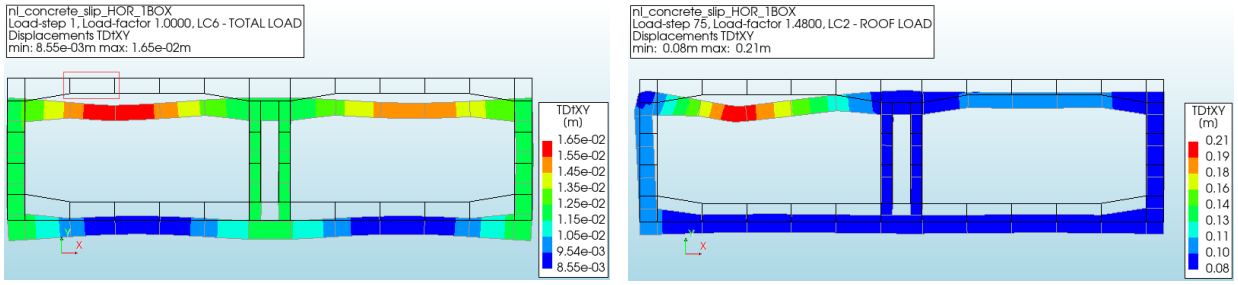

(a) First load step (b) Last load step

Figure 7.47: Displacements in Y direction for the first and last load step

Large displacements are observed in case of weak connection for the top and bottom interface connection of concrete "box", as noted in the figure. These displacements are particularly pronounced where the slip is applied, with the boxes exhibiting low shear stiffness at the interface experiencing greater displacement compared to the other sections of the roof element.

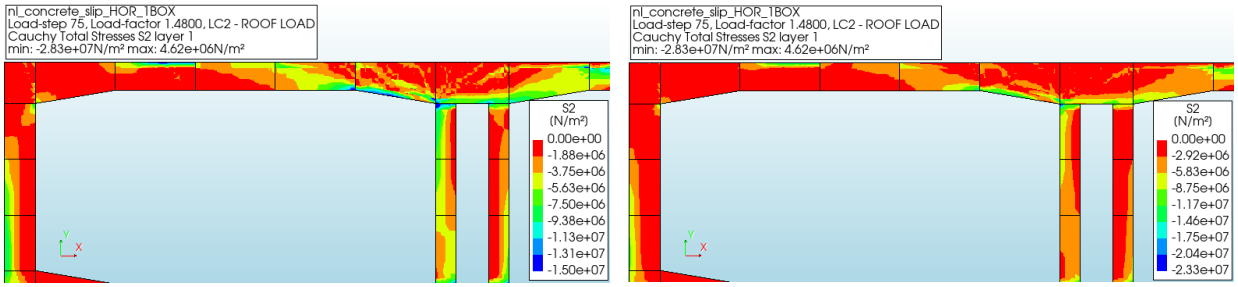

(a) Principal stresses S2 - last load step (fixed legend) (b) Principal stresses S2 - last load step

Figure 7.48: Compressive principal stresses S2 - last converged step

Compressive strut schematization at the middle joint of the roof element with the inside walls is visible in both figures. Figure 7.48 gives a better visualization of the formed compressive strut at the right part of the roof element.

7.5.5 Weak connection at the middle box of the roof's opening

The behavior observed in this analysis yields results similar to those of the box selected to the middle left part of the opening. The displacement deformations for the first and last converged steps of the analysis are presented in the figure below.

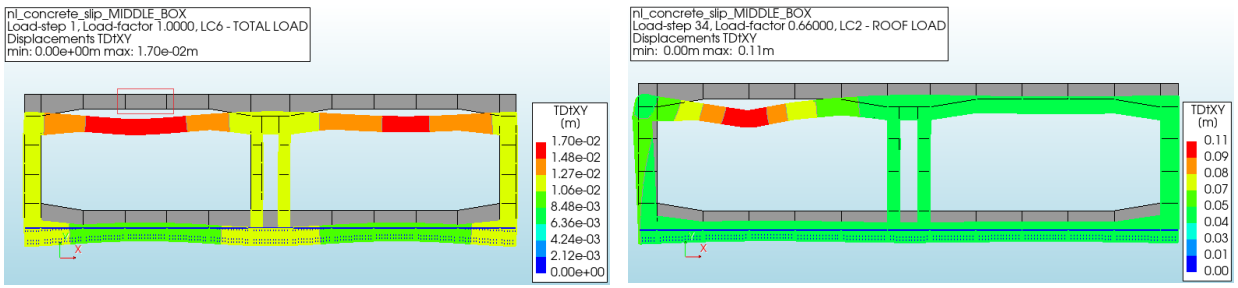

(a) First load step (b) Last load step

Figure 7.49: Displacements in Y direction for the first and last load step

Figure 7.50 illustrates the global behavior of the middle box weak connection model analysis. Several critical points have been selected for close examination to provide a clearer understanding of the behavior.

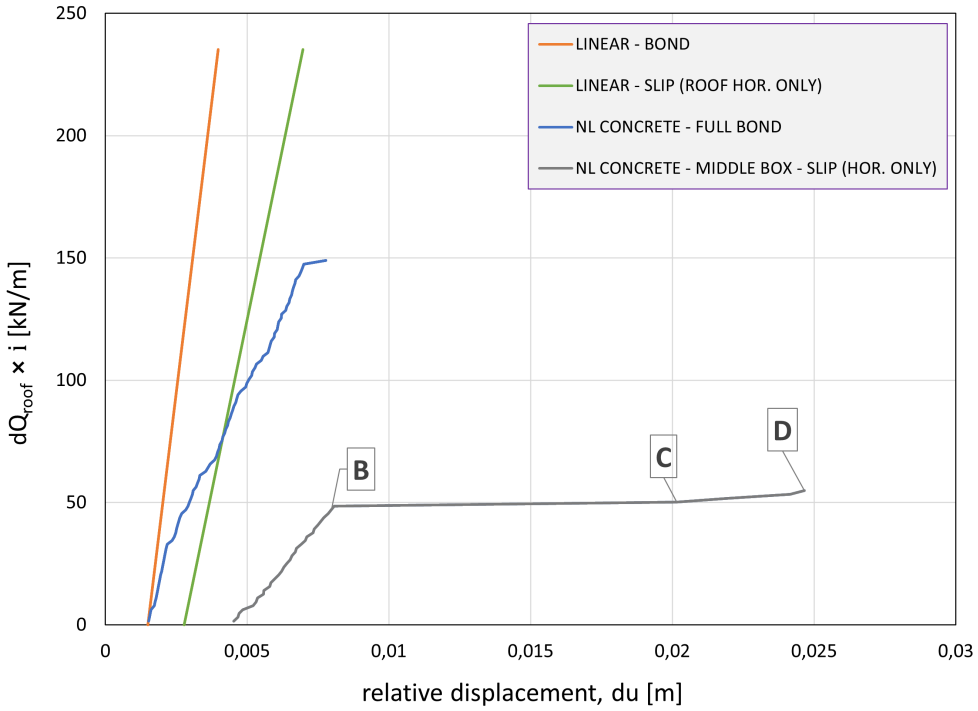

Figure 7.50: Distributed load - displacement graph (middle box)

There are observed similarities regarding the nonlinear concrete analysis of the other two cases. However, the analysis is stopped earlier thus it is concluded that the middle box slipping is a more critical situation for the stability of the immersed tunnel. Below are presented the contour plots for crack-width, the tensile stress distribution and the compression.

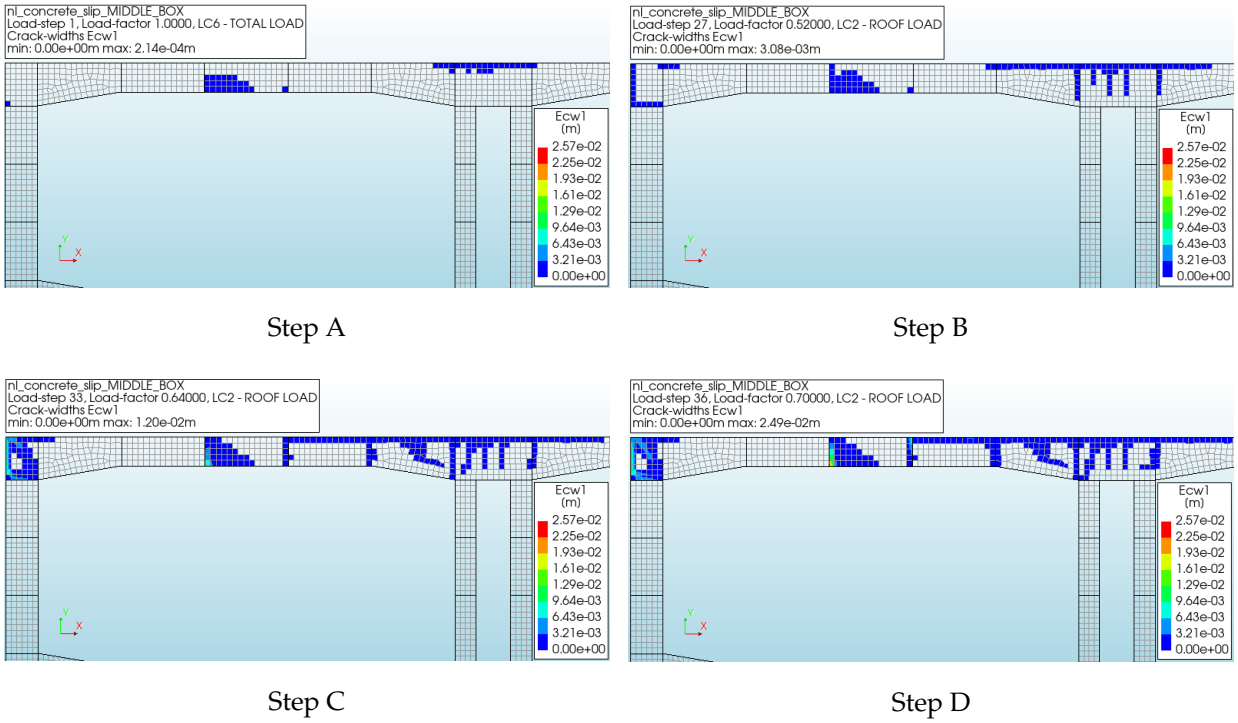

Figure 7.51: Crack-width

Figure 7.51 presents the propagation of cracking along the roof element throughout the analysis. As expected, a significant cracking zone is observed in the middle box, where weak connections are applied at the top and bottom interfaces. It appears that the cracking zones are larger than those associated with the bottom line weak connection, indicating larger crack - width values.

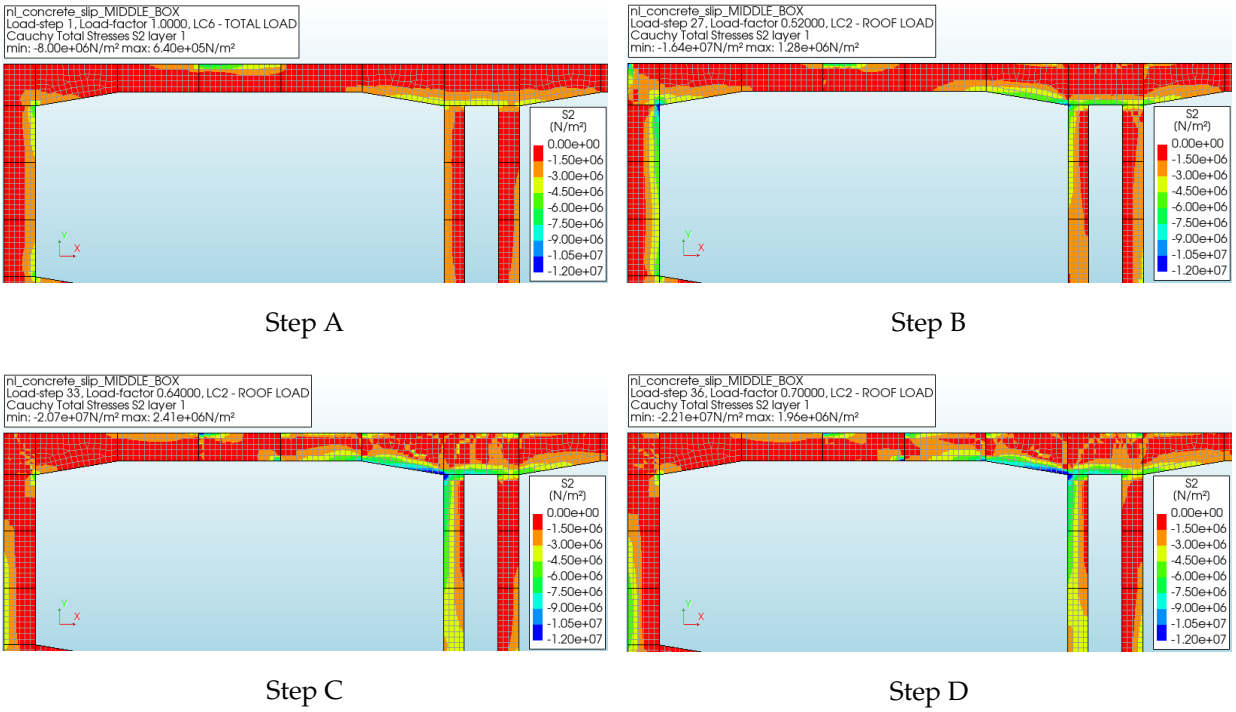

Figure 7.52: Compressive principal stresses S2 with fixed legend

Figure 7.52 illustrates the concentration of principal compressive stresses on the roof element. Compressive struts are formed starting from the middle joint of the roof element with the inner walls and extending into the adjacent boxes. However, the formation of the compressive strut is interrupted at the middle box, where it remains incomplete at the last step. This incomplete development prevents the left section of the roof from exhibiting a full schematization of the compressive strut, thereby restricting effective load transfer.

7.5.6 Conclusions for box interface

As previously mentioned, the primary failure mechanism observed in the finite element model analysis - where the non-linearity of concrete is applied - has been identified as the strut-and-tie model. The effects of non-linearity significantly impact the structure, making load transfer increasingly difficult until the compressive strut ultimately fails. In this analysis, the compressive strut can fail in two distinct ways: first, through the crushing of concrete when its maximum compressive strength is reached, and second, through concrete splitting, which manifests as tensile cracking in the direction of the compressive strut. Various analyses have confirmed the failure of the compressive strut primarily due to concrete crushing. The following figure illustrates results showing that maximum compressive strength has been achieved in at least one of the model analyses.

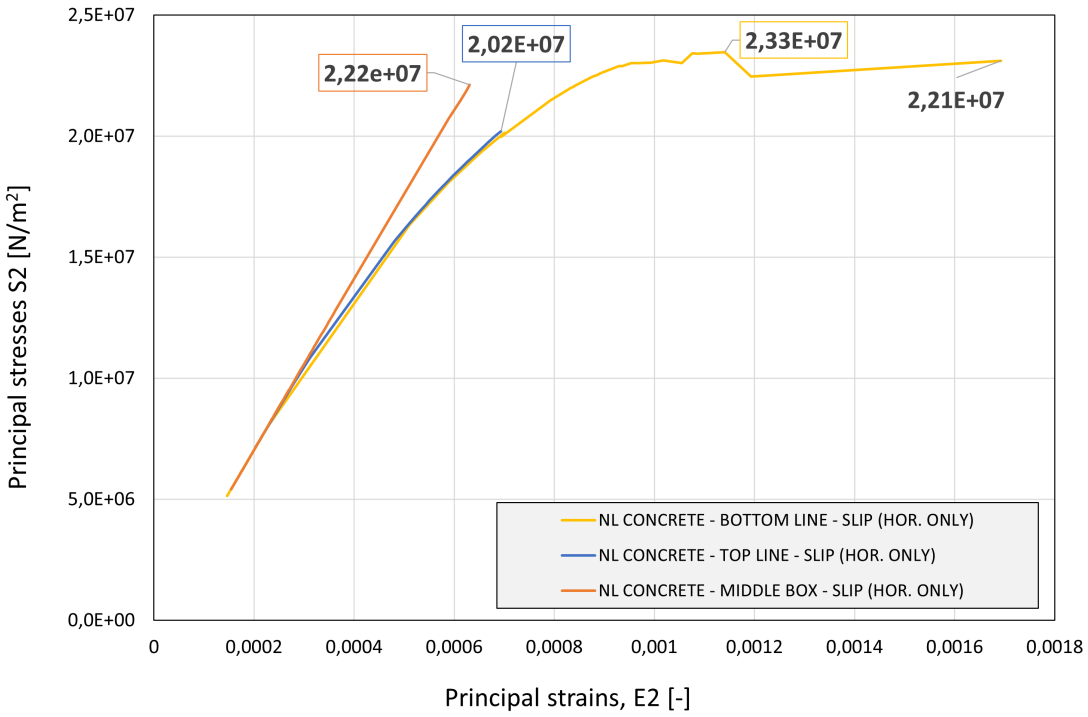

Figure 7.53: Stress - strain relationship of concrete in compression (S2 - E2)

7.6 Conclusion

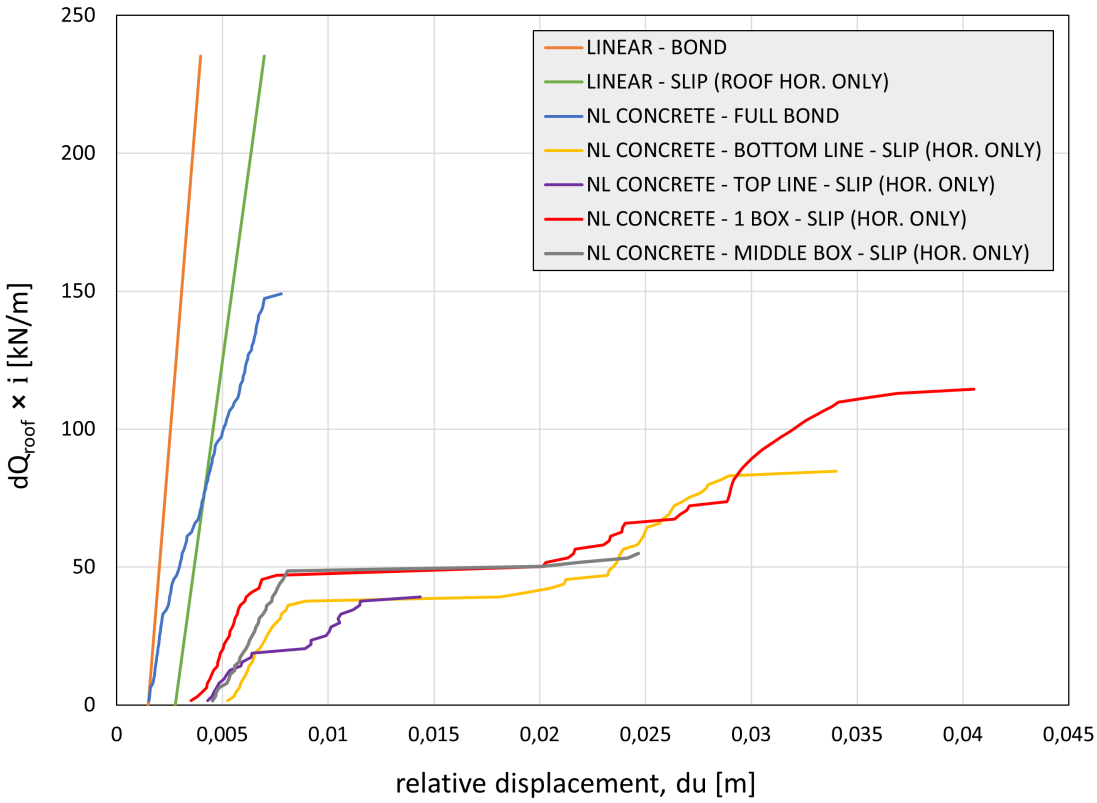

Figure 7.54: Distributed load - displacement graph

- Based on the graph above, it can be observed that it is of major influence the non-linearity of concrete on the cross-section. In addition to the non-linearity of concrete, weak connection can lead to significant decrease of the structural capacity of the structure. In all nonlinear concrete analysis with slip (red, yellow, grey and purple lines) it is observed a similar behaviour of slops in the curves, where firstly cracking from the joints propagates towards the span and finally compressive strut schematization occurs. As the extent of the slip horizontal interface increases, the stability and capacity of the structure decrease. This observation aligns with the results from the curves. Specifically, when weak connection is applied solely to a single "box" (i.e., the top and bottom horizontal interfaces), the structure has a better performance and higher capacity. However, when the weak connection is applied across the entire bottom line of the roof element, the structure's capacity diminishes.

- The global behavior graphs illustrate the effect of weak connection location and size. The red line (slip in one box between joint and middle-span) shows a less dramatic reduction in capacity compared to the yellow line (slip along the entire bottom interface). The grey line (slip in the middle-span box) falls somewhere in between, showing a slightly higher load-carrying capacity but also a quicker onset of instability. The worst-case scenario occurs when a weak connection is applied along the entire top edge of the roof element. In this situation, the lowest capacity is observed (despite the same behavioral pattern), indicating that the alignment of the slip location with the load application point is critical. This comparison highlights the importance of the weak connection location in determining its impact on the structure's capacity.

- Overall structural behaviour: The weak connection models result in higher flexibility but also greater stress concentrations, leading to increased cracking and crushing. The strong connection condition (blue line graph) provides higher stiffness and better load distribution, reducing the risk of failure.

- Compressive strut and load transfer: The "compressive strut" describes the path along which compressive forces are transferred within a structure. In the composite cross-section, the compressive struts are likely to form along the concrete's strongest direction (i.e., in compression). The weak connections (slip condition) at the horizontal interfaces allow for some relative movement between the concrete and steel plates, which can affect the formation and orientation of these compressive struts. If the compressive struts are not properly aligned with the principal stress trajectories, it could lead to inefficient load transfer and increased stress concentrations, leading to failure of the structure.

Chapter 8

Discussion

The objective of this thesis investigation is focused on the impact of construction-induced irregularities on the complex SCS tunnel design. Despite recent findings and research, the interface connection between the concrete core and the steel plates of the structure remains a field which still requires further investigation. Thus, the imperfections that have been taken into account for this research are divided in two distinct categories:

- **Interface stiffness variation:** It was investigated the influence of the extreme stiffness variations in the interface connection of the design. The stiffness variation was divided in two different scenarios: A strong connection (bond) connection was implemented to represent a high-stiffness interface, where the steel plates and the concrete core are effectively bonded. A weak connection (slip) was applied to represent a numerical-zero-value of stiffness for the interface, where the steel plates and the concrete core display significant slip.

- **Interface disconnection:** The study explored the impact of disconnections (gaps) in the interface connection. Specifically, the gap definition is considered based on different imperfections that may occur in the different construction phases of the structure. Possible imperfections could be due to absence of interface elements, such as shear connectors, or the improper design and placement during construction. Another imperfection could be related to voids in the concrete core due to incomplete filling or uneven pouring/casting during construction. Lastly, deformation or failure of the shear connectors may also lead to localized gaps in the interface, representing another potential imperfection.

The study began with a simplified composite beam model in DIANA software representing a portion of the roof element to enable a preliminary understanding of the structure's behavior. The initial research was then followed by the development of a detailed cross-section model representing the entire tunnel design, allowing for a more comprehensive analysis of the structure's performance in a real-world context.

The simplified composite beam model, that was firstly designed, consisted of a 5-meter-long concrete block with two horizontal steel plates positioned along the horizontal top and bottom surfaces. The connection between the steel plates and the concrete core was modeled using interface elements that incorporated both normal and shear stiffness. To start the investigation, a linear static analysis was performed, assuming linear material behavior for both steel and concrete. Regarding the interface elements, a strong connection was applied, characterized by high normal and shear stiffness, equal to 1×10^9 N/mm^3. The strong connection decision explored the best-case scenario where no imperfection is taken into account, and the

structure is perfectly designed and constructed. The next stage of the investigation involved a linear static analysis of the model using weak connection for the interface elements. Weak connection is characterized by a low shear stiffness of $1 \times 10^{-}9\,\mathrm{N/mm^3}$ while the normal stiffness is maintained the same as the strong connection. This approach was adopted to study the worst-case scenario, considering potential imperfections (as mentioned and explained above) in the interface between the steel plates and the concrete core. The force - displacement graph displayed a significant difference in the capacity, demonstrating a linear pattern with more favorable overall performance for the fully bonded connection design compared to the weak connection design, as it was expected. To improve the simulation of the SCS design, an additional model was developed including the vertical plates (webs). Linear static analyses where performed and the resulting graphs presented a higher capacity compared to the graphs obtained from the initial model. Based on the stress distribution contour plots, it was observed that the webs act as fixation points and are responsible for transferring part of the load to the concrete boxes in case of weak connection in the interface. To draw further conclusions, the model including webs (which is closest to the actual design) was tested with material non-linearity. Initially, the non-linearity of concrete was introduced. The first observation, based on the global behavior graph, was a large difference in capacity. Regardless of whether a strong or weak connection was used for the interface, significant decrease of the capacity was noticed when the nonlinear characteristics of concrete were activated. Additionally, the stress distribution contour plots of the model in both cases presented the formation of a compressive strut as the load-bearing mechanism of the structure. Following this, the non-linearity of steel was activated, producing similar results to those of the model which considered solely the non-linearity of concrete. This indicated that the non-linearity of steel does not have a significant impact on the capacity of the model as long as the non-linearity of concrete is activated. Thus, the general outcome so far from the investigation was that the nonlinear behavior of concrete is critical, with the compressive strut serving as the primary mechanism for load-bearing capacity. Based on the general conclusion, it was important to investigate the influence of a disconnection (gap, e.i. voids due to incomplete filling of concrete) as an imperfection, in case of possible disruption of the compressive strut. Therefore, various gap sizes, in different locations, were introduced in the model, in order to examine the structure's performance. Subsequently, the gap imperfection was introduced by removing the interface element between the concrete core and the steel plates. This resulted in a lack of actual connection between the two materials, leading to no load transfer. The model was tested with three different disconnection placements: first, a gap was applied to the top left section of the beam; second, it extended along the entire top of the composite beam; third; the disconnection was placed along the bottom line of the composite structure; and finally, it was positioned solely at the bottom right section. The global behavior graph provided significant insights, indicating that as long as the non-linearity of concrete is activated, the gap has little influence on the structure's bearing capacity. The capacity results of the model were similar to those obtained with a poor connection at the horizontal interfaces. The worst-case scenario involved a weak connection at both the horizontal and vertical interfaces (including the webs) of the SCS tunnel, simultaneously with a pre-existing disconnection. This resulted in a significant capacity reduction. The analysis revealed the crucial role of the webs in mitigating this failure. When concrete non-linearity was present and horizontal connections were poor, the strong connected webs helped to maintain some residual capacity. Regardless of the size of the initial disconnection, applying a weak connection at any interface disrupted the compressive strut, leading to structural instability and failure.

Before advancing to the complete cross-section model, the critical points were identified and considered as worst-case scenarios for the investigation. In summary, the model incorporating webs was chosen as the most suitable option for simulating the cross-section tunnel in a real-world context. The analysis with weak connection for both interfaces in parallel with a placed disconnection was confirmed to be the worst-case scenario, and thus the majority of the following analyses were focused on implementing weak connection, as it more accurately represents imperfections or irregularities in the design. Additionally, the non-linearity of concrete and the poor connected webs were identified as the most critical component for structural performance, while the non-linearity of steel did not provide significant additional insights.

*Analysis of the simplified composite beam (Chapter 6) definitively established the webs' critical role in maintaining structural integrity, particularly under conditions of concrete non-linearity and weak horizontal interface connections. Consequently, in the subsequent full cross-section analysis, only the horizontal interfaces were modeled with weak connections; the webs remained fully bonded to assess the independent effect of horizontal interface failure.

The entire cross-section was modeled in detail, incorporating the horizontal and vertical plates based on the dimensions provided from the design calculations. The first step of the investigation mirrored that of the simplified composite beam. The cross-section was subjected to linear static analysis for both strong and weak connection. As expected, the global behavior graphs demonstrated a higher capacity for the full bond connection compared to the slip connection. The bonded connection results in a rigid structure, allowing for less flexibility. In the next stage, the non-linearity of concrete was applied to the fully bonded connections at the interfaces. During the initial phases of the analysis, relatively small displacements were observed, indicating the stability of the structure. However, as the load increased, instability was introduced, leading to larger deformations and displacements. Initially, cracking began at the symmetry axis of the cross-section. As the load continued to increase, cracks appeared at the most critical points of the roof element, specifically at the joints between the roof and the wall, as well at the span. By the final stage of the nonlinear analysis, and before reaching instability and failure, the compressive strut became visible in the boxes located near the joint at the vertical symmetry axis of the roof element. In the following stage of the study, the model was examined using nonlinear concrete and weak connection along the bottom line interface between the concrete core and steel plates. The global behavior graph revealed a significant difference in structural capacity. Specifically, the graph illustrated distinct flat sections, which serve as indicators of periodic slip occurrences. In contrast, the graph representing the bonded connection exhibited a higher capacity than expected, displaying a more consistent and gradual increase in load that lacked the pronounced changes in slope evident in the graph associated with weak connection. This distinction emphasizes the advantages of strong connection in maintaining structural integrity and performance under load. Upon examining the crack-width contour plots, it became clear that cracking propagates gradually from the joints toward the span of the roof element, resulting in elevated tensile stresses. The contour plots demonstrated a direct correlation between the applied load and the increase in crack-width. The significant large crack-width values imply that the weak connection permits movement, which ultimately led to the development of significant cracks. Further analysis of the contour plots displaying compressive stress revealed that the formation of the compressive strut occurred prior to structural failure, demonstrated behavior similar to that seen in the analysis of strong connection interface. As a final step, a similar study was conducted using a weak connection limited to one box adjacent to the middle box (located at the span), which facilitated a comparison of the effects observed at different weak connection locations. This approach provided valuable insights into how the positioning of the slip connection influenced the overall structural performance.

In summary, the global behavior graphs for the finite element models illustrated the critical influence of concrete non-linearity in combination with weak connection on the structural capacity of the SCS design. It was demonstrated a consistent behavior in nonlinear concrete analysis with slip, where cracking began at the joints of the roof element with the walls and advanced toward the span, concluding in the formation of the compressive strut. As slip at the horizontal interfaces increased, the structure's stability and capacity diminished. However, limiting slip to specific areas led (weak connection at 1 single box vs at the bottom line interface of the roof element) to a better performance. While weak connection introduced greater flexibility, it also resulted in large stress concentrations, increasing the likelihood of cracking and crushing of concrete. In contrast, strong connection condition maintained superior stiffness and effective load distribution, thereby limiting the risk of failure. Furthermore, the proper formation and alignment of compressive struts proved to be essential for efficient load transfer within the structure. Misalignment or disruption of the compressive strut caused by the periodic slip led to inefficient load distribution and increased stress concentrations, ultimately compromising the structure's integrity.

* Various nonlinear analyses were performed without interface connection, previously identified as disconnection (gap). Unfortunately, these analyses proved unsuccessful, as the models exhibited instability almost immediately during the initial stages of evaluation. This outcome highlights the importance of shear connectors in the SCS structural design. When there is no effective connection between the concrete core and the steel plates, the overall stability of the structure becomes severely compromised, making it difficult to sustain under load.

Chapter 9

Conclusions and Recommendations

9.1 Conclusions

1. What are the most critical components in SCS tunnel design that contribute significantly to the overall strength, stiffness, and stability of the structure?

   Based on the global behavior graphs subtracted from the finite element analysis with DIANA software, it is obvious that the non-linearity of concrete is a critical factor influencing the structure's load carrying capacity and failure. Specifically, the ranking of importance is based on the two following points:

   - Nonlinear concrete material: The nonlinear behavior of concrete core is the most crucial element impacting the performance of the SCS tunnel. This non-linearity is evident as the concrete starts cracking and crushing under tension and compression, respectively. A key finding was the failure of the compressive strut, the structure's primary load-bearing mechanism, as the concrete's capacity is exceeded. This failure is the ultimate cause of structural instability and collapse.

   - Interface connection: While the horizontal and vertical (webs) steel plates contribute to overall strength, the horizontal interface connection between the concrete core and steel plates is crucial. A strong connection ensures efficient load transfer and even stress distribution. However, imperfections resulting in slip at these horizontal interfaces dramatically reduce load-carrying capacity, especially as the concrete approaches failure. The vertical webs, however, play a vital role in sustaining capacity. When the structure was modeled with fully bonded webs (while concrete non-linearity, weak horizontal connections, and interface disconnections were present), the webs helped to maintain some residual load-bearing capacity. Conversely, when the webs were also poorly connected in a model simulating all these adverse conditions, the structure experienced effectively zero capacity and immediate failure. This reinforces the criticality of the horizontal interface while demonstrating the even greater importance of well-bonded vertical interfaces (webs) for overall structural stability.

2. How are stresses distributed in the roof element of the composite cross-section?

   In the SCS composite tunnel roof element, stresses are distributed according to the strut-and-tie model. High compressive stresses concentrate along diagonal paths within the concrete core, forming

the compressive strut. This diagonal path is the most efficient way to transfer compressive forces. High tensile stresses develop in the directions perpendicular to the compressive strut, primarily resisted by the outer and inner steel plates. Shear stresses are distributed across the shear connectors (studs and stiffeners), transferring shear forces between the steel and the concrete.

The distribution of these stresses is complex and significantly influenced by the different combinations of imperfections applied, including:

- Weak interface connection: The quality of the connection between the steel plates and the concrete core dramatically affects stress distribution. A strong bond promotes efficient load transfer and a uniform stress distribution; however, for both the simplified composite beam and complete cross-section models, weak connection imperfections applied solely at the horizontal interfaces (shear connector imperfections) caused the strut to form but become disrupted. The slip effect misaligned the load transfer direction, resulting in earlier compressive strut failure compared to strong connections.

- Weak interface connection and disconnection: In the simplified model, when disconnection and weak connection were simultaneously applied at both horizontal and vertical interfaces (concrete-web connection), the compressive strut failed to form entirely. The weak connection at the webs proved to be the worst-case scenario, preventing load transfer, and resulting in immediate structural failure.

Finite element analysis (FEA) of the SCS composite tunnel roof element, under the condition of a strong connection between the concrete core and steel plates (i.e., no imperfections), revealed the formation of a well-defined compressive strut within the concrete. This strut efficiently transferred compressive loads. The global load-displacement curve exhibited a smooth increase in load resistance up to failure. Failure of the roof element occurred only when the applied load reached approximately twice the design load for the roof element.

3. What are the governing bearing mechanism and global failure mechanisms of the structure?

The **bearing mechanism** is the load-carrying factor that ensures the stability and integrity of a structure. Thus, whatever serves as a load path could be considered the bearing mechanism. The load paths for this composite structure are proven to be the compressive struts and shear connectors. The formation of the compressive struts within the concrete core act as a load path that transfers the compressive forces through the structure, while the shear connectors are responsible for the shear load transfer and ensure a strong bond between the steel plates and the concrete core. The **global failure mechanisms** for this composite structure vary depending on the interface connection and the presence of non-linearity in the concrete.

- Non-linear concrete with strong connection at the interface: When non-linear concrete behavior is considered with a bonded interface, the compressive struts, which are crucial for transferring compressive forces, can fail. This failure occurs due to the disruption and misalignment of the compressive struts, triggered by the combined effects of the high compressive stresses developed and the severe cracking within the structure. The failure of the compressive struts leads to an inability to effectively transfer compressive forces, resulting in structural instability. Importantly, even in an idealized scenario with a perfectly bonded interface, the primary failure mechanism observed was the failure of the compressive strut. This highlights the significant role of the compressive strut in load transfer, irrespective of the interface connection quality.

- Non-linear concrete with weak connection at the interface: In scenarios where non-linear con-

crete is combined with a weak connection at the interface, the structure shows a significant reduction in capacity and a distinct failure mode. The models with slip experience failure when the slip has disrupted the compressive struts, leading to extensive cracking within the concrete core and inability to sustain the compressive forces. While the capacity is significantly reduced with a weak connection, the ultimate failure mode remained consistent—the failure or disruption of the compressive strut. Although the weak connection resulted in a more gradual failure, with larger displacements before ultimate failure, it ultimately still resulted in compressive strut failure. This observation reinforces the conclusion that compressive strut integrity is paramount to overall structural performance.

  - Compressive strut mobilization: Despite the initial failure due to slip, as the load increases, the compressive strut can be mobilized, leading to a temporary recovery period where the stiffness of the structure starts to increase again.

  - Failure due to misalignment: However, the formation of the compressive strut, in combination with the non-linear concrete and the existing severe cracking, ultimately leads to its disruption and misalignment, resulting in its failure and the inability to effectively transfer the load.

- Influence of web connections: The addition of weak connections at the vertical webs (vertical interface slip) proved to be the worst - case scenario, resulting in significantly lower capacity and a more rapid failure. This scenario is, however, not realistic, as it assumes a poorly constructed structure where even the fundamental web connections - integral parts of the design, typically bonded to the concrete core without shear connectors - fail. In a realistic design, the webs would typically be strongly bonded to the concrete, thereby providing substantial shear capacity and contributing to load transfer. This makes the pure weak connection scenario at the vertical interface highly unlikely.

  In summary, the primary failure mechanism in the composite structure, regardless of interface connection (strong or weak) at the horizontal interface, is consistently the failure or disruption of the compressive strut due to nonlinear concrete behavior. The model with slip at only the vertical webs, though showing significantly lower capacity and more rapid failure, is not representative of real-world construction practices. Therefore, the focus should remain on designing to maintain the integrity and functionality of the compressive struts within the concrete core to prevent structural failure.

4. How does the presence of shear connectors influence the structure in case of disconnections (gaps)?

   The shear connectors, primarily referring to the horizontal interface connection between the concrete core and steel plates, significantly influence the structure's behavior in the presence of gaps (disconnections). The impact depends on the type of connection:

   - Strong interface connection, disconnection present: Even with a strong bond, a gap reduces the load-carrying capacity. The structure remains stable due to redundancy, but the reduction in capacity is notable. The degree of reduction depends on the size and location of the gap, with larger, more extensive gaps resulting in more significant capacity loss.

   - Weak interface, disconnection present (worst-case scenario): This represents the most critical scenario. The combination of a weak interface (slip) and a gap results in a dramatic reduction in capacity and often leads to near-immediate failure. The structure has significantly reduced load-bearing capacity and exhibits instability under load.

- Weak horizontal interface, strong vertical interface, disconnection present: This scenario highlights the critical role of horizontal connections. A strong vertical interface connection (full bond), even with a weak horizontal interface and gap, improves the structural response, maintaining some capacity. However, the capacity is still significantly reduced compared to a fully bonded model without a gap, emphasizing the essential contribution of horizontal interface strength.

The presence of disconnections (gaps) at horizontal interfaces (regardless of their location and size), particularly when combined with weak interface connections (slip), severely compromises the capacity and stability of SCS immersed tunnels. Figure 6.42 shows that the simultaneous occurrence of both weak connections and disconnections (e.g. model with gap at the top line - bond) reduces the capacity by approximately 47% compared to a model with only disconnections and strong interface connections. Consequently, it can be concluded that the presence of both types of imperfections - disconnections and weak connections - negatively impacts the stability of the structure, with each imperfection influencing and exacerbating the effects of the other. Therefore, strong horizontal interface connections are crucial for reliable performance. While vertical steel plates (webs) enhance capacity, they do not fully compensate for the detrimental effects of weak horizontal connections and disconnections.

5. To what extent the interface irregularities between the steel plates (weak connection) and the concrete core influence the strength level of the structure? Is it insignificant?

   - Horizontal interface irregularities: The irregularities at the horizontal interface between the steel plates and the concrete core significantly impact the structural integrity and load-carrying capacity of the system. Based on the global behavior graph presented in figure 7.54, it is evident that a weak connection along the entire top line interface (indicated by the purple line) leads to a substantial reduction in load-carrying capacity. In contrast, a localized imperfection in the interface connection - specifically, the connection in one box between the middle span and the joint of the roof element (represented by the red line) - demonstrates less immediate impact.

     The global behavior graph shows that the strong connection model utilizing nonlinear concrete achieves a peak load of approximately 150 kN/m. In comparison, the weak connection at the bottom line interface (yellow line), also with nonlinear concrete, reaches a peak load of about 85 kN/m, resulting in a significant reduction of 43,33% in load-carrying capacity. The localized weak connection in one box between the joint and the middle span of the roof element (red line) exhibits a peak load of approximately 115 kN/m, which signifies a less pronounced reduction in capacity of 23,33% compared to the bottom line weak connection.

     When analyzing the model with a weak connection at the middle box of the roof element, a peak load of around 55 kN/m is observed. This indicates a 23,33% reduction in capacity compared to the strong connection scenario and a 52,8% reduction relative to the weak connection across the entire bottom line interface. This comparison emphasizes the detrimental effect of interface slip or gap on the structure's load-carrying capability.

     The lowest capacity occurs when the weak connection is applied along the entire top line of the roof element, where loads are directly applied. This results in a reduction of 73,33% when compared to the nonlinear model with no interface irregularities and a 65,3% reduction in comparison to the optimal weak connection model (illustrated by the red line graph for the box between the middle span and the left edge of the roof element). As anticipated, the model with a strong connection exhibits the highest load - carrying capacity. As slip is introduced - whether along the bottom line interface or in localized regions—the capacity declines significantly.

- Vertical interface irregularities: Concerning the irregularities in the interface connection between the concrete core and the webs, it was noted that the analysis could not proceed due to instability issues when a weak connection was applied. Therefore, it is consistent with the conclusions drawn from the analysis of the SCS composite beam that the webs are critical components in the design.

In summary, the analysis reveals that irregularities in the interface connections between the steel plates and the concrete core significantly reduce the structural load-carrying capacity, particularly at the top line interfaces where the load is directly applied. The reduction percentages indicate that these irregularities have a substantial impact, especially when they occur between the concrete and the webs, which are crucial components of the design that contribute greatly to the overall stability of the structure.

Based on the answers on the sub-questions the main research question of the master thesis can be answered as follow:

"How do the irregularities produced during the different construction phases affect the local and global behavior of the composite cross section?"

Construction irregularities significantly affect both the local and global behavior of the SCS composite cross -section. These effects are primarily driven by two factors:

1. Nonlinear concrete behavior: Imperfections worsen the inherent non-linearity of concrete. Stress concentrations around disconnections (gaps) lead to premature cracking and crushing, disrupting the compressive strut – the primary load-carrying mechanism – and causing significant reductions in overall capacity.

2. Interface connection integrity: Imperfections at the interfaces between the steel plates and the concrete core severely compromise load transfer. Weak horizontal connections (slip) significantly reduce capacity, especially in the presence of disconnections (gaps). While strong vertical connections (webs) enhance stability, they cannot fully compensate for poor horizontal connections.

The combination of these factors leads to a complex interaction of localized and global effects. Localized effects include stress concentrations and cracking around imperfections. Global effects include reduced load-carrying capacity, increased deflections, and instability. The severity of these impacts depends on both types of irregularities. The worst - case scenario involves a combination of concrete non-linearity, weak horizontal interfaces, and disconnections at these interfaces. The weak connection applied on the vertical interfaces is the most critical in terms of reduced capacity and immediate failure of the structure, but unrealistic and not practically possible in terms of construction.

9.2 Recommendations

1. Refine design based on compressive strut behavior: The thesis highlights the compressive strut within the concrete core as the primary load-carrying mechanism. Future designs should explicitly consider the formation and integrity of this strut. This requires a deeper understanding of the stress - strain behavior of the concrete under complex loading conditions, as well as techniques to mitigate strut disruption due to cracking or crushing. This might involve optimizing concrete mix designs, reinforcement patterns, or the use of high-strength materials.

2. Incorporate webs strategically: While the investigations shows that webs (vertical steel plates) en-

hance the structural capacity and stability, especially when horizontal interface connections are compromised, it is crucial to ensure strong connections between the webs and both the horizontal steel plates and the concrete core. This would require careful detailing and strong design procedures for the web connections. Analysis needs to ensure that webs are properly incorporated to maximize their capacity-enhancing effect.

3. Prioritize strong horizontal interface connections: The thesis strongly emphasizes the critical role of the horizontal interface connection between the steel plates and concrete core. Design and construction practices should prioritize strong connections to ensure effective load transfer and prevent slip, even under nonlinear concrete behavior. This could involve improved detailing of shear connectors, stricter quality control during construction, and the use of high-performance materials to enhance bond strength.

4. Further development of FEM model and experimental studies: The research on SCS sandwich immersed tunnels should explore more sophisticated FEM models to improve the simulation of complex phenomena such as crack propagation, the interaction between concrete and steel, compressive strut formations, and the impact of localized stress concentrations. In addition, it should be conducted further experimental investigation on a representative specimen of an SCS composite beam (including webs) subjected to various loading conditions. This will provide important data to validate the numerical models and improve design parameters, especially regarding the behavior of the compressive strut and the influence of interface imperfections on overall structural performance.

These recommendations aim to improve the design and construction of SCS immersed tunnels, mitigating the risks identified by the thesis and leading to a more reliable and efficient design.

Appendix A

Small beam analysis - Sensitivity study - Appendix

In the preceding chapters, it was developed a design for a "Base Case" of an SCS tunnel. To gain a comprehensive understanding of the structural behavior under various loading conditions, it is crucial to employ a finite element model (FEM). Initially, a small beam —part of the cross section — will be designed and analyzed using both linear and nonlinear methods. By examining a simplified model, it becomes easier to understand and analyze the entire 2D cross-section model, which is inherently more complex. The chosen finite element analysis (FEA) program is DIANA. The dimensions from the previously designed "Case Study" of the SCS sandwich tunnel will serve as input for this model. DIANA is capable of both linear and nonlinear structural analyses. Before diving into the actual modeling within DIANA, it will be thoroughly studied the fundamentals of FEM analysis, linear analysis, and nonlinear analysis.

A.1 Dimensions of the simplified model - small beam

The simplified model for analysis will consist of a small composite beam with a length of 5 meters, representing the roof component of the tunnel. This composite beam will be constructed using steel plates and concrete, mirroring the original design for the entire cross section. The table below explicitly depicts the dimensions of the simplified model.

Dimensions	m
Length	5,0
Concrete core height	1,045
Top steel plate height	0,025
Bottom steel plate height	0,035
Thickness	1,0

Table A.1: Small beam dimensions

To accurately model the connections between the steel plates and the concrete core, which are joined together using stiffeners and studs, interface elements will be incorporated. The analysis of this simplified model will involve both linear and nonlinear methods. Through this analysis, it is aimed a better understanding of the behavior of each material and validation of its performance.

A.2 Material model

This chapter will detail the selected material models available in finite element programs' databases, which are capable of replicating the response of materials under specific load conditions. Additionally, the rationale for selecting these particular models will be elucidated.

A.2.1 Concrete behavior

Concrete exhibits remarkable performance in compression due to its high compressive strength. It is commonly used in construction projects where the primary forces are compressive. However, concrete's performance in tension is relatively weaker. When subjected to pulling or stretching forces, concrete tends to crack and deform. The main concrete failure modes are divided in the following:

- In compression, concrete fails due to crushing of the material. The stress distribution is relatively uniform across the section.
- In tension, concrete fails due to cracking. The stress concentration occurs at the crack tip, leading to localized failure.

Stress-Strain Curve for Concrete

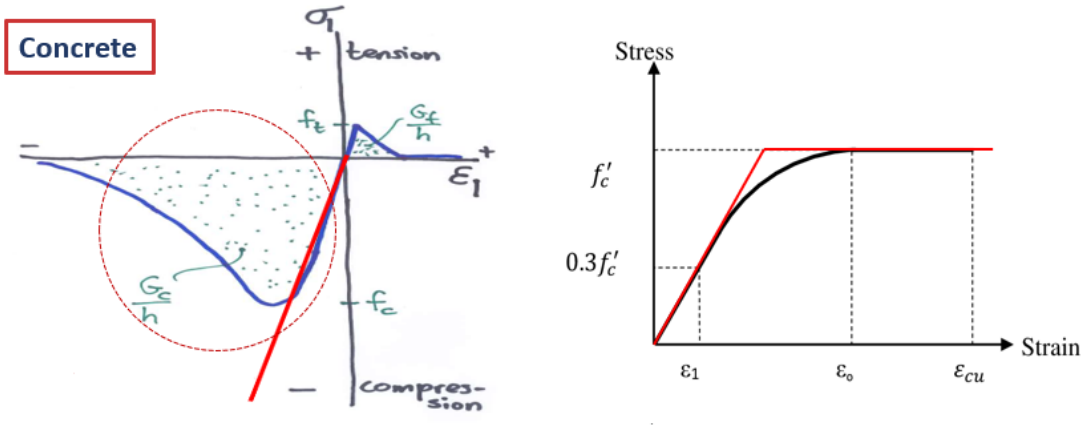

Figure A.1: Concrete behaviour

The stress-strain curve for concrete shows how stress (force per unit area) changes with strain (deformation). In compression, concrete exhibits a linear elastic behavior up to a certain point (proportional limit), after which it starts to exhibit non-linear behavior due to microcracking and aggregate interlock. The ulti-

mate compressive strength is reached at the peak stress. In tension, concrete behaves differently, showing a brittle response with little or no plastic deformation before failure.

Thus, in case of a normal beam, two zones generally arise: the compression zone at the top and the tension zone at the bottom. The strength of concrete is often ignored in the tension zone compared to the compression zone. However, for this model it is important to take into account the tension part in order to understand the relation between the core and the steel connectors. The assumption for the analytical method for the small beam analysis is based on neglecting the parabolic behavior in the compression zone and considering the idealized graph which is depicted on the right. However, for the modeling part it is significant to take into account the original strain stress curve relationship of the concrete shown on the left. For the self-compacting concrete class which will be applied to the SCS sandwich element is class C35. The elasticity modulus of concrete applied for the SCS beam is $E_{cm} = 35000N/mm^2$. For the Poisson's ratio a value v = 0,2 is applied.

A.2.2 Steel behavior

Steel material exhibits different behaviors under compression and tension. When subjected to tension, steel elongates, and the ratio of applied force to cross-sectional area is called tensile stress. Young's modulus measures the material's stiffness. In compression, steel shortens, and the stress-strain relationship is similar but with opposite signs.

The stress-strain curve for steel shows how stress (force per unit area) changes with strain (deformation). In tension, steel exhibits a linear elastic behavior up to a certain point (proportional limit), after which it starts to exhibit non-linear behavior. The ultimate tensile strength is reached at the peak stress. In compression, steel behaves similarly but with higher compressive strength.

Stress-Strain Curve for Steel

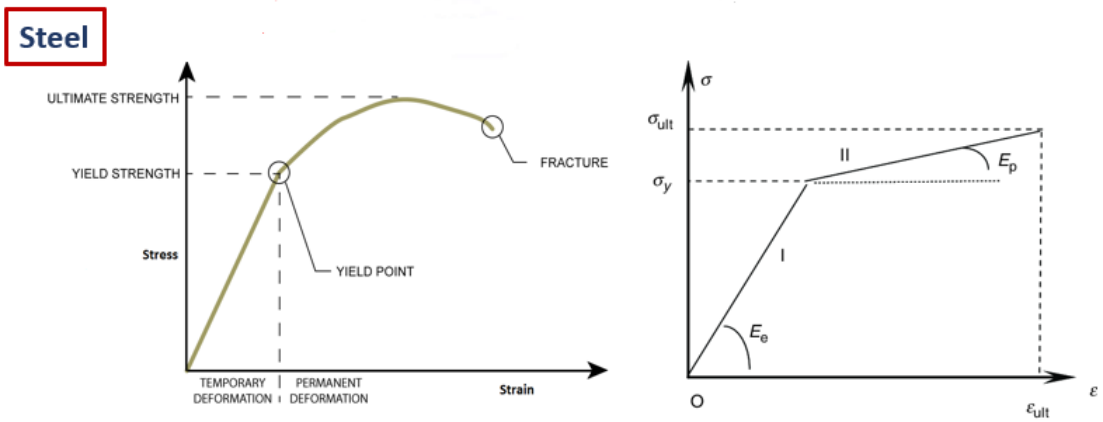

Figure A.2: Steel behaviour

Steel class S355 will be used for the model of the composite small beam for the plates, stiffeners and studs. The elasticity modulus applied for the linear domain of steel is $E_s = 210000N/mm^2$. Poisson's ratio v= 0,2

will be applied.

A.2.3 Interface between concrete and steel plates

The interface between concrete and steel in the finite element model (FEM) plays a crucial role in simulating the behavior of the composite structure, especially when considering stiffeners and stud connections, as it is in this case study of the small beam.

- **Steel-Concrete Composite Beams**
  The design of a steel-concrete composite beam is widely used in civil engineering due to its high bearing capacity, stiffness, and seismic performance. However, during bending, interface sliding occurs between the steel beam and the concrete slab of the composite beam. This sliding reduces the effective combination between the components.To address this, shear connectors are introduced to resist relative slip and vertical lifting at the interface, ensuring that the components work together.

- **Shear Connection Degree**
  The shear connection degree of a steel-concrete composite beam quantifies the interaction between the steel beam and the concrete slab. While it is often assumed experimentally that the connection is infinitely stiff, partial interaction will occur in the composite beam to some extent.

- **Finite Element Modeling (FEM)**
  Finite element modeling allows us to simulate the static performance of the composite beam, including the behavior at the steel-concrete interface. As it will be explained later on, due to this simulation it is easier to obtain a detailed insight of the connection's performance between the concrete core and the steel plates.

A.3 Determination of stiffness

As there was emphasized in the preliminary study of this research project, the ultimate strength of SCS composite sandwich elements depends on the strength and ductility of the shear connection. The gap imperfection which may occur after the different loading phases may lead to failure. Thus, it is needed an investigation of the gap range that the interface's connection can sustain. In order to simulate as accurately as possible this imperfection there should be calculated the required stiffness between the steel plates and the concrete core. The approach that has been used to determine the shear stiffness of the connection is described analytically below.

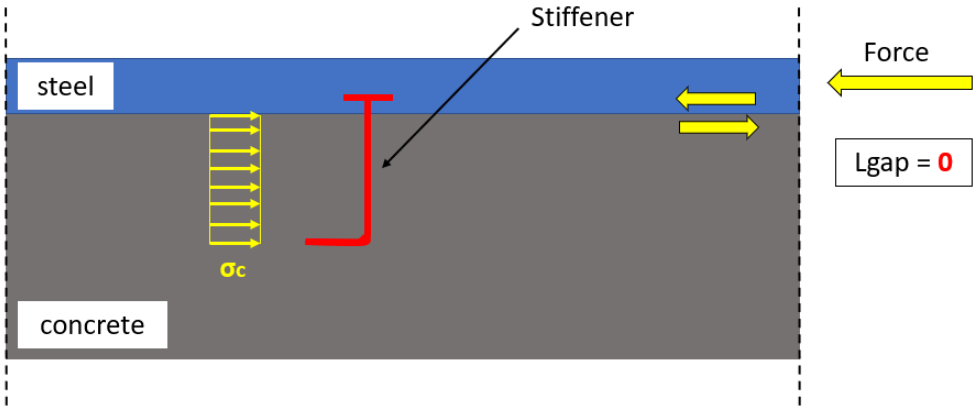

Figure A.3: Cross section without gap

The analytical problem is divided in two phases, the cross section without and with a gap. In figure A.3 is presented the cross section without the schematization of a gap. In the case of an applied horizontal force and a gap length equal to 0 it is reasonably assumed a uniform distribution of stressed on the stiffener in order to maintain equilibrium in the cross section. The same theory applies for the studs which are normally placed between the stiffeners. However, in case of a schematization of a gap between the steel plate and the concrete core, the stress distribution is assumed differently. The figure below presents the distribution which was taken into account for the equilibrium of the cross section with Lgap $\neq 0$.

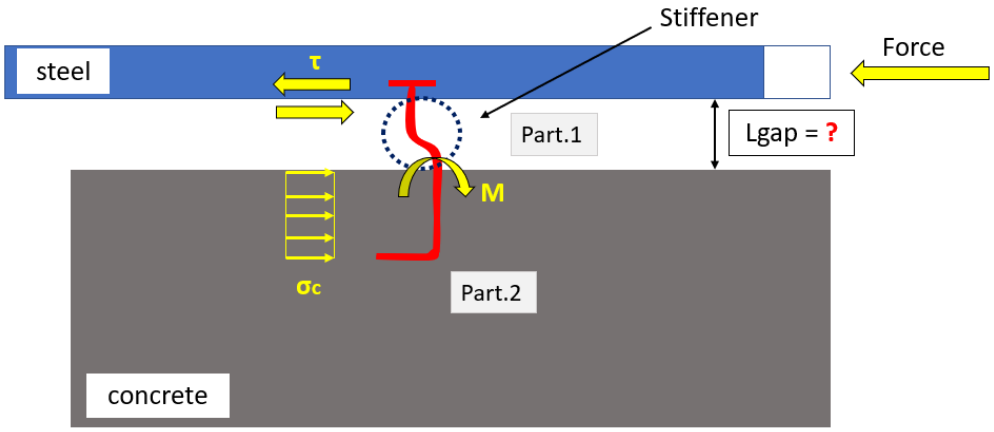

Figure A.4: Cross section with gap

The horizontal applied force is transmitted to the interface connection as a shear force. This shear force induces deformation in the portion of the stiffener located between the steel plate and the concrete core gap. Additionally, the shear force generates a bending moment in the section that remains within the concrete core due to eccentricity. These components are analytically described in the figure below.

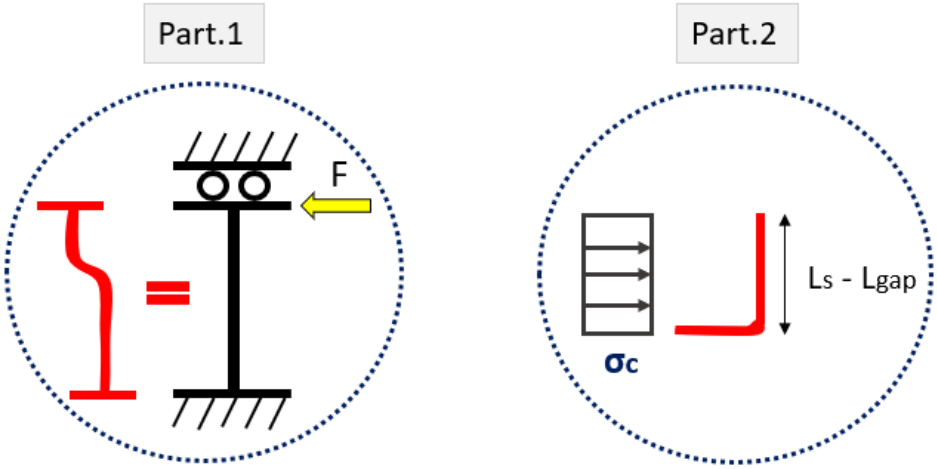

Figure A.5: Part.1, Part.2 of stiffener

Part 1 can be represented by a simply supported beam, with a sliding support at the top end where the shear force is applied, and a fixed support at the end embedded in the concrete. As a result, motion is restricted. On the other hand, Part 2 corresponds to the portion of the stiffener that remains within the concrete. It is expected to experience minimal deformation and a uniform linear stress distribution. While the ideal stress distribution should be triangular for greater accuracy, assuming an orthogonal distribution provides a conservative estimate and yields a wider range of results.

Based on these two cases, the failure mechanisms due to shear in the gap are yielding of steel and crushing of concrete. To calculate the stiffness of the connection, we need to determine analytically the stiffness separately due to yielding and crushing. Additionally, for the normal direction of the cross-section, it is important to calculate the normal stiffness based on Hooke's Law. The following section provides a detailed description of the procedure used to determine each stiffness component. (The procedure is followed for both studs and stiffeners.)

A.3.1 Stiffness due to shear failure mechanism of yielding steel

The determination of stiffness due to yielding of steel primarily relies on Hooke's Law and the theory of Von Mises.

$$F = k_{yielding} \times u$$

$$\sigma_{VonMises} = \sqrt{\sigma_M^2 + 3\tau^2}$$

Solving the equations based on Part.1 of the analytical problem yields a final equation for the bending moment and the applied shear force. To determine the stiffness matrix for the small section of the stiffener (or stud) between the steel plate and the concrete core gap, we apply a unit load at the top end of the supported beam in Part.1. Thus, the stiffness matrix for u_2=1 that it is obtained is the following:

$$\boldsymbol{k_{yielding}} = \begin{bmatrix} \frac{12EI}{L^3} & \frac{6EI}{L^2} & -\frac{12EI}{L^3} & \frac{6EI}{L^2} \\ \frac{6EI}{L^2} & \frac{4EI}{L} & -\frac{6EI}{L^2} & \frac{2EI}{L} \\ -\frac{12EI}{L^3} & -\frac{6EI}{L^2} & \frac{12EI}{L^3} & -\frac{6EI}{L^2} \\ \frac{6EI}{L^2} & \frac{2EI}{L} & -\frac{6EI}{L^2} & \frac{4EI}{L} \end{bmatrix} \quad and \quad \boldsymbol{F} = \begin{bmatrix} \mathrm{F}_1 \\ \mathrm{M}_1 \\ \mathrm{F}_2 \\ \mathrm{M}_2 \end{bmatrix}, \ \boldsymbol{u} = \begin{bmatrix} \mathrm{u}_1 \\ \theta_1 \\ \mathrm{u}_2 \\ \theta_2 \end{bmatrix}$$

Next, we use the Hooke's Law equation to solve for the applied horizontal force F and bending moment M. It is:

$$\begin{bmatrix} \mathbf{F_1} \\ \mathbf{M_1} \\ \mathbf{F_2} \\ \mathbf{M_2} \end{bmatrix} = \begin{bmatrix} \frac{12EI}{L^3} \\ \frac{6EI}{L^2} \\ -\frac{12EI}{L^3} \\ \frac{6EI}{L^2} \end{bmatrix}$$

Combining these two final equations provides the relationship between the bending moment and the applied horizontal force, F.

$$\boldsymbol{F} = \frac{12EI}{L^3}$$

and

$$\boldsymbol{M} = \frac{6EI}{L^2}$$

By substituting the one into the other it is obtained the following relation: $M = 0,5 \times F$.

By considering the bending stress $\sigma_M = \frac{M}{W}$, shear stress $\tau = \frac{V}{A}$, and equating $F = V$ with the shear force, V, it is obtained a relation for the Von Mises stress, which is depending on the displacement du, and the ultimate yielding stress of steel which is concluded as: $\sigma_{VonMises}(du) \leq \sigma_{yielding}$. Finally, it can be derived the yielding force for a stiffener with a varying Lgap and the stiffness can be described by the formula:

$$\boldsymbol{k_{\text{yielding}}} = \frac{\tau}{du}$$

where du represents the displacement.

Thus, based on the a distribution of a stiffener every 500 mm, in 1000 mm there are going to be located 2 stiffeners. So, the final shear force calculared is presented on the following table where there are also depicted the results of the maximum stiffener's capacity and its displacement based on the rspective gap length.

Stiffener L 150 x 150 x 15 [mm] & Stud 20 $\boldsymbol{\phi}$ - 80 mm

In this paragraph will be presented an example of the analytical calculation of the yielding stiffness for Lgap = 10 mm.

Stiffener dimensions		
Thickness	15	mm
Area	15000	mm^2
Es	210000	N/mm^2
Moment of inertia	281250,00	mm^4
Section modulus	137500,00	mm^3

Table A.2: L shape stiffener 150 X 150 X 15 mm

Stud dimensions		
Diameter	20	mm
Area	314,16	mm^2
Es	210000	N/mm^2
Moment of inertia	7853,98	mm^4
Section modulus	785,40	mm^3

Table A.3: Stud 20 $\boldsymbol{\phi}$ - 80 mm

Based on the a distribution of a stiffener every 500 mm, in 1000 mm there are going to be located 2 stiffeners. So, the final shear force calculated is presented on the following table A.4 where there are also depicted the maximum capacity for a stiffener, the respective displacement and finally the total shear capacity for the n number of stiffeners placed every 1000 mm in the cross section.

$L_{gap}[mm]$	$F_{stiffener}[N]$	$du[mm]$	$V_{total,stiffener}[N]$
0,0001	214,799	1E-13	4,296
10	2466218,186	3,4797E-03	4,932
20	1496937,664	0,0169	2,9939
30	1044836,204	0,0398	2,0897
40	797155,624	0,0720	1,5943
50	64297,354	0,1134	1,2859

Table A.4: Stiffener's results for length range 0 to 50 mm

In Table A.5 is presented the maximum capacity for a stud and its respective displacement, as well as the final total shear capacity for the total number n of studs placed every 1000 mm in the cross section. The distribution of studs is 250 mm / 1000 mm.

$L_{gap}[mm]$	$F_{stud}[N]$	$du[mm]$	$V_{total,stud}[N]$
0,0001	4498,745	2E-19	719799,2
10	51652,353	0,0026	826437,6
20	31351,789	0,0127	2559330,0
30	21882,998	0,0299	178636,7
40	16695,588	0,0539	136290,5
50	13465,439	0,0851	109922,0

Table A.5: Stud's results for length range 0 to 50 mm

Figure A.6 describes graphically the capacities for n stiffeners and n studs for a 1000 mm width/length of cross section.

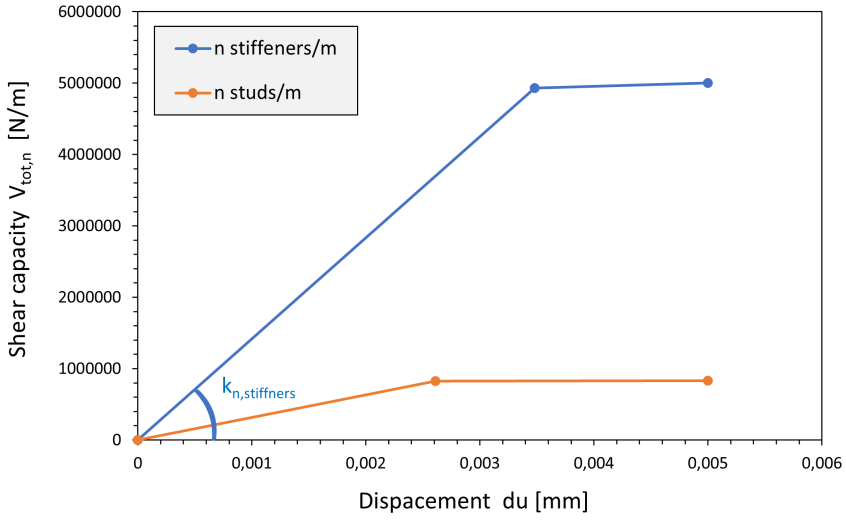

Figure A.6: Capacities of the connectors

However, to determine the final stiffness for use in the finite element simulation of the connection's interface, there are several additional steps to follow. Specifically, we need to merge the two graphs into one and define two distinct yielding points. In reality, either the stiffener or the stud connector will fail first, so it is crucial to investigate which one is responsible for the initial yielding point.

For the actual solution of the analytical problem, we require a formula that combines both yielding points. Based on the tables provided for each capacity for a 10 mm gap length, it is observed that the total number of connectors' capacity governing is primarily determined by the studs. Therefore, the first yielding point corresponds to the studs. As for yielding point 2, it will be the summation of the total capacities of all the connectors. Analytically, yielding point 2 can be expressed as follows:

$$V_{yieldingpoint_1} = n_{stiff} F(du_{stiffener})_{stiffener} + n_{stud} F(du_{stud})_{stud}$$

or

$$V_{yieldingpoint_1} = V(du_{stiffener})_{total,stiffener} + V(du_{stud})_{total,stud}$$

Yielding point 1 corresponds to the governing capacity connector (lowest total shear capacity). Since the studs have a lower yielding point, we will substitute the corresponding displacement into the same formula used for the stiffeners. Specifically, we consider the total number of studs yielding for the same 10 mm gap length. The formula to be used is as follows:

$$V_{yieldingpoint_2} = V(du_{stud})_{total,stiffener} + V(du_{stud})_{total,stud}$$

Table A.6 presents the results for both yielding points across a gap length range from 0 mm to 50 mm. These yielding points are crucial for characterizing the behavior of the connection. Specifically, the graphical example is focused on the gap length of 10 mm, which is depicted in Figure A.7.

	Yielding Point 1		**Yielding Point 2**	
$L_{gap}[mm]$	$\tau_1[N/mm^2]$	$du_1[mm]$	$\tau_{total} = \tau_2[N/mm^2]$	$du_2[mm]$
0,0001	0,3942	2E-19	0,5016	1E-13
10	4,5258	0,0026	5,7589	0,0035
20	2,5013	0,0127	3,2498	0,0169
30	1,7459	0,0299	2,2683	0,0398
40	1,3320	0,0540	1,7306	0,0720
50	1,0743	0,0851	1,3958	0,1134

Table A.6: Total stiffness

In order to calculate the final stiffness which is going to be used as an input for the finite element small beam model it is used the following formula:

$$k_{yielding} = \frac{\tau_1}{du_1}$$

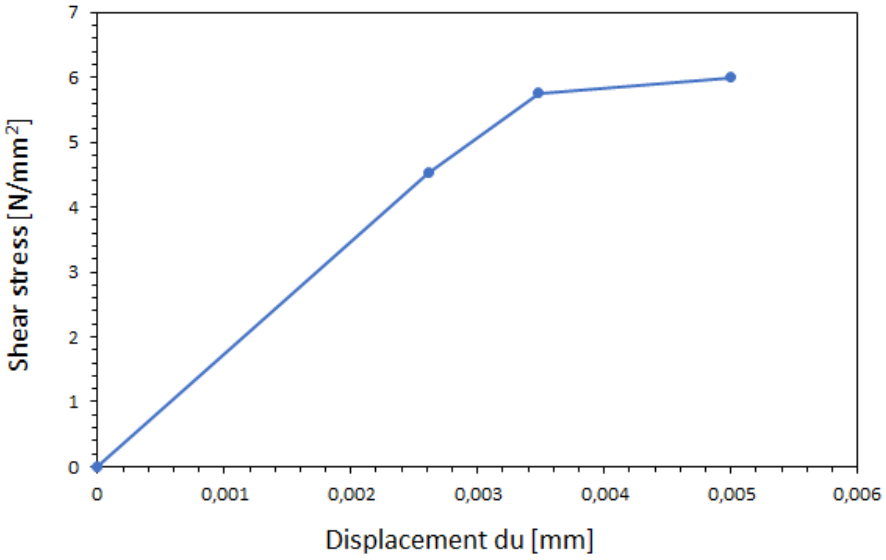

Figure A.7: Shear capacity of the connection

A.3.2 Stiffness due to shear failure mechanism of crushing concrete

The determination of stiffness due to concrete crushing primarily relies on the following formula: $\sigma = \frac{F}{A}$. Based on the stress distribution in Part.2 and the requirement for equilibrium in the remaining section of the stiffener or the stud it is aimed to achieve the relation: $\sigma_c \leq f_{cd}$. Here f_{cd} represents the compressive design strength of concrete. By combining these equations and solving for the force (F), using varying gap lengths (Lgap), it is obtained a range of different forces due to crushing, denoted as $\sigma_{crushing}$. Finally, the crushing stiffness can be expressed as:

$$k_{\mathbf{crushing}} = \frac{\sigma_{F_{\mathbf{crushing}}}}{du}$$

where du represents the displacement.

A.3.3 Normal stiffness

The determination of normal stiffness relies completely on Hooke's law formula: $\sigma_n = E \times \epsilon$. Thus, based on the formula of strain which is described as: $\epsilon = \frac{E \times dL}{L}$, where E is the modulus of elasticity, dL is the change in length of the cross section and L the original length. By combining these two formulas it is concluded the following relation:

$$\sigma_n = \frac{E_c \times du}{t_{slab}}$$

which leads to the equation of the normal stiffness:

$$k_{normal} = \frac{\sigma_n}{du}$$

A.4 Schematization of the small beam model

Since the whole cross -section model will perform linear and nonlinear elastic analysis the computation time is limited. Thus the schematizaton of the small beam model will is needed in order to have a better and clearer idea of its behavior. One of the aspects that will be covered first is the modelling process that has been followed.

A.4.1 Geometry

The geometry of the small beam is described in the following figure. The table 6.1 above presents the dimensions of the model.

A.4.2 Boundary conditions

The small beam model represents the behavior of a fixed-end supported beam. In this model, constraints are applied exclusively at the left end. Specifically, two distinct support cases are implemented, as depicted in Figure A.8. The first case involves constraining vertical displacements along the entire left edge of the beam, while the second case focuses on constraining three specific points along that edge. As shown in Figure A.9, the horizontal displacements of the top, middle, and bottom points of the beam are subject to constraint.

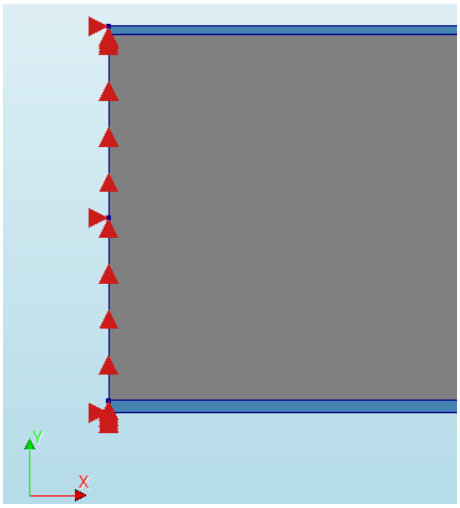

Figure A.8: Support case 1 & 2

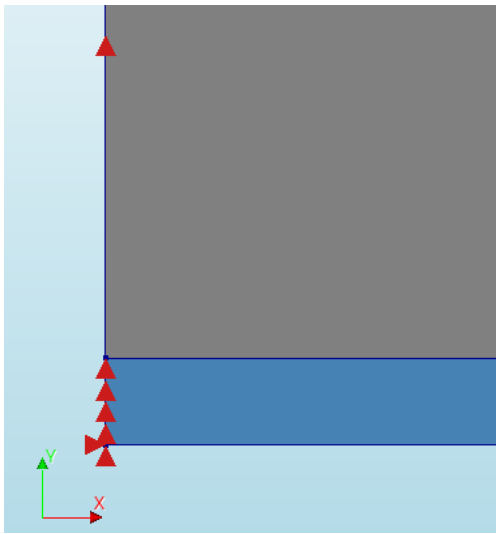

Figure A.9: Horizontal displacement constraint of bottom point

Figure A.10: Constraints small beam model

A.4.3 Tyings

As discussed in section A.2.3, accurately simulating the connection between steel plates and the concrete core requires the use of interface elements. In DIANA software, we achieve this connection through tyings. Tyings represent linear dependencies between nodal variables. Specifically, a tying consists of a degree of freedom in a master node and one or more degrees of freedom in slave nodes. For our small beam model, it is employed multi-point tyings in two categories:

- **Vertical Edge Tying**
  It is applied to the right vertical edge of the beam. The aim is to ensure a stiff edge and also enable displacement control at the top point of the edge.

- **Horizontal Edge Tyings (top and bottom)**
  It also creates stiff edges which move together, allowing shear deformation of the beam and maintaining solid shear movement.

By using these tyings, we can accurately model the behavior of the steel-concrete connection for the small beam simulation.

A.4.4 Concrete material

For modeling the non-linearity of concrete in finite element analysis, input parameters are derived from both tensile and compressive behavior.

Specifically, the Hordijk graph is selected to represent the tensile behavior, as depicted in the figure A.11 below. For the tensile zone, when concrete is subjected to tensile forces, its behavior is nonlinear due to presence of micro-cracks and the gradual development of micro-cracks. The Hordijk graph illustrates this behavior by showing the stress - strain relationship for concrete in tension. Initially, the stress increases linearly with the strain (elastic behavior). However, as the strain continues to increase, micro-cracks form and propagate, leading to reduction in stiffness (softening behavior). Eventually the concrete reaches its ultimate tensile strength and the micro-cracks become dominant, causing sudden drop in stress (failure).

In compression, concrete exhibits distinct nonlinear behavior, as illustrated in Figure A.12. The stress-strain curve for concrete in compression typically follows a normal distribution, resembling a bell-shaped curve. Initially, as the load increases, the stress rises linearly (representing elastic behavior) until it reaches the peak compressive strength (maximum stress). Beyond this peak, the curve gradually descends due to micro-cracking and material softening (strain hardening). Ultimately, the concrete fails precisely at the point where the stress drops sharply (resulting in rupture or failure).

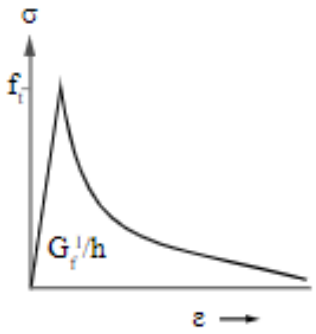

Figure A.11: Tension (Hordijk)

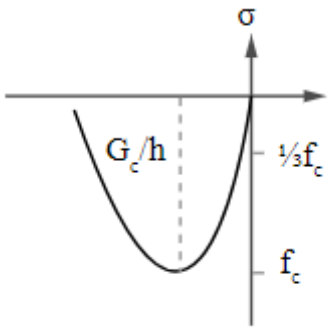

Figure A.12: Compression (Parabolic)

Figure A.13: Nonlinear behavior of concrete

A.4.5 Steel material

In the context of finite element modeling, the input parameters for steel non-linearity are based on the idealized stress-strain curve. Specifically, the chosen curve represents the nonlinear behavior of steel, as

depicted in the figure below.

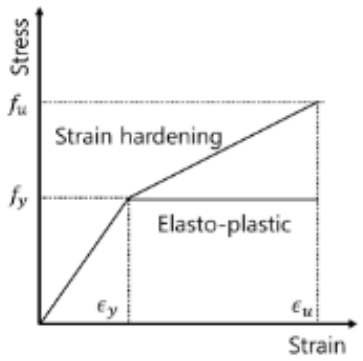

Figure A.14: Nonlinear behavior of steel

The idealized stress-strain curve for nonlinear steel typically consists of several regions. First region is about the elastic part which actually corresponds to the linear behavior of the material. In this region, stress is directly proportional to strain (deformation) according to Hooke's Law. The slope of this linear portion represents the material's elastic modulus (stiffness). Next region is about the yielding point and the plastic deformation. Specifically, beyond the elastic limit, steel enters the plastic deformation range. The yield point is where permanent deformation begins, and the material no longer returns to its original shape after unloading. In this region, the stress-strain curve becomes nonlinear due to dislocation movement and rearrangement within the crystal lattice. Following region is about the strain hardening of steel. As strain continues to increase, steel undergoes strain hardening. The curve steepens, indicating that additional force is required to achieve further deformation. Strain hardening occurs due to dislocation interactions and material strengthening. The peak of the stress-strain curve represents the ultimate tensile strength region. At this point, steel reaches its maximum strength before necking or localized deformation occurs.

A.4.6 Interface material

As previously mentioned, to apply the interface material, it is needed to solve the analytical model for the stiffeners and stud connectors. Based on the solution presented earlier and considering the graph in Figure A.7, it becomes crucial to use this solution as an input function in the small beam model. For the interface material, we have chosen a type of 2D line interface with the following properties: normal stiffness modulus-y $k_{normal} = \frac{\sigma_n}{du} = 33653.8\ N/mm^3$ and a shear stiffness modulus-x $k_{yielding} = \frac{\tau_1}{du_1} = 1734.17\ N/mm^3$. The function describing the non-linearity of the material is presented in the table below.

Shear relative displacement [mm]	Shear traction [N/mm^2]
-500	-6
-0.00347967	-5.75887
-0.00260976	-4.52576
0	0
0.00260976	4.52576
0.00347967	5.75887
500	6

Table A.7: Nonlinear interface function input

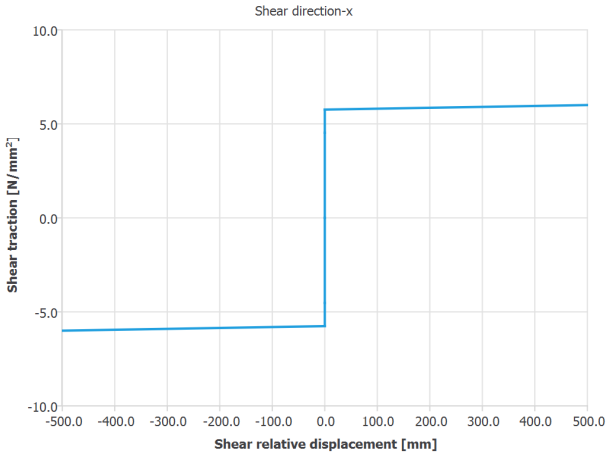

Figure A.15: Interface function input

A.4.7 Meshing

In order to ensure accurate simulations, computational efficiency, and consistent results, selecting an appropriate mesh is crucial. For this project, quadratic mesh types and quadratic mesh order are used. Specifically, for the interfaces is used CL12I element type, and the concrete core and steel plates are used both CQ16M and CT12M elements (figure A.12).

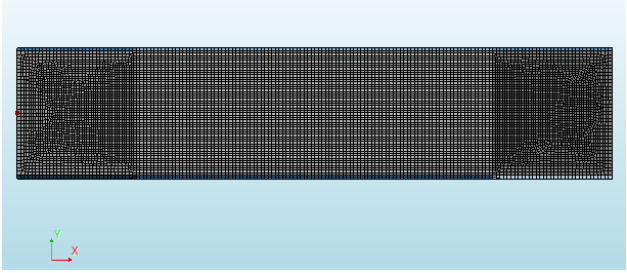

Figure A.16: Small beam mesh

A.4.8 Loads

The small beam model will undergo evaluation under two distinct load cases. In the first case, we apply a bending moment, utilizing only the vertical interface mentioned earlier. This approach ensures accurate representation of bending deformation. In the second case, we introduce shear load based on the incorporated horizontal tying (interfaces) that were mentioned before in section A.4.3. The desired deformations are illustrated in the following figure.

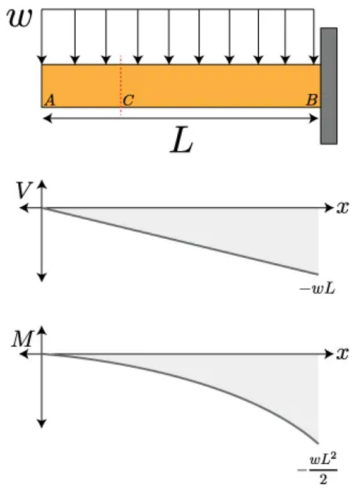

Figure A.17: Shear and bending deformation of the small beam

The loads are applied, as mentioned before, with displacement control on the right end of the beam at the top point. Specifically it is applied a vertical displacement of 20 mm. In order to apply this displacement it is important to constrain the vertical direction on the top point of application.

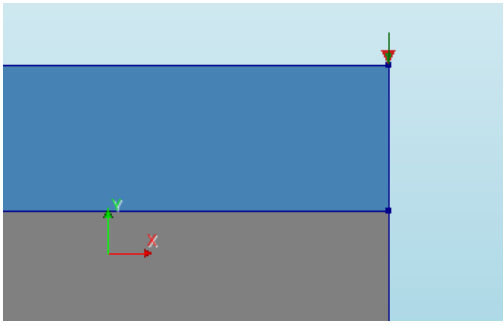

Figure A.18: Displacement control - Applied vertical displacement

With displacement control, it is prescribed the displacement (movement) of at specific degree of freedom (DOF) at a reference point in the structure. As the analysis progresses, the software incrementally applies the proscribed displacement to achieve equilibrium. This method is particularly useful for models with nonlinear responses like the small beam case of the composite tunnel.

A.4.9 Results & Conclusions

To gain insight into the behavior of each load case for varying gap sizes in the small beam model, there will be investigated eight different scenarios. These scenarios will be detailed in the following table, where the linearity and non-linearity of the materials will be alternated for each gap to validate the model.

No	Interface	Steel plates	Concrete core
[1]	Nonlinear	Linear	Linear
[2]	Nonlinear	Nonlinear	Linear
[3]	Nonlinear	Linear	Nonlinear
[4]	Nonlinear	Nonlinear	Nonlinear
[5]	Linear	Nonlinear	Nonlinear
[6]	Linear	Linear	Nonlinear
[7]	Linear	Nonlinear	Linear
[8]	Linear	Linear	Linear

Table A.8: Material behavior scenarios

This section presents the results of each model under shear conditions. It will visually depict material behavior scenarios using graphs, which will validate the small beam model based on the selected constitutive models and corresponding inputs.

In Figure A.19, there are observed the force-displacement graphs for different material behavior scenarios with a gap length of 10 mm. Notably, Analysis [3] exhibits behavior similar to that of Analysis [4], where the non-linearity of concrete becomes apparent before the failure of the interface or the steel plates. Similarly, Analysis [8] follows a linear behavior akin to that of Analysis [7], indicating that the steel plates have not yet reached the yielding point and continue to exhibit linear behavior.

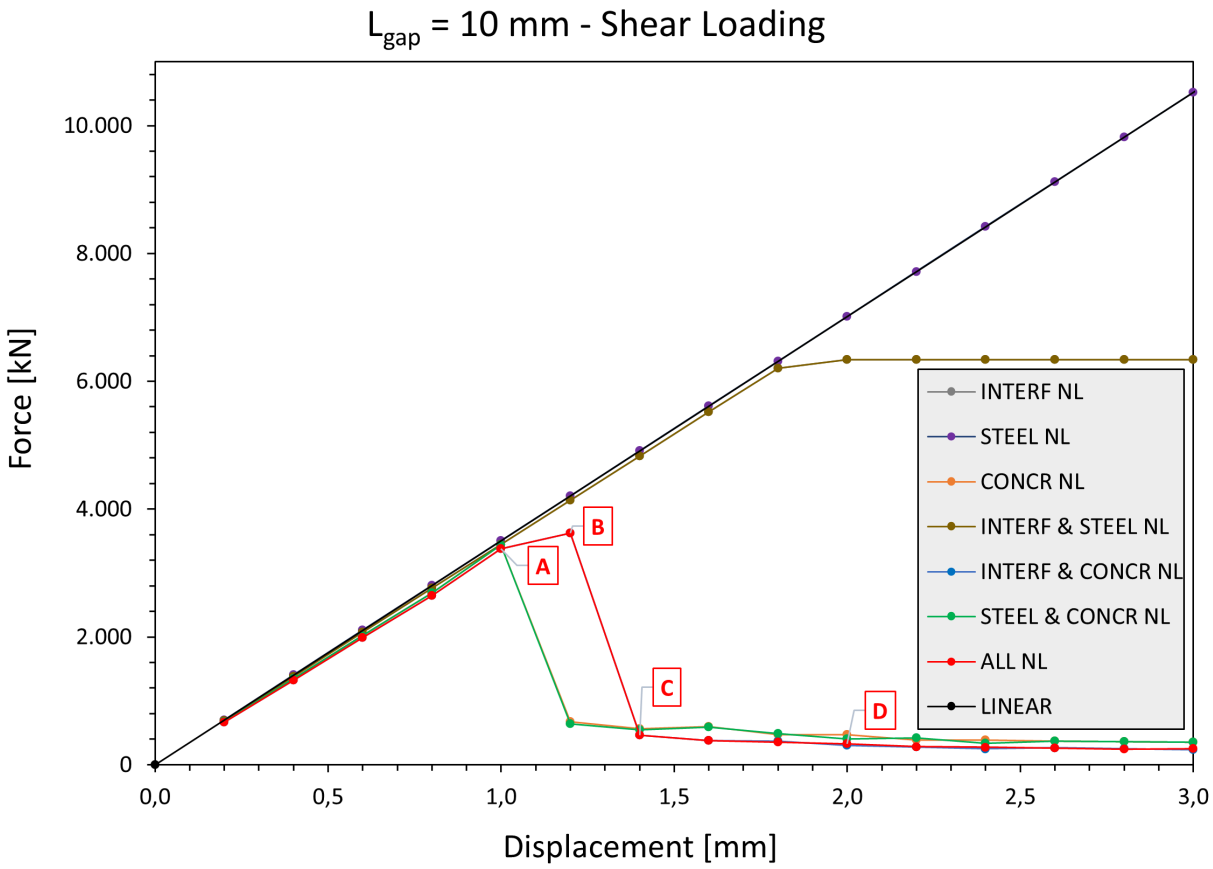

Figure A.19: Force - Displacement graph due to shear load (Lgap = 10 mm)

Based on figure A.19, the conclusions for each one of the analysis is summarized below:

- Nonlinear - Interface Analysis: This line shows a high initial stiffness, as indicated by the steep slope at the beginning, which suggests a strong resistance to shear forces. However, it quickly reaches a plateau, indicating that the interface's capacity to resist shear forces does not increase with further displacement.

- Nonlinear - Steel Analysis: The steel material represented by this line exhibits a consistent increase in force with displacement, indicating a linear elastic behavior without a clear yielding point within the range shown for the specific applied load. (The Linear Analysis is also described with the same behavior as the Nonlinear - Steel Analysis).

- Nonlinear - Concrete Analysis: The concrete material starts with a similar trend to steel but becomes steeper, implying that concrete may have a higher rate of force increase with displacement, possibly due to cracking of the concrete core.

- Nonlinear - Steel, Concrete Analysis: This line suggests a composite behavior of steel and concrete, starting less steeply and then increasing in steepness, which could be due to the combined effects of both materials' responses to shear loading. (This analysis is has the same behavior as the analysis

with non-linearity in concrete, explained in the bullet point above)

- Nonlinear Analysis (All materials nonlinear): The solid line represents a model that includes all non-linearities, showing the steepest slope throughout its length. This indicates a material or system with a high rate of force increase with displacement, suggesting a strong resistance to shear forces before reaching a yielding or failure point. (This analysis is has the same behavior as the analysis with non-linearity in interface and concrete)

In Figure A.20 are presented the force-displacement graphs for different material behavior scenarios with a gap length of 10 mm for the load case of bending. For this specific load case, a larger displacement load was applied to achieve non-linear behavior.

Based on the graph below, there are observed similarities in the behavior of analyses [2] and [7], attributed to the common input characteristic of steel non-linearity. Similarly, analyses [2] and [3] exhibit similarity due to the combined non-linearity of concrete and steel. Meanwhile, analyses [4] and [5] demonstrate approximately similar force-displacement behavior, primarily influenced by concrete non-linearity. Interestingly, the non-linearity of the interface has minimal impact on the overall model behavior when combined with the non-linearity of concrete and steel.

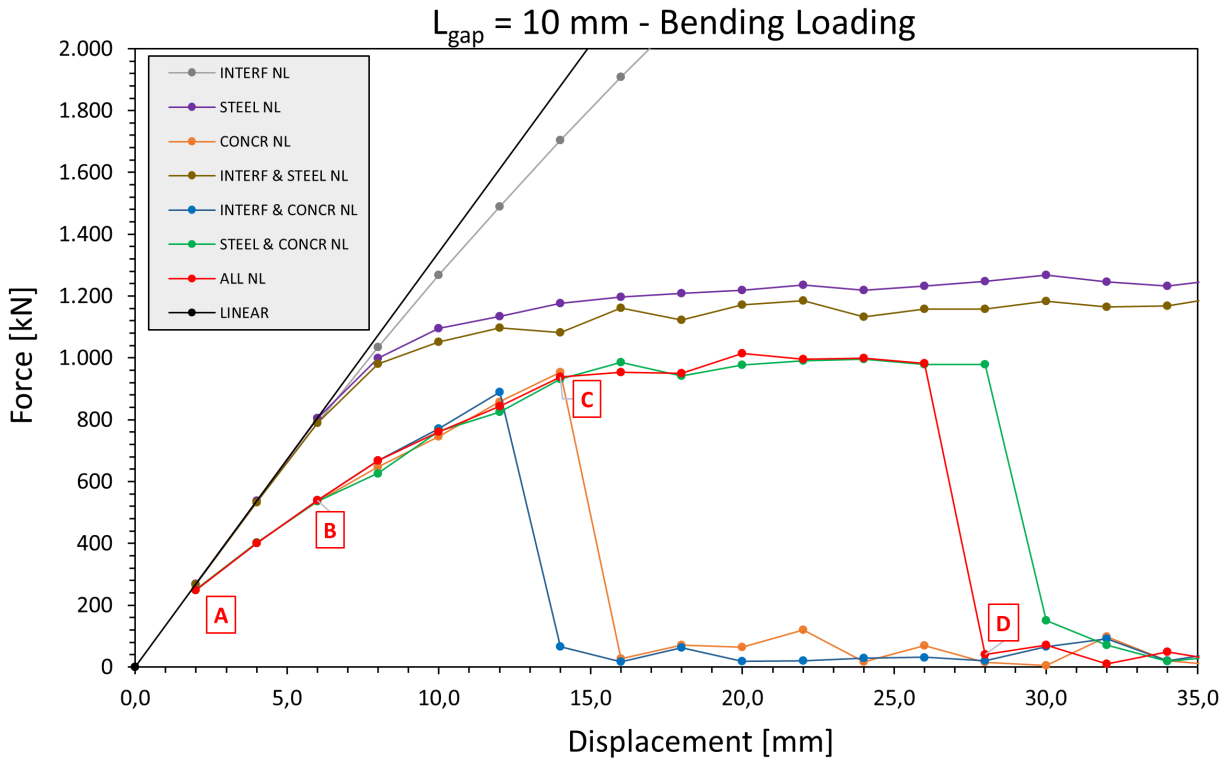

Figure A.20: Force - Displacement graph due to bending (Lgap = 10 mm)

Based on figure A.20, the conclusions for each one of the analysis is summarized below:

- Nonlinear - Interface Analysis: Demonstrates a similar trend to nonlinear - steel analysis but with a less pronounced peak before leveling off, indicating the interface's non-linear response.

- Nonlinear - Steel Analysis: This analysis exhibits a linear increase in force with displacement, indicating elastic behavior until reaching a peak force, after which it plateaus, suggesting yielding or maximum capacity.

- Nonlinear - Concrete Analysis: The corresponding line remains flat, implying no change in force with displacement, which could suggest a lack of contribution to the overall bending resistance in this model.

- Nonlinear - Interface, Steel Analysis: The line of this analysis increases more gradually, reaches a lower peak force, and then drops off sharply, showing the influence of interface non-linearity combined with steel's response.

- Nonlinear - Interface, Concrete Analysis: This line shows a steep initial increase, reflecting high stiffness, and then levels off, indicating a limit to force increase despite further displacement.

- Nonlinear - Steel, Concrete Analysis: In this analysis it is observed a line which increases similarly to the nonlinear - steel line but with a slightly lower peak force, indicating combined behavior of steel and concrete under bending.

- Nonlinear Analysis (All materials nonlinear): The solid line demonstrates a steep initial increase and then levels off at a lower force value, suggesting that when all nonlinearities are considered, the system has a lower overall force capacity.

- Linear Analysis: The line maintains a constant linear relationship between displacement and force, representing an idealized elastic behavior without yielding.

To validate the model, there will be considered the worst-case scenarios, which include nonlinear behavior of the materials. It is sufficient to validate one of the two models, either the one with shear load or the one with bending load. Thus, based on the shear load case (figure A.19), the model's different behaviors fall into three categories. The first category addresses the non-linearity of a single material. The second category involves a combination of non-linearity in two materials, while the third category combines non-linearity in all three different materials. Thus, for the validation, results of Analysis [1] will explain the basic case of only one material with non-linearity. Later, the results of Analysis [2] will combine the non-linearity of two materials: interface and steel plates. Finally, Analysis [4] will address the nonlinear behavior of all the materials used in the composite beam.

In case of Analysis [1] where the only non-linearity is in the interfaces, the following graphs shows and validates the material behavior. For the interfaces the input is based on stiffness's results which are shown in section A.4.6 and also based on figure A.15. The second yielding point, determined by the arrangement of stiffeners and studs in the model, is 5.7588 N/mm^2. This value is substantiated by the accompanying graph.

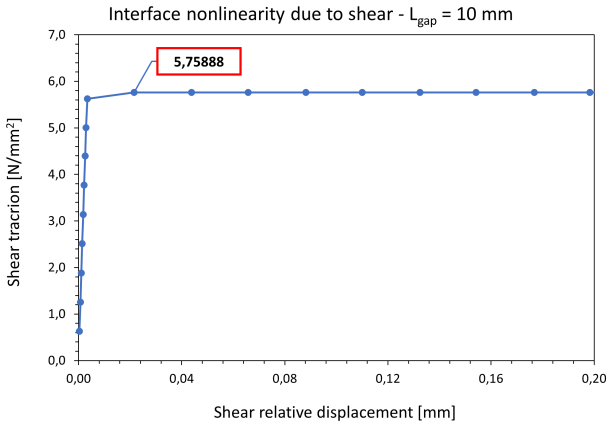

Figure A.21: Non-linear behavior of interfaces

In Analysis [2], where non-linearity is applied to both the interface and steel plates, linear behavior is observed in the steel plates. This phenomenon occurs because the interface reaches the yielding point before the steel plates. Consequently, a nonlinear behavior graph is expected for the interface, while the steel plates exhibit a linear behavior graph.

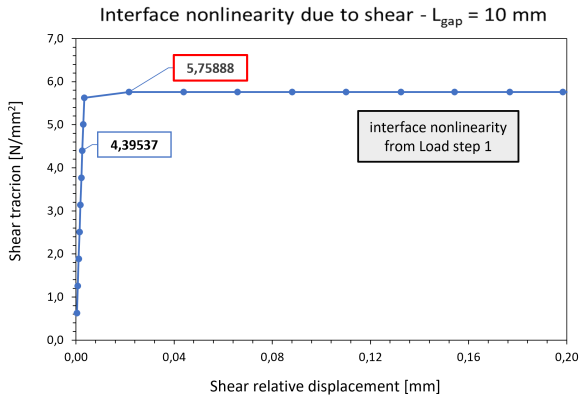

Figure A.22: Interface behavior

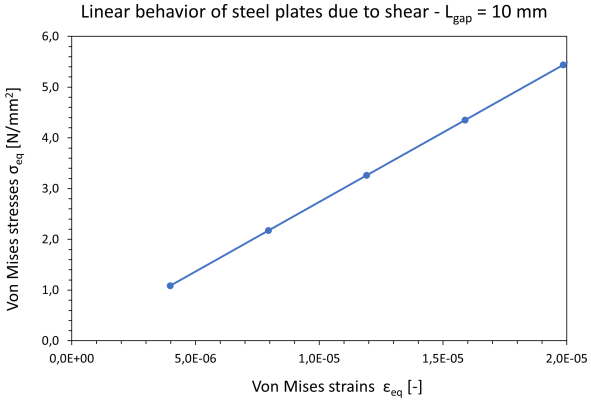

Figure A.23: Steel plates behavior

Figure A.24: Behavior of interface and steel plates for the analysis NL INTERF & STEEL

In Analysis [4], where non-linearity is applied to all the materials of the small beam, four different load levels (points A, B, C, D) are chosen to accurately describe the damage caused in the small beam. Point A represents the end of the linear regime and the occurrence of the first cracks. Point B corresponds to shear cracks dominating the beam's response due to shear loading. Point C refers to the moment when flexural cracks appear and spread diagonally from the point where the displacement is applied and lastly, Point D marks approximately the stage where the loss of strength stabilizes, and significant shear damage is present in the structure. The different load levels are briefly explained in the following table (Table A.9) for the reader's convenience.

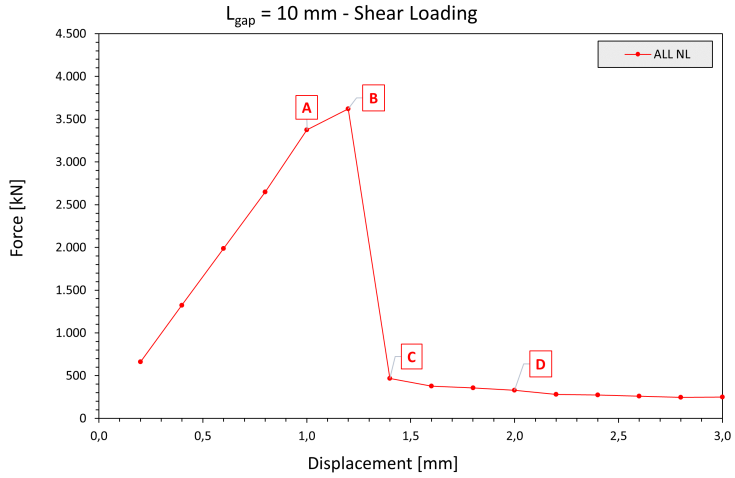

Figure A.25: Analysis ALL NL

A	End of linear regime - Occurrence of first cracks
B	Shear cracks dominate the response and are spreaded entirely allover the beam's length
C	Flexural cracks appear diagonally from the point of the applied displacement
D	Cracks are expanded diagonally - Large shear damage and deformation has occurred

Table A.9: Different behavioral phases of Analysis [4]

Based on the chosen constitutive models for concrete behavior, the following graphs (Figure A.28) demonstrate the expected non-linearity in the concrete core. In tension, where cracking occurs, the concrete core begins to crack at load step 5 and reaches the maximum tensile strength input of approximately 3.21 N/mm^2. Similarly, in compression, the concrete core exhibits a value close to the maximum compressive strength of 23.33 N/mm^2.

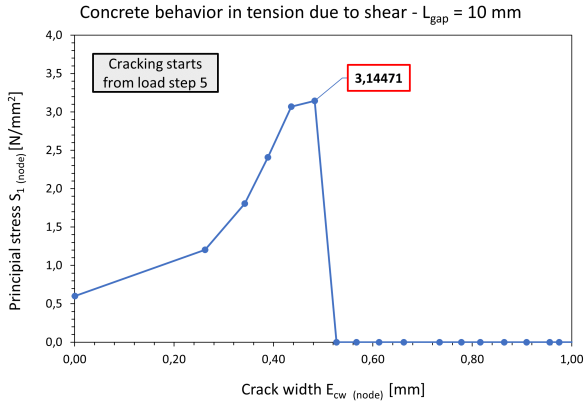

Figure A.26: Figure 1

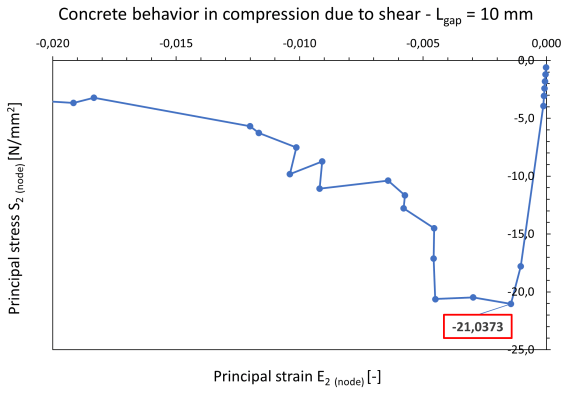

Figure A.27: Figure 2

Figure A.28: Tensile (cracking) and compressive (crushing) behavior of concrete for the analysis ALL NL

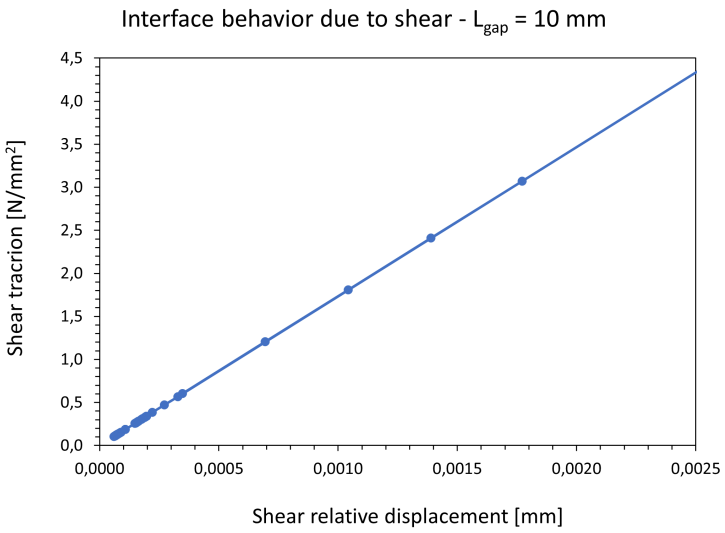

Figure A.29: Interface behavior for the analysis ALL NL

Conversely, Figure A.29 above reveals a linear behavior in the interfaces between the steel plates and the concrete core. This phenomenon can be attributed to the fact that cracking initiates in the concrete core, preventing the interfaces from reaching the yielding point. The same reasoning applies to the steel, where the expected graph for the steel plates exhibits linearity similar to that of the interfaces.

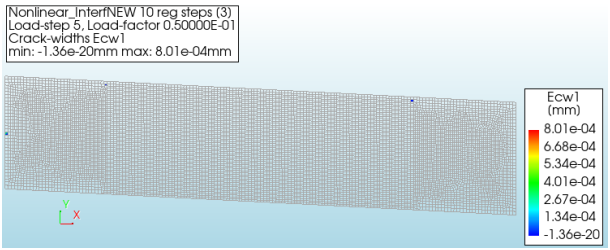

Figure A.30: Point A

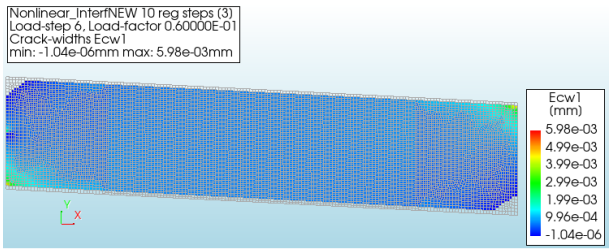

Figure A.31: Point B

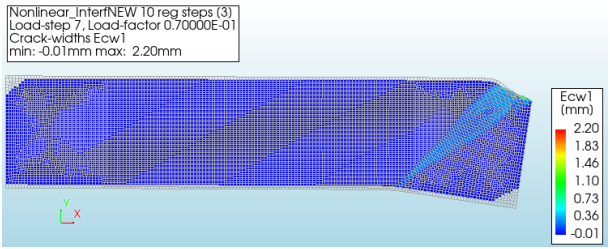

Figure A.32: Point C

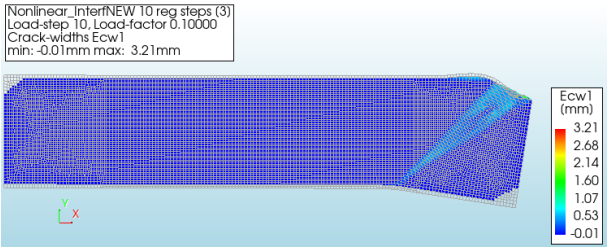

Figure A.33: Point D

Figure A.34: Crack-width results (tension) of Analysis [4] (scale factor: 5)

The figure provided above (figure A.34) depicts the tensile behavior of due to shear load on the small composite beam, focusing on the crack width of the concrete core. Initial figures A.30 and A.31 show stress

distributions with low stress values, indicating the early stages of load application. Figure A.31 presents a detailed visualization of crack widths under tension with increasing values, highlighting areas where cracks are likely to develop or widen. Specifically, at load step 7 rapid crack propagation occurs, resulting in a large diagonal crack pattern originating from the applied displacement point. This leads to significant deformations at the right free end of the beam. At the final stress state depicted in figure A.33 (step D), it is observed a higher range of stress values, suggesting further progression in the beam's response to the applied shear load and furthermore, failure as it is reached the maximum tensile strength of 3.21 N/mm^2.

Referring to the same observations, the compression of the concrete core is evident in the following figure.

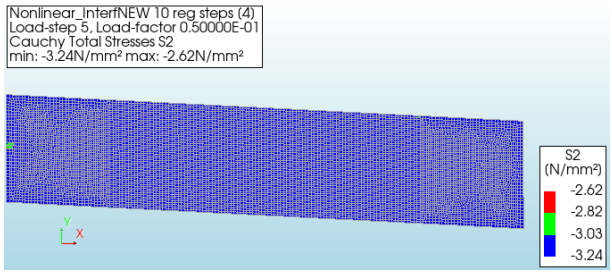

Figure A.35: Point A

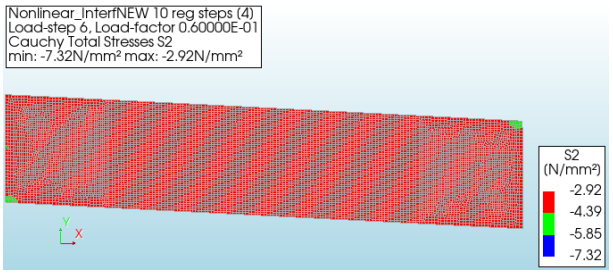

Figure A.36: Point B

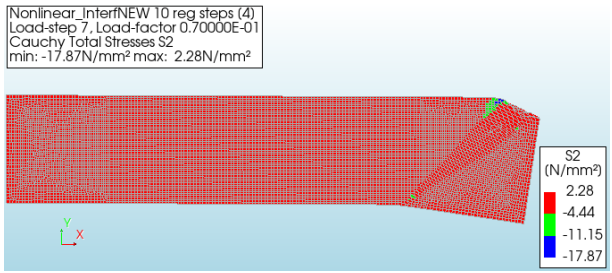

Figure A.37: Point C

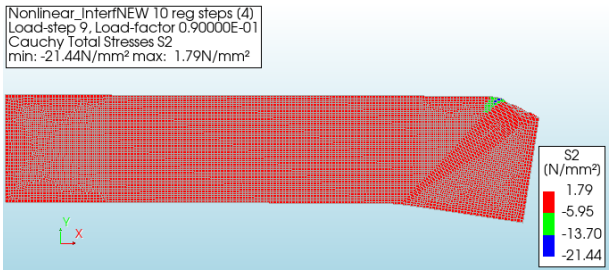

Figure A.38: Point D

Figure A.39: Crushing of concrete core of Analysis [4] (scale factor: 5)

The first figure (figure A.35) highlights the initial stress levels. which start in load step 5 of the analysis, and indicates low stress levels with minimal deformation, as shown by the predominance of blue color. As the load increases, the following figure A.35, shows increased stress concentration, particularly at the top and bottom of the core, where red areas become more prominent. The figure A.37 demonstrates a progression of stress and deformation, with the final figure A.38 depicting almost the entire sample in red, indicating a critical stress level and the crushing of the concrete core approximating the maximum compression strength of concrete (23.33 kN).

In addition, for better understanding of the worst-case scenario for the different load cases of shear and bending, it is needed a direct comparison. By analyzing the results from analysis [4] (where all materials are nonlinear) for both shear and bending, it can be drawn meaningful conclusion about the behavior of the small beam. Below, it is presented a graph that facilitates this comparison.

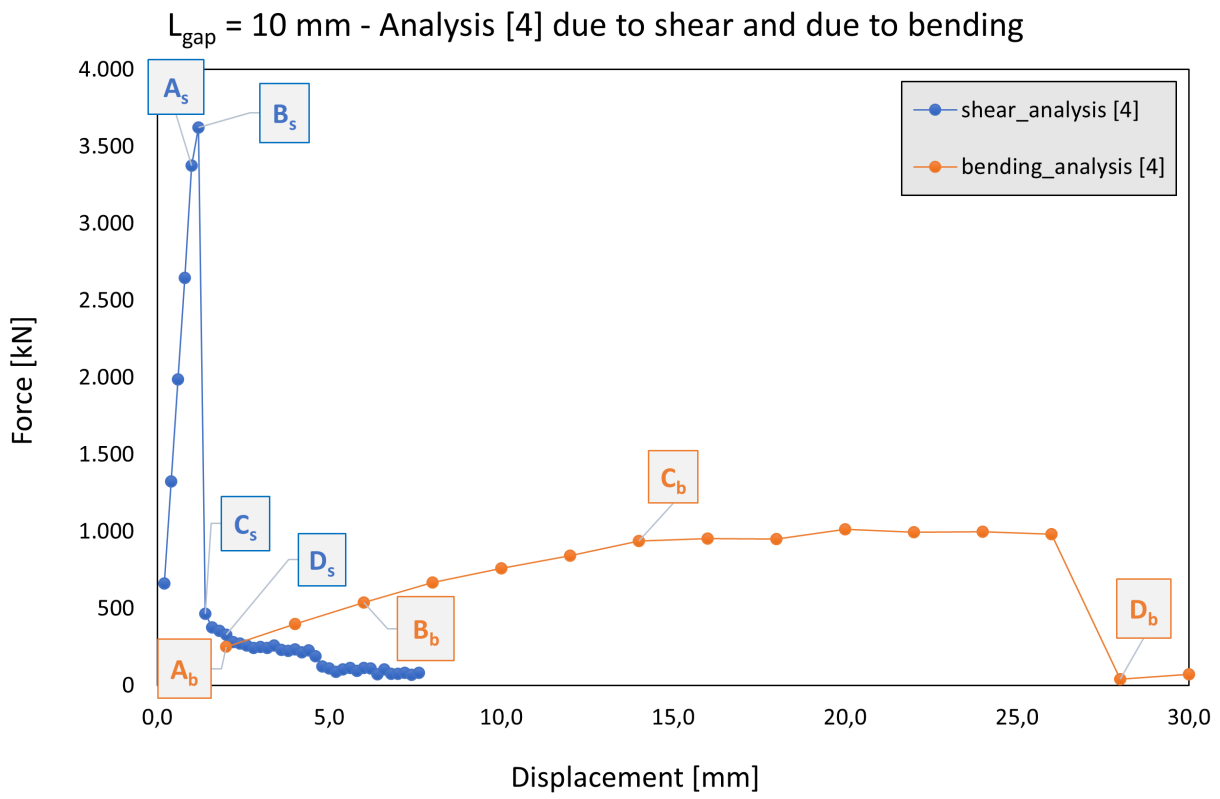

Figure A.40: Analysis [4] - Shear Vs Bending

The graph presents a comparative analysis of the concrete core's response of the composite small beam under shear and bending load case. The horizontal axis measures displacement in millimeters, while the vertical axis measures force in kilonewtons.

Regarding the shear analysis, the line representing shear analysis shows a steep initial increase in force with minimal displacement, reaching a peak force of 3500 kN at a displacement of 1 mm. This suggests a high resistance to shear forces. Following the peak, there is a sharp decline, indicating a failure or yielding point in the material. In contrast, the bending analysis line rises more gradually, peaking at 500 kN with a 5 mm displacement. This indicates a lower resistance to bending forces and a more ductile behavior, as the force decreases slowly after the peak.

A key conclusion is that the concrete core of the composite small beam exhibits significantly higher resistance to shear forces compared to bending forces. Both shear and bending analyses show a decrease in force beyond specific displacement points, indicating material damage or structural yielding. The shear analysis demonstrates less ductility with a sharp peak, brittle behavior, while the bending analysis displays a more gradual force increase and decrease.

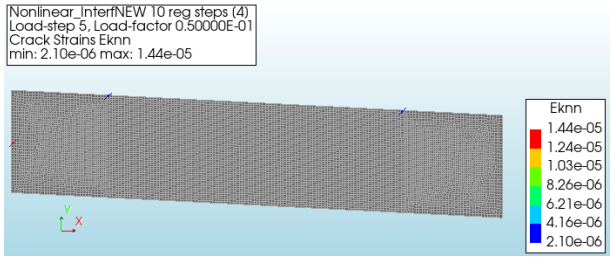

Figure A.41: Shear - *Step* A_s

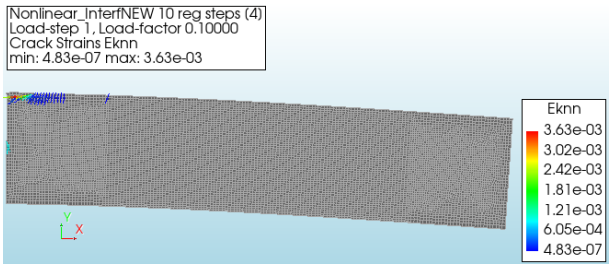

Figure A.42: Bending - *Step* A_b

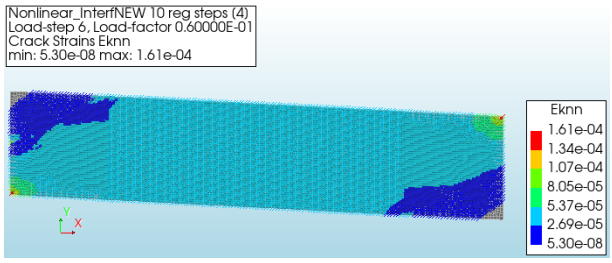

Figure A.43: Shear - *Step* B_s

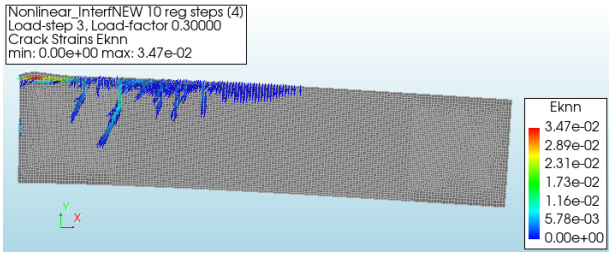

Figure A.44: Bending - *Step* B_b

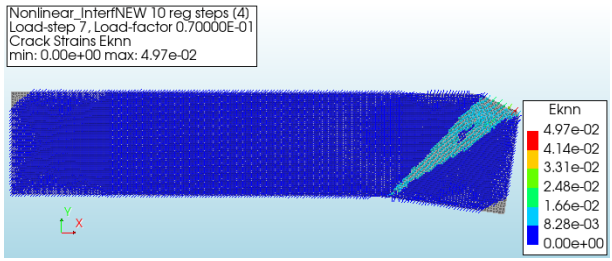

Figure A.45: Shear - *Step* C_s

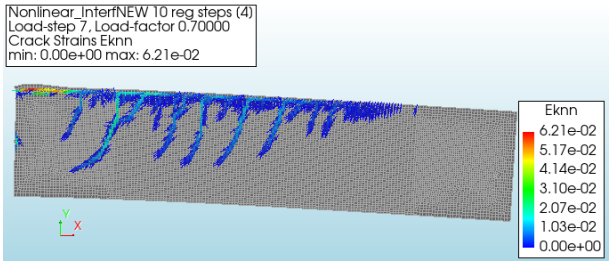

Figure A.46: Bending - *Step* C_b

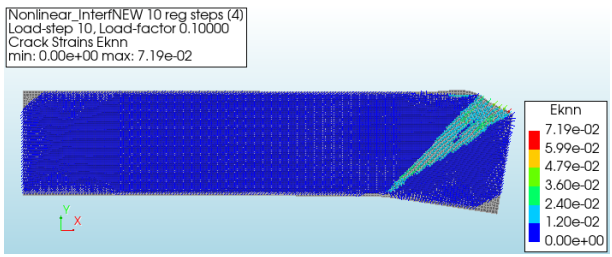

Figure A.47: Shear - *Step* D_s

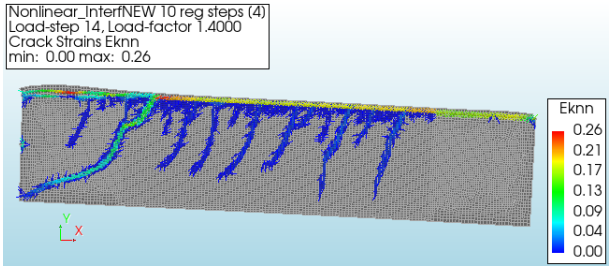

Figure A.48: Bending - *Step* D_b

Figure A.49: Crack strains Eknn - Shear Vs Bending- Analysis [4]

The figure provided illustrates the progression of crack strains (E_knn) in the small composite beam under shear and bending load case, observed at different steps (A to D). Figures A.41 (shear) and A.42 (bending), which correspond to the initial strain distribution (step A), show low strain values, indicating the initial response of the beam to the applied loads. Figures A.43 to A.46 are about strain progression (Steps B and C) which depict increasing strain values with advancing load steps, highlighting areas of the beam experiencing higher stress concentrations. At the final strain state (Step D), Figures A.47 (shear) and A.48 (bending) reveal the final strain distribution, with red areas indicating the highest strain levels, likely where cracks

would initiate or propagate.

The comparison in Figure A.49 shows different strain patterns for the different shear and bending load case, essential for understanding the beam's behavior and its potential failure modes.

In the figure A.50 below, force-displacement graphs from analysis [4] depict the behavior of the small composite beam with gap sizes of 5 mm, 10 mm, 15 mm, and 20 mm. Non-linearity is considered for each material in the beam.

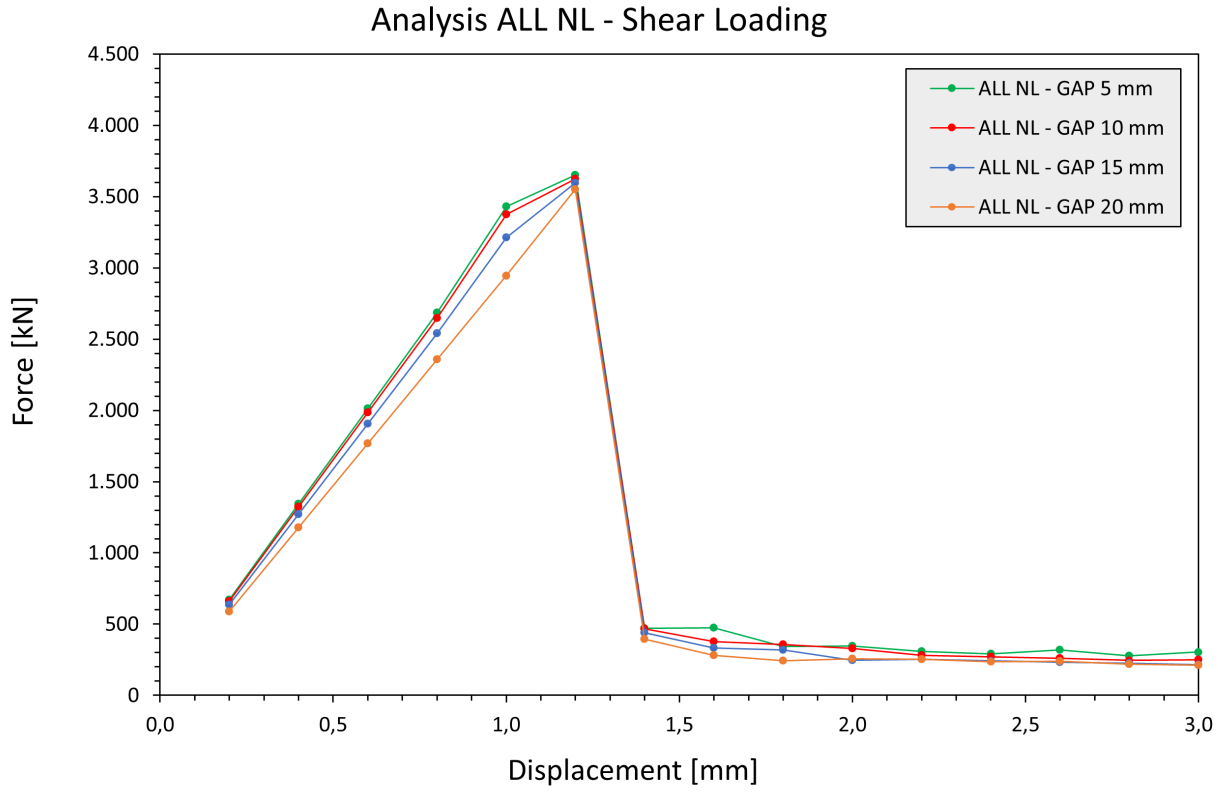

Figure A.50: All gaps - Analysis [4]: ALL NL

The significant observations can be categorized into the following:

- Peak Force Consistency: All gap sizes (5 mm, 10 mm, 15 mm, and 20 mm) exhibit similar peak forces before failure. This suggests that the initial stiffness due to the gaps does not significantly affect the maximum load-carrying capacity of the beam.

- Post-Peak Behavior: After reaching the peak force, there's a sharp reduction in force with increased displacement. This indicates rapid deterioration of structural integrity post-failure initiation.

The nonlinear analysis of concrete, steel, and interface materials is crucial, as it influences the structural performance, especially after the peak load capacity is reached.

A key conclusion is that the 20 mm gap is the most critical and risky one for the composite beam. The

20 mm gap exhibits a lower peak force compared to the other gap sizes. This means that it reaches its maximum load-carrying capacity earlier during deformation. After reaching the peak force, the 20 mm gap experiences a rapid drop in force with increased displacement. This indicates that failure initiates sooner for the larger gap. Thus, the 20 mm gap provides less initial stiffness, making the beam more vulnerable to deformation. Once failure begins, any additional displacement leads to a significant reduction in resistance.

Bibliography

[1] Nestor S Rasmussen. "Immersed tunnels". In: *Structural Engineering International* 5.4 (1995), pp. 213–213.

[2] Richard Lunniss and Jonathan Baber. *Immersed tunnels*. CRC Press, 2013.

[3] Allison LC de Cerreño. *State Arterial Highway System Peer City Study*. Tech. rep. 2006.

[4] Bo Larsson and Ole Thomassen. "Urban planning in Denmark". In: *Planning and Urban Growth in Nordic Countries*. Routledge, 2003, pp. 21–81.

[5] Shogo Matsuo. "An overview of the Seikan tunnel project". In: *Tunnelling and Underground Space Technology* 1.3-4 (1986), pp. 323–331.

[6] Yikai Cheng et al. "FuzhouXiamen high-speed railway: a new paradigm for Chinas cross-sea railways". In: *Proceedings of the Institution of Civil Engineers - Civil Engineering* 176.4 (2023), pp. 156–163. ISSN: 0965-089X. DOI: https://doi.org/10.1680/jcien.23.00034. URL: https://www.sciencedirect.com/science/article/pii/S0965089X23000101.

[7] Søren Spangenberg et al. "The construction of the Øresund Link between Denmark and Sweden: the effect of a multi-faceted safety campaign". In: *Safety Science* 40.5 (2002), pp. 457–465.

[8] Yao-Yu Zhu et al. "Experimental and Numerical Investigation of the Cross-Sectional Mechanical Behavior of a Steel–Concrete Immersed Tube Tunnel". In: *Buildings* 12.10 (2022), p. 1553.

[9] Keiichi Akimoto et al. "Immersed tunnels in Japan: Recent technological trends". In: *Proceedings of the 2002 Interntional Symposium on Underwater Technology (Cat. No. 02EX556)*. IEEE. 2002, pp. 81–86.

[10] J Hawley and R Pöttler. "The Channel Tunnel: numerical models used for design of the United Kingdom undersea crossover". In: *Tunnelling 91, IMM* (1991).

[11] A Glerum. "Immersed tunnels: Why, when and where". In: *Tunnelling and underground space technology* 3.4 (1988), pp. 347–351.

[12] Arjan Luttikholt et al. "Consideration of concrete and steel sandwich tunnel elements". In: *Tunnelling and Underground Space Technology* 121 (2022), p. 104309.

[13] Jin Wenliang Liu Jian Chen Yue and Song Shenyou. "Shenzheng-Zhongshan mega sea link". In: *Shen-Zhong Link Administration Center - Tunnel Talk* (2021). URL: https://www.tunnelsandtunnelling.com/analysis/shenzhen-zhongshan-mega-sea-link/?cf-view&Top-Article-Share-Button-clicked:%20Copy%20Link&Bottom-Article-Share-Button-clicked:%20Copy%20Link#.

[14] Weile Chen et al. "Lateral static analysis on steel-concrete-steel composite structure in immersed tunnel of Shenzhen-Zhongshan Link". In: *Ninth International Conference on Advances in Steel Structures*. 2018, pp. 717–728.

[15] Yu-Tao Guo, Jian-Sheng Fan, Jian-Guo Nie, et al. "THE NEW TREND OF COMPARTMENT STEEL-CONCRETE-STEEL COMPOSITE STRUCTURES IN IMMERSED TUNNELS". In: (2018).

[16] Man Zhou et al. "New Technologies and Challenges in the Construction of the Immersed Tube Tunnel of the Hong Kong-Zhuhai-Macao Link". In: *Structural Engineering International* 32.4 (2022), pp. 455–464.

[17] Nandolia Usamaa et al. *Comparative Analysis of Underground & Underwater Tunnel*. 2020.

[18] Jia-Bao Yan et al. “Experimental and analytical study on ultimate strength behavior of steel–concrete–steel sandwich composite beam structures”. In: *Materials and Structures* 48 (2015), pp. 1523–1544.
[19] Peng Liu et al. “Mechanical model for joints of immersed tunnel considering the influence of joint differential settlement”. In: *International Journal of Geosynthetics and Ground Engineering* 6 (2020), pp. 1–10.
[20] JY Richard Liew, Jia-Bao Yan, and Zhen-Yu Huang. “Steel-concrete-steel sandwich composite structures-recent innovations”. In: *Journal of constructional Steel research* 130 (2017), pp. 202–221.
[21] Fengyong Xia et al. “Full-Scale Model Experimental Research on Concrete Construction Technology of Steel Shell Immersed Tube Tunnel”. In: *IOP Conference Series: Earth and Environmental Science*. Vol. 719. 3. IOP Publishing. 2021, p. 032088.
[22] Yu-Tao Guo et al. “Investigation of the shear resistances of steel–concrete–steel composite structures with bidirectional webs”. In: *Journal of Constructional Steel Research* 164 (2020), p. 105846.
[23] Kaythar Ibrahim. “INVESTIGATING THE EFFECT OF THE REPEATED LOADS ON THE BEHAVIOR OF JOINT IN A BRIDGE BETWEEN STEEL AND CONCRETE SECTIONS”. PhD thesis. Apr. 2022. DOI: 10.13140/RG.2.2.28003.63527.